TECHNISCHE UNIVERSITÄT MÜNCHEN

Lehrstuhl für Theoretische Chemie

Quantum Dynamics of Ultrafast Electron Transfer Processes in Dye-Semiconductor Systems

Jingrui Li

Vollständiger Abdruck der von der Fakultät für Chemie der Technischen Universität München zur Erlangung des akademischen Grades eines

Doktors der Naturwissenschaften

genehmigten Dissertation.

Vorsitzender:		Univ.-Prof. Dr. Christian F. W. Becker
Prüfer der Dissertation:	1.	Univ.-Prof. Dr. Michael Thoss Friedrich-Alexander-Universität Erlangen-Nürnberg
	2.	Univ.-Prof. Moniek Tromp, Ph. D.

Die Dissertation wurde am 11.02.2011 bei der Technischen Universität München eingereicht und durch die Fakultät für Chemie am 29.03.2011 angenommen.

Abstract

Ultrafast photoinduced heterogeneous electron transfer processes in dye-semiconductor systems are studied employing a first-principles based methodology. A partitioning scheme is used to define localized donor and acceptor states and to parametrize a model Hamiltonian based on electronic structure calculations for the dye-semiconductor systems. On the basis of this modeling procedure, accurate quantum dynamical simulations are performed employing the multilayer multiconfiguration time-dependent Hartree method. As representative examples, applications of this methodology to several dye-semiconductor systems are presented. Simulations for the dye molecule alizarin adsorbed at a titanium oxide nanocluster show that the electron injection process in this system takes place on an ultrafast femtosecond timescale and is accompanied by significant electronic coherence effects. A detailed analysis reveals that the electron transfer process in this system proceeds via a two-step mechanism involving an intermediate state localized at the adsorbate-substrate interface. For systems containing pyridine- or perylene-based adsorbates anchored at titanium oxide nanoclusters via different groups, the results of simulations show that the ultrafast electron injection dynamics is significantly influenced by the chemical nature of the adsorbate, especially that of the anchor groups and the spacer groups. Furthermore, the effect of Dushinsky rotation on the electron transfer dynamics is investigated for coumarin 343 adsorbed at titanium oxide nanoparticles.

Kurzfassung

Gegenstand der Arbeit sind theoretische Untersuchungen von ultraschnellen photoinduzierten Elektrontransfer(ET)-Prozessen in Farbstoff-Halbleiter-Systemen. Die theoretische Beschreibung verwendet einen Modellhamiltonoperator, dessen Parameter durch first-principles Elektronenstruktur-Rechnungen auf der Basis von Dichtefunktionaltheorie charakterisiert werden. Die Donor- und Akzeptorzustände der heterogenen ET-Prozesse werden dabei mittels einer Projektionsmethode bestimmt. Auf der Basis dieser Modellierung werden unter Verwendung der Multilayer Multiconfiguration Time-Dependent Hartree (ML-MCTDH) Methode akkurate quantendynamische Simulationen durchgeführt. Die betrachteten Anwendungsbeispiele umfassen eine Reihe repräsentativer Farbstoffmoleküle adsorbiert auf Titanoxid-Substraten. Für den Farbstoff Alizarin, adsorbiert auf Titanoxid-Nanopartikeln, ergeben die Simulationen eine ultraschnelle Elektroneninjektion auf einer Zeitskala von nur wenigen Femtosekunden, die von ausgeprägten elektronischen Kohärenzeffekten begleitet ist. Die genaue Analyse zeigt, dass der ET-Prozess in diesem System einem zweistufigen Mechanismus folgt, mit einem Zwischenzustand, der an der Adsorbat-Substrat-Grenzfläche lokalisiert ist. Rechnungen für Pyridin- und Perylen-basierte Farbstoffe auf Titanoxid ergeben, dass der genaue Verlauf der ultraschnellen ET-Dynamik von der chemischen Natur des Adsorbats, insbesondere der Anker- und Brückengruppen, stark beeinflusst wird. Als ein weiterer interessanter Mechanismus wird der Einfluss der Duschinski-Rotation der Normalmoden auf die ET-Dynamik am Beispiel von Coumarin-343, adsorbiert auf Titanoxid-Nanopartikeln, untersucht.

Contents

Chapter 1

Introduction

Electron transfer (ET) reactions in molecular systems are elementary processes that involve the translocation of an electron (or several electrons) within a single molecule, a molecular aggregate or an arrangement of molecules embedded in various types of environments [1]. ET reactions are of importance in many different fields of physics, inorganic chemistry, organic chemistry and biochemistry [1–3]. Important examples include isotopic exchange reactions and cross reactions [4, 5], redox reactions among coordination compounds of metals [6], intramolecular charge transfer in organic compounds [7], electron transfer in photosynthesis [8–10], as well as electron transport in single-molecule junctions [11].

This thesis will focus on theoretical studies of photoinduced ET reactions at dye-semiconductor interfaces. These reactions represent interesting examples of *heterogeneous* surface ET processes, which play an important role in many fields [12]. An ET reaction in these systems can be described as the electron injection process from an electronically excited state of a chemisorbed dye molecule (the *donor*) into a semiconductor substrate (the *acceptor*). This process represents the key step for photonic energy conversion in *dye-sensitized solar cells* (DSSC, sometimes also called *Grätzel cells*) [13–19]. A DSSC is a photovoltaic device based on transition-metal or organic dye molecules that are adsorbed to a highly porous, nanocrystalline semiconductor and embedded in an electrolyte. The operation principle of a DSSC is sketched in Fig. 1.1 [13, 18]. Visible light ($h\nu$) excites the dye molecule from its ground state S_0, which is energetically located in the band gap of the semiconductor, to an excited state S_1, which is resonant with the conduction band of the semiconductor. The photoexcited dye adsorbate then injects electrons to the semiconductor (the photoanode). The thus oxidized adsorbate in turn oxidizes the mediator, which is formed by a redox species (R/R^-) dissolved in the electrolyte. The mediator is regenerated in a reduction process at the cathode by electrons which flow through the external circuit.

In recent years, the process of electron injection in dye-semiconductor systems has

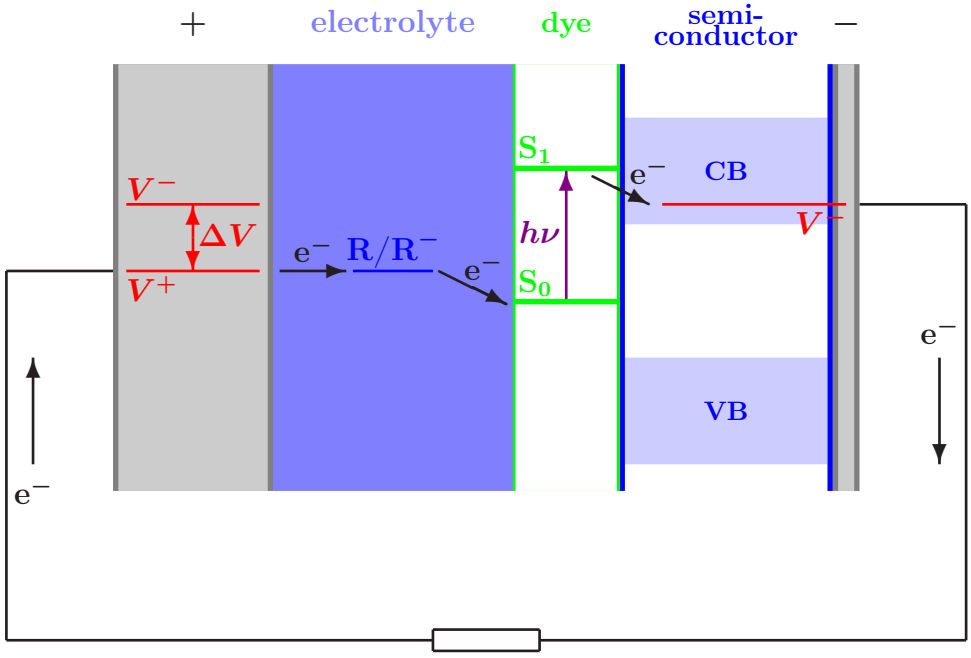

Figure 1.1: Schematic representation of the principle of a dye-sensitized solar cell (DSSC). Shown are the conducting-glass photoanode (in gray, labeled as "−"), the semiconductor (in light blue, with its conduction band and valence band labeled as CB and VB, respectively), the dye (green) which is adsorbed to the surface of the semiconductor, the electrolyte (dark blue) which can be a liquid, a gel or an organic solid, and the conducting-glass cathode (in gray, labeled as "+"). The photoexcitation ($h\nu$) of the dye-adsorbate from its ground state S_0 to its excited state S_1, the flow of electrons in the closed circuit and the redox pair R/R^- of the electrolyte are indicated. The maximum voltage ΔV is determined by the difference between the (quasi-)Fermi level of the semiconductor under illumination (shown by the red line labeled as V^-) and the electrochemical potential of the electrolyte (shown by the red line labeled as V^+).

been studied in great detail experimentally for many different systems [15, 17, 20–33]. Employing femtosecond laser spectroscopy techniques, which allow the observation of ultrafast photoreactions in real time by monitoring the electronic and vibrational spectra of the products of the electron injection reactions (*i.e.*, the oxidized adsorbate molecules and the electrons in the semiconductors), it has been shown that electron injection processes at interfaces of dye-semiconductor systems often take place on an ultrafast sub-picosecond timescale [17, 26, 29, 30, 34, 35]. These experimental studies were performed on different dye-semiconductor systems. The employed dye adsorbates include transition-metal (mostly ruthenium) / ligand complexes (in particular the so-called N3-dye [13,15–18]) and purely organic dyes. Besides the most commonly used titanium oxide nanoparticles, zirconium oxide, zinc oxide and tin oxide have also been used as semiconductor substrate [17, 24, 27, 29]. An electron-injection time as

fast as 6 fs has been reported for alizarin adsorbed at titanium oxide nanoparticles in time-resolved experiments [29]. A faster electron-injection time (3 fs) has been reported for bi-isonicotinic acid adsorbed at titanium oxide employing resonant photoemission spectroscopy techniques [30].

Theoretical studies of interfacial ET reactions require a quantum mechanical description of the overall processes including a characterization of the electronic structure of the system as well as a simulation of the ET dynamics and the associated nuclear dynamics. For complex systems such as dye-semiconductor interfaces, a fully quantum mechanical treatment of the electronic-nuclear dynamics associated with the ET process is challenging. In recent years, a variety of different theories and methods [36–40] have been developed. These methods can be classified into two categories. In some methods [37, 38], the dynamics of electron injection is simulated based on first-principles electronic structure calculations of the ET system. Thereby the nuclear motion is treated approximately using classical mechanics. On the other hand, methods which employ a parametrized model Hamiltonian [36, 39] often allow a fully quantum mechanical treatment. In these studies, however, the parameters were often determined semiempirically from experimental results.

In this thesis, the quantum dynamics of ET processes in dye-semiconductor systems will be studied employing a recently proposed methodology [41]. In this method, the dye-semiconductor system is characterized based on first-principles electronic structure calculations, and the electronic-nuclear dynamics associated with the ET process is simulated at a fully quantum mechanical level employing a numerically exact approach. We will employ this first-principles based approach to analyze photoinduced interfacial ET processes in several dye-semiconductor systems, including alizarin, coumarin 343 and different pyridine- and perylene-based dye molecules adsorbed at titanium oxide nanoparticles. In particular, interesting aspects of ET processes in these systems, including the ultrafast ET timescale, the influence of the coupling to the nuclear motion, electronic coherence effects and their quenching due to dephasing processes, as well as the mechanism of the ET reaction, will be analyzed in detail.

This thesis is structured as follows. In Chapter 2, we outline the details of the first-principles models and the multilayer multiconfigurational time-dependent Hartree (ML-MCTDH) method [42], which is used to simulate the ET dynamics. Chapter 3 presents the results of electronic structure calculations and the ET dynamics for alizarin adsorbed at titanium oxide nanoparticles. In particular, we will study the mechanism of ET reaction in this system based on the analysis of electronic coherence effects. Chapter 4 focuses on systems containing different pyridine- and perylene-based dye molecules adsorbed at titanium oxide nanoparticles. In particular, we

discuss the influence of different anchor groups and spacer groups on the ET dynamics. In Chapter 5, we analyze the ET dynamics in the dye-semiconductor system coumarin 343 - titanium oxide, focusing on effects caused by Dushinsky rotation. Chapter 6 concludes with a summary and a perspective.

Chapter 2

Theoretical Methodology

In this chapter, we introduce the theoretical methodology which is employed in the studies of ET dynamics in the dye-semiconductor systems in the following chapters. This chapter is structured as follows. In Section 2.1, we present a brief overview of ET reactions and the general theoretical background of ET and traditional approaches. Previous studies of heterogeneous ET in dye-semiconductor systems are briefly reviewed in Section 2.2. A detailed introduction of the first-principles based methodology of quantum dynamics, which will be employed throughout this thesis, are given in Sections 2.3 and 2.4. Thereby Section 2.3 focuses on the determination of parameters required in the first-principles based model and Section 2.4 describes the quantum dynamical methods. Finally, Section 2.5 discusses the observables of interest in ET reactions and computational details.

2.1 A brief introduction to electron transfer reactions and traditional kinetic theories

An ET process in a molecular system can be characterized as a charge redistribution between an initially prepared reactant state and a product state [1]. Specifically, it can be formulated as a charge transfer from the donor part to the acceptor part of the system as

$$\mathrm{DA} \rightarrow \mathrm{D}^{+}\mathrm{A}^{-}. \tag{2.1}$$

The overall molecular system is sometimes referred to as a "donor-acceptor complex". According to Eq. (2.1), we can denote the reactant state and the product state by $|\Psi_{\mathrm{reac}}\rangle = |\mathrm{DA}\rangle$ and $|\Psi_{\mathrm{prod}}\rangle = \left|\mathrm{D}^{+}\mathrm{A}^{-}\right\rangle$, respectively.

Eq. (2.1) can be extended to describe most ET reactions. For example, a photoinduced heterogeneous ET process in a dye-semiconductor system can be formulated

as

$$\mathrm{DA} \overset{h\nu}{\rightarrow} \mathrm{D^*A} \rightarrow \mathrm{D^+A^-}, \tag{2.2}$$

where the superscript * indicates that the donor part is photoexcited.

The reactant state $|\Psi_{\mathrm{reac}}\rangle$ and the product state $|\Psi_{\mathrm{prod}}\rangle$ are eigenstates of the overall donor-acceptor complex only when there is no interaction between the donor part and the acceptor part and thus no ET occurs. In this limit, $|\Psi_{\mathrm{reac}}\rangle$ corresponds to the product of the state $|\mathrm{D}\rangle$ localized at the donor part and the state $|\mathrm{A}\rangle$ localized at the acceptor part, and $|\Psi_{\mathrm{prod}}\rangle$ corresponds to the product of the state $\left|\mathrm{D^+}\right\rangle$ localized at the donor part and the state $\left|\mathrm{A^-}\right\rangle$ localized at the acceptor part.

In general, the change of the wave function of the overall system from $|\Psi_{\mathrm{reac}}\rangle$ to $|\Psi_{\mathrm{prod}}\rangle$ during the ET reaction involves a redistribution of electron density. This causes a change of nuclear configuration of the molecular system as well as a polarization of the environment. Thus, an ET process is usually accompanied by the change of the equilibrium configuration of the nuclei and coupled to the nuclear (vibrational) motion of the system. Therefore, when studying an ET reaction, it is often necessary to include the vibrational degrees of freedom (DoF) and the electronic-vibrational coupling in the theoretical treatment.

An overall wave function of an ET system is a function of both electronic and vibrational (nuclear) DoF. In this thesis, we refer to the electronic part of the reactant state, in which the transfered electron is localized at the donor part of the overall system, as the *donor state* (denoted by $\left|\psi^{\mathrm{d}}\right\rangle$), and the electronic part of the product state, in which the transfered electron is localized at the acceptor part, as the *acceptor state* (denoted by $|\psi^{\mathrm{a}}\rangle$). For a fixed nuclear configuration, a non-vanishing electronic *coupling* between the donor state and the acceptor state, which describes the interaction between the donor and the acceptor part in the overall complex, is necessary for an ET reaction.

A simple homogeneous ET reaction as given by Eq. (2.1) can be characterized as a transfer of an electron from a localized (diabatic) donor state to a localized acceptor state accompanied with the nuclear motion. The Hamiltonian which describes a simple homogeneous ET reaction in the diabatic picture reads

$$\hat{H} = \hat{T}_{\mathrm{nucl}} + \left|\psi^{\mathrm{d}}\right\rangle V^{\mathrm{dd}} \left\langle\psi^{\mathrm{d}}\right| + |\psi^{\mathrm{a}}\rangle V^{\mathrm{aa}} \langle\psi^{\mathrm{a}}| + \left|\psi^{\mathrm{d}}\right\rangle V^{\mathrm{da}} \langle\psi^{\mathrm{a}}| + |\psi^{\mathrm{a}}\rangle V^{\mathrm{ad}} \left\langle\psi^{\mathrm{d}}\right|. \tag{2.3}$$

Here, $\hat{T}_{\mathrm{nucl}}$ denotes the nuclear kinetic energy operator. V^{dd} and V^{aa} denote the energies of the diabatic donor state and the acceptor state, respectively. The offdiagonal matrix elements V^{da} and V^{ad} characterize the electronic *coupling* between the donor state and the acceptor state. For a Hermitian Hamiltonian, we have $V^{\mathrm{da}} = \left(V^{\mathrm{ad}}\right)^*$.

In Eq. (2.3), all matrix elements of the potential energy operator, V^{dd}, V^{aa} and V^{da}, depend on nuclear coordinates. The diagonal elements V^{dd} and V^{aa} describe the *potential energy surfaces* (PES) as functions of nuclear configuration. For a fixed nuclear configuration, the Hamiltonian given in Eq. (2.3) describes an electronic two-level system, which can be solved analytically: the population of each diabatic state oscillates with the Rabi-period given by $2\pi \left[\left(V^{\mathrm{dd}} - V^{\mathrm{aa}}\right)^2 + 4\left|V^{\mathrm{da}}\right|^2\right]^{\frac{1}{2}}$. Thus, the characteristic timescale for the electronic transition at the intersection of the two PES (where $V^{\mathrm{dd}} = V^{\mathrm{aa}}$) is proportional to $\left|V^{\mathrm{da}}\right|^{-1}$.

The diagonalization of the potential energy matrix transforms the electronic part of Hamiltonian to $(|-\rangle\, V_- \,\langle\psi_-| + |+\rangle\, V_+ \,\langle\psi_+|)$. The thus obtained states $|-\rangle$ and $|+\rangle$ are eigenstates of the electronic Hamiltonian for fixed nuclei, in the following referred to as the lower and upper *adiabatic* states. The corresponding energy eigenvalues are given by

$$V_\pm = \frac{1}{2}\left[V^{\mathrm{dd}} + V^{\mathrm{aa}} \pm \sqrt{\left(V^{\mathrm{dd}} - V^{\mathrm{aa}}\right)^2 + 4\left|V^{\mathrm{da}}\right|^2}\right]. \tag{2.4}$$

V_- and V_+ are also functions of nuclear configuration. As an example, Fig. 2.1 shows the PES of the diabatic donor and acceptor states and the PES of the lower and upper adiabatic states involved in a two-state ET reaction.

The interstate coupling matrix element V^{da} in Eq. (2.3) plays an important role in the ET process. In case of a large $\left|V^{\mathrm{da}}\right|$, Fig. 2.1 (b) shows that two adiabatic PES exhibit a significant splitting at the intersection of the PES of two diabatic states. In this case, the upper adiabatic state does not participate in the ET reaction. The ET process occurs as indicated by the blue arrow in Fig. 2.1 (a) along the PES of the lower adiabatic state (the double well in black in Fig. 2.1 (a)). This type of ET reactions can be classified as *adiabatic ET*. According to the theory of chemical reaction kinetics, an activation energy $E_{\mathrm{act}}^{\mathrm{ad}}$ as indicated in Fig. 2.1 (b) is required to overcome the potential energy barrier, which separates the reactant state and the product state. Alternatively, a tunneling transition through the barrier as indicated by the cyan arrow in Fig. 2.1 (a) is possible. Usually, an adiabatic ET process is accompanied by a rather large change of nuclear configuration along the reaction coordinate, which implies a possible atomic rearrangement.

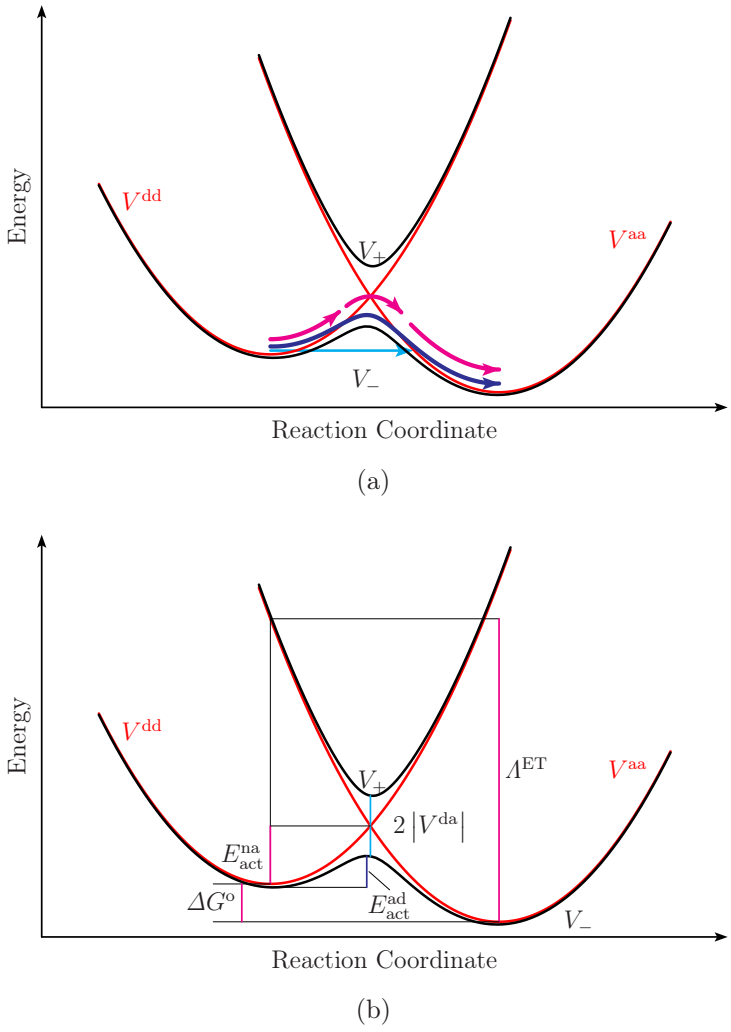

Figure 2.1: Physical model of two-state ET reactions. Shown are the PES for the diabatic donor (reactant) state (V^{dd}, the left red parabola) and the diabatic acceptor (product) state (V^{aa}, the right red parabola), and the PES of the adiabatic states (in black, the lower one labeled by V_- and the upper one by V_+). All PES are shown along a single reaction coordinate. (a) The nonadiabatic ET is indicated by magenta arrows, and the adiabatic ET is indicated by the blue arrow and the cyan arrow (the latter indicating a tunneling transition). (b) The splitting $2\left|V^{\mathrm{da}}\right|$ between the PES of the adiabatic lower and upper states at the intersection of PES of the two diabatic states, the activation energy of the nonadiabatic ET $E^{\mathrm{na}}_{\mathrm{act}}$, the Gibbs free-energy change ΔG^{o}, the reorganization energy Λ^{ET} and the activation energy of the adiabatic ET $E^{\mathrm{ad}}_{\mathrm{act}}$ are indicated.

In contrast, if the interstate coupling $\left|V^{\mathrm{da}}\right|$ is small, a near degeneracy will be observed at the intersection of the PES of two diabatic states. Thus both adiabatic states are involved in the ET reaction. In this case, the ET process is often understood as electronic transition between two diabatic states. This type of ET reactions is classified as *nonadiabatic ET*, which often involves a spatial redistribution of charge within the molecular system. Magenta arrows in Fig. 2.1 (a) indicate a nonadiabatic ET reaction. In a nonadiabatic ET reaction, an activation energy $E_{\mathrm{act}}^{\mathrm{na}}$ as indicated in Fig. 2.1 (b) is required to reach the intersection, where, as a result of the coupling between the donor state and the acceptor state, there is a certain probability that a transition to the acceptor state occurs.

The rate constant for a nonadiabatic ET reaction including the coupling to the nuclear (vibrational) DoF, k^{na}, can be obtained in different ways. By regarding the donor-acceptor coupling as a perturbation to the Hamiltonian describing a system containing non-interacting donor and acceptor, the relationship $k^{\mathrm{na}} \propto \left|V^{\mathrm{da}}\right|^2$ can be obtained from Fermi's Golden Rule theory (*cf.* following discussion and Appendix A). On the other hand, the rate constant is related to the activation energy $E_{\mathrm{act}}^{\mathrm{na}}$ via the Arrhenius equation. Therefore, the rate constant for the nonadiabatic ET obeys

$$k^{\mathrm{na}} \propto \left|V^{\mathrm{da}}\right|^2 \exp\left(-\frac{E_{\mathrm{act}}^{\mathrm{na}}}{k_{\mathrm{B}}T}\right), \tag{2.5}$$

where T denotes the temperature and k_{B} is the Boltzmann constant. In contrast, the rate constant for an adiabatic ET reaction, which only involves the PES of the lower adiabatic state, obeys the Arrhenius equation[1]:

$$k^{\mathrm{ad}} \propto \exp\left(-\frac{E_{\mathrm{act}}^{\mathrm{ad}}}{k_{\mathrm{B}}T}\right). \tag{2.6}$$

As indicated in Fig. 2.1 (b), $E_{\mathrm{act}}^{\mathrm{ad}}$ differs from $E_{\mathrm{act}}^{\mathrm{na}}$.

A general theory for a kinetic description of ET reactions was developed by Marcus [43] in 1950-1960s. In the earliest version of this theory, the motion of nuclear DoF was treated classically. Later this theory was extended to include quantum effects of the nuclear motion [44, 45]. In the Marcus theory for a two-state homogeneous ET reaction, which can be described by Eq. (2.3), the vibrational motion on the PES of both diabatic (donor and acceptor) states can be approximated by classical harmonic oscillators, and V^{da} is considered to be independent of the nuclear configuration. Furthermore, along each individual nuclear coordinate, the vibrational frequency of the donor state is assumed to be identical to that of the acceptor state. By regarding the weak donor-acceptor coupling as a perturbation, the resulting nonadiabatic ET

[1] This does not mean that the rate constant for an adiabatic ET reaction is independent of V^{da}, because V_- and thus $E_{\mathrm{act}}^{\mathrm{ad}}$ can be determined based on the matrix elements V^{dd}, V^{aa} and V^{da} of the ET Hamiltonian represented in the diabatic picture.

rate constant in the Marcus theory is given by an approximation to Fermi's Golden Rule [46, 47] as

$$k^{\mathrm{na}} = \sqrt{\frac{\pi}{\Lambda^{\mathrm{ET}} k_{\mathrm{B}} T}} \left|V^{\mathrm{da}}\right|^2 \exp\left(-\frac{E_{\mathrm{act}}^{\mathrm{na}}}{k_{\mathrm{B}} T}\right) \tag{2.7}$$

in atomic units[2]. It can be rewritten in the form

$$k^{\mathrm{na}} = \sqrt{\frac{\pi}{\Lambda^{\mathrm{ET}} k_{\mathrm{B}} T}} \left|V^{\mathrm{da}}\right|^2 \exp\left(-\frac{\left(\Lambda^{\mathrm{ET}} + \Delta G^{\mathrm{o}}\right)^2}{4\Lambda^{\mathrm{ET}} k_{\mathrm{B}} T}\right) = 2\pi \left|V^{\mathrm{da}}\right|^2 \mathrm{FC}, \tag{2.8}$$

where

$$\mathrm{FC} = \frac{1}{\sqrt{4\pi\Lambda^{\mathrm{ET}} k_{\mathrm{B}} T}} \exp\left(-\frac{\left(\Lambda^{\mathrm{ET}} + \Delta G^{\mathrm{o}}\right)^2}{4\Lambda^{\mathrm{ET}} k_{\mathrm{B}} T}\right) \tag{2.9}$$

denotes the classical approximation for the Franck-Condon (FC) factor. Here, Λ^{ET} is the *ET reorganization energy*, and ΔG^{o} denotes the change of the *Gibbs free energy*, which, when neglecting the entropy change, is given by

$$\Delta G^{\mathrm{o}} = \min\left\{V^{\mathrm{aa}}\right\} - \min\left\{V^{\mathrm{dd}}\right\}. \tag{2.10}$$

Both Λ^{ET} and ΔG^{o} are indicated in Fig. 2.1 (b). The activation energy of the nonadiabatic ET is given by

$$E_{\mathrm{act}}^{\mathrm{na}} = \frac{\left(\Lambda^{\mathrm{ET}} + \Delta G^{\mathrm{o}}\right)^2}{4\Lambda^{\mathrm{ET}}}. \tag{2.11}$$

Similarly, the rate constant for the back reaction reads

$$k_{-}^{\mathrm{na}} = \sqrt{\frac{\pi}{\Lambda^{\mathrm{ET}} k_{\mathrm{B}} T}} \left|V^{\mathrm{da}}\right|^2 \exp\left(-\frac{\left(\Lambda^{\mathrm{ET}} - \Delta G^{\mathrm{o}}\right)^2}{4\Lambda^{\mathrm{ET}} k_{\mathrm{B}} T}\right).$$

Hence, the equilibrium constant of the ET reaction is given by

$$K = \frac{k^{\mathrm{na}}}{k_{-}^{\mathrm{na}}} = \exp\left(-\frac{\Delta G^{\mathrm{o}}}{k_{\mathrm{B}} T}\right). \tag{2.12}$$

Thus, the ET rate depends on the temperature and the activation energy, while the change of the Gibbs free energy, which is sometimes regarded as the "driving force" of the reaction, determines the chemical equilibrium of the reaction.

Marcus has extended the theory for homogeneous ET to a unified approach which can also describe heterogeneous ET reactions [3,43,48], *e.g.*, ET from an initially prepared diabatic donor state $\left|\psi^{\mathrm{d}}\right\rangle$ to a manifold of diabatic acceptor states $\left|\psi_j^{\mathrm{a}}\right\rangle$. Here we only introduce the rate formula for a simplest (purely electronic) heterogeneous ET reaction (as sketched in Fig. 2.2). When the nuclear motion is not considered, the

[2] Atomic units are used throughout this thesis.

rate of electronic transition from the discrete donor state to the set of acceptor states is given by the Golden Rule formula (a detailed discussion is given in Appendix A)

$$k^{\mathrm{GR}} = \Gamma\left(\varepsilon^{\mathrm{d}}\right) = 2\pi \sum_{j} \left|V_j^{\mathrm{da}}\right|^2 \delta\left(\varepsilon^{\mathrm{d}} - \varepsilon_j^{\mathrm{a}}\right). \tag{2.13}$$

Here ε^{d} denotes the energy of the donor state, $\varepsilon_j^{\mathrm{a}}$ denotes the energy of the j-th acceptor state. $V_j^{\mathrm{da}} = \left(V_j^{\mathrm{ad}}\right)^*$ characterizes the coupling between the donor state and the j-th acceptor state. $\Gamma\left(\varepsilon\right)$ is the *energy-dependent decay-width* function. It describes the density of acceptor states weighted by the donor-acceptor coupling.

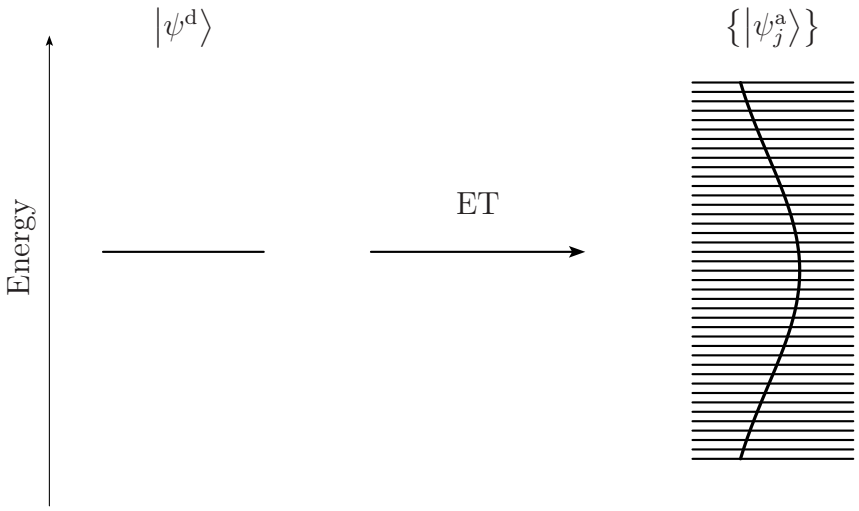

Figure 2.2: ET from a discrete electronic donor state to the continuum of electronic acceptor states. The distribution of the magnitude of interstate coupling $|V_j^{\mathrm{da}}|$ is shown by the curve over the continuum.

The approaches introduced above are rate theories (*kinetic theories*) to describe ET reactions. They characterize the ET reaction by a single rate constant. However, in many practical applications a kinetic theory is not sufficient since there are many other observables of interest besides the rate constant. For a detailed study of ET reactions, including the investigation of population dynamics as well as electronic and vibrational coherence effects, a *dynamical theory* of ET is required.

2.2 Survey of previous studies of photoinduced electron transfer in dye-semiconductor systems

In the last decade, various theories and methods have been developed and applied to studies of dye-semiconductor systems [36–40, 49–75]. The electronic structure of dye

molecules adsorbed at semiconductor substrates, in particular titanium oxide, was studied employing cluster models of nanoparticles [50, 62, 65, 72, 74, 75] or the slab model with periodic boundary conditions to describe an extended surface [37, 38, 55, 56, 59, 64, 67, 68].

Quantum dynamics of electron injection at dye-semiconductor interfaces was studied employing models based on a parametrized Hamiltonian [36,39,49,51–54,58,60,63, 69–71, 73] as well as employing first-principles simulations [37, 38, 56, 59, 62, 64, 66, 68]. The former class of methods of quantum dynamics often allows a fully quantum-dynamical treatment on the ET process. On the other hand, the dynamical studies of ET processes based on the first-principles electronic structure characterization of the systems often use an approximate classical treatment of the nuclear dynamics.

Ramakrishna and Willig modeled the dynamics and the pump-probe spectroscopy of photoinduced ultrafast electron injection in the perylene-TiO_2 system [36]. In their study, the model molecular Hamiltonian was represented in a diabatic basis set constructed by three discrete states (the ground state, the first excited state and a higher excited state) of the dye molecule and a continuum of acceptor states representing the conduction-band levels of the semiconductor. Later, together with May, they applied this model in the simulation of the vibronic dynamics including one and two vibrational modes [51, 52]. Based on these model studies, Wang, May and co-workers simulated the laser pulse control of the ultrafast ET and the absorption spectra of some dye-semiconductor systems with different perylene-based dyes adsorbed at TiO_2 [60, 63, 69]. In their studies, the electronic-vibrational wavepacket propagation was performed at a fully quantum-mechanical level within a single-reaction-coordinate model with the parameters adopted from the experimental results of absorption spectra.

Thoss, Kondov and Wang modeled photoinduced ultrafast ET reactions in dye-semiconductor systems [39] using the Anderson-Newns model Hamiltonian [76, 77] with a tight-binding parameterization [49]. They also applied this model to study the coumarin 343 - titanium oxide system [70]. In their studies, the donor-state energy relative to the conduction-band states was calculated by fitting the experimental results of absorption spectra. The electronic-vibrational coupling parameters were obtained from electronic structure calculations of the isolated dye molecule. The tight-binding parameters of the semiconductor as well as the parameters concerning the bath modes modeling the solution environment were taken from literature. The fully quantum-dynamical simulations were carried out employing the self-consistent hybrid (SCH) approach [78, 79] in combination with the ML-MCTDH method [42].

Rego, Abuabara and Batista studied ET processes from catechol to titanium oxide

in detail [38, 62, 68]. In their studies, the tight-binding model Hamiltonian was constructed using a semiempirical extended Hückel approach based on density functional theory (DFT) electronic structure calculations. The ET dynamics was simulated at a mixed quantum-classical level with the nuclear DoF treated classically using the Ehrenfest mean-field nuclear dynamics.

Stier, Duncan and Prezhdo performed a series of nonadiabatic molecular dynamics (NAMD) studies for various dye-semiconductor systems (isonicotinic acid, isonicotinic acid - silver cyanide complex or alizarin adsorbed at a titanium oxide substrate) [37,56,59,64,66]. In their studies, the real time electronic-vibrational dynamics of ET at the atomistic level was simulated using a mixed quantum-classical approach with the electronic DoF treated by the quantum-mechanical electronic structure theory and the nuclear DoF described classically or semiclassically.

2.3 First-principles model

In this section and Section 2.4, the theoretical methodology which is employed to describe photoinduced ET reactions in dye-semiconductor systems is outlined. This approach, which combines a first-principles based model Hamiltonian and accurate quantum dynamical simulations, was first proposed by Kondov and co-workers [41]. This method has been successfully applied to investigate photoinduced interfacial ET processes in several dye-semiconductor systems [41, 80, 81]. In this section, the major focus is on the approach to determine electronic energies and donor-acceptor coupling matrix elements. We also discuss the method used to characterize the nuclear DoF. The dynamical approach employed in the simulation will be introduced in Section 2.4.

2.3.1 Determination of the electron transfer Hamiltonian

To study ET dynamics in dye-semiconductor systems, we use an first-principles based model for heterogeneous ET reactions. Within this model, the ET Hamiltonian is represented in a basis of the following diabatic (charge-localized) electronic states which are relevant for the photoreaction: the electronic ground state of the overall system $|\psi^{\mathrm{g}}\rangle$, the donor state of the ET process $\left|\psi^{\mathrm{d}}\right\rangle$ (which, in the limit of vanishing coupling between the dye molecule and the semiconductor substrate, corresponds to the product of an electronically excited state of the dye and an empty conduction band of the semiconductor), and the (quasi-)continuum of acceptor states of the ET reaction $\left\{\left|\psi_j^{\mathrm{a}}\right\rangle\right\}$ (corresponding to the product of the ground state of the dye-cation and a conduction-band state of the semiconductor-anion in the zero-coupling limit).

Thus, the ET Hamiltonian reads

$$\hat{H} = \hat{T}_{\text{nucl}} + |\psi^{\text{g}}\rangle V^{\text{g}} \langle\psi^{\text{g}}| + \left|\psi^{\text{d}}\right\rangle V^{\text{dd}} \left\langle\psi^{\text{d}}\right| + \sum_j \left|\psi_j^{\text{a}}\right\rangle V_j^{\text{aa}} \left\langle\psi_j^{\text{a}}\right| + \sum_j \left(\left|\psi^{\text{d}}\right\rangle V_j^{\text{da}} \left\langle\psi_j^{\text{a}}\right| + \left|\psi_j^{\text{a}}\right\rangle V_j^{\text{ad}} \left\langle\psi^{\text{d}}\right|\right). \tag{2.14}$$

Here, V^{g} denotes the potential energy in the electronic ground state. The diagonal elements of the diabatic potential energy matrix, V^{dd} and V_j^{aa}, describe the energies of the electronic donor state and the j-th acceptor states, respectively. They all depend on nuclear coordinates. The offdiagonal matrix elements $V_j^{\text{da}} = \left(V_j^{\text{ad}}\right)^*$ characterize the donor-acceptor coupling. The kinetic energy of the nuclear DoF is given by

$$\hat{T}_{\text{nucl}} = \sum_l \frac{1}{2}\hat{p}_l^2, \tag{2.15}$$

where $\hat{p}_l$ is the canonical momentum of the l-th mass-scaled nuclear coordinate q_l.

The potential energy in the electronic ground state, V^{g}, can (at least in principle) be determined by electronic structure calculations. However, the characterization of the diabatic (donor-acceptor) potential energy matrix elements, V^{dd}, $\left\{V_j^{\text{aa}}\right\}$ and $\left\{V_j^{\text{da}}\right\}$, requires the introduction of appropriate diabatic donor and acceptor states $\left|\psi^{\text{d}}\right\rangle$ and $\left\{\left|\psi_j^{\text{a}}\right\rangle\right\}$. In a previous work [74] on heterogeneous ET, a semiempirical method was employed to characterize the diabatic donor and acceptor states and donor-acceptor coupling matrix elements. This semiempirical approach was motivated by the Newns model of chemisorption [77] with a parametrization based on a tight-binding model [49]

In this thesis, a first-principles description of quantum dynamics for ET processes in dye-semiconductor systems based on electronic structure calculations is employed. This approach is motivated by the projection-operator approach [82] of resonant electron-molecule scattering [83]. This projection-operator approach has been proven to be a very useful concept to introduce localized diabatic states [83–85]. Specifically, we employ a partitioning scheme based on DFT calculations for a dye-semiconductor complex (with a finite semiconductor cluster). As an example, the partitioning scheme applied to the dye-semiconductor system 3-peryleneacrylic acid - $(TiO_2)_{60}$ is illustrated in Fig. 2.3. The scheme for defining the localized donor and acceptor states $\left|\psi^{\text{d}}\right\rangle$ and $\left\{\left|\psi_j^{\text{a}}\right\rangle\right\}$ in the Hamiltonian given by Eq. (2.14) includes three steps: (i) a partitioning of the Hilbert space into a donor and an acceptor subspace using a localized basis, (ii) a partitioning of the Hamiltonian according to the donor-acceptor separation, and (iii) a separate diagonalization of the donor and the acceptor blocks of the partitioned Hamiltonian. In this thesis, we will work within the mean-field single-electron picture, where we consider that the configuration of all other electrons

is left unchanged during the ET process. Thus, we identify the effective Hamiltonian with the Fock (or Kohn-Sham) matrix and use the orbitals and orbital energies to represent the corresponding system states and the energies in the partitioning method.

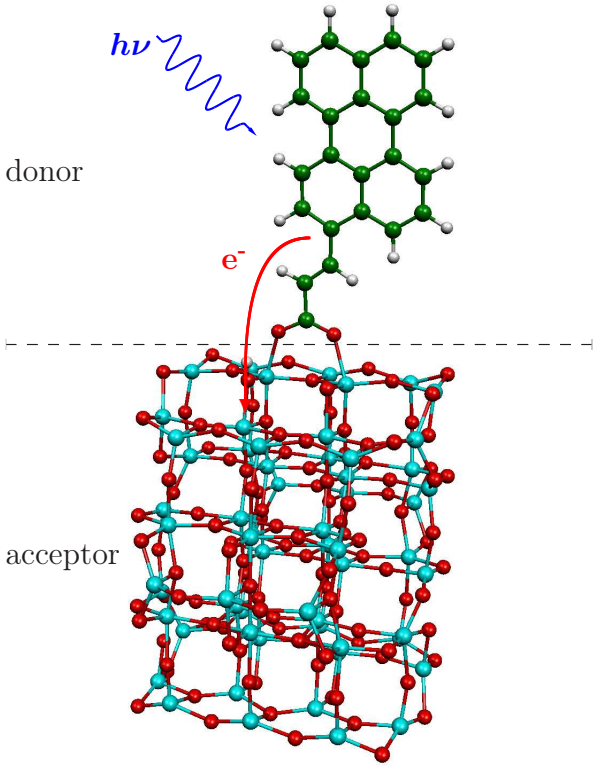

Figure 2.3: Partitioning scheme for the dye-semiconductor system 3-peryleneacrylic acid - $(TiO_2)_{60}$. The donor part includes all atoms of the dye adsorbate (3-peryleneacrylic acid) and the acceptor part includes all atoms of the $(TiO_2)_{60}$ semiconductor substrate as indicated.

In the first step, we employ the set of (Gaussian-type-of) atomic orbitals (AO) $\{|\phi_k\rangle\}$, which are used in the electronic structure calculation for the overall system, as the localized basis functions in the separation of donor and acceptor space. This set of AO is divided into two groups: the donor group $\{|\phi_k^{\mathrm{d}}\rangle\}$ which comprises the AO centered at the atoms of the donor part (*i.e.*, the dye adsorbate, *cf.* Fig. 2.3), and the acceptor group $\{|\phi_{k'}^{\mathrm{a}}\rangle\}$ which includes the AO centered at the atoms of the acceptor part (*i.e.*, the semiconductor substrate, *cf.* Fig. 2.3).

Since it is advantageous to work with orthogonal orbitals [86,87], the set of all AO is orthogonalized according to Löwdin [88,89]:

$$\left|\tilde{\phi}_{k'}\right\rangle = \sum_k \left(S^{-\frac{1}{2}}\right)_{k'k} |\phi_{k'}\rangle \,. \tag{2.16}$$

Here $\boldsymbol{S}$ denotes the overlap matrix of AO with elements

$$S_{kk'} = \langle \phi_k | \phi_{k'} \rangle \,. \tag{2.17}$$

The thus obtained new basis functions $\left\{\left|\tilde{\phi}_k\right\rangle\right\}$ exhibit a minimal deviation from the original ones in a least-squares sense, and hence, their localization is preserved. In particular, the classification with donor orbitals $\left\{\left|\tilde{\phi}_k^{\mathrm{d}}\right\rangle\right\}$ and acceptor orbitals $\left\{\left|\tilde{\phi}_{k'}^{\mathrm{a}}\right\rangle\right\}$ is still valid.

The set of orthogonal basis functions, $\left\{\left\{\left|\tilde{\phi}_k^{\mathrm{d}}\right\rangle\right\}, \left\{\left|\tilde{\phi}_{k'}^{\mathrm{a}}\right\rangle\right\}\right\}$, is then used to partition the Fock or Kohn-Sham matrix from the converged self-consistent field (SCF) or DFT calculation into two (donor and acceptor) subspaces. The Fock (or Kohn-Sham) matrix in the orthogonal basis is given by

$$\tilde{\boldsymbol{F}} = \boldsymbol{S}^{-\frac{1}{2}} \boldsymbol{F} \boldsymbol{S}^{-\frac{1}{2}}, \tag{2.18}$$

where $\boldsymbol{F}$ denotes the Fock (or Kohn-Sham) matrix in the original AO basis. $\tilde{\boldsymbol{F}}$ can be rearranged into the following donor-acceptor block structure

$$\tilde{\boldsymbol{F}} = \begin{pmatrix} \tilde{\boldsymbol{F}}^{\mathrm{dd}} & \tilde{\boldsymbol{F}}^{\mathrm{da}} \\ \tilde{\boldsymbol{F}}^{\mathrm{ad}} & \tilde{\boldsymbol{F}}^{\mathrm{aa}} \end{pmatrix}, \tag{2.19}$$

where the matrix elements are given by

$$\tilde{F}_{kk'}^{\alpha\beta} = \left\langle \tilde{\phi}_k^{\alpha} \middle| \hat{F} \middle| \tilde{\phi}_{k'}^{\beta} \right\rangle = \sum_m \epsilon_m \left\langle \tilde{\phi}_k^{\alpha} \middle| \chi_m \right\rangle \left\langle \chi_m \middle| \tilde{\phi}_{k'}^{\beta} \right\rangle. \tag{2.20}$$

Here $\hat{F}$ is the Fock operator, $\{\alpha, \beta\} = \{\mathrm{d}, \mathrm{a}\}$ denote the donor (d) or the acceptor (a) subspace, $|\chi_m\rangle$ is the m-th MO (*i.e.*, $\hat{F}\,|\chi_m\rangle = \epsilon_m\,|\chi_m\rangle$) obtained from the converged SCF (or DFT) calculation.

The separated diagonalization of diagonal blocks, $\tilde{\boldsymbol{F}}^{\mathrm{dd}}$ and $\tilde{\boldsymbol{F}}^{\mathrm{aa}}$, can be written as

$$\bar{\boldsymbol{F}}^{\alpha\alpha} = (\boldsymbol{U}^{\alpha})^{\dagger} \tilde{\boldsymbol{F}}^{\alpha\alpha} \boldsymbol{U}^{\alpha} = \begin{pmatrix} \bar{\epsilon}_1^{\alpha} & 0 & \cdots \\ 0 & \bar{\epsilon}_2^{\alpha} & \cdots \\ \vdots & \vdots & \ddots \end{pmatrix}. \tag{2.21}$$

The transformation matrix

$$\boldsymbol{U} = \begin{pmatrix} \boldsymbol{U}^{\mathrm{d}} & \boldsymbol{0} \\ \boldsymbol{0} & \boldsymbol{U}^{\mathrm{a}} \end{pmatrix} \tag{2.22}$$

can prediagonalize $\tilde{\boldsymbol{F}}$ as

$$\begin{aligned} \boldsymbol{U}^{\dagger} \tilde{\boldsymbol{F}} \boldsymbol{U} &= \begin{pmatrix} (\boldsymbol{U}^{\mathrm{d}})^{\dagger} & \boldsymbol{0} \\ \boldsymbol{0} & (\boldsymbol{U}^{\mathrm{a}})^{\dagger} \end{pmatrix} \begin{pmatrix} \tilde{\boldsymbol{F}}^{\mathrm{dd}} & \tilde{\boldsymbol{F}}^{\mathrm{da}} \\ \tilde{\boldsymbol{F}}^{\mathrm{ad}} & \tilde{\boldsymbol{F}}^{\mathrm{aa}} \end{pmatrix} \begin{pmatrix} \boldsymbol{U}^{\mathrm{d}} & \boldsymbol{0} \\ \boldsymbol{0} & \boldsymbol{U}^{\mathrm{a}} \end{pmatrix} \\ &= \begin{pmatrix} (\boldsymbol{U}^{\mathrm{d}})^{\dagger} \tilde{\boldsymbol{F}}^{\mathrm{dd}} \boldsymbol{U}^{\mathrm{d}} & (\boldsymbol{U}^{\mathrm{d}})^{\dagger} \tilde{\boldsymbol{F}}^{\mathrm{da}} \boldsymbol{U}^{\mathrm{a}} \\ (\boldsymbol{U}^{\mathrm{a}})^{\dagger} \tilde{\boldsymbol{F}}^{\mathrm{ad}} \boldsymbol{U}^{\mathrm{d}} & (\boldsymbol{U}^{\mathrm{a}})^{\dagger} \tilde{\boldsymbol{F}}^{\mathrm{aa}} \boldsymbol{U}^{\mathrm{a}} \end{pmatrix} \\ &= \begin{pmatrix} \bar{\boldsymbol{F}}^{\mathrm{dd}} & \bar{\boldsymbol{F}}^{\mathrm{da}} \\ \bar{\boldsymbol{F}}^{\mathrm{ad}} & \bar{\boldsymbol{F}}^{\mathrm{aa}} \end{pmatrix} \\ &= \bar{\boldsymbol{F}}. \end{aligned} \tag{2.23}$$

The prediagonalized block structure of the Fock matrix reads

$$\bar{\boldsymbol{F}} = \begin{pmatrix} \bar{\boldsymbol{F}}^{\mathrm{dd}} & \bar{\boldsymbol{F}}^{\mathrm{da}} \\ \bar{\boldsymbol{F}}^{\mathrm{ad}} & \bar{\boldsymbol{F}}^{\mathrm{aa}} \end{pmatrix} = \begin{pmatrix} \bar{\epsilon}_1^{\mathrm{d}} & 0 & \cdots & \bar{F}_{11}^{\mathrm{da}} & \bar{F}_{12}^{\mathrm{da}} & \cdots \\ 0 & \bar{\epsilon}_2^{\mathrm{d}} & \cdots & \bar{F}_{21}^{\mathrm{da}} & \bar{F}_{22}^{\mathrm{da}} & \cdots \\ \vdots & \vdots & \ddots & \vdots & \vdots & \ddots \\ \bar{F}_{11}^{\mathrm{ad}} & \bar{F}_{12}^{\mathrm{ad}} & \cdots & \bar{\epsilon}_1^{\mathrm{a}} & 0 & \cdots \\ \bar{F}_{21}^{\mathrm{ad}} & \bar{F}_{22}^{\mathrm{ad}} & \cdots & 0 & \bar{\epsilon}_2^{\mathrm{a}} & \cdots \\ \vdots & \vdots & \ddots & \vdots & \vdots & \ddots \end{pmatrix}. \tag{2.24}$$

The corresponding "projected" donor and acceptor orbitals $\left\{\left|\bar{\chi}_j^{\alpha}\right\rangle\right\}$ are given as the column vectors of $\boldsymbol{U}$ (*i.e.* eigenvectors or $\tilde{\boldsymbol{F}}^{\alpha\alpha}$), which are related to the orthogonalized AO $\left\{\left|\tilde{\phi}_k^{\alpha}\right\rangle\right\}$ and the original AO $\{|\phi_{k'}\rangle\}$ via

$$\left|\bar{\chi}_j^{\alpha}\right\rangle = \sum_k U_{kj}^{\alpha} \left|\tilde{\phi}_k^{\alpha}\right\rangle = \sum_{k,k'} U_{kj}^{\alpha} \left(S^{\frac{1}{2}}\right)_{k'k} |\phi_{k'}\rangle \,. \tag{2.25}$$

The diagonal blocks of the thus obtained Fock matrix (Eq. (2.24)), $\bar{\boldsymbol{F}}^{\mathrm{dd}}$ and $\bar{\boldsymbol{F}}^{\mathrm{aa}}$, contain energies of the localized dye adsorbate states and those of the localized semiconductor substrate states, respectively. The offdiagonal blocks contain electronic coupling matrix elements between adsorbate and substrate sites. Identifying the donor state $\left|\psi^{\mathrm{d}}\right\rangle$ with one of the states $\left|\bar{\chi}_n^{\mathrm{d}}\right\rangle$ (based, *e.g.*, on the orbital energy or the transition dipole moment to the ground state) and the acceptor states $\left|\psi_j^{\mathrm{a}}\right\rangle$ with states $\left|\bar{\chi}_j^{\mathrm{a}}\right\rangle$, electronic energies of donor and acceptor states are given by the corresponding diagonal elements $\bar{\epsilon}_n^{\mathrm{d}}$ and $\bar{\epsilon}_j^{\mathrm{a}}$ of the prediagonalized Fock matrix, respectively. The donor-acceptor coupling matrix elements are accordingly given by $V_j^{\mathrm{da}} = \bar{F}_{nj}^{\mathrm{da}}$.

The partitioning method discussed above is not limited to dye-semiconductor systems with a finite semiconductor cluster but can, in principle, also be applied to a dye molecule adsorbed on an extended ("infinite") surface. One possibility is to employ a slab model and electronic structure calculations with periodic boundary conditions [67]. Alternatively, the effect of an infinite semiconductor substrate can also be described using surface Green's function techniques [90]. Within this method, the effect of the infinite substrate enters via the self-energy. In this thesis, we use a simpler approximate version [41] of surface Green's function approach to mimic the effect of an extended surface. Thereby a constant imaginary part is added to the AO energies (in the orthogonal basis $\left|\tilde{\phi}_k^{\alpha}\right\rangle$) at the "boundary atoms" of the cluster. The details of this approach are given in Appendix B. The classification of boundary atoms and the specification of the imaginary energy can be determined by test calculations. In this thesis, a value of 1 eV is used for the imaginary part. Employing this approach, the interaction of the donor state with acceptor states is fully characterized

by the (continuous) energy-dependent decay-width function

$$\Gamma(\varepsilon) = 2\pi \sum_j \left|V_j^{\mathrm{da}}\right|^2 \delta\left(\varepsilon - \varepsilon_j^{\mathrm{a}}\right). \tag{2.26}$$

This function describes the density of states of the semiconductor substrate weighted by the donor-acceptor coupling strength (*cf.* Eq. (2.13)). A practical approach to approximately calculate $\Gamma(\varepsilon)$ is described in Appendix B.

2.3.2 Characterization of nuclear degrees of freedom

To characterize the nuclear DoF involved in the ET process, the partitioning procedure outlined above has to be performed for each nuclear geometry, thus resulting in PES $V^{\alpha\alpha}(\{q_l\})$ of ET-related diabatic states and coordinate-dependent donor-acceptor coupling matrix elements $V^{\mathrm{da}}(\{q_l\})$. If many DoF are considered in the simulation of ET dynamics, such a global characterization of PES is not feasible. In this thesis, we adopt a more practical and local strategy, where a local low-order polynomial expansion of the diabatic potential energy matrix elements $V^{\alpha\beta}(\{q_l\})$ around the equilibrium geometry of the neutral ground state of the system is employed.

In principle, nuclear DoF of the overall system include both phonons of the semiconductor substrate and intramolecular vibrations of the dye adsorbate. In this thesis, we only consider the intramolecular vibrations, which are expected to have a larger influence on the electron injection process due to the ultrafast timescale (from a few femtoseconds to a few tens of femtoseconds) of the ET reactions considered in this thesis. Thus, the corresponding vibrational parameters are determined based on electronic structure calculations for the isolated dye molecule, thereby neglecting the coupling to the semiconductor substrate and to the phonons of the semiconductor.

To describe the vibrational DoF of the isolated dye molecule, we employ the harmonic approximation for the potential energy in its electronic ground state as

$$V^{\mathrm{g}}(\{q_l\}) = \varepsilon^{\mathrm{g}} + \sum_l \frac{1}{2}\omega_l^2 q_l^2. \tag{2.27}$$

Here, q_l denotes the mass-scaled coordinate of the l-th normal mode in the electronic ground state of the isolated dye molecule, ω_l denotes the corresponding frequency. Both are determined by electronic structure calculations for the isolated dye molecule. ε^{g} is the ground-state equilibrium energy.

We assume that the donor-acceptor coupling matrix elements V^{da} are approximately independent of the nuclear geometry[3]. To account for electronic vibrational

[3]This corresponds to the Condon approximation, which is often employed in ET theory and is

coupling, we expand the PES of other electronic states about the equilibrium geometry of the electronic ground state ($\{q_l = 0\}$) as

$$V_j^{\alpha\alpha}\left(\{q_l\}\right) = V_j^{\alpha\alpha}\left(\{0\}\right) + \sum_l \kappa_l^{\alpha} q_l + \sum_{l,l'} \gamma_{ll'}^{\alpha} q_l q_{l'}. \tag{2.28}$$

In the simplest approximation, only linear terms of the expansion are taken into account. The frequencies are approximated by their ground-state values, and Dushinsky rotation [91] of normal modes is neglected. In this way we obtain

$$V_j^{\alpha\alpha}\left(\{q_l\}\right) = V_j^{\alpha\alpha}\left(\{0\}\right) + \sum_l \kappa_l^{\alpha} q_l + \sum_l \frac{1}{2}\omega_l^2 q_l^2. \tag{2.29}$$

This approximation has been successfully used to describe Franck-Condon and resonance Raman spectra [92]. It is also used in the linear vibronic coupling model of conical intersections [93] and in the Marcus theory of ET [3].

Within the description of nuclear DoF employed as introduced above, parameters of PES of diabatic donor and acceptor states are obtained from the potential energy functions of the excited state of the neutral dye molecule and the ground state of the cation of the dye, respectively. Accordingly, we have

$$V^{\mathrm{dd}}\left(\{q_l\}\right) = \varepsilon^{\mathrm{d}} + \sum_l \kappa_l^{\mathrm{d}} q_l + \sum_l \frac{1}{2}\omega_l^2 q_l^2, \tag{2.30}$$

$$V_j^{\mathrm{aa}}\left(\{q_l\}\right) = \varepsilon_j^{\mathrm{a}} + \sum_l \kappa_l^{\mathrm{a}} q_l + \sum_l \frac{1}{2}\omega_l^2 q_l^2. \tag{2.31}$$

Here ε^{d} and $\varepsilon_j^{\mathrm{a}}$ denote the energy of the donor and the j-th acceptor state at the equilibrium geometry of the ground state, respectively. They are obtained from the partitioning procedure based on the electronic structure calculation of the overall system. The electronic-vibrational coupling constants κ_l^{d} and κ_l^{a} are obtained from the gradients (along the l-th intramolecular normal mode) of the potential energy functions of the electronically excited state of the neutral dye molecule (corresponding to the donor state) and the ground state of the cation of the dye (corresponding to the acceptor states) at the equilibrium geometry of the ground state of the neutral dye molecule, respectively.

The electronic-vibrational coupling constants κ_l^{d} and κ_l^{a} are related to *reorganization energies* of the l-th intramolecular normal mode via

$$\lambda_l^{\mathrm{d}} = \frac{\left(\kappa_l^{\mathrm{d}}\right)^2}{2\omega_l^2}, \tag{2.32}$$

$$\lambda_l^{\mathrm{a}} = \frac{\left(\kappa_l^{\mathrm{a}}\right)^2}{2\omega_l^2}, \tag{2.33}$$

expected to be valid for relatively rigid systems considered in this thesis.

which are associated with transitions from the electronic ground state to the excited state and to the cation of the dye molecule, respectively. For the l-th intramolecular mode, the reorganization energy for the ET process, which corresponds to a transition from the excited state of the dye to the cation, is given by

$$\lambda_l^{\mathrm{ET}} = \frac{\left(\kappa_l^{\mathrm{a}} - \kappa_l^{\mathrm{d}}\right)^2}{2\omega_l^2}. \tag{2.34}$$

The corresponding total donor-state, acceptor-state and ET reorganization energies are given by $\Lambda^{\mathrm{d/a/ET}} = \sum_l \lambda_l^{\mathrm{d/a/ET}}$.

In the calculations of electronic-vibrational dynamics presented in the following chapters, we select the intramolecular modes according to their electronic-vibrational coupling strength in the following way. A vibrational mode q_l, for which at least one of the parameters

$$\left|\frac{\kappa_l^{\mathrm{d}}}{\sqrt{\omega_l}}\right| = \sqrt{2\omega_l \lambda_l^{\mathrm{d}}}, \quad \left|\frac{\kappa_l^{\mathrm{a}}}{\sqrt{\omega_l}}\right| = \sqrt{2\omega_l \lambda_l^{\mathrm{a}}}, \quad \left|\frac{\kappa_l^{\mathrm{ET}}}{\sqrt{\omega_l}}\right| = \sqrt{2\omega_l \lambda_l^{\mathrm{ET}}}$$

is larger than a certain threshold (set as 100 cm^{-1} in this thesis), is included in the dynamical calculation. This criterion is motivated by the ET Hamiltonian rewritten in the form

$$\begin{aligned}\hat{H} = \hat{T}_{\mathrm{nucl}} + \left|\psi^{\mathrm{d}}\right\rangle \varepsilon^{\mathrm{d}} \left\langle\psi^{\mathrm{d}}\right| + \sum_j \left|\psi_j^{\mathrm{a}}\right\rangle \varepsilon_j^{\mathrm{a}} \left\langle\psi_j^{\mathrm{a}}\right| + \sum_j \left(\left|\psi^{\mathrm{d}}\right\rangle V_j^{\mathrm{da}} \left\langle\psi_j^{\mathrm{a}}\right| + \left|\psi_j^{\mathrm{a}}\right\rangle V_j^{\mathrm{ad}} \left\langle\psi^{\mathrm{d}}\right|\right) \\ + \sum_l \left[\frac{\kappa_l^{\mathrm{d}}}{\sqrt{\omega_l}} \left(\left|\psi^{\mathrm{d}}\right\rangle \left\langle\psi^{\mathrm{d}}\right| + \sum_j \left|\psi_j^{\mathrm{a}}\right\rangle \left\langle\psi_j^{\mathrm{a}}\right|\right) + \sum_j \left|\psi_j^{\mathrm{a}}\right\rangle \frac{\kappa_l^{\mathrm{a}} - \kappa_l^{\mathrm{d}}}{\sqrt{\omega_l}} \left\langle\psi_j^{\mathrm{a}}\right|\right].\end{aligned}$$

In this thesis, the photoexcitation of the dye adsorbate by the laser pulse will not be included explicitly in the dynamical simulations. Instead, we will assume that it can be approximated by an instantaneous transition from the electronic ground state to the donor state. Therefore, the electronic ground state will also not be explicitly involved in the dynamical calculations. However, the position of the electronic ground state with respect to the donor and acceptor states plays an important role in the vibronic dynamics of ET, because it determines to the position of the photoexcited vibrational wavepacket at $t = 0$. In principle, along each intramolecular mode, there are three possible relationships among the positions of the PES, corresponding to three possible results when comparing the reorganization energies: $\max\left\{\lambda_l^{\mathrm{d}}, \lambda_l^{\mathrm{a}}, \lambda_l^{\mathrm{ET}}\right\} = \lambda_l^{\mathrm{d}}, \lambda_l^{\mathrm{a}}$ or λ_l^{ET}. All three different situations are illustrated in Fig. 2.4. In a model system described by Fig. 2.4 (a), if the electronically excited wavepacket is located at the intersection of the FC geometry (dashed line) and the parabola describing V^{dd}, it will move along the PES V^{dd} towards its minimum and thus intersect the acceptor states $\left\{V_j^{\mathrm{aa}}\right\}$ with a decreasing quantum number j. This

trend is more pronounced for a model system described by Fig. 2.4 (c). In contrast, for a model system described by Fig. 2.4 (b), the wavepacket will move along the PES V^{dd} and intersect $\left\{V_j^{\mathrm{aa}}\right\}$ with an increasing quantum number j.

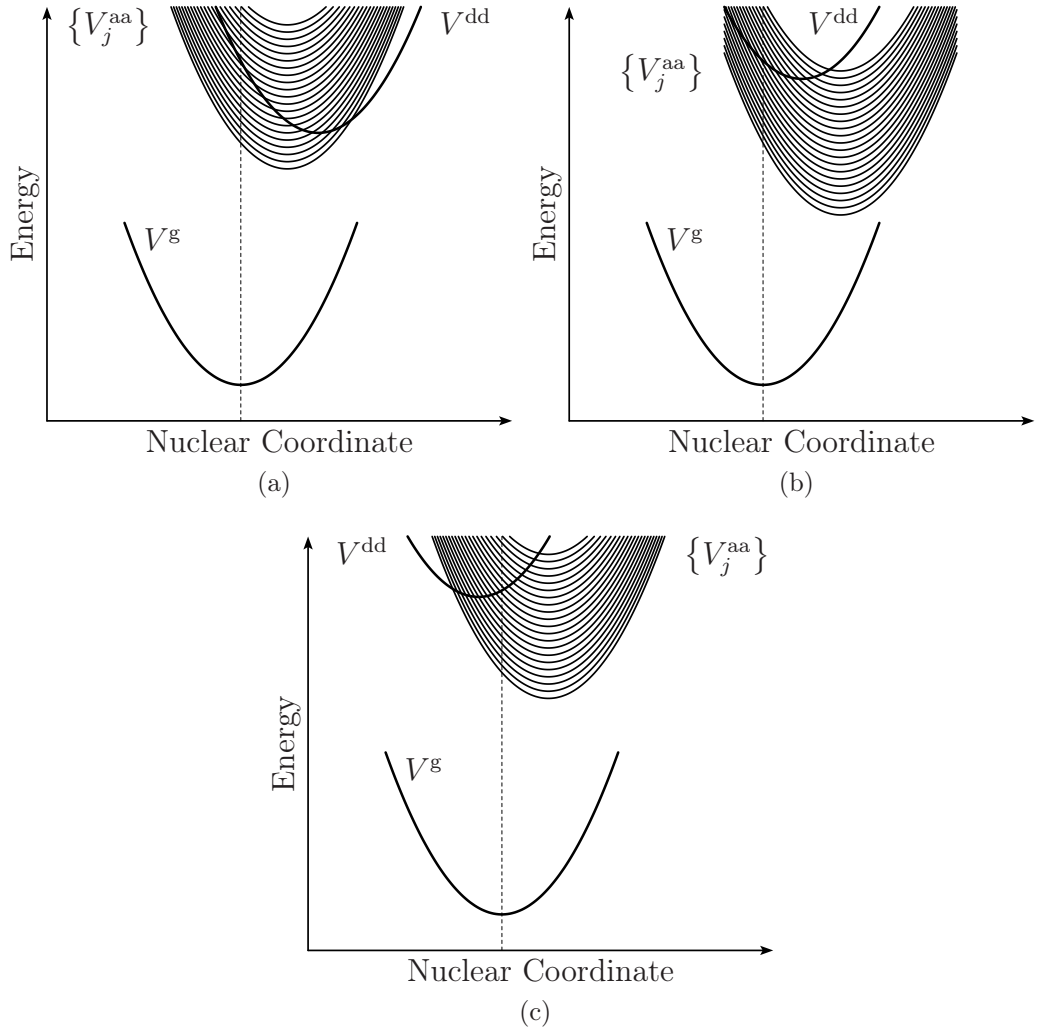

Figure 2.4: Schematic illustrations of PES of the donor and acceptor states along a single nuclear coordinate. Shown are PES of the ground state (V^{g}), the donor state (V^{dd}) and the acceptor states ($\{V_k^{\mathrm{aa}}\}$). The FC geometry (corresponding to the minimum of the ground-state PES) is indicated by the vertical dashed line. Three different situations are shown: (a) the minimum of an acceptor-state PES lies between that of the ground-state PES and that of the donor-state PES (corresponding to $\max\left\{\lambda_l^{\mathrm{d}}, \lambda_l^{\mathrm{a}}, \lambda_l^{\mathrm{ET}}\right\} = \lambda_l^{\mathrm{d}}$), (b) the minimum of the donor-state PES lies between that of the ground-state PES and that of an acceptor-state PES (corresponding to $\max\left\{\lambda_l^{\mathrm{d}}, \lambda_l^{\mathrm{a}}, \lambda_l^{\mathrm{ET}}\right\} = \lambda_l^{\mathrm{a}}$) and (c) the minimum of the ground-state PES lies between that of the donor-state PES and that of an acceptor-state PES (corresponding to $\max\left\{\lambda_l^{\mathrm{d}}, \lambda_l^{\mathrm{a}}, \lambda_l^{\mathrm{ET}}\right\} = \lambda_l^{\mathrm{ET}}$).

The discussions about electronic-vibrational coupling constants, reorganization energies and PES above are all based on the approximation applied in Eq. (2.29) or equivalently, in Eqs. (2.30) and (2.31). If this approximation is not employed, the PES of the donor and acceptor states is expanded up to quadratic terms using Eq. (2.28). Thereby, *Dushinsky rotation* is introduced in the PES of the donor and acceptor states. This requires the determination of both κ_l^α and γ_{ll}^α parameters for each normal mode q_l of the electronic ground state as well as $\gamma_{ll'}^\alpha$ parameters for each pair of modes q_l and $q_{l'}$[4]. Effects caused by Dushinsky rotation (often classified as Dushinsky effects) on the ET dynamics in dye-semiconductor systems will be analyzed in Chapter 5 in detail.

In most experiments on electron injection from adsorbed dye molecules to semiconductor substrates, a colloidal solution of dye-sensitized nanoparticles was employed [22, 23, 34, 35]. In principle, we can account for the influence of the surrounding solvent on the ET dynamics. In this thesis, we will not include the motion of surrounding environment in dynamical simulation of ET reactions. For studies of solvent effects on interfacial ET processes in dye-semiconductor systems, we refer to Refs. [39, 41, 70].

In the dynamical simulations discussed below, we also consider for analysis the purely electronic dynamics, which is obtained with all nuclear DoF frozen at their equilibrium positions. The corresponding approximate electronic Hamiltonian is given by

$$\begin{aligned}\hat{H}_{\text{elec}} = &\left|\psi^{\text{g}}\right\rangle \varepsilon^{\text{g}} \left\langle\psi^{\text{g}}\right| + \left|\psi^{\text{d}}\right\rangle \varepsilon^{\text{d}} \left\langle\psi^{\text{d}}\right| + \sum_j \left|\psi_j^{\text{a}}\right\rangle \varepsilon_j^{\text{a}} \left\langle\psi_j^{\text{a}}\right| \\ &+ \sum_j \left(\left|\psi^{\text{d}}\right\rangle V_j^{\text{da}} \left\langle\psi_j^{\text{a}}\right| + \left|\psi_j^{\text{a}}\right\rangle V_j^{\text{ad}} \left\langle\psi^{\text{d}}\right|\right). \end{aligned} \tag{2.35}$$

2.4 Quantum dynamical methods

In this thesis, we will study the dynamics of ET reactions in dye-semiconductor systems. The dynamics of a quantum mechanical system is described by the time-dependent wave function $|\Psi(t)\rangle$, which is given by the solution of the time-dependent Schrödinger equation (TDSE)

$$\mathrm{i}\frac{\partial}{\partial t}\left|\Psi(t)\right\rangle = \hat{H}\left|\Psi(t)\right\rangle. \tag{2.36}$$

[4]Based on Eq. (2.28), normal modes $\{q_l\}$ of the ground state are no longer normal modes of the donor or acceptor states due to the non-vanishing mode-mixing terms in the expressions of potential energies.

Here $\hat{H}$ is the Hamiltonian given, *e.g.*, by Eq. (2.14).

Several approaches can be used to solve the TDSE. If the Hamiltonian $\hat{H}$ is not explicitly time-dependent, solving the quantum-dynamical problem within a *time-independent picture* is a straightforward approach. The key step of such an approach is the diagonalization of the Hamiltonian matrix. The Hamiltonian operator and the state vector of the system are usually represented in an appropriate product basis. In a time-independent approach, we need to solve the eigenvalue problem of the Hamiltonian matrix and to perform transformation between the product basis-function representation and the eigenfunction representation. The detailed procedure is not discussed here. The application of the time-independent approach is restricted to systems containing only a few DoF, since the computational effort grows exponentially with the number of DoF that the system contains.

Various numerical methods of solving the TDSE within a *time-dependent picture* have been developed [94]. The scheme of wavepacket propagation consists of three components: the construction of an initial wavepacket in a proper representation, the propagation of the wavepacket, and the analysis of dynamical properties based on the propagated wavepacket. Compared with time-independent methods, wavepacket propagation approaches have revealed differences and advantages: (i) for most applications, the computational efforts of solving the set of first-order differential equations in a time-dependent approach is smaller than the effort of diagonalizing the Hamiltonian matrix in the time-independent approach; (ii) the time-dependent wavepacket usually remains more localized even after a long propagation time, while usually the eigenstates involved in time-independent approaches are very delocalized; and (iii) it is easier to develop approximate methods based on a time-dependent method.

In this thesis, we will study the dynamics in dye-semiconductor systems using time-dependent approaches. Methods that will be employed to simulate ET dynamics in the following chapters, including the conventional wavepacket-propagation method, the routine multiconfiguration time-dependent Hartree (MCTDH) method [95–99] and the multilayer (ML) formulation [42,100] of MCTDH method, will be introduced in this section. These methods are applicable to dynamical problems in systems with different sizes. For example, conventional wavepacket-propagation approaches are applicable to the simulation of purely electronic dynamics, while the ML-MCTDH approach allows the treatment of the vibronic dynamics including many vibrational modes.

2.4.1 From conventional wavepacket propagation to the multiconfiguration time-dependent Hartree method

The equations of motion for a variational basis set approach to quantum dynamics can be obtained from the Dirac-Frenkel variational principle [101, 102]

$$\langle \delta\Psi(t)| \hat{H} - \mathrm{i}\frac{\partial}{\partial t} |\Psi(t)\rangle = 0. \tag{2.37}$$

In the past few decades, most of computational implementations of wavepacket propagation methods have expressed the wave function as a linear combination of *time-independent* configurations as

$$|\Psi(t)\rangle = \sum_{\boldsymbol{J}} A_{\boldsymbol{J}}(t) |X_{\boldsymbol{J}}\rangle, \tag{2.38}$$

where $\boldsymbol{J} = j_1 \cdots j_N$ is a multiindex that runs through all combinations of basis functions in F DoF, *i.e.*,

$$|\Psi(t)\rangle = \sum_{j_1=1}^{J_1} \cdots \sum_{j_N=1}^{J_N} A_{j_1\cdots j_N}(t) \prod_{n=1}^{N} \left|\chi_{j_n}^{(n)}\right\rangle. \tag{2.39}$$

Here,

$$|X_{\boldsymbol{J}}\rangle = \left|\chi_{j_1}^{(1)}\right\rangle \cdots \left|\chi_{j_N}^{(N)}\right\rangle \tag{2.40}$$

represents a time-independent *configuration* of the system. $\left|\chi_{j_n}^{(n)}\right\rangle$ only describes the motion of the n-th DoF. Eq. (2.38) can be alternatively written in the form

$$\Psi(q_1, \cdots, q_N, t) = \sum_{j_1=1}^{J_1} \cdots \sum_{j_N=1}^{J_N} A_{j_1\cdots j_N}(t) \prod_{n=1}^{N} \chi_{j_n}^{(n)}(q_n).$$

For convenience, the basis functions for each DoF are usually chosen to be orthonormal

$$\left\langle \chi_{j_n}^{(n)} \middle| \chi_{j_n'}^{(n)} \right\rangle = \delta_{jj'},$$

which yields orthonormal time-independent configurations:

$$\langle X_{\boldsymbol{J}} | X_{\boldsymbol{J}'} \rangle = \delta_{\boldsymbol{J}\boldsymbol{J}'}. \tag{2.41}$$

Because the configurations $|X_{\boldsymbol{J}}\rangle$ are considered fixed and time-independent, the variation and the time derivative of the wave function are only performed with respect to the expansion coefficients as given by

$$\delta|\Psi(t)\rangle = \sum_{\boldsymbol{J}} \delta A_{\boldsymbol{J}}(t) |X_{\boldsymbol{J}}\rangle, \tag{2.42}$$

$$\frac{\partial}{\partial t}|\Psi(t)\rangle = \sum_{\boldsymbol{J}} \dot{A}_{\boldsymbol{J}}(t) |X_{\boldsymbol{J}}\rangle. \tag{2.43}$$

After substitution into Eq. (2.37) and application of the orthonormality condition given by Eq. (2.41), we obtain the usual expression for the time evolution of expansion coefficients:

$$\mathrm{i}\dot{A}_{\boldsymbol{J}}(t) = \sum_{\boldsymbol{J}'} H_{\boldsymbol{J}\boldsymbol{J}'} A_{\boldsymbol{J}'}(t)\,, \tag{2.44}$$

where

$$H_{\boldsymbol{J}\boldsymbol{J}'} = \langle X_{\boldsymbol{J}}|\,\hat{H}\,|X_{\boldsymbol{J}'}\rangle \tag{2.45}$$

are the Hamiltonian matrix elements in the basis $\{|X_{\boldsymbol{J}}\rangle\}$.

The equation of motion for the expansion coefficient $A_{\boldsymbol{J}}$, Eq. (2.44), is coupled to the equations of motion for other expansion coefficients. All these equations form a system of coupled linear ordinary differential equations, which are employed as the major scheme used for most of the time-dependent wavepacket propagations. Although considerable progress has been made in order to optimize the methodology from various aspects, including the choice of basis functions, the choice of coordinate systems and different methods of propagation, the practical application of this approach to large systems is severely restricted. This is due to the fact that, in this scheme, the configurations are time-independent and only the expansion coefficients are varied, which corresponds to a full configuration interaction (FCI) approach in electronic structure theory. From Eq. (2.39), we can observe that the total number of configurations $|X_{\boldsymbol{J}}\rangle = \prod_{n=1}^{N} \left|\chi_{j_n}^{(n)}\right\rangle$ (*i.e.*, combinations of primitive basis functions for individual DoF) and coefficients $A_{\boldsymbol{J}}(t) = A_{j_1\cdots j_N}(t)$ scales exponentially versus the number of DoF (N). Thus, the application of the numerically exact wavepacket-propagation approach based on Eqs. (2.39) and (2.44) is limited to systems containing up to four atoms. For larger systems, *e.g.*, systems with more than 10 DoF which roughly corresponds to 10^{10} configurations, a numerically exact dynamical calculation is rather unrealistic with the current computer hardware.

However, for many systems, only a relatively small number of *time-dependent* combinations of fixed configurations are important for describing the correct quantum dynamics. Thus, it appears to be more promising to describe the wave function in the functional of the variational procedure in terms of *time-dependent* configurations. One approximate method developed for solving the TDSE for larger systems, the *time-dependent self-consistent field* (TDSCF) approach [101], employs the *time-dependent Hartree* (TDH) ansatz for the wave function as

$$\Psi(q_1, \cdots, q_M, t) = \prod_{m=1}^{M} \varphi^{(m)}(q_m, t)\,. \tag{2.46}$$

This TDH product ansatz for the wave function can remarkably reduce the computational effort. On the other hand, it represents a significant approximation to

the exact solution of the TDSE if the Hamiltonian is not variable-separable, since it neglects the coupling among the DoF.

By generalizing the single TDH-product ansatz for the wave function to a linear combination of TDH products, the ansatz for the wave function in the *multiconfiguration* (MC) TDH approach [95–99] is given by

$$|\Psi(t)\rangle = \sum_{\boldsymbol{J}} A_{\boldsymbol{J}}(t)\,|\Phi_{\boldsymbol{J}}(t)\rangle\,. \tag{2.47}$$

Here, each *time-dependent* configuration $|\Phi_{\boldsymbol{J}}(t)\rangle$ is expressed in the form of a Hartree product

$$|\Phi_{\boldsymbol{J}}(t)\rangle = \prod_{m=1}^{M} \left|\varphi_{j_m}^{(m)}(t)\right\rangle, \tag{2.48}$$

where $\left|\varphi_{j_m}^{(m)}\right\rangle$ is referred to as the *single-particle* (SP) function for the m-th SP-DoF, and M is the total number of SP-DoF. The expansion scheme for the MCTDH wave function thus reads

$$|\Psi(t)\rangle = \sum_{j_1=1}^{J_1}\cdots\sum_{j_M=1}^{J_M} A_{j_1\cdots j_M}(t)\prod_{m=1}^{M}\left|\varphi_{j_m}^{(m)}(t)\right\rangle = \sum_{\boldsymbol{J}} A_{\boldsymbol{J}}(t)\,|\Phi_{\boldsymbol{J}}(t)\rangle\,, \tag{2.49}$$

or alternatively,

$$\begin{aligned}\Psi(q_1,\cdots,q_M,t) &= \sum_{j_1=1}^{J_1}\cdots\sum_{j_M=1}^{J_M} A_{j_1\cdots j_M}(t)\prod_{m=1}^{M}\varphi_{j_m}^{(m)}(q_m,t)\\ &= \sum_{\boldsymbol{J}} A_{\boldsymbol{J}}(t)\,\Phi_{\boldsymbol{J}}(q_1,\cdots,q_M,t)\,.\end{aligned}$$

The error introduced by the TDH ansatz is eliminated in the MCTDH approach, since the coupling among the DoF is represented through the linear combination of different configurations (TDH products). MCTDH is thus, in principle, a numerically exact approach.

The main difference between the conventional wavepacket-propagation approach given by Eq. (2.39) or (2.38) and the MCTDH approach is that the MCTDH-configurations are also adjusted in the variational procedure. In this way, the Dirac-Frenkel variational principle [101, 102] can be separated into two parts:

$$\langle\delta\Psi(t)|\,\hat{H} - \mathrm{i}\frac{\partial}{\partial t}\,|\Psi(t)\rangle_{\text{coefficients}} = 0, \tag{2.50}$$

$$\langle\delta\Psi(t)|\,\hat{H} - \mathrm{i}\frac{\partial}{\partial t}\,|\Psi(t)\rangle_{\text{configurations}} = 0. \tag{2.51}$$

Here, only the expansion coefficients $A_{\boldsymbol{J}}$ are varied in Eq. (2.50), while in Eq. (2.51) only the configurations $|\Phi_{\boldsymbol{J}}\rangle$.

Without loss of generality, the SP functions are chosen to be orthonormal [95, 96] in most practical implementations as

$$\left\langle \varphi_{j_m}^{(m)}(t) \middle| \varphi_{j'_m}^{(m)}(t) \right\rangle = \delta_{j_m j'_m}, \tag{2.52}$$

which is equivalent to the combination of

$$\left\langle \varphi_{j_m}^{(m)}(0) \middle| \varphi_{j'_m}^{(m)}(0) \right\rangle = \delta_{j_m j'_m} \tag{2.53}$$

and

$$\mathrm{i}\left\langle \varphi_{j_m}^{(m)}(t) \middle| \dot{\varphi}_{j'_m}^{(m)}(t) \right\rangle = \left\langle \varphi_{j_m}^{(m)}(t) \middle| \hat{g}^{(m)} \middle| \dot{\varphi}_{j'_m}^{(m)}(t) \right\rangle. \tag{2.54}$$

Here the *constraint operator* $\hat{g}^{(m)}$ is an arbitrary Hermitian operator that acts exclusively on the m-th SP-DoF. It does not affect the quality of the multiconfigurational expansions of the wave function. For simplicity we will choose these constraint operators as

$$\hat{g}^{(m)} = 0, \tag{2.55}$$

which yields the differential orthonormality condition

$$\left\langle \varphi_{j_m}^{(m)}(t) \middle| \dot{\varphi}_{j'_m}^{(m)}(t) \right\rangle = 0. \tag{2.56}$$

As a result, the configurations also satisfy the orthonormality condition

$$\langle \Phi_{\boldsymbol{J}}(0) | \Phi_{\boldsymbol{J}'}(0) \rangle = \delta_{\boldsymbol{J}\boldsymbol{J}'}, \tag{2.57}$$

$$\left\langle \Phi_{\boldsymbol{J}}(t) \middle| \dot{\Phi}_{\boldsymbol{J}'}(t) \right\rangle = 0. \tag{2.58}$$

Since variations in Eqs. (2.50) and (2.51) involve two parts, it is useful to define the *single-hole* function $\left|G_{j_m}^{(m)}\right\rangle$ for the m-th SP-DoF [95–99] as

$$\begin{aligned}\left|G_{j'_m}^{(m)}(t)\right\rangle = \sum_{j_1=1}^{J_1} \cdots \sum_{j_{m-1}=1}^{J_{m-1}} \sum_{j_{m+1}=1}^{J_{m+1}} \cdots \sum_{j_M=1}^{J_M} A_{j_1 \cdots j_{m-1} j'_m j_{m+1} \cdots j_M}(t) \\ \times \left|\varphi_{j_1}^{(1)}(t)\right\rangle \cdots \left|\varphi_{j_{m-1}}^{(m-1)}(t)\right\rangle \left|\varphi_{j_{m+1}}^{(m+1)}(t)\right\rangle \cdots \left|\varphi_{j_M}^{(M)}(t)\right\rangle,\end{aligned} \tag{2.59}$$

so that the MCTDH expansion of wave function can be written as

$$|\Psi(t)\rangle = \sum_{j_m=1}^{J_m} \left|\varphi_{j_m}^{(m)}(t)\right\rangle \left|G_{j_m}^{(m)}(t)\right\rangle. \tag{2.60}$$

The variation with respect to the expansion coefficients leads to a result in a form similar to Eq. (2.44):

$$\mathrm{i}\dot{A}_{\boldsymbol{J}}(t) = \sum_{\boldsymbol{J}'} H_{\boldsymbol{J}\boldsymbol{J}'}(t) A_{\boldsymbol{J}'}(t) \tag{2.61}$$

where the only difference is that the Hamiltonian matrix element

$$H_{\boldsymbol{J}\boldsymbol{J}'}(t) = \langle \Phi_{\boldsymbol{J}}(t) | \hat{H} | \Phi_{\boldsymbol{J}'}(t) \rangle \tag{2.62}$$

becomes time-dependent. On the other hand, the variation with respect to the configurations is explicitly expressed in terms of each SP function as

$$\left\langle \delta\varphi_{j_m}^{(m)}(t)\right| \left\langle G_{j_m}^{(m)}(t)\right| \hat{H} - \mathrm{i}\frac{\partial}{\partial t}\left|\Psi(t)\right\rangle = 0. \tag{2.63}$$

Further derivation (given in Appendix C and related references) results in

$$\begin{aligned}&\left\langle \delta\varphi_{j_m}^{(m)}(t)\right| \mathrm{i}\sum_{j'_m=1}^{J_m} \rho_{j_m j'_m}^{(m)}(t)\left|\dot{\varphi}_{j'_m}^{(m)}(t)\right\rangle \\ &= \left\langle \delta\varphi_{j_m}^{(m)}(t)\right| \left[1-\hat{P}^{(m)}(t)\right] \sum_{j'_m=1}^{J_m} \left\langle \hat{H}\right\rangle_{j_m j'_m}^{(m)}(t)\left|\varphi_{j'_m}^{(m)}(t)\right\rangle .\end{aligned} \tag{2.64}$$

Here, we have introduced compact notations for the *mean-field operator* $\left\langle \hat{H}\right\rangle^{(m)}(t)$[5], the *reduced density matrix* $\hat{\rho}^{(m)}(t)$ and the *projection operator* $\hat{P}^{(m)}(t)$ onto the m-th SP-space:

$$\left\langle \hat{H}\right\rangle_{j_m j'_m}^{(m)}(t) = \left\langle G_{j_m}^{(m)}(t)\right| \hat{H}\left|G_{j'_m}^{(m)}(t)\right\rangle , \tag{2.65}$$

$$\rho_{j_m j'_m}^{(m)}(t) = \left\langle G_{j_m}^{(m)}(t)\middle| G_{j'_m}^{(m)}(t)\right\rangle \tag{2.66}$$

$$= \sum_{j_1=1}^{J_1}\cdots\sum_{j_{m-1}=1}^{J_{m-1}}\sum_{j_{m+1}=1}^{J_{m+1}}\cdots\sum_{j_M=1}^{J_M} A^*_{j_1\cdots j_{m-1}j_m j_{m+1}\cdots j_M}(t)\, A_{j_1\cdots j_{m-1}j'_m j_{m+1}\cdots j_M}(t) \tag{2.67}$$

$$\hat{P}^{(m)}(t) = \sum_{j_m=1}^{J_m}\left|\varphi_{j_m}^{(m)}(t)\right\rangle\left\langle\varphi_{j_m}^{(m)}(t)\right| . \tag{2.68}$$

Here $\hat{P}^{(m)}(t)$ is related to the *projection operator* onto the configuration space

$$\hat{P}(t) = \sum_{\boldsymbol{J}} |\Phi_{\boldsymbol{J}}(t)\rangle\langle\Phi_{\boldsymbol{J}}(t)| \tag{2.69}$$

via the identity

$$\left[1-\hat{P}(t)\right]\left|G_m^{(m)}\right\rangle = \left|G_m^{(m)}\right\rangle\left[1-\hat{P}^{(m)}(t)\right] . \tag{2.70}$$

For practical implementations, the variations of the SP functions needs to be specified. In the MCTDH method, this is achieved by expanding SP functions in a chosen *time-independent* primitive basis set $\left\{\left|X_{\boldsymbol{I}}^{(m)}\right\rangle\right\}$ as

$$\left|\varphi_{j_m}^{(m)}(t)\right\rangle = \sum_{\boldsymbol{I}} B_{\boldsymbol{I}}^{(m\sim j_m)}(t)\left|X_{\boldsymbol{I}}^{(m)}\right\rangle \tag{2.71}$$

$$= \sum_{i_1=1}^{I_1}\cdots\sum_{i_F(m)}^{I_F(m)} B_{i_1\cdots i_F(m)}^{(m\sim j_m)}(t)\prod_{f=1}^{F(m)}\left|\chi_{i_f}^{(m,f)}\right\rangle \tag{2.72}$$

[5]Since $\left\langle \hat{H}\right\rangle^{(m)}$ denotes the mean-field operator, where the superscript $^{(m)}$ indicates that the "mean-field" is defined for the m-th SP-DoF, the notation $\left\langle \hat{H}^{(m)}(t)\right\rangle$ which is commonly used in the references, is not used in this thesis.

with the multiindex $\boldsymbol{I} = i_1 \cdots i_{F(m)}$. Here $F(m)$ is the total number of Cartesian (physical) DoF within the m-th SP group, and $\left|\chi_{i_f}^{(m,f)}\right\rangle$ denotes a corresponding *time-independent* primitive basis functions for the f-th Cartesian DoF in the m-th SP group[6]. Thus $\left|\delta\varphi_{j_m}^{(m)}(t)\right\rangle$ in Eq. (2.64) becomes the variation with respect to each of the coefficients $B_{\boldsymbol{I}}^{(m\sim j_m)}(t)$, which finally gives the equations of motion for the SP functions in the form

$$\mathrm{i}\sum_{j'_m=1}^{J_m}\rho_{j_m j'_m}^{(m)}(t)\left|\dot{\varphi}_{j'_m}^{(m)}(t)\right\rangle = \left[1-\hat{P}^{(m)}(t)\right]\sum_{j'_m=1}^{J_m}\left\langle\hat{H}\right\rangle_{j_m j'_m}^{(m)}(t)\left|\varphi_{j'_m}^{(m)}(t)\right\rangle. \tag{2.73}$$

The formal solution of this set of linear equations can be written as

$$\mathrm{i}\left|\underline{\dot{\varphi}}^{(m)}(t)\right\rangle = \left[1-\hat{P}^{(m)}(t)\right]\left[\hat{\rho}^{(m)}(t)\right]^{-1}\left\langle\hat{H}\right\rangle^{(m)}(t)\left|\underline{\varphi}^{(m)}(t)\right\rangle, \tag{2.74}$$

where

$$\left|\underline{\varphi}^{(m)}\right\rangle = \left(\begin{array}{ccc}\left|\varphi_1^{(m)}\right\rangle & \cdots & \left|\varphi_{J_m}^{(m)}\right\rangle\end{array}\right)^{\mathrm{T}} \tag{2.75}$$

denotes the symbolic column vector of (coefficients of) SP functions for the m-th SP-DoF, and $\left[\hat{\rho}^{(m)}(t)\right]^{-1}$ denotes the pseudoinverse of the reduced density matrix.

Eqs. (2.61) and (2.74) are the MCTDH equations of motion for expansion coefficients and SP functions, respectively. Eq. (2.47) shows that the total number of time-dependent configurations scales exponentially versus the number of SP-DoF (M), which resembles that in the FCI-type expression of Eq. (2.39). However, the MCTDH method is applicable to more complex systems due to two reasons: (i) the base of the exponential in the MCTDH approach, *i.e.*, the number of physically important SP functions, is always much smaller than the number of time-independent basis functions in the FCI-type (conventional wavepacket-propagation) approach; and (ii) each SP group can contain several physical DoF so that the number of SP-DoF (M) is usually much smaller than the total number of physical DoF (N). As a result, the overall computational effort in the MCTDH approach scales more slowly with respect to the number of physical DoF, which makes MCTDH capable of handling rather large molecular systems in a numerically converged manner [78, 79, 103].

The main limitation of the MCTDH approach lies in its way of constructing the SP functions which is also based on a multidimensional expansion given by Eq. (2.71). The FCI-type expansion of the SP function in Eq. (2.71) is usually limited to a

[6]This is indicated by the superscript $^{(m,f)}$; similarly, the superscript $^{(m\sim j_m)}$ for $B_{i_1\cdots i_F(m)}^{(m\sim j_m)}$ indicates that, in the m-th SP group, the expansion coefficient $B_{i_1\cdots i_F(m)}^{(m\sim j_m)}$ depends not only on the index $i_1\cdots i_F(m)$ but also on the index j_m of the SP function $\left|\varphi_{j_m}^{(m)}\right\rangle$. The sign $\sim$ but not a comma is used to separate m and j_m in order to distinguish from $^{(m,f)}$: the former indicates "the j_m-th configuration of the m-th SP group" while the latter indicates "the f-th physical DoF of the m-th SP group. This notation system is adopted in the next subsection.

few (about 10) DoF, and the multiconfigurational expansion of the wave function in Eq. (2.47) is typically limited to about 10 SP groups. As a result, a routine MCTDH calculations is limited to systems with a few tens of quantum DoF (which is much more than that can be treated via conventional wavepacket-propagation approaches). A further improvement can be achieved by employing static basis set contraction techniques [78, 79, 103], but due to the limitations discussed above, the quantum dynamical treatment of a system with more than a hundred DoF is still beyond the current computer power.

2.4.2 Multilayer formulation of the MCTDH theory

In order to extend the applicability of the MCTDH method to substantially larger systems, the number of physical DoF contained in each SP group must be significantly increased. To this end, the multilayer (ML) MCTDH approach was developed [42] in order to circumvent the limitations in the MCTDH method. The basic idea is to use *dynamical* contraction of the basis functions that constitute the SP functions by building further layers in the MCTDH functional. The resulting ML-MCTDH approach can be regarded as a "cascading" of the original MCTDH method to the SP functions, *i.e.*, the basic MCTDH strategy is adopted to treat each SP group. Thereby the FCI-type construction of the SP functions in Eq. (2.71) is replaced by a *time-dependent* multiconfigurational expansion as

$$\left|\varphi_{j_m}^{(m)}(t)\right\rangle = \sum_{\boldsymbol{I}} B_{\boldsymbol{I}}^{(m\sim j_m)}(t)\left|U_{\boldsymbol{I}}^{(m)}(t)\right\rangle.$$

This can be extended into a recursive and layered expansion of the time-dependent wave function as follows:

$$\begin{aligned}
|\Psi(t)\rangle &= \sum_{\boldsymbol{J}} A_{\boldsymbol{J}}(t)\,|\Phi_{\boldsymbol{J}}(t)\rangle \\
&= \sum_{j_1=1}^{J_1}\cdots\sum_{j_M=1}^{J_M} A_{j_1\cdots j_M}(t)\prod_{m=1}^{M}\left|\varphi_{j_m}^{(m)}(t)\right\rangle, \qquad (2.76)\\
\left|\varphi_{j_m}^{(m)}(t)\right\rangle &= \sum_{\boldsymbol{I}} B_{\boldsymbol{I}}^{(m\sim j_m)}(t)\left|U_{\boldsymbol{I}}^{(m)}(t)\right\rangle \\
&= \sum_{i_1=1}^{I_1}\cdots\sum_{i_{F(m)}}^{I_{F(m)}} B_{i_1\cdots i_{F(m)}}^{(m\sim j_m)}(t)\prod_{f=1}^{F(m)}\left|u_{i_f}^{(m,f)}(t)\right\rangle, \qquad (2.77)\\
\left|u_{i_f}^{(m,f)}(t)\right\rangle &= \sum_{\boldsymbol{L}} C_{\boldsymbol{L}}^{(m,f\sim i_f)}(t)\left|\Xi_{\boldsymbol{L}}^{(m,f)}(t)\right\rangle \\
&= \sum_{l_1=1}^{L_1}\cdots\sum_{l_{K(m,f)}}^{L_{K(m,f)}} C_{l_1\cdots l_{K(m,f)}}^{(m,f\sim i_f)}(t)\prod_{k=1}^{K(m,f)}\left|\xi_{l_k}^{(m,f,k)}(t)\right\rangle, \qquad (2.78)
\end{aligned}$$

...

The ansatz for the wave function expansion in the multilayer (ML) formulation of the MCTDH theory is given by combining Eqs. (2.76), (2.77), (2.78), *etc.* Here, $A_{\boldsymbol{J}}(t) = A_{j_1\cdots j_M}(t)$, $B^{(m\sim j_m)}_{\boldsymbol{I}}(t) = B^{(m\sim j_m)}_{i_1\cdots i_{F(m)}}(t)$, $C^{\left(m,f\sim i_f\right)}_{\boldsymbol{L}}(t) = C^{\left(m,f\sim i_f\right)}_{l_1\cdots l_{K(m,f)}}(t)$, *etc.* are the expansion coefficients for the first, second, third layers, *etc.*, respectively; $\left|\varphi^{(m)}_{j_m}(t)\right\rangle$, $\left|u^{(m,f)}_{i_f}(t)\right\rangle$, $\left|\xi^{(m,f,k)}_{l_k}(t)\right\rangle$, *etc.* are the SP functions for the first, second, third layers, *etc.*, respectively; $|\Phi_{\boldsymbol{J}}(t)\rangle$, $\left|U^{(m)}_{\boldsymbol{I}}(t)\right\rangle$, $\left|\Xi^{(m,f)}_{\boldsymbol{L}}(t)\right\rangle$, *etc.* are the first-, second-, third-layer configurations, *etc.*, respectively. Other notations are as follows. M is the total number of level-1 (L1) SP groups; $F(m)$ is the number of level-2 (L2) SP groups in the second layer that belong to the m-th L1-SP group in the first layer, *i.e.*, there are a total of $\sum_{m=1}^{M} F(m)$ L2-SP groups. Continuing along the multilayer hierarchy, $K(m,f)$ is the number of level-3 (L3) SP groups in the third layer that belong to the f-th L2-SP group of the second layer in the m-th L1-SP group of the first layer, resulting in a total of $\sum_{m=1}^{M}\sum_{f=1}^{F(m)} K(m,f)$ L3-SP groups. Such a recursive expansion can be carried out to an arbitrary number of layers. To terminate the multilayer hierarchy at a particular level, SP functions in the deepest layer are expanded in terms of time-independent configurations. For example, in the four-layer version of the ML-MCTDH theory, the fourth layer is expanded in time-independent basis functions (configurations), each of which may still contain several Cartesian (physical) DoF.

The ML-MCTDH method [42] is a rigorous variational approach to study quantum dynamics in systems with many DoF. Applying the Dirac-Frenkel variational principle [101, 102]

$$\langle \delta\Psi(t)|\,\hat{H} - \mathrm{i}\frac{\partial}{\partial t}\,|\Psi(t)\rangle = 0$$

with the functional form given by a combination of Eqs. (2.76), (2.77), (2.78), *etc.*, the equations of motion can be obtained as[7]

$$\mathrm{i}\left|\dot{\Psi}(t)\right\rangle_{\text{L1 coefficients}} = \hat{H}(t)\,|\Psi(t)\rangle\,, \tag{2.79}$$

$$\mathrm{i}\left|\underline{\dot{\varphi}}^{(m)}(t)\right\rangle_{\text{L2 coefficients}} = \left[1-\hat{P}^{(m)}_{\text{L1}}(t)\right]\left[\hat{\rho}^{(m)}_{\text{L1}}(t)\right]^{-1}\left\langle\hat{H}\right\rangle^{(m)}_{\text{L1}}(t)\left|\underline{\varphi}^{(m)}(t)\right\rangle, \tag{2.80}$$

$$\mathrm{i}\left|\underline{\dot{u}}^{(m,f)}(t)\right\rangle_{\text{L3 coefficients}} = \left[1-\hat{P}^{(m,f)}_{\text{L2}}(t)\right]\left[\hat{\rho}^{(m,f)}_{\text{L2}}(t)\right]^{-1}\left\langle\hat{H}\right\rangle^{(m,f)}_{\text{L2}}(t) \times\left|\underline{u}^{(m,f)}(t)\right\rangle, \tag{2.81}$$

$$\mathrm{i}\left|\underline{\dot{\xi}}^{(m,f,r)}(t)\right\rangle_{\text{L4 coefficients}} = \left[1-\hat{P}^{(m,f,r)}_{\text{L3}}(t)\right]\left[\hat{\rho}^{(m,f,r)}_{\text{L3}}(t)\right]^{-1}\left\langle\hat{H}\right\rangle^{(m,f,r)}_{\text{L3}}(t) \times\left|\underline{\xi}^{(m,f,r)}(t)\right\rangle, \tag{2.82}$$

[7] In Eq. (2.79), $\hat{H}(t)$ is represented as time-dependent because it is represented in a time-dependent L1 configuration.

...

Here, the mean-field operators, reduced density matrices and projection operators are defined similar to Eqs. (2.65), (2.66) and (2.68), respectively [42]. A detailed derivation is given in Appendix C. For clarity, we refer to the top layer as the L1 SP space, the second layer as the L2 SP space, *etc.* All time-derivatives denoted by an overhead dot on the left-hand side of each equation are meant to be carried out only with respect to the expansion coefficients of the particular layer that appear in that equation[8]. For an N-layer version of MCTDH, there are $(N+1)$ levels of expansion coefficients because we need to expand SP functions of the deepest layer in terms of time-independent basis functions (configurations). In this sense, the conventional wavepacket-propagation method can be referred to as a "zero-layer" MCTDH approach, while the original MCTDH method is a one-layer MCTDH approach.

The inclusion of several dynamically optimized layers in the ML-MCTDH method provides more flexibility in the variational functional, which significantly advances the capabilities of performing wavepacket propagations in complex systems. This has been demonstrated by several applications to quantum dynamics in the condensed phase including many DoF [39, 41, 42, 81, 100, 104–107]. In the calculation considered in this thesis, up to four dynamical layers are employed.

2.5 Observables of interest and computational details

Several observables are of interest to analyze heterogeneous ET reactions in dye-semiconductor systems. In this thesis, we focus on the electron injection dynamics which is most directly reflected by the time-dependent population of the donor state $\left|\psi^{\mathrm{d}}\right\rangle$

$$P_{\mathrm{d}}(t) = \frac{\mathrm{tr}\left[\exp\left(-\beta\hat{H}^{\mathrm{g}}_{\mathrm{nucl}}\right)\left|\psi^{\mathrm{d}}\right\rangle\left\langle\psi^{\mathrm{d}}\right|\exp\left(\mathrm{i}\hat{H}t\right)\left|\psi^{\mathrm{d}}\right\rangle\left\langle\psi^{\mathrm{d}}\right|\exp\left(-\mathrm{i}\hat{H}t\right)\right]}{\mathrm{tr}\left[\exp\left(-\beta\hat{H}^{\mathrm{g}}_{\mathrm{nucl}}\right)\right]}. \tag{2.83}$$

Thereby, we have assumed that the system is initially prepared by an ultrashort laser pulse in the donor state $\left|\psi^{\mathrm{d}}\right\rangle$. In principle, the photoexcitation may also result in a direct population of acceptor states [64]. An analysis of this mechanism would require the inclusion of the laser pulse in the simulation, which is not considered in this thesis.

In studies of electronic-vibrational dynamics, the initial state of the nuclear DoF is specified by the corresponding density operator, *i.e.*, the Boltzmann operator

[8] For example, the time-derivative in Eq. (2.79), (2.80) or (2.81) acts only on the L1, L2 or L3 expansion coefficient $A_{\boldsymbol{J}}(t)$, $B^{(m\sim j_m)}_{\boldsymbol{I}}(t)$ or $C^{(m,f\sim i_f)}_{\boldsymbol{L}}(t)$, respectively.

$\exp\left(-\beta\hat{H}^{\mathrm{g}}_{\mathrm{nucl}}\right)$ of the nuclear Hamiltonian in the electronic ground state

$$\hat{H}^{\mathrm{g}}_{\mathrm{nucl}} = \hat{T}_{\mathrm{nucl}} + \sum_{l} \frac{1}{2}\omega_l^2 q_l^2 \tag{2.84}$$

with the kinetic energy of the nuclei given by $\hat{T}_{\mathrm{nucl}} = \sum_l \frac{1}{2}\hat{p}_l^2$. The denominator in Eq. (2.83),

$$Z^{\mathrm{g}}_{\mathrm{nucl}} = \mathrm{tr}\left[\exp\left(-\beta\hat{H}^{\mathrm{g}}_{\mathrm{nucl}}\right)\right], \tag{2.85}$$

denotes the partition function of the Boltzmann operator.

In simulations of purely electronic dynamics, *i.e.*, when the electronic-vibrational coupling is not included, the time-dependent population of the donor state is given by

$$P_{\mathrm{d}}(t) = \left|\left\langle\psi^{\mathrm{d}}\right| \mathrm{e}^{-\mathrm{i}\hat{H}t} \left|\psi^{\mathrm{d}}\right\rangle\right|^2. \tag{2.86}$$

Traditionally, ET processes have been characterized by a single rate constant k by, *e.g.*, fitting $P_{\mathrm{d}}(t)$ as an exponential function of t. Thereby the ET reaction is assumed to follow first-order kinetics,

$$-\dot{P}_{\mathrm{d}}(t) = kP_{\mathrm{d}}(t). \tag{2.87}$$

One possibility to approximately characterize the overall timescale of a (complete) injection from the donor state to acceptor states is provided by the time when the population of the donor state has decreased to e^{-1} of its initial value, *i.e.*,

$$P_{\mathrm{d}}(\tau_{\mathrm{e}^{-1}}) = \mathrm{e}^{-1}. \tag{2.88}$$

For incomplete decays, *i.e.*, $P_{\mathrm{d}}(+\infty) > 0$, the e^{-1}-time can be determined via

$$\frac{P_{\mathrm{d}}(\tau_{\mathrm{e}^{-1}}) - P_{\mathrm{d}}(+\infty)}{1 - P_{\mathrm{d}}(+\infty)} = \mathrm{e}^{-1}. \tag{2.89}$$

On the other hand, a time-dependent rate of injection from the donor state to the acceptor states is given by

$$k(t) = -\frac{\dot{P}_{\mathrm{d}}(t)}{P_{\mathrm{d}}(t)}. \tag{2.90}$$

Assuming that the population dynamics, after a transient regime, corresponds to first-order kinetics, the (time-independent) injection rate can be defined as the long-time limit of $k(t)$ [80] as

$$k = -\lim_{t\to+\infty} \frac{\dot{P}_{\mathrm{d}}(t)}{P_{\mathrm{d}}(t)}. \tag{2.91}$$

Due to their definitions, $\tau_{\mathrm{e}^{-1}}$ and $k = \lim_{t\to+\infty} k(t)$ describe the dynamics from different aspects. The e^{-1}-time is more related to the early dynamics, while the k (or its reciprocal k^{-1}) shows information mainly about the long-time dynamics.

It is important to note that for most of dye-semiconductor systems (especially those with a finite semiconductor substrate, *cf.* following chapters), the population dynamics of the donor state shows that the electron injection process is not a simple exponential decay and can thus not be fully characterized by a single (first-order) rate constant [41, 80, 81]. Therefore, characteristic timescales (*i.e.*, the reciprocal of rate constants defined by various rate theories) can only provide some information about the ET dynamics. For a detailed understanding of ET dynamics, an analysis of the time-evolution of the population of the donor state is necessary.

Chapter 3

Quantum Dynamics of Electron Transfer Processes in the Dye-Semiconductor System Alizarin - Titanium Oxide

3.1 Introduction

As a representative system for heterogeneous ET processes, the dye-semiconductor complex alizarin-TiO_2 has raised significant interest in recent years. In the last two decades, a number of experimental studies of the ET process in this system have been carried out [20, 24, 29, 32, 35, 108, 109]. For example, an electron-injection time as fast as 6 fs was reported for alizarin adsorbed at TiO_2 nanoparticles in time-resolved experiments [29]. In a later experimental study [109], a slower injection was reported for nanostructured TiO_2 films. On the other hand, there are several theoretical studies of alizarin-TiO_2 systems in the last decade [59, 61, 64]. The electronic structure and spectra of the system containing alizarin and anatase TiO_2 were studied by Duncan *et al.* [61] and Kondov *et al.* [74]. Theoretical simulations of ET dynamics in the related system alizarin - titanium oxide (rutile) were carried out employing an *ab initio* NAMD approach [59, 64].

In this chapter, we apply the first-principles based methodology outlined in Chapter 2 to study the photoinduced ET in the dye-semiconductor system alizarin-TiO_2. Several features of the ET reaction are of interest, including the ultrafast timescale of ET, the effect of electronic-vibrational coupling, and, especially, the mechanisms of the reaction.

Section 3.2 of this chapter describes the methods for the electronic structure calculations for the investigated systems. Diabatic ET-related electronic states and donor-acceptor coupling matrix elements are determined employing the partitioning approach introduced in Section 2.3.1 based on electronic structure calculations for

the overall alizarin-TiO_2 systems. The corresponding results are discussed in Section 3.3. In Section 3.4, we present the electronic-vibrational coupling parameters which are obtained from the vibrational analysis for an isolated alizarin molecule and the alizarin-cation. Simulation results of ET dynamics are analyzed in Section 3.5. In Section 3.6, electronic coherence effects in the ET dynamics are discussed in detail. Furthermore, it is shown that the ET proceeds in a stepwise mechanism. Based on model studies, Section 3.7 provides further examples that exhibit significant effect of electronic-vibrational coupling.

3.2 Characterization of the system

To study the quantum dynamics of electron injection from alizarin to the TiO_2 substrate, we have considered complexes consisting of alizarin and anatase TiO_2 nanoparticles of different sizes (two examples are depicted in Fig. 3.1 and others in Fig. D.1). All geometric parameters of the TiO_2 clusters are taken from the X-ray structure of bulk anatase [110]. In order to avoid artificial effects due to dangling bonds, the clusters are saturated by adding hydrogen atoms and hydroxyl groups to the surface oxygen and titanium atoms, respectively, in a way that neutral closed-shell clusters with high coordination of all titanium and oxygen atoms are obtained. Similar cluster models for the (101) anatase surfaces have been used in Refs. [111, 112]. Specifically, we have considered complexes with seven different TiO_2 clusters, which comprise between one and four (101) layers of anatase with 10 TiO_2 units per layer or between one and three (101) layers with 18 TiO_2 units per layer. The results obtained for the ET dynamics are qualitatively similar for all cluster sizes considered as shown below[1]. Therefore, only results obtained for the largest complex alizarin-$(TiO_2)_{54}(H_2O)_{58}$ (Fig. 3.1 (b)) are discussed in detail.

The following protocol is used to obtain the structure of the dye-semiconductor complex alizarin-$(TiO_2)_{54}(H_2O)_{58}$. The geometry of the alizarin anion $C_{14}H_6O_4^{2-}$ attached to a $(TiO_2)_{10}(H_2O)_{18}H_2^{2+}$ substrate (corresponding to one (101) anatase layer) is optimized. Thereby, all nuclear DoF of the TiO_2 substrate are kept frozen, and a 1,2-bidentate adsorption mode is used. This binding mode is energetically the most favorable as indicated by test calculations. Using the thus obtained geometry and relative orientation of the alizarin-TiO_2 complex, alizarin is attached to the larger TiO_2 substrates.

The geometry optimization and the characterization of nuclear DoF of the isolated alizarin molecule are performed with TURBOMOLE [113] using DFT with the

[1] Detailed results are presented in Appendix D.

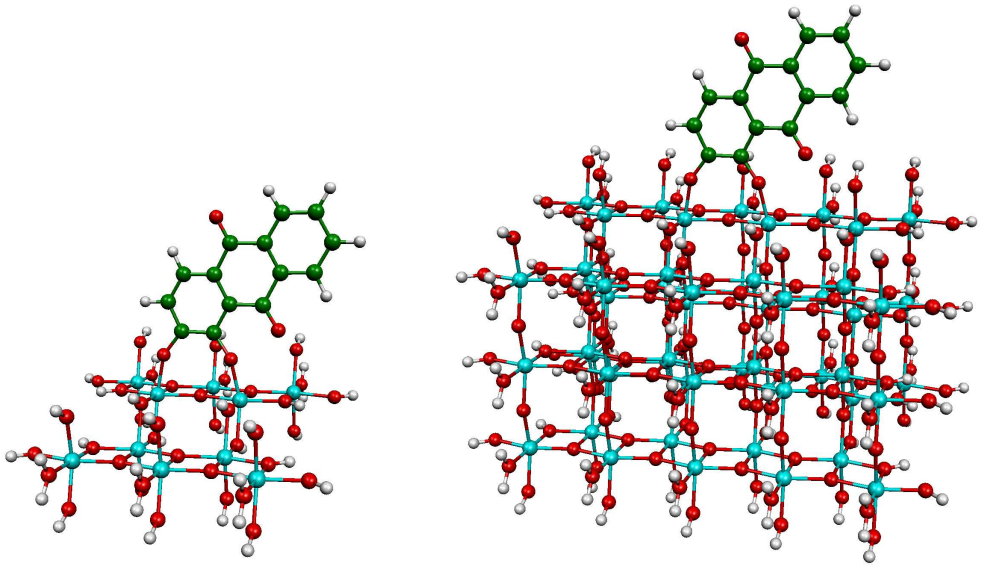

(a) (b)

Figure 3.1: Complexes of alizarin ($C_{14}H_8O_4$) with titanium oxide clusters of different sizes: (a) $(TiO_2)_{10}(H_2O)_{18}$ (1 layer of 10 TiO_2 units) and (b) $(TiO_2)_{54}(H_2O)_{58}$ (3 layers of 18 TiO_2 units).

B3LYP functional and the TZV(P) basis set. The geometry optimization of alizarin-$(TiO_2)_{10}(H_2O)_{18}$ is carried out with DFT using the GAUSSIAN 03 package [114] with the B3LYP functional and the 3-21G basis set. The single-point electronic structure calculations for all complexes are performed using the TURBOMOLE package [113] with the B3LYP functional and the SV(P) basis set.

3.3 Energy-level scheme, donor-acceptor separation and coupling matrix elements

An important aspect of interfacial ET reactions is the energy-level scheme, in particular the location of the energy levels of the dye adsorbate relative to those of the semiconductor substrate. Fig. 3.2 shows energies of MO of the overall alizarin-$(TiO_2)_{54}(H_2O)_{58}$ complex as well as those of the donor and acceptor orbitals obtained by the partitioning procedure described in Section 2.3.1. Also shown, in comparison, are the energy levels of the isolated alizarin molecule and those of the isolated $(TiO_2)_{54}(H_2O)_{60}$ cluster.

The energies of the MO of the isolated $(TiO_2)_{54}(H_2O)_{60}$ cluster exhibit a dense level structure with a valence and a conduction band separated by a band gap. The

calculated value for this band gap is 2.4 eV, which is smaller than the calculated (4.0 eV [115]) and experimental (3.4 eV [116]) value for anatase TiO_2 nanoparticles. This underestimation of the band gap is presumably due to the added hydrogen atoms and hydroxyl groups which are used to saturate the cluster. A detailed analysis (data not shown) reveals that the lowest unoccupied orbitals have predominant contributions from the oxygen atoms of saturation groups. As discussed previously in a study of similar clusters [111], this deficiency of the saturated cluster model is not expected to have a significant influence on the electronic levels involved in the interfacial reactions. Defining the "true" lower edge of the conduction band by the energy of the lowest unoccupied (3d) orbital of the titanium atoms, a value of about 3.3 eV is obtained for the "band gap" in $(TiO_2)_{54}(H_2O)_{60}$, which is in good agreement with to the experimental value for bulk anatase.

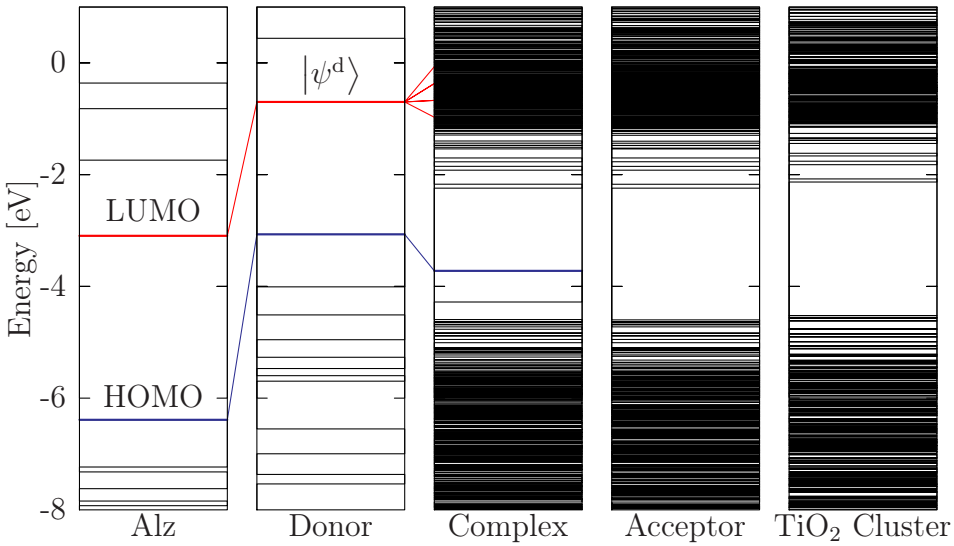

Figure 3.2: Energy-level scheme of the investigated dye-semiconductor complex alizarin-$(TiO_2)_{54}(H_2O)_{58}$. From left to right: energy levels of the isolated dye molecule (alizarin), energy levels of the donor orbitals (obtained from the partitioning procedure) which are localized in the adsorbate, energy levels of the overall complex, energy levels of the acceptor orbitals (obtained from the partitioning procedure) which are localized in the semiconductor substrate, and energy levels of the pure titanium oxide cluster $(TiO_2)_{54}(H_2O)_{60}$. The selected donor state $|\psi^{\mathrm{d}}\rangle$ as well as the correlations among some energy levels relevant for the ET reaction are indicated.

The energy-level scheme of the overall system (shown in the middle panel of Fig. 3.2) shows that the adsorption of the dye molecule (alizarin) on the titanium oxide cluster changes the level structure noticeably. Two energy levels are introduced in the lower part of the band gap through the adsorption of the alizarin molecule. Analysis of the orbitals corresponding to these two levels shows that they can be related to the highest occupied MO (HOMO) and the (HOMO-1) of the isolated alizarin molecule. Thus, the two highest occupied levels of alizarin remain located in the band gap during the adsorption and thus retain their discrete structure in the complex. On the other hand, the lowest unoccupied levels of alizarin are located energetically in the conduction band of TiO_2. As a consequence, in the complex these levels are dissolved in the dense manifold of conduction-band levels.

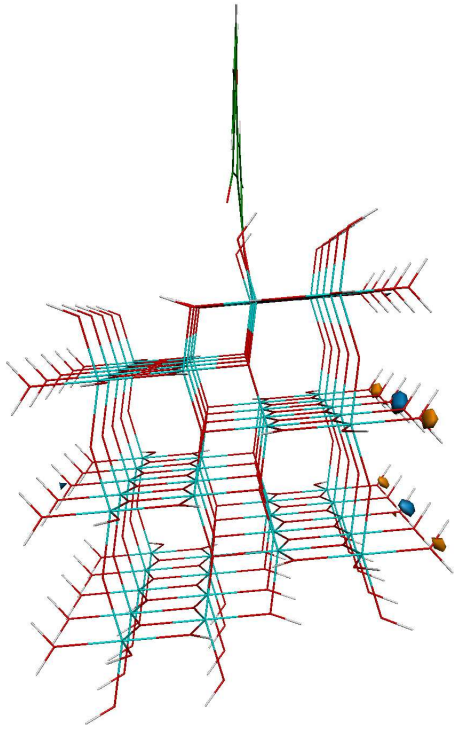

Figure 3.3: Example of an "acceptor" (substrate) orbital of the investigated complex alizarin-$(TiO_2)_{54}(H_2O)_{58}$ with energy in the upper part of the band gap. The orbital is predominantly localized in the saturation groups.

The partitioning procedure results in orbitals localized in the alizarin adsorbate and the $(TiO_2)_{54}(H_2O)_{58}$ substrate, respectively, which are depicted in Fig. 3.2 as donor and acceptor levels. The energy-level scheme of acceptor orbitals in Fig. 3.2 shows a structure very similar to that of the isolated $(TiO_2)_{54}(H_2O)_{60}$ cluster. Similar to the results for the isolated TiO_2 cluster, the acceptor levels in the upper part of the band gap are predominantly localized in the oxygen atoms of the saturation groups. An example for such an orbital is shown in Fig. 3.3. The electronic coupling between these levels in the upper part of the band gap and the donor levels of adsorbate is

negligible in the complex and thus these states do not participate in the ET reaction. The energy-level scheme of the orbitals localized in the adsorbate shows two energy levels in the band gap which correspond to the HOMO and (HOMO-1) of the overall system and are closely related to the HOMO and (HOMO-1) of the isolated dye molecule. For instance, the overlap between the HOMO of the complex and the projected donor orbital that is associated with the HOMO of the alizarin is larger than 0.80 thus demonstrating the close relation.

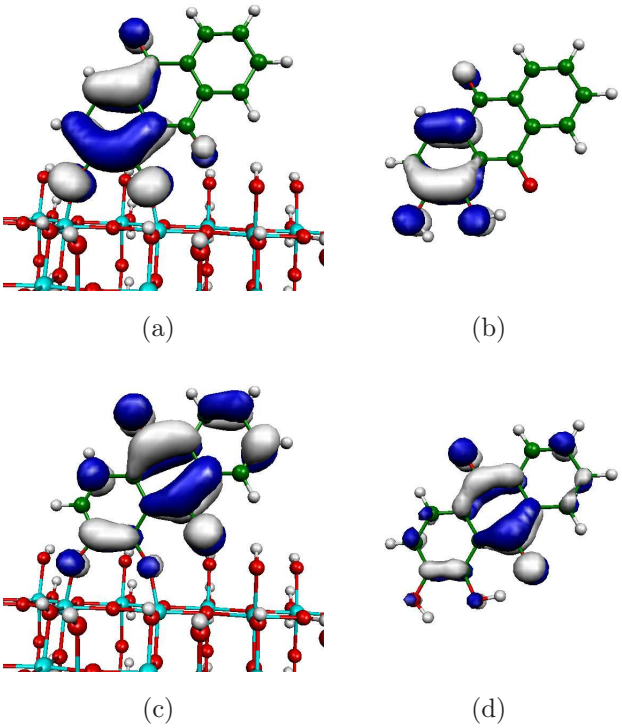

Figure 3.4: Selected localized adsorbate orbitals of the dye-semiconductor complex alizarin-$(TiO_2)_{54}(H_2O)_{58}$ obtained from the partitioning procedure (compared with the corresponding MO of the isolate dye molecule alizarin): (a) the localized orbital of the complex which is associated with the HOMO of the isolated alizarin, (b) the HOMO of the isolated alizarin, (c) the localized orbital of the complex which is associated with the lowest unoccupied MO (LUMO) of the isolated alizarin (*i.e.*, the donor orbital in the ET reaction) and (d) the LUMO of the isolated alizarin.

The localized adsorbate orbital that corresponds to the LUMO of the isolated alizarin is chosen as the donor state of the ET reaction. Time-dependent (TD) DFT calculation for an isolated alizarin shows that the HOMO-LUMO excitation contributes more than 95% to the $S_0 \rightarrow S_1$ excitation. Due to the coupling to the dense manifold of conduction-band states of TiO_2, this donor level does not have a predominant overlap to any single level of the complex. The local character of the two frontier orbitals localized in the adsorbate and the resemblance between them and the corresponding orbitals (HOMO and LUMO) of the isolated alizarin are illustrated in Fig. 3.4.

The acceptor states included in the dynamical calculation of the ET process comprise all orbitals localized in the TiO_2 substrate that are associated with unoccupied orbitals in the conduction band of the isolated titanium oxide cluster. As in the isolated TiO_2 cluster, the acceptor orbitals are dominated by the $3d_{xy}$, $3d_{yz}$ and $3d_{xz}$ orbitals of titanium atoms due to the 3d level splitting caused by the octahedral coordination of oxygen atoms (as indicated by the X-ray structure of bulk anatase [110], here we considered that the titanium atom in each TiO_6 octahedron is located at the origin while the oxygen atoms are located at or near to the coordinate axes, in particular). Fig. 3.5 depicts two examples of the projected acceptor orbitals. The one shown in Fig. 3.5 (a) is delocalized in the substrate part of the complex, while the one shown in Fig. 3.5 (b) has significant contribution from a titanium atom that directly binds to the dye.

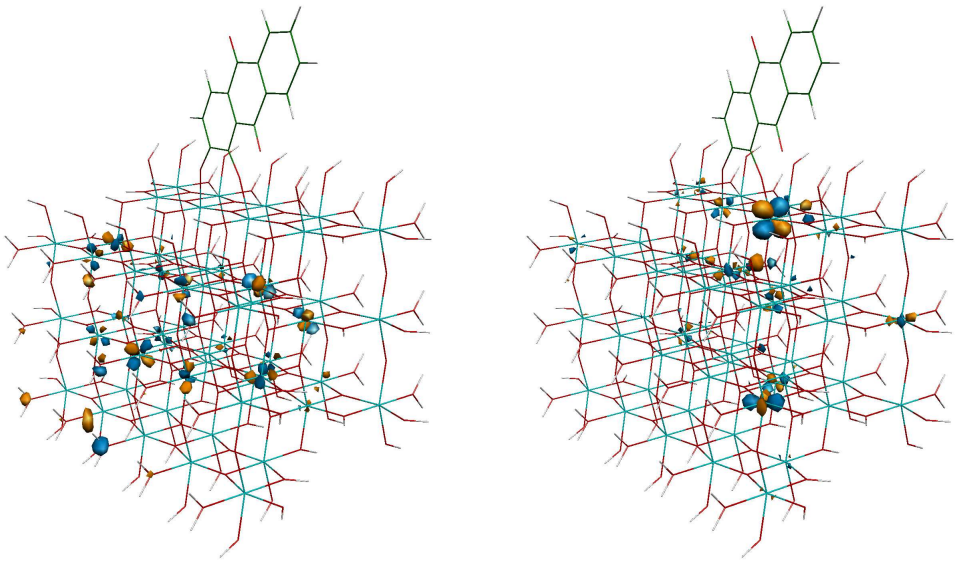

(a) (b)

Figure 3.5: Examples of localized substrate orbitals of the investigated complex alizarin-$(TiO_2)_{54}(H_2O)_{58}$ obtained from the partitioning procedure. Each of these orbitals is associated with an unoccupied orbital in the conduction band of the isolated titanium oxide cluster.

An important parameter for the electron injection dynamics is the location of the donor level relative to the conduction-band minimum. In the present model, the donor level is located about 0.70 eV above the conduction-band minimum, where the latter is defined by the lowest unoccupied 3d orbital of the titanium atoms as discussed above. This location is higher than that reported by Duncan *et al.*, where the donor level has an energy close to the conduction-band minimum [59, 61, 64, 66]. This difference is presumably due to the different adsorption motifs and different forms of titanium oxide (rutile *vs.* anatase) considered and may also be caused by the different functionals and basis sets used. It should also be noted that the donor

level, as defined in the present method, is not a molecular orbital, *i.e.*, an eigenstate of the overall complex. The coupling to the acceptor states will result in a lowering of the energy of the corresponding resonance in the overall complex.

Another key factor for heterogeneous ET reactions is the strength and the distribution of the donor-acceptor coupling. Fig. 3.6 shows the modulus of the donor-acceptor coupling matrix elements V_j^{da} for the system investigated. It is seen that the first-principles based model results in a distribution of donor-acceptor coupling matrix elements V_j^{da} that exhibits a rather complicated structure. This finding agrees with results obtained previously for other dye-adsorbates on the (101) surface of anatase-TiO_2 [41, 80]. For an extended substrate, the donor-acceptor coupling can be characterized by the energy-dependent decay-width function $\Gamma(\varepsilon)$ as defined in Eq. (2.13). The $\Gamma(\varepsilon)$ function, which is obtained based on the discrete V_j^{da} data as discussed in Sections 2.1 and 2.3.1, is also shown in Fig. 3.6. The position of the peak of $\Gamma(\varepsilon)$ is in good agreement with the positions of the two acceptor states with the largest coupling to the donor state (one of which depicted in Fig. 3.5 (b)).

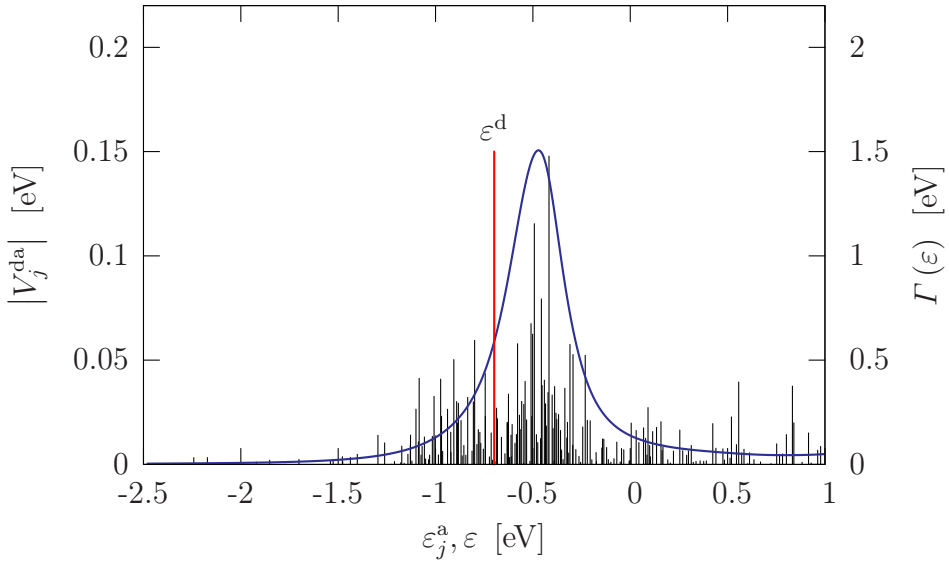

Figure 3.6: Modulus of donor-acceptor electronic coupling matrix elements V_j^{da} (discrete lines) and the decay-width function $\Gamma(\varepsilon)$ (continuous line) of the investigated complex alizarin-$(TiO_2)_{54}(H_2O)_{58}$. The red vertical line indicates the energy of the donor state ε^{d}.

3.4 Analysis of vibrational degrees of freedom and electronic-vibrational coupling

The vibrational frequencies ω_l and the corresponding electronic-vibrational coupling constants $\kappa_l^{\mathrm{d/a}}$ in the donor and acceptor states have been determined for all 72 vibrational modes of alizarin as described in Section 2.3.2. For the l-th normal mode, the electronic-vibrational coupling constants are related to the reorganization energies λ_l^{d}, λ_l^{a} and λ_l^{ET} given by Eqs. (2.32), (2.33) and (2.34), which are associated with transitions from the electronic ground state to the excited state of alizarin, from the electronic ground state of alizarin to the ground state of alizarin-cation, and from the excited state of alizarin to the ground state of alizarin-cation, respectively.

The calculated frequencies and reorganization energies for the donor state and the ET transition are depicted in Fig. 3.7. It is seen that the electronic-vibrational coupling is distributed over a rather large number of vibrational modes. The overall reorganization energies obtained are $\Lambda^{\mathrm{d}} = 0.301$ eV, $\Lambda^{\mathrm{a}} = 0.240$ eV, and $\Lambda^{\mathrm{ET}} = 0.156$ eV for the donor state, the acceptor state, and the ET transition, respectively. These values for the reorganization energies suggest a moderate electronic-vibrational coupling with respect to the electronic excitation but a rather weak coupling to the ET process itself.

For the simulation of the vibronic dynamics in the alizarin-TiO_2 system, 37 of the total 72 vibrational normal modes are selected based on the ET related electronic-vibrational coupling strength $\left(2\omega_l\lambda_l^{\mathrm{d/a/ET}}\right)^{\frac{1}{2}}$. The thus selected modes incorporate more then 98% of the three total reorganization energies and are therefore expected to give a proper representation of the electronic-nuclear coupling in alizarin. All parameters of the normal modes selected in the dynamical simulation are given in Table 3.1.

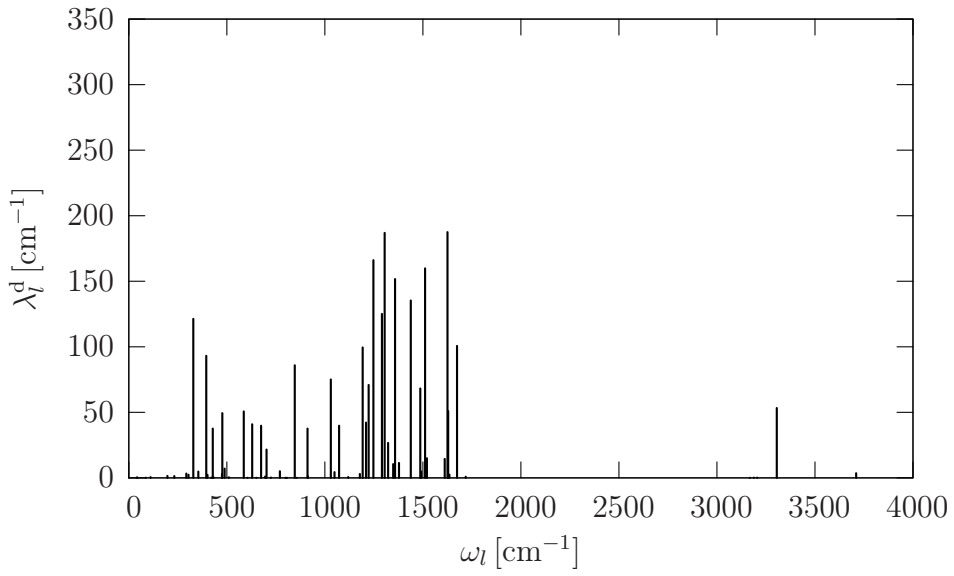

(a)

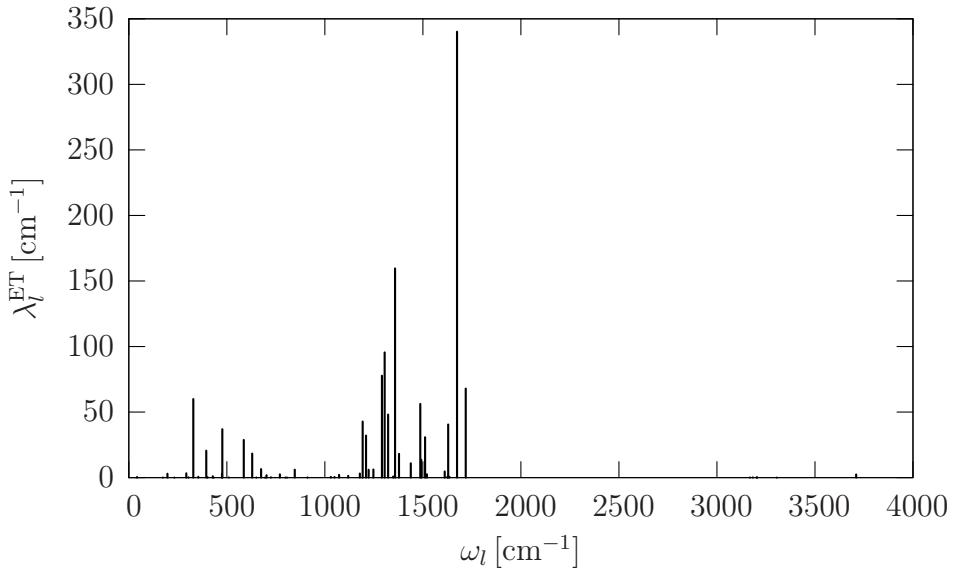

(b)

Figure 3.7: Reorganization energies of all intramolecular modes of alizarin associated with (a) the transition from the ground to the electronically excited state and (b) the ET transition.

Table 3.1: Vibrational parameters of selected normal modes of alizarin included in the dynamical simulation of the ET process. Listed are the ground state harmonic vibrational frequencies and the electronic-vibrational coupling constants in the excited state of alizarin and in the ground state of the alizarin-cation. All data are given in cm^{-1}.

mode No.	ω	$\kappa^{d}\omega^{-\frac{1}{2}}$	$\kappa^{a}\omega^{-\frac{1}{2}}$	mode No.	ω	$\kappa^{d}\omega^{-\frac{1}{2}}$	$\kappa^{a}\omega^{-\frac{1}{2}}$
10	329.0	282.5	83.9	49	1305.2	698.5	199.2
12	395.2	271.3	398.8	50	1322.7	−265.8	−622.5
15	428.2	179.4	149.5	51	1348.7	−168.3	−120.7
18	477.1	217.1	29.3	52	1358.2	641.9	−16.5
21	586.5	−243.9	−60.3	53	1378.2	177.3	400.9
23	629.4	−226.9	−378.8	54	1438.3	623.9	446.5
25	674.9	231.8	138.0	55	1486.7	−450.3	−859.1
27	702.5	−174.2	−224.9	56	1491.7	120.9	−81.1
29	770.6	88.7	150.5	57	1511.2	−695.0	−389.9
32	846.6	−381.4	−280.0	58	1520.4	213.6	301.5
34	911.5	261.8	246.0	59	1611.3	216.2	93.3
39	1030.5	393.4	427.1	60	1625.6	−780.8	−831.6
41	1072.5	−292.2	−224.5	61	1629.2	407.7	44.2
43	1178.4	−84.1	−170.3	62	1635.4	90.4	136.5
44	1192.9	−487.2	−167.8	63	1674.2	580.7	−486.5
45	1210.1	319.6	41.2	64	1718.5	−55.6	427.6
46	1223.3	−416.5	−538.0	71	3305.4	593.6	613.3
47	1247.7	643.8	519.1	72	3710.1	−163.4	−297.2
48	1291.2	568.4	120.3				

According to the electronic-vibrational coupling constants, these vibrational normal modes can be classified into four groups: (i) the normal modes with relatively large $\kappa^{d}\omega^{-\frac{1}{2}}$ but small $\kappa^{a}\omega^{-\frac{1}{2}}$, (ii) the normal modes with relatively small $\kappa^{d}\omega^{-\frac{1}{2}}$ but large $\kappa^{a}\omega^{-\frac{1}{2}}$, (iii) the normal modes with both relatively large $\kappa^{d}\omega^{-\frac{1}{2}}$ and $\kappa^{a}\omega^{-\frac{1}{2}}$ with the same sign, and (iv) the normal modes with both relatively large $\kappa^{d}\omega^{-\frac{1}{2}}$ and $\kappa^{a}\omega^{-\frac{1}{2}}$ with different sign. The normal modes with both small $\kappa^{d}\omega^{-\frac{1}{2}}$ and $\kappa^{a}\omega^{-\frac{1}{2}}$ (and thus also small $\kappa^{ET}\omega^{-\frac{1}{2}}$) are not included in the simulation (also not listed in Table 3.1), since the probability of vibrational excitation of this mode through either the electronic excitation or the ET process is very small. The modes with large $\kappa^{d}\omega^{-\frac{1}{2}}$ have significant probability to be excited through the electronic excitation, while the probability of vibrational excitation through the ET transition is large for the modes with large $\kappa^{ET}\omega^{-\frac{1}{2}}$. Thus, normal modes in different groups are supposed to play different roles in the ET dynamics.

Some vibrational normal modes of alizarin are depicted in Fig. 3.8. Subfigs. (a), (b), (c) and (d) of Fig. 3.8 represent a normal mode of group (iii), (i), (iv) and (ii) as discussed above, respectively.

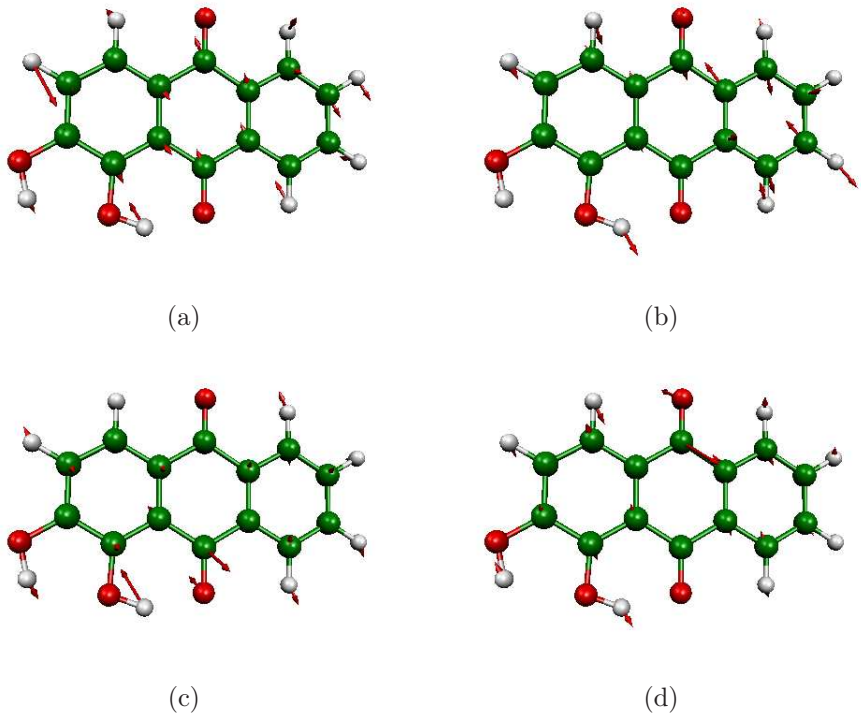

(a) (b)

(c) (d)

Figure 3.8: Selected vibrational normal modes of an isolated alizarin molecule: (a) normal mode No. 39 ($\omega = 1030.5$ cm^{-1}), (b) normal mode No. 52 ($\omega = 1358.2$ cm^{-1}), (c) normal mode No. 63 ($\omega = 1674.2$ cm^{-1}) and (d) normal mode No. 64 ($\omega = 1718.5$ cm^{-1}).

Employing the vibrational modes of the free alizarin molecule (*e.g.* the normal modes depicted in Fig. 3.8) to characterize the electronic-vibrational coupling in the ET dynamics is only an approximation to the vibronic dynamics of ET, since the vibrational motion of the bound alizarin adsorbate is not exactly identical to the vibrational motion of an isolated alizarin molecule, especially for those modes that exhibit significant vibrational motion around the oxygens atoms that bind to the semiconductor substrate. A better approximation can be achieved by specifying some metal atoms at the reaction center to represent the cluster when performing the vibrational analysis for the adsorbate part.

3.5 Electron injection dynamics

The ET dynamics in the alizarin-TiO_2 system is simulated based on the first-principles model outlined in Chapter 2. Fig. 3.9 (a) shows the result of the simulation for the

population of the donor state after photoexcitation (red line). The initial decay of the population of the donor state reveals an ultrafast injection of the electron from the donor state localized in the adsorbate (dye) into the quasi-continuum of acceptor states localized in the TiO_2 substrate on a timescale of a few femtoseconds. The result also exhibits pronounced oscillations on different timescales. A comparison with results of a purely electronic calculation (black line), where the nuclear DoF are frozen at their equilibrium geometry, reveals that the oscillations are due to electronic motion, *i.e.*, reflect electronic coherences. A further analysis of these oscillations is given in Section 3.6.

The comparison between the purely electronic and the vibronic calculation also shows that the coupling to the vibrational modes results in a somewhat slower decay of the population of the donor state, in particular in the short-time dynamics (shown by the inset of Fig. 3.9 (a)). This is due to the fact that during the dynamics the nuclear wavepacket enters regions of phase space with an effectively smaller donor-acceptor coupling [70]. From the reorganization energy data, it is seen that the physical model sketched in Fig. 2.4 (a) is qualitatively suitable for a description for the present system. In this model of an ET reaction, the nuclear wavepacket is found at the intersection of the dashed line (marking the the FC geometry) and the parabola V^{dd} (describing the PES of the donor state) when $t = 0$. At the early stage of the dynamics, the wavepacket is moving along the PES of the donor state towards its minimum due to the vibrational motion, meanwhile intersecting the acceptor states V_j^{aa} with a decreasing quantum number j. As the donor-acceptor coupling matrix elements V_j^{da} are assumed to be independent of the nuclear coordinates, this effect is equivalent to that the wavepacket moving towards the conduction-band minimum, *i.e.*, away from the maximum of the decay-width function $\Gamma(\varepsilon)$ function (*cf.* Fig. 3.6). However, as a result of the relatively small ET reorganization energy (0.155 eV), the total effect is not significant, as the wavepacket is not supposed to leave the region of strong donor-acceptor coupling ($\varepsilon_j^{\mathrm{a}} \in [-1.2\ \mathrm{eV}, 0.0\ \mathrm{eV}]$).

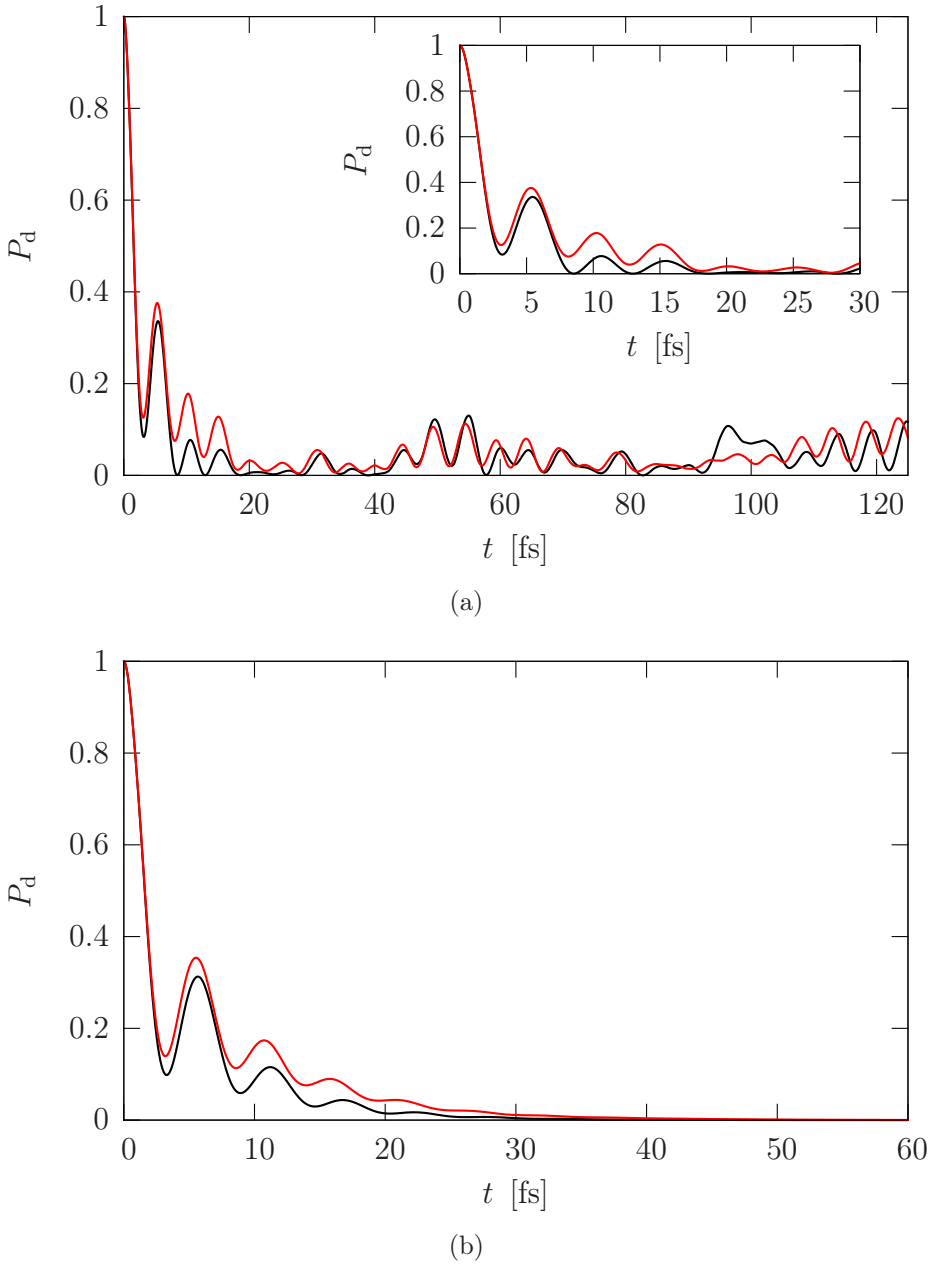

Figure 3.9: Population dynamics of the donor state after photoexcitation in the alizarin-TiO_2 system. Shown are results obtained (a) for the finite $(TiO_2)_{54}$ substrate and (b) for the model of an infinite TiO_2 surface. Both results with vibronic coupling (red lines) and without vibronic coupling (black lines) are depicted.

This finding is different to the results of theoretical simulations for the ET systems with alizarin adsorbed at rutile TiO_2 [59, 61, 64, 66], where, as a consequence of the fact that the donor level has an energy close to the conduction-band minimum, the electronic-coupling is supposed to play an important role in the dynamics. A test calculation based on the present alizarin-TiO_2 system can be performed by shifting the donor level towards the conduction-band minimum. Fig. 3.10 shows the results of ET dynamics with lowering the donor level by 0.25 eV (2000 cm^{-1}), while the acceptor levels and the donor-acceptor coupling matrix elements are left unchanged. The inclusion of the electronic-vibrational coupling (red line) results in a significantly slower electron injection than the purely electronic dynamics (black line) even from the very early stage of the dynamics. The amplitude of the oscillatory structures is also globally reduced.

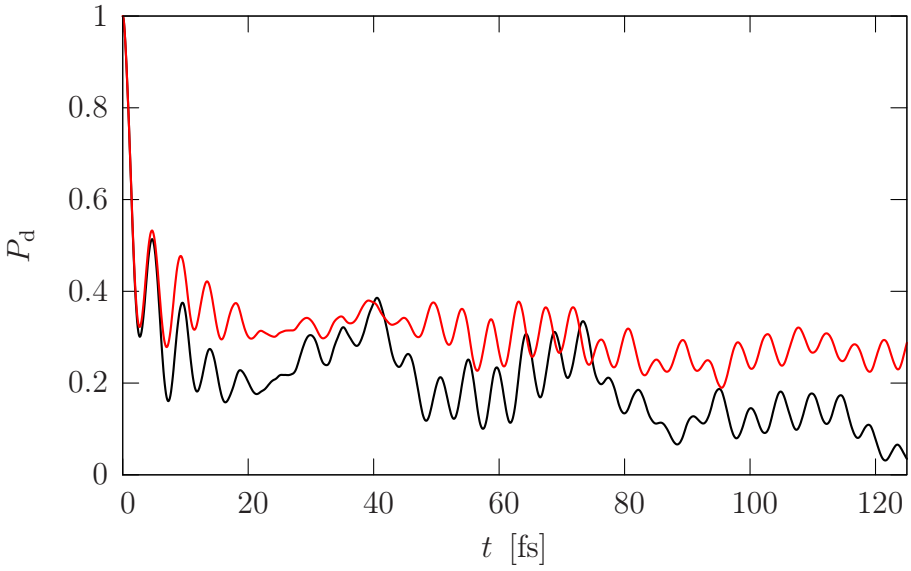

Figure 3.10: Population dynamics of the donor state after photoexcitation in the alizarin-$(TiO_2)_{54}$ system with the donor level shifted by 0.25 eV towards the conduction-band minimum. Both results with vibronic coupling (red lines) and without vibronic coupling (black lines) are depicted.

Due to the coherent oscillatory character of the dynamics, the electron injection dynamics cannot be characterized by a single rate constant. However, the overall timescale of about $5 \sim 10$ fs found in the simulations depicted in Fig. 3.9 agrees well with the experimental result of 6 fs [29] for a colloidal solution of TiO_2 nanoparticles and with previous results of mixed quantum-classical calculations [56, 59, 64]. Very recent experimental result for alizarin adsorbed at nanostructured TiO_2 films shows a slower injection time [109].

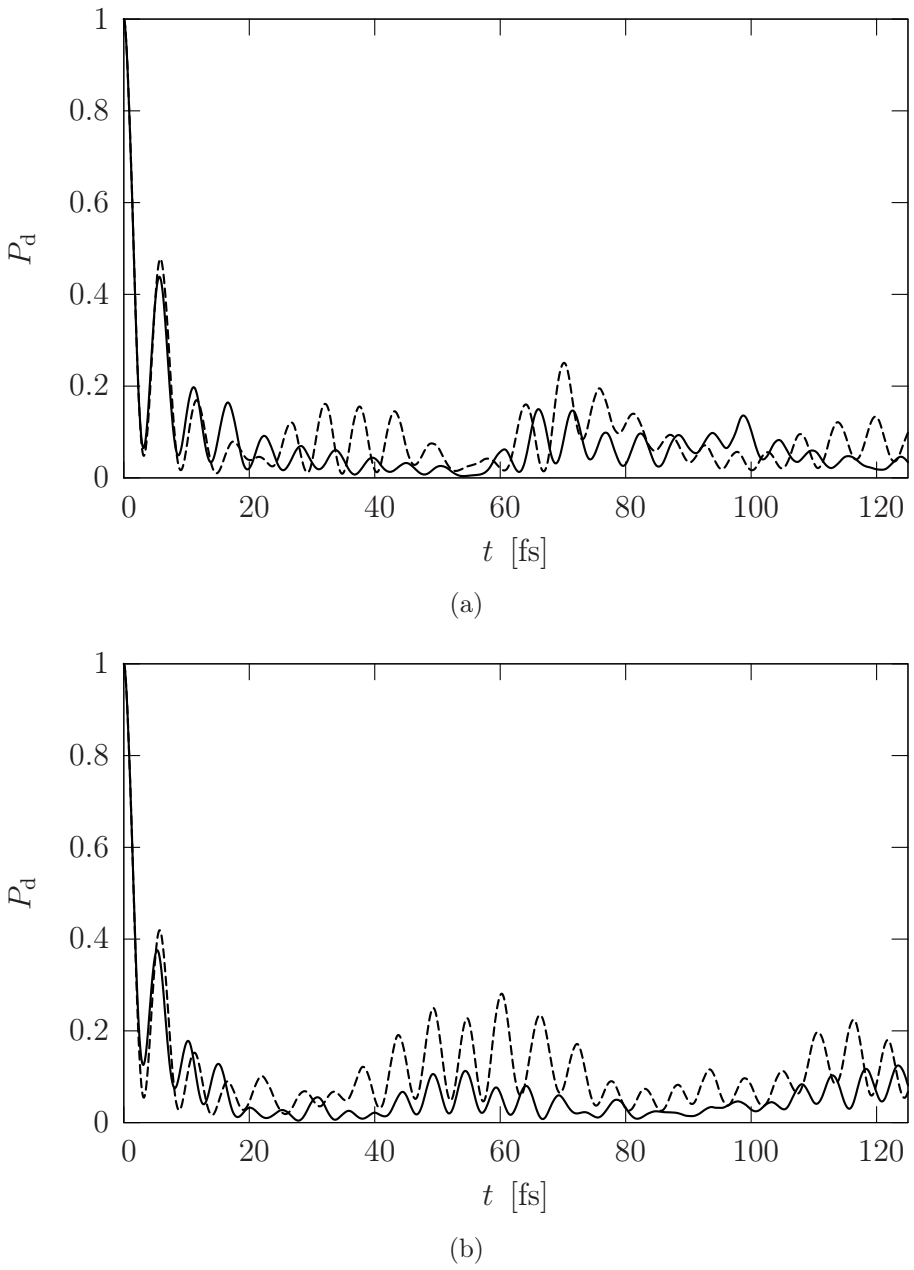

Figure 3.11: Dependence of ET dynamics on the size of TiO_2 cluster used to model the substrate in the alizarin-TiO_2 systems. Shown are results for the vibronic dynamics obtained with the TiO_2 clusters containing (a) 4 (solid line) and 2 (dashed line) layers with 10 TiO_2 units per layer, and (b) 3 layers with 18 (solid line) and 10 (dashed line) TiO_2 units per layer.

The results shown in Fig. 3.9 (a) also show that the population of the donor state does not decay to zero for longer times. This is a result of the finite TiO_2 substrate used in the calculation [105]. Reflection of the wavepacket at the boundaries of the substrate results in recurrences in the population dynamics, *e.g.*, at about 50 fs. The dependence of the ET dynamics on the size of the TiO_2 substrate is illustrated in Fig. 3.11(a more detailed comparison is given in Figs. D.4 - D.9). Fig. 3.11 (a) shows

that an increase of the number of layers of the substrate from two to four (each layer containing 10 TiO_2 units) results in an increase of the recurrence period (due to the reflection at the boundaries) by about a factor of two. On the other hand, an increase of the lateral size of the TiO_2 clusters results in a smaller intensity of recurrences but has negligible effect on the recurrence period, as illustrated in Fig. 3.11 (b). The results in Fig. 3.11 also demonstrate that the influence of the finite size of the TiO_2 cluster is negligible on the timescale of the ultrafast ET process in alizarin.

As discussed in Section 2.3.1 and Appendix B, electron injection at an extended surface can be mimicked using absorbing boundary conditions by including an imaginary part in the orbital energies at the boundary of the substrate. As a result, the recurrences in the dynamics as well as the incompleteness of electron injection are quenched. The corresponding results, depicted in Fig. 3.9 (b), agree for short times well with the results obtained for finite TiO_2 substrates (Fig. 3.9 (a)) but decay to zero for longer times.

3.6 Electronic coherence effects and analysis of electron transfer mechanism

The electron injection dynamics depicted in Fig. 3.9 exhibits pronounced oscillations on a time-scale of about 6 fs. These oscillations are also present in the calculations for the extended system (red lines in Fig. 3.9 (b)) and are therefore not a finite-size effect. The presence of the same oscillations in the results of purely electronic calculations (black lines in Fig. 3.9) as well as the ultrafast timescale of 6 fs show that these oscillations are not related to vibrational dynamics but rather to electronic motion, *i.e.*, can be classified as electronic coherence effects.

This finding suggests that the electron injection process proceeds with a two-step mechanism, *i.e.*, there exists a single (or a few) intermediate state(s) localized in the surface through which the electron in the originally populated donor state decays to the conduction band of the substrate according to the scheme

$$\text{donor state} \rightleftharpoons \text{intermediate state(s)} \rightarrow \text{acceptor states.} \tag{3.1}$$

The fact that the population of the donor state (in the extended system) decays for long time, *i.e.*, the oscillations do not persist, shows that these intermediate states cannot be truly bound surface states with energies in the band gap but rather surface resonances with energies in the conduction band.

To analyze the oscillations in more detail, we consider for simplicity the purely

electronic dynamics in the following. The two-step ET mechanism can be seen more explicitly if the electronic part of Hamiltonian is unitarily transformed to the form

$$\begin{aligned}\hat{H}_{\mathrm{elec}} = &\left|\psi^{\mathrm{d}}\right\rangle \varepsilon^{\mathrm{d}} \left\langle\psi^{\mathrm{d}}\right| + \left|\psi^{\mathrm{m}}\right\rangle \varepsilon^{\mathrm{m}} \left\langle\psi^{\mathrm{m}}\right| + \sum_{j'} \left|\tilde{\psi}^{\mathrm{a}}_{j'}\right\rangle \tilde{\varepsilon}^{\mathrm{a}}_{j'} \left\langle\tilde{\psi}^{\mathrm{a}}_{j'}\right| \\ &+ \left|\psi^{\mathrm{d}}\right\rangle V^{\mathrm{dm}} \left\langle\psi^{\mathrm{m}}\right| + \left|\psi^{\mathrm{m}}\right\rangle V^{\mathrm{md}} \left\langle\psi^{\mathrm{d}}\right| \\ &+ \sum_{j'} \left(\left|\psi^{\mathrm{m}}\right\rangle V^{\mathrm{ma}}_{j'} \left\langle\tilde{\psi}^{\mathrm{a}}_{j'}\right| + \left|\tilde{\psi}^{\mathrm{a}}_{j'}\right\rangle V^{\mathrm{am}}_{j'} \left\langle\psi^{\mathrm{m}}\right| \right). \end{aligned} \tag{3.2}$$

Here we have introduced an intermediate state defined as

$$\left|\psi^{\mathrm{m}}\right\rangle = \sum_{j} \frac{V^{\mathrm{da}}_{j}}{V^{\mathrm{dm}}} \left|\psi^{\mathrm{a}}_{j}\right\rangle \tag{3.3}$$

with energy

$$\varepsilon^{\mathrm{m}} = \sum_{j} \frac{\left(V^{\mathrm{da}}_{j}\right)^2}{\left(V^{\mathrm{dm}}\right)^2} \varepsilon^{\mathrm{a}}_{j}, \tag{3.4}$$

and coupling matrix element to the donor state

$$V^{\mathrm{dm}} = \sqrt{\sum_{j} \left(V^{\mathrm{da}}_{j}\right)^2}. \tag{3.5}$$

The states $\left\{\left|\tilde{\psi}^{\mathrm{a}}_{j'}\right\rangle\right\}$ constitute the "secondary" acceptor states. Eqs. (3.4) and (3.5) show that the intermediate state $\left|\psi^{\mathrm{m}}\right\rangle$ carries all coupling to the donor state and is in turn coupled to the secondary acceptor states.

The intermediate state $\left|\psi^{\mathrm{m}}\right\rangle$ for the alizarin-TiO_2 system studied here is depicted in Fig. 3.12. It is localized in the two titanium atoms that bind to the alizarin and is dominated by the 3d orbitals of titanium atoms. As to be expected from the distribution of their orbitals (*cf.* Figs. 3.4 (c) and 3.12), the interaction between the intermediate state and the donor state is rather strong ($V^{\mathrm{dm}} = 0.336$ eV). Furthermore, the energy of the intermediate state, $\varepsilon^{\mathrm{m}} = -0.513$ eV, is in good agreement with the maximum of the decay-width function of the donor state, $\Gamma(\varepsilon)$ (*cf.* Fig. 3.6) and also close to the donor level ($\varepsilon^{\mathrm{d}} = -0.699$ eV).

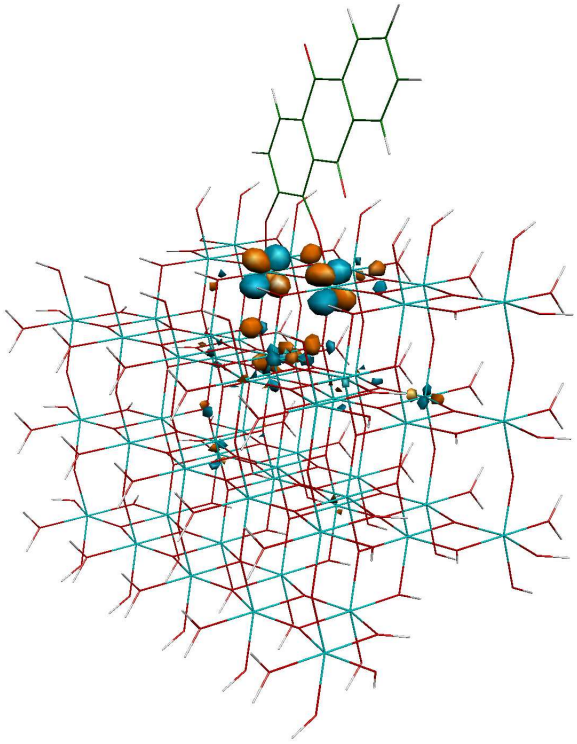

Figure 3.12: Orbital that represents the intermediate state $|\psi^{\mathrm{m}}\rangle$ for the analysis of ET dynamics in the alizarin-TiO_2 system.

The transformed Hamiltonian (3.2) allows an analysis of the two-step mechanism of the ET process. The part of the Hamiltonian without the secondary acceptor states is given by the two-level system of the donor and the intermediate state

$$\hat{H}_{\mathrm{elec}}^{\mathrm{d\text{-}m}} = \left|\psi^{\mathrm{d}}\right\rangle \varepsilon^{\mathrm{d}} \left\langle\psi^{\mathrm{d}}\right| + \left|\psi^{\mathrm{m}}\right\rangle \varepsilon^{\mathrm{m}} \left\langle\psi^{\mathrm{m}}\right| + \left|\psi^{\mathrm{d}}\right\rangle V^{\mathrm{dm}} \left\langle\psi^{\mathrm{m}}\right| + \left|\psi^{\mathrm{m}}\right\rangle V^{\mathrm{md}} \left\langle\psi^{\mathrm{d}}\right| \tag{3.6}$$

and describes the Rabi-oscillations of the electronic population between the donor and the intermediate state:

$$P_{\mathrm{d}}^{\mathrm{d\text{-}m}}(t) = 1 - \frac{4\left(V^{\mathrm{dm}}\right)^2}{4\left(V^{\mathrm{dm}}\right)^2 + \left(\varepsilon^{\mathrm{d}} - \varepsilon^{\mathrm{m}}\right)^2} \sin^2 \frac{\sqrt{4\left(V^{\mathrm{dm}}\right)^2 + \left(\varepsilon^{\mathrm{d}} - \varepsilon_{\mathrm{m}}\right)^2} t}{2} \tag{3.7}$$

with the Rabi-period

$$T^{\mathrm{d\text{-}m}} = \frac{2\pi}{\sqrt{4\left(V^{\mathrm{dm}}\right)^2 + \left(\varepsilon^{\mathrm{d}} - \varepsilon^{\mathrm{m}}\right)^2}}. \tag{3.8}$$

The value of the Rabi-period, $T^{\mathrm{d\text{-}m}} = 6$ fs, agrees well with the oscillation of the donor-state population found for the overall system in Fig. 3.9. Due to the coupling of the intermediate state to the secondary acceptor states, $V_{j'}^{\mathrm{ma}}$, these oscillations are damped.

Fig. 3.13 shows an analysis of the population dynamics employing the intermediate state representation introduced above. After the initial excitation of the donor state,

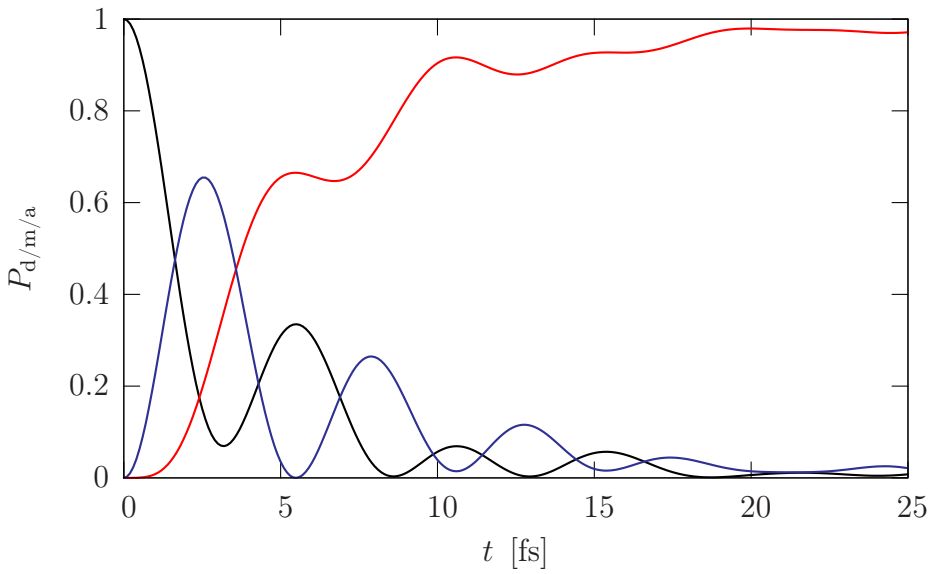

Figure 3.13: Analysis of mechanism of the ET process in the alizarin-TiO_2 system based on the scheme given by Eq. (3.1). Shown are the population dynamics of the donor state (black line), the intermediate state (blue line) and the sum of the population of the remaining ("secondary") acceptor states (red line). All results are obtained employing a finite $(TiO_2)_{54}$ substrate without including electronic-vibrational coupling.

the population oscillates between the donor state and the intermediate state and decays from the intermediate state to the secondary acceptor states in the TiO_2 substrate. The increase of the population of the secondary acceptor states in the substrate is almost monotonous. An overall timescale of $5 \sim 6$ fs based on the e^{-1}-time concept is obtained for the dynamics of the total population in the secondary acceptor states. Thus the overall ET mechanism can be considered as a coherent two-step procedure in accordance with the scheme given by Eq. (3.1).

These findings are in accordance with previous theoretical studies and experimental results. Theoretical simulations [37, 38] for other dyes adsorbed at TiO_2 have shown that the injected electron is initially localized on titanium sites at the surface similar to those represented by the intermediate state $|\psi^{\mathrm{m}}\rangle$ (*cf.* Fig. 3.12). Furthermore, experimental studies for dye-semiconductor systems with a slower injection timescale, in particular, dye molecules adsorbed at ZnO, indicate a stepwise mechanism with an intermediate state that has been attributed to an interface-bound charge-separated pair state or exciplex state [117–120]. Our results show that intermediate states can also be important in systems with very short electron-injection times. In this case, the first step of the ET process may have significantly coherent character.

3.7 Model study of a series of alizarin - titanium oxide complexes with larger donor-acceptor distances

In this section, the results of ET dynamics in several alizarin-$(TiO_2)_{54}(H_2O)_{58}$ systems with larger distances between the alizarin adsorbate and the TiO_2 substrate are discussed. The geometries of the investigated systems are obtained by increasing the distance between the alizarin adsorbate and the anatase TiO_2 substrate along the (100) direction of the cluster by 0.1 Å, 0.2 Å, 0.3 Å, 0.4 Å and 0.5 Å (denoted by $\delta d_{\text{d-a}}$ in the following discussions). As an example, Fig. 3.14 shows the structure of the complex with $\delta d_{\text{d-a}} = 0.5$ Å.

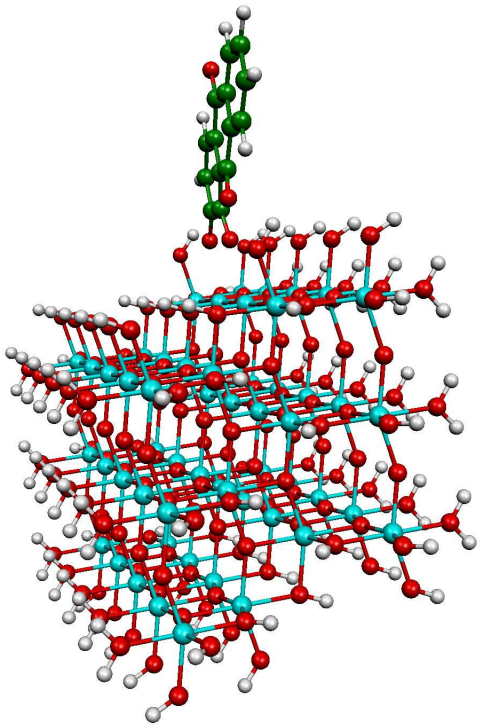

Figure 3.14: Complex alizarin-$(TiO_2)_{54}(H_2O)_{58}$ with the alizarin adsorbate located 0.5 Å away from its equilibrium position to the TiO_2 substrate along the (100) direction.

The energy-level schemes (Fig. D.10 in Appendix D) of the systems investigated, obtained by the partitioning procedure applied based on the electronic structure calculations, show overall similar band structure of the localized substrate levels. The energies of localized adsorbate levels of these systems, on the other hand, are overall higher than those of the original system without increasing the adsorbate-substrate distance. One important feature illustrated in Fig. D.10 is that by increasing the adsorbate-substrate distance, the localized donor orbital, which is associated with the LUMO of the isolated alizarin, becomes less dissolved in the dense manifold of

the acceptor (conduction-band) levels (as shown by the red lines representing the correlation between $\left|\psi^{\mathrm{d}}\right\rangle$ and some unoccupied MO of the complex). This reflects a weaker interaction between the adsorbate (donor) and the substrate (acceptor), which is an obvious consequence of the increased adsorbate-substrate distance.

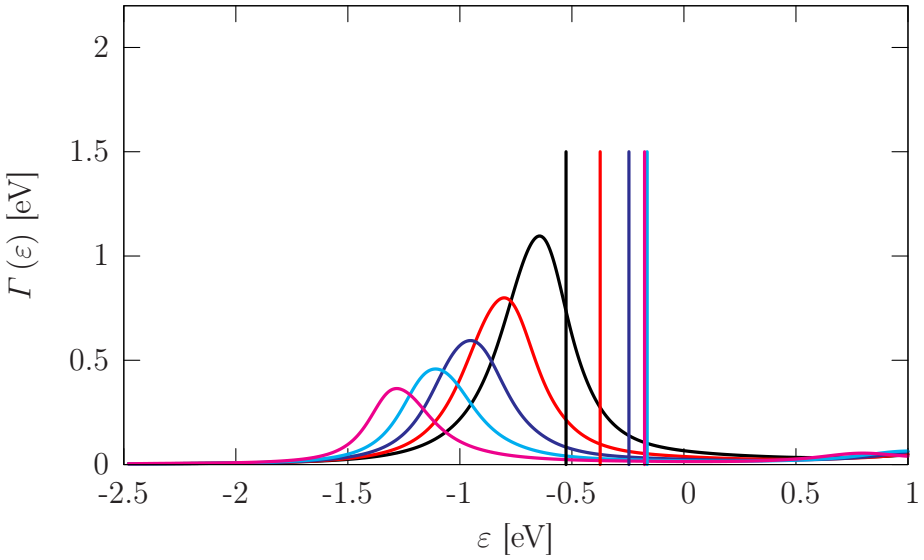

Figure 3.15: Energy-dependent decay-width functions $\Gamma(\varepsilon)$ (continuous curves) and energies of the donor states ε^{d} (vertical lines) of the investigated complexes alizarin-$(TiO_2)_{54}(H_2O)_{58}$ with the alizarin adsorbate 0.1 Å (black lines), 0.2 Å (red lines), 0.3 Å (blue lines), 0.4 Å (cyan lines) and 0.5 Å (magenta lines) away from its equilibrium position to the TiO_2 substrate along the (100) direction.

The donor-acceptor coupling schemes for the investigated systems are illustrated in Fig. 3.15. For simplicity, only the decay-width functions $\Gamma(\varepsilon)$ and the donor-state energies ε^{d} are shown. For each system, the position of the peak of $\Gamma(\varepsilon)$ is in good agreement with the region of maximal donor-acceptor coupling shown by the discrete scheme of donor-acceptor coupling matrix elements (*cf.* Fig. D.11). From Fig. 3.15, it is seen that, with an increasing adsorbate-substrate distance, (i) the strength of the donor-acceptor coupling monotonically decreases and (ii) the region of strongest donor-acceptor coupling monotonically moves towards the conduction-band minimum.

This trend can be understood by the following analysis. In order to simplify the notations, we define the direction that the TiO_6 octahedra are slightly prolonged (as shown by the X-ray structure of bulk anatase [110]) as z, and the direction perpendicular to the (100) planes of anatase as y (as indicated in Fig. 3.16). Thereby the unoccupied orbital of titanium that the most strongly interacts with the donor orbital is $3d_{yz}$. Fig. 3.16 shows the x-, y- and z-directions and the orbital which represents the intermediate state in alizarin-$(TiO_2)_{58}$ ($\delta d_{\text{d-a}} = 0$), which is mainly

contributed from the two acceptor orbitals (both are $3d_{yz}$) with the largest coupling to the donor orbital. For a system with a larger $\delta d_{\text{d-a}}$ (thus less stable), the energies of bonding MO of the overall system are higher (as shown in Fig. D.10) due to the weaker interaction between the occupied orbitals of the dye and the unoccupied orbitals of the substrate. In particular, the energy of HOMO, which can mainly be considered as a result of the ($\pi\pi^*$) interaction between the HOMO of the dye and the $3d_{yz}$ of titanium, is higher for a system with a larger $\delta d_{\text{d-a}}$. As a consequence, the corresponding anti-bonding MO of the overall system, which also reflects the interaction between the HOMO of the dye and the two $3d_{yz}$ of titanium atoms (corresponding to the localized acceptor orbitals with the largest coupling to the donor orbital), has a lower energy. This can rationalize the monotonic decrease of energy region of strongest donor-acceptor coupling with an increasing adsorbate-substrate distance.

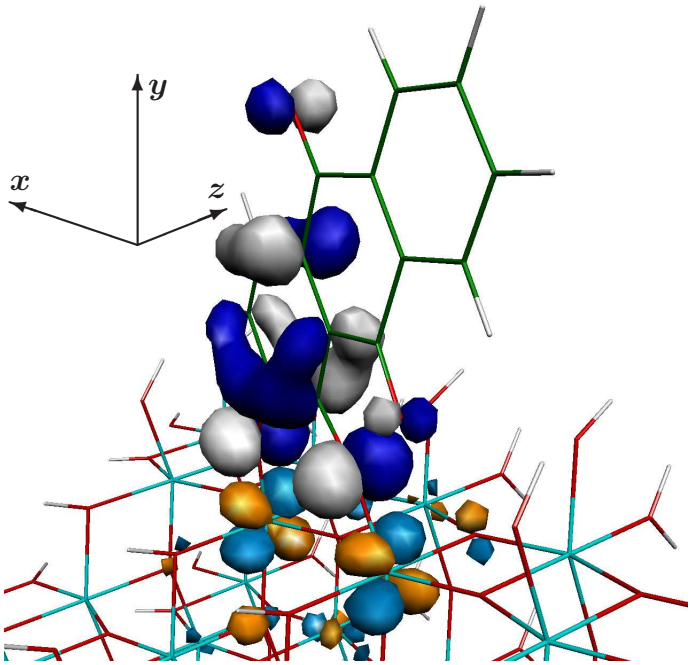

Figure 3.16: The localized adsorbate orbital that is associated with the HOMO of the isolated alizarin (in blue and white, identical to that shown by Fig. 3.4 (a)) and the intermediate orbital (in light blue and light brown, identical to that shown by Fig. 3.12) of the investigated complex alizarin-$(TiO_2)_{58}$. The latter represents the two acceptor orbitals with the strongest coupling to the donor orbital. The x-, y- and z-axes are also indicated, which are defined in order to simplify the analysis. Thus, the intermediate orbital in light blue and light brown has pronounced contribution from the $3d_{yz}$ orbitals of the two titanium atoms that directly bind to the dye adsorbate.

On the other hand, ε^{d} values from left to right correspond to the complexes with adsorbate-substrate distances extracted by 0.1 Å, 0.2 Å, 0.3 Å, 0.5 Å and 0.4 Å, respectively, and thus do not show a completely monotonic tendency versus the

adsorbate-substrate distances. In particular, the difference between the ε^{d} of the system with $\delta d_{\text{d-a}} = 0.4$ Å and that with $\delta d_{\text{d-a}} = 0.5$ Å is rather small.

Table 3.2: Energy parameters for alizarin-$(TiO_2)_{54}(H_2O)_{58}$ systems with adsorbate-substrate distances extracted for $\delta d_{\text{d-a}}$ (given in Å). For each system, the decay-width of the donor state $\Gamma\left(\varepsilon^{\mathrm{d}}\right)$ (given in eV) as well as the energy difference (given in eV) between the donor-state energy ε^{d} and the maximum of the decay-width function $\max\{\Gamma(\varepsilon)\}$ are listed. Corresponding data for the system with unmodified geometry ($\delta d_{\text{d-a}} = 0.0$ Å) is also shown for comparison.

$\delta d_{\text{d-a}}$	$\varepsilon^{\mathrm{d}} - \max\{\Gamma(\varepsilon)\}$	$\Gamma\left(\varepsilon^{\mathrm{d}}\right)$
0.0	−0.227	0.590
0.1	0.118	0.735
0.2	0.428	0.098
0.3	0.707	0.036
0.4	0.945	0.021
0.5	1.106	0.016

As a total effect, the energy difference between the donor level and the region of strongest donor-acceptor coupling increases monotonically when the adsorbate-substrate distance increases. In particular, the donor state is further away from the region of strongest donor-acceptor coupling in a system with larger adsorbate-substrate distance when $\delta d_{\text{d-a}} > 0.1$ Å. This parameter is listed in the second column of Table 3.2. The fact that, for $\delta d_{\text{d-a}} > 0.1$ Å, the localized donor orbital (obtained from the partitioning procedure) that is associated to the LUMO of the isolated alizarin becomes less dissolved in the dense manifold of the acceptor levels with larger $\delta d_{\text{d-a}}$ (as shown by Fig. D.10) can be rationalized by the combination of the monotonic increase of the $\left|\varepsilon^{\mathrm{d}} - \max\{\Gamma(\varepsilon)\}\right|$ value and the monotinic decrease of the strength of the donor-acceptor coupling.

Also seen from Table 3.2 is the monotonic decrease of the decay-width of the donor state $\Gamma\left(\varepsilon^{\mathrm{d}}\right)$ in the region $\delta d_{\text{d-a}} \in \left[0.1\text{ Å}, 0.5\text{ Å}\right]$, which can, in the Golden-Rule theory, characterize the reaction rate constant of the transition from the initial discrete state to the continuum of the final states.

The ET dynamics in these modified alizarin-TiO_2 systems has been simulated based on the first-principles model with all other parameters concerning the motion of the nuclear DoF left unchanged. The results of vibronic dynamics for the donor-state populations obtained for the model of an infinite TiO_2 surface for the systems with $\delta d_{\text{d-a}} \in \left[0.1\text{ Å}, 0.3\text{ Å}\right]$ are shown in Fig. 3.17 (the results for the systems with $\delta d_{\text{d-a}} \in \left[0.4\text{ Å}, 0.5\text{ Å}\right]$ are shown in Fig. D.12 with a different scale of the t-axis).

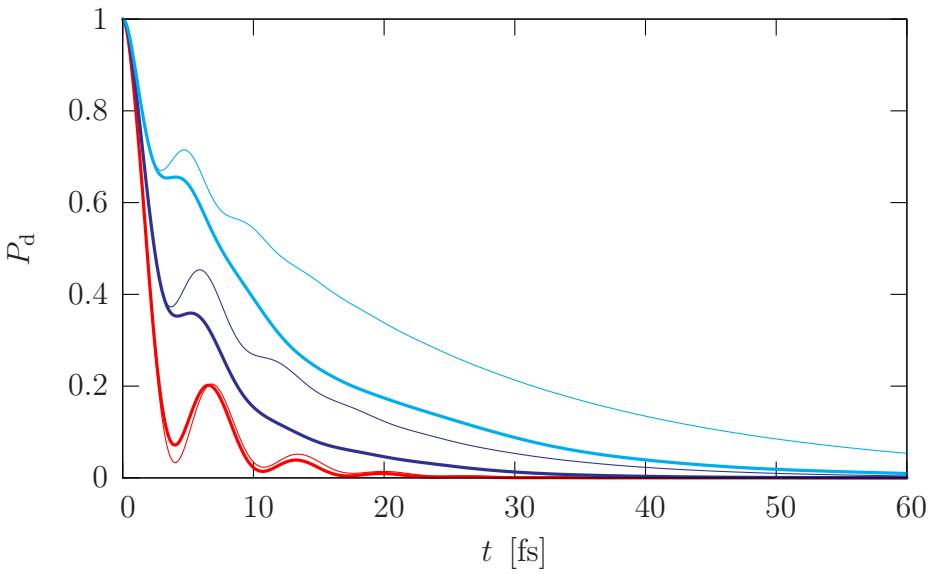

Figure 3.17: Population dynamics of the donor state after photoexcitation in the alizarin-TiO_2 systems with the alizarin adsorbate away from its equilibrium position to the TiO_2 substrate along the (100) direction for 0.1 Å (red lines), 0.2 Å (blue lines), 0.3 Å (cyan lines). Shown are results obtained for the model of an infinite TiO_2 surface. Both results with vibronic coupling (thick lines) and without vibronic coupling (thin lines) are depicted.

From Fig. 3.17 and Fig. D.12, some interesting features can be observed for the systems with $\delta d_{\text{d-a}} \in [0.1\ \text{Å}, 0.5\ \text{Å}]$. First of all, the electron injection becomes monotonically slower with an increasing adsorbate-substrate distance (the overall timescales are about 5 fs, 8 fs, 12 fs, 25 fs and 33 fs for $\delta d_{\text{d-a}} = 0.1$ Å, 0.2 Å, 0.3 Å, 0.4 Å and 0.5 Å, respectively), which agrees well with the trend of the $\Gamma\left(\varepsilon^{\text{d}}\right)$ values. Second, the results for all systems exhibit pronounced oscillations on a timescale less than 6 fs which reflect electronic coherences. The amplitude of these oscillatory structures decreases with an increasing $\delta d_{\text{d-a}}$. Third, the inclusion of electronic-vibrational coupling results in an obviously faster decay of the population of the donor state except for the system with $\delta d_{\text{d-a}} = 0.1$ Å, where the effect of electronic-vibrational coupling is rather small. Furthermore, complete electron injection can be achieved for all systems with mimicking an extended TiO_2 surface (for the system with $\delta d_{\text{d-a}} = 0.3$ Å, P_{d} decays to 0 in the region of $t > 60$ fs).

The effect of the electronic-vibrational coupling can be rationalized by a combination of the donor-acceptor coupling schemes (Fig. 3.15) and the reorganization energy data. The latter factor implies that, as already mentioned above, Fig. 2.4 (a) gives a qualitative model to describe the alizarin-TiO_2 systems. The initially prepared wavepacket moves along the PES of the donor state towards the conduction-band minimum at the early stage of the dynamics. For the system with $\delta d_{\text{d-a}} = 0.1$ Å,

as a result of $\Lambda^{\mathrm{ET}} = 0.155$ eV and $\varepsilon^{\mathrm{d}} - \max\{\Gamma(\varepsilon)\} = 0.118$ eV, the wavepacket remains within the region of $\max\{\Gamma(\varepsilon)\}$ (thus the region of strongest donor-acceptor coupling) during its motion. This results in a fast decay of the donor-state population and a weak effect of electronic-vibrational coupling. However, for all other four systems, since the $\left[\varepsilon^{\mathrm{d}} - \max\{\Gamma(\varepsilon)\}\right]$ values are all positive and larger than Λ^{ET} (*cf.* Table 3.2), the wavepacket moves significantly towards the region of strongest donor-acceptor coupling during its vibrational motion along the donor-state PES. This results in a pronounced effect of electronic-vibrational coupling, which accelerates the ET dynamics.

3.8 Summary

In this chapter, we have studied the quantum dynamics of photoinduced heterogeneous ET processes in the dye-semiconductor system alizarin-TiO_2. The study was based on a method which uses first-principles electronic structure calculations to characterize the system and to parametrize a model Hamiltonian including electronic-vibrational coupling. Based on this model, the quantum dynamics of the ET process has been simulated using the ML-MCTDH method.

The results of the simulations reveal that the electron injection in the investigated system takes place on an ultrafast timescale of about 10 fs, which is in good agreement with experimental results [29]. The results also show that the electron injection dynamics is accompanied by significant electronic coherence effects and thus cannot be characterized by a single rate constant. A detailed analysis shows that the ET process in the alizarin-TiO_2 can be described by a two-step mechanism, which involves an intermediate state localized at the dye-semiconductor interface. The strong coupling between the donor and the intermediate state results in coherent electronic motion, which is damped due to the interaction with the substrate.

We have also performed an analysis of the electronic-vibrational coupling in the ET process. The quantum-dynamical simulations show that the coupling to the vibrational modes of the dye-adsorbate results in a somewhat slower injection dynamics. However, due to the ultrafast timescale of the ET process and the relatively small reorganization energy, the overall effect of electronic-vibrational coupling in the alizarin-TiO_2 system is rather small. A model study of systems with an increased distance between the dye-adsorbate and the titanium oxide substrate results in more pronounced effect of electronic-vibrational coupling with the presence of much weaker donor-acceptor coupling.

Chapter 4

Effects of Anchor and Spacer Groups: Electron Transfer Processes in the Dye-Semiconductor Systems Pyridine / Perylene - Titanium Oxide

4.1 Introduction

In this chapter, we apply the first-principles based methodology of quantum dynamics outlined in Chapter 2 to various dye-semiconductor systems in order to study effects of different anchor and spacer groups on the ET dynamics. The systems investigated in this chapter contain different pyridine- and perylene-based adsorbates, which are adsorbed on surfaces of titanium oxide clusters. Thereby an *anchor group* is defined as the functional group that connects the chromophore group of the dye molecule and the surface atom(s) of the semiconductor substrate, while the group that connects the chromophore group of the dye molecule and the anchor group is referred to as the *spacer group*. Thus, dye molecules (or adsorbates) studied in this chapter can be understood as different chromophore-anchor or chromophore-spacer-anchor combinations. We expect that using different anchor group (or spacer-anchor group) in the dye-semiconductor system will affect the energy-level structure of the localized adsorbate orbitals and introduce difference in both strength and distribution of the donor-acceptor coupling. The ET dynamics in dye-semiconductor systems can be modulated due to these two aspects.

In practical applications, dye molecules used in dye-semiconductor systems can be classified into two categories: purely organic conjugated molecules and transition-metal complexes. All dye molecules in the systems investigated in this thesis belong to the first category. There are various chemical structures of purely organic dye molecules, most of which possess planar conjugated π-structures. Some organic dye molecules, such as catechol, alizarin, coumarin 343 and bi-isonicotinic acid (Fig. 4.1), contain heteroatomic functional groups. Thus they can directly adsorb to the surface

of the semiconductor substrate via metal-heteroatom chemical bonds. On the other hand, some organic chromophore molecules, such as pyridine and perylene (Fig. 4.2), do not have any heteroatomic functional groups. For these chromophore groups, an anchor group is often required to bind to the surface (transition-metal) atoms of the semiconductor substrate.

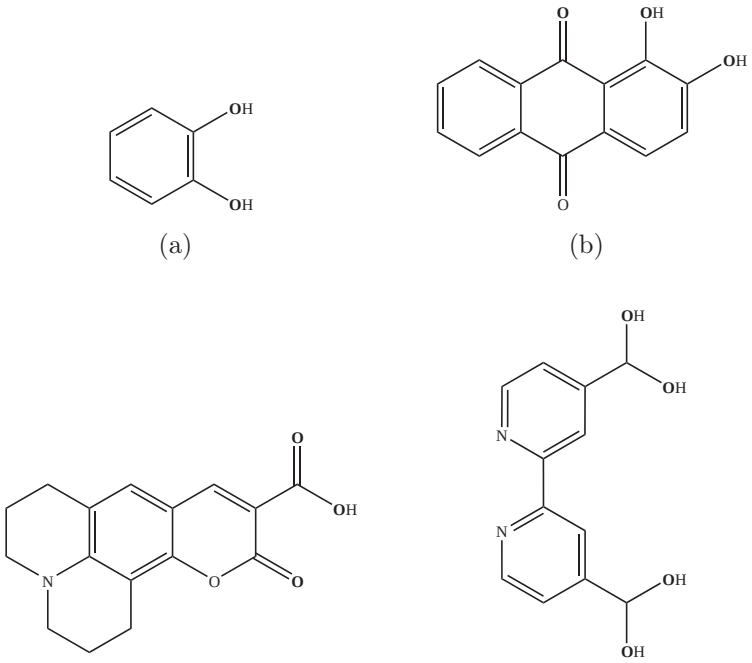

Figure 4.1: Examples of purely organic aromatic molecules, (a) catechol, (b) alizarin, (c) coumarin 343 and (d) bi-isonicotinic acid, which can be used as dye molecules for dye-semiconductor ET systems. The heteroatoms (oxygen atoms) which can directly bind to the surface metal atoms of semiconductor substrates are boldfaced.

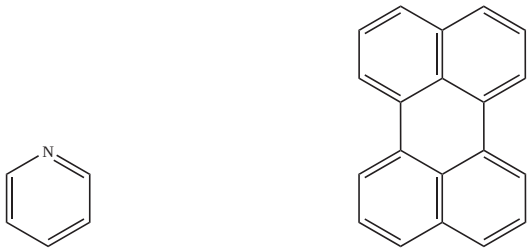

Figure 4.2: Examples of purely organic conjugated molecules, (a) pyridine and (b) perylene, which can be used as dyes for dye-semiconductor ET systems. In these systems, there are no heteroatomic functional groups which can directly bind to the surface metal atoms of semiconductor substrates.

The dye-semiconductor systems containing pyridine-based dye molecules mainly serve as models [55] for adsorbate-substrate interactions for common ruthenium polypyridyl sensitizer systems [121–126]. In contrast, the perylene-based systems allow direct comparisons with ultrafast laser spectroscopy measurements [25,26,33,72,127, 128]. Both electronic structures of dye-semiconductor complexes and electron injection rates have been previously studied for these systems [67, 72, 75]. Thereby the rates of ET reactions were characterized using the broadening of the initially excited donor state motivated by the fundamental idea of the Anderson-Newns model [77]. In this chapter, the electronic structure of the investigated systems is studied in combination with the partitioning procedure outlined in Section 2.3.1, and the time-dependent electron injection dynamics is simulated within the first-principles based model. A comparison of different rate-theory approaches is presented.

In Section 4.2, we discuss the ET processes in the systems containing pyridine- and perylene-based adsorbates with different anchor groups, while Section 4.3 focuses on systems containing perylene-based adsorbates with different spacer groups between the perylene chromophore group and the carboxylic-acid anchor group. Both sections include results of electronic structure calculations, discussions about the donor-acceptor separation and coupling matrix elements, and analysis on the ET dynamics.

4.2 Influence of the anchor group on the electron transfer dynamics

4.2.1 Characterization of the systems

To study the influence of the anchor group on the ET dynamics, we have considered the quantum dynamics of electron injection in dye-semiconductor systems with four different dye molecules. In each system, a bulky $(TiO_2)_{46}$ cluster is used to model the semiconductor substrate. The model chromophores considered include pyridine and perylene, which are bound to the titanium dioxide substrate via two different anchor groups, carboxylic acid and phosphonic acid. The thus obtained four different dyes are denoted by PyC, PyP, PeC and PeP in the following. In all four cases, we have used a monodentate (ester) binding mode between the adsorbate and the substrate. Fig. 4.3 shows the chemical structures of the four dyes considered. The four dye-semiconductor systems are depicted in Fig. 4.4.

The structures of the four investigated dye-semiconductor systems were obtained according to the following protocol: (i) the systems consisting of the different anchor

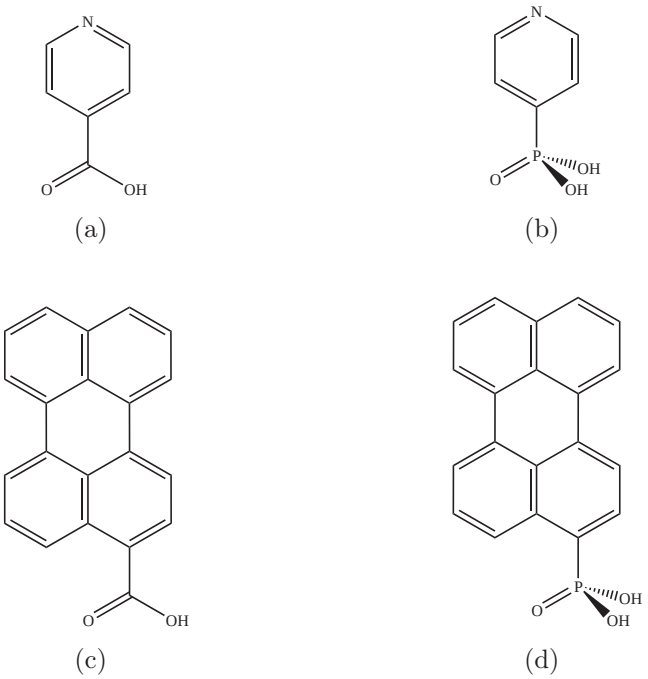

Figure 4.3: Chemical structure of the four dyes considered in the study: (a) pyridine-COOH (PyC), (b) pyridine-PO_3H_2 (PyP), (c) perylene-COOH (PeC) and (d) perylene-PO_3H_2 (PeP).

groups and the involved titanium dioxide cluster were optimized; (ii) the bonding geometries between different aromatic molecules and different anchor-TiO_2 systems are optimized using a periodic model [67]; and (iii) the pyridine or perylene moiety is mounted onto the parts obtained in step (i) according to the corresponding geometries obtained in step (ii). The calculations were performed using DFT with the B3LYP functional and a 31G/311G/41G basis set (VDZ), which is used to respectively describe the valence electrons of $\{\mathrm{H, C, N, O}\}/\mathrm{P/Ti}$ atoms, combined with large effective core potentials (ECP) [129, 130] describing the core electrons.

In the electronic structure calculations, an additional diffuse sp-shell for oxygen atoms is included in the basis set in order to allow a realistic description of the negative ions in the nanocrystallines with significant ionic character. This method, denoted by B3LYP/VD(T)Z, has proved capable to give good results in describing the electronic structure of systems comprising organic adsorbates on TiO_2 surfaces [55]. All calculations mentioned above were carried out using the GAUSSIAN 03 package [114].

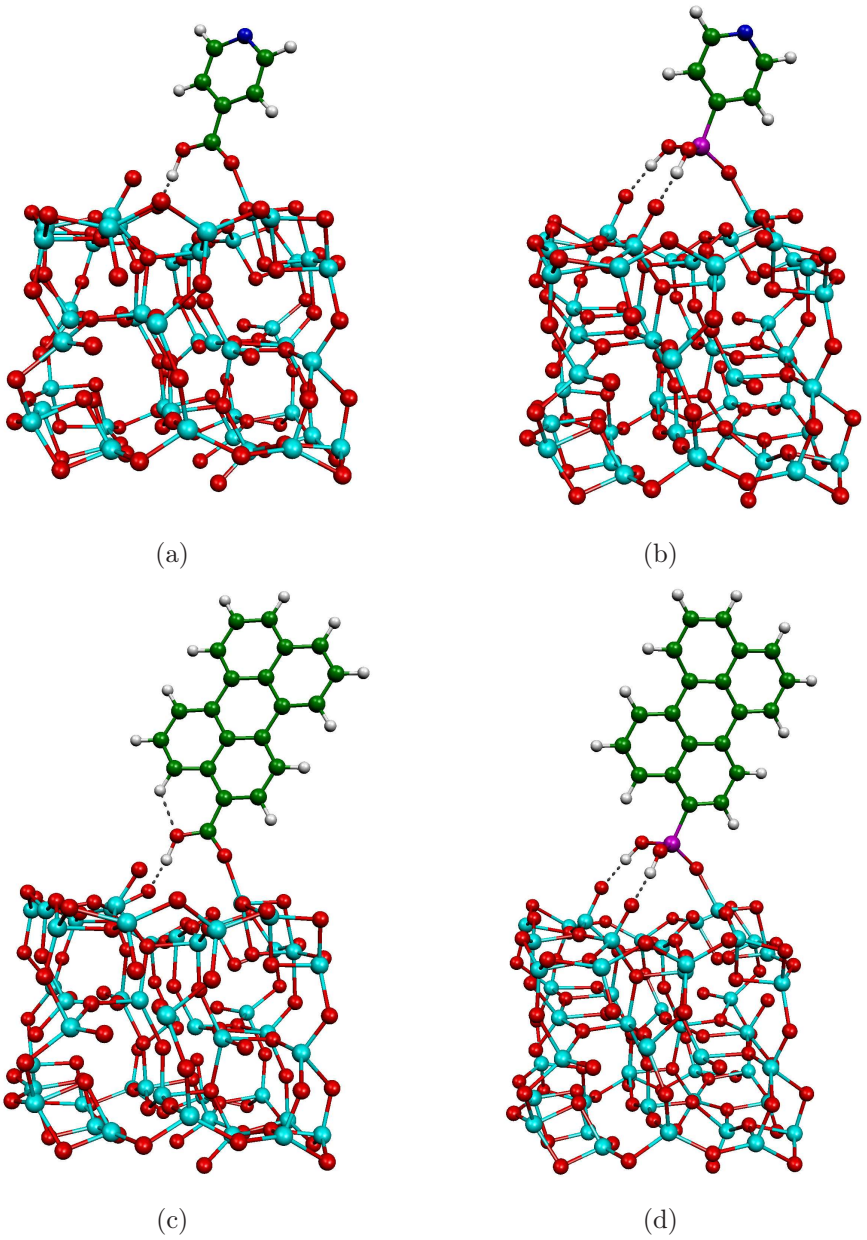

(a) (b)

(c) (d)

Figure 4.4: The four complexes considered in the study: (a) PyC-$(TiO_2)_{46}$, (b) PyP-$(TiO_2)_{46}$, (c) PeC-$(TiO_2)_{46}$ and (d) PeP-$(TiO_2)_{46}$.

4.2.2 Energy-level scheme, donor-acceptor separation and coupling matrix elements

To discuss the donor-acceptor partitioning, we first consider the energy-level scheme. Figs. 4.5 and 4.6 show energies of the MO of the overall dye-TiO_2 complexes as well as those of the donor and acceptor orbitals obtained from the partitioning procedure for the four systems investigated. For each system, the MO-energies (shown in the middle panel of the corresponding subfigure) exhibit a dense level structure with a valence and a conduction band separated by a band gap. In addition, there are a few isolated levels in the band gap. The calculated value for the band gap is 4.8 eV, which is somewhat larger than experimental value (3.4 eV [116]) for anatase TiO_2 nanoparticles.

The partitioning procedure results in donor and acceptor orbitals that are localized in the adsorbate and the $(TiO_2)_{46}$ substrate, respectively. The energy-level scheme of the acceptor orbitals shows a structure very similar to that of the isolated $(TiO_2)_{46}$ cluster [75]. All energy levels in the band gap of the complex are localized in the adsorbate, and, therefore, result within the partitioning procedure in donor orbitals. These orbitals can be associated with the occupied orbitals of the isolated dye molecules. The number of orbitals in the band gap depends on the specific system. While in each of the two pyridine-based complexes only the HOMO and $(\mathrm{HOMO}-1)$ are located in the band gap, there are several occupied levels in the band gap in the perylene-based complexes. The results in Figs. 4.5 and 4.6 also show that energies of the donor levels in the band gap are very close to those in the complex, indicating almost negligible interaction with the substrate. This is corroborated by the fact that the overlap of the donor orbitals in the band gap with the corresponding orbitals of the complex is larger than 0.99.

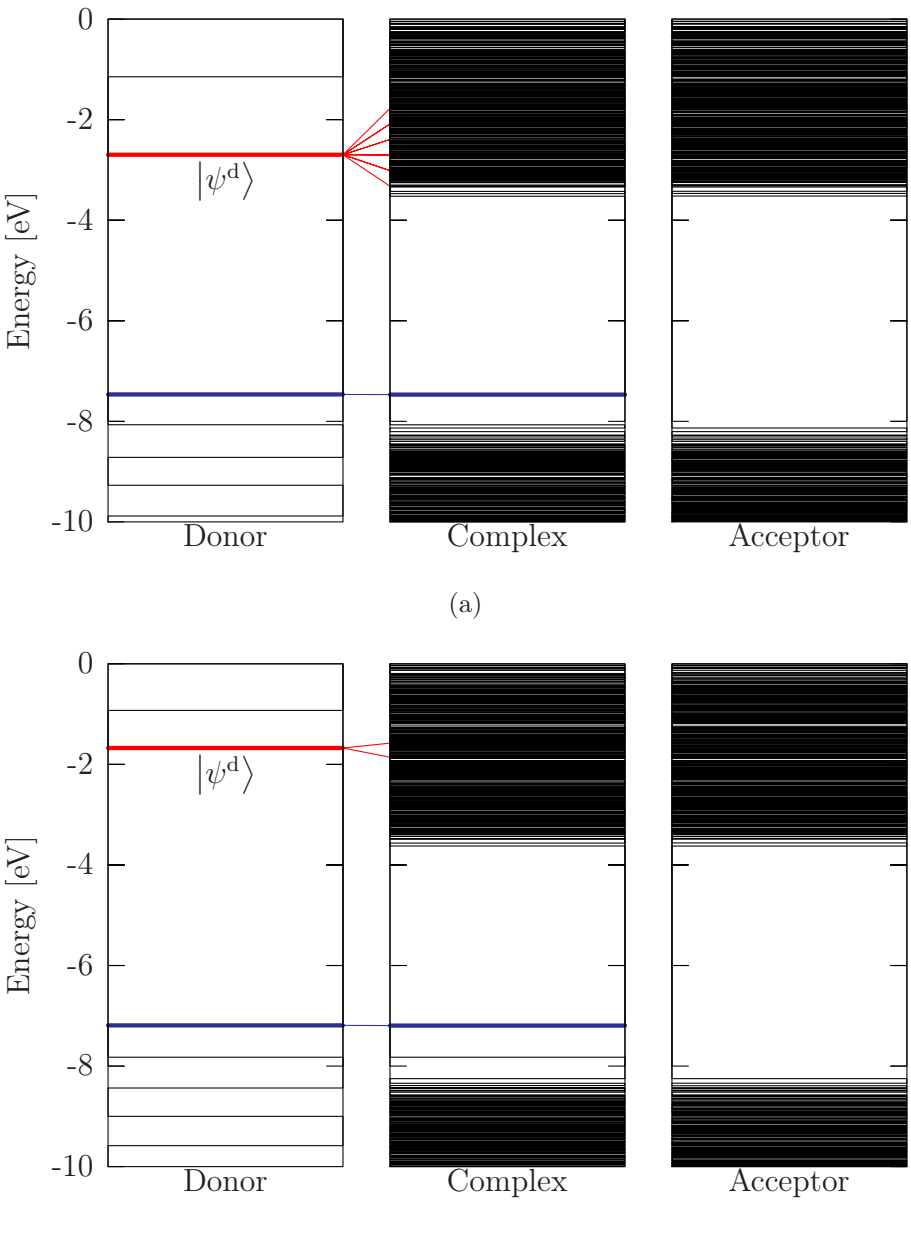

Figure 4.5: Energy-level schemes of the complexes with pyridine-based adsorbates: (a) PyC and (b) PyP adsorbed at the $(TiO_2)_{46}$ substrate. From left to right in each subfigure: energy levels of the donor orbitals (obtained from the partitioning procedure) which are localized in the adsorbate, energy levels of the overall complex, and energy levels of the acceptor orbitals (obtained from the partitioning procedure) which are localized in the semiconductor substrate. The selected donor state $|\psi^{\mathrm{d}}\rangle$ as well as the correlations among some energy levels relevant for the ET reaction are indicated.

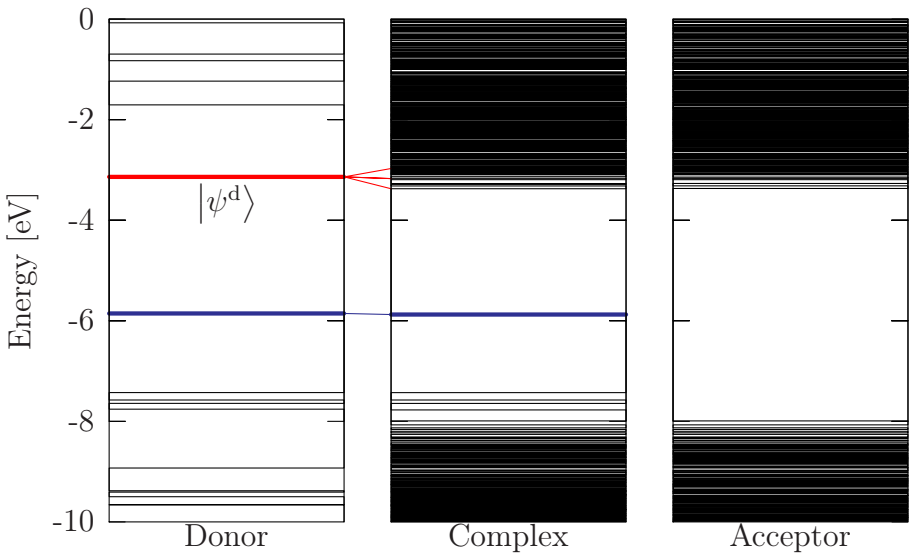

(a)

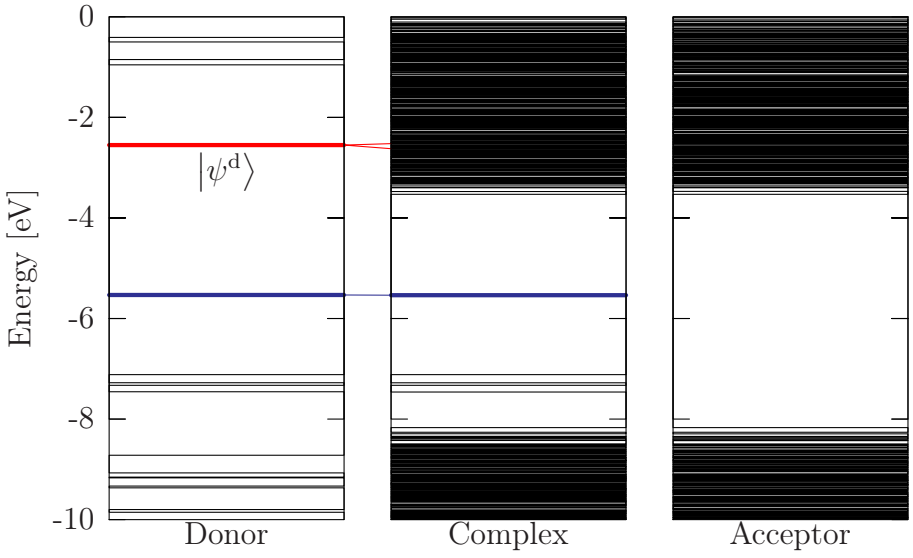

(b)

Figure 4.6: Energy-level schemes of the complexes with pyridine-based adsorbates: (a) PeC and (b) PeP adsorbed at the $(TiO_2)_{46}$ substrate. From left to right in each subfigure: energy levels of the donor orbitals (obtained from the partitioning procedure) which are localized in the adsorbate, energy levels of the overall complex, and energy levels of the acceptor orbitals (obtained from the partitioning procedure) which are localized in the semiconductor substrate. The selected donor state $|\psi^{\mathrm{d}}\rangle$ as well as the correlations among some energy levels relevant for the ET reaction are indicated.

For each system, energies of the lowest unoccupied orbitals of the dye, on the other hand, are located in the conduction band of TiO_2. As a consequence, these levels are dissolved in the dense manifold of conduction-band levels of TiO_2. In

the dynamical calculations discussed below, we have chosen the lowest donor orbital which corresponds to the LUMO of the isolated dye molecule as the donor state $|\psi^{\mathrm{d}}\rangle$. TD-DFT calculations for the isolated dye molecules indicate that the first excited states of pyridine and perylene correspond almost exclusively to the HOMO-LUMO excitation [131]. Therefore, the use of the LUMO as a model for the excited state is well justified in these systems.

An important parameter for the ET process is the energy of the donor state relative to the conduction-band minimum of the TiO_2. This parameter varies significantly for the four systems investigated. While the energy of the donor state for PyP-TiO_2 is well above the lower edge of the conduction band, it is very close in PeC-TiO_2. This trend can be rationalized by the excited-state energies of the two chromophores and the coupling strength between the chromophores and the different anchor groups. For each chromophore, the coupling to the carboxylic-acid anchor group is stronger and tends to lower the donor state as compared to the phosphonic-acid bridge.

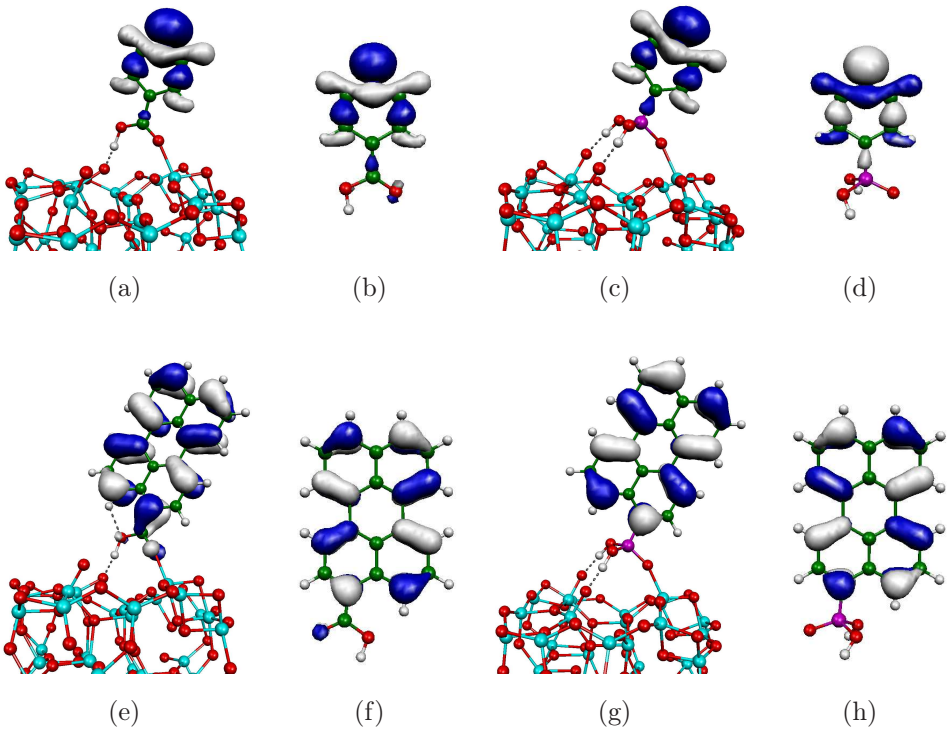

Figure 4.7: Selected localized adsorbate orbitals of the investigated systems (a) PyC-$(TiO_2)_{46}$, (c) PyP-$(TiO_2)_{46}$, (e) PeC-$(TiO_2)_{46}$ and (g) PeP-$(TiO_2)_{46}$ that are associated with the HOMO of corresponding isolated dye molecules (b) PyC, (d) PyP, (f) PeC and (h) PeP.

The local character of the two frontier orbitals for each investigated system and the resemblance between them and the corresponding orbitals (HOMO and LUMO) of isolated dye molecules are illustrated in Figs. 4.7 and 4.8, respectively. For each system, the localized orbital associated with the HOMO is almost identical to the

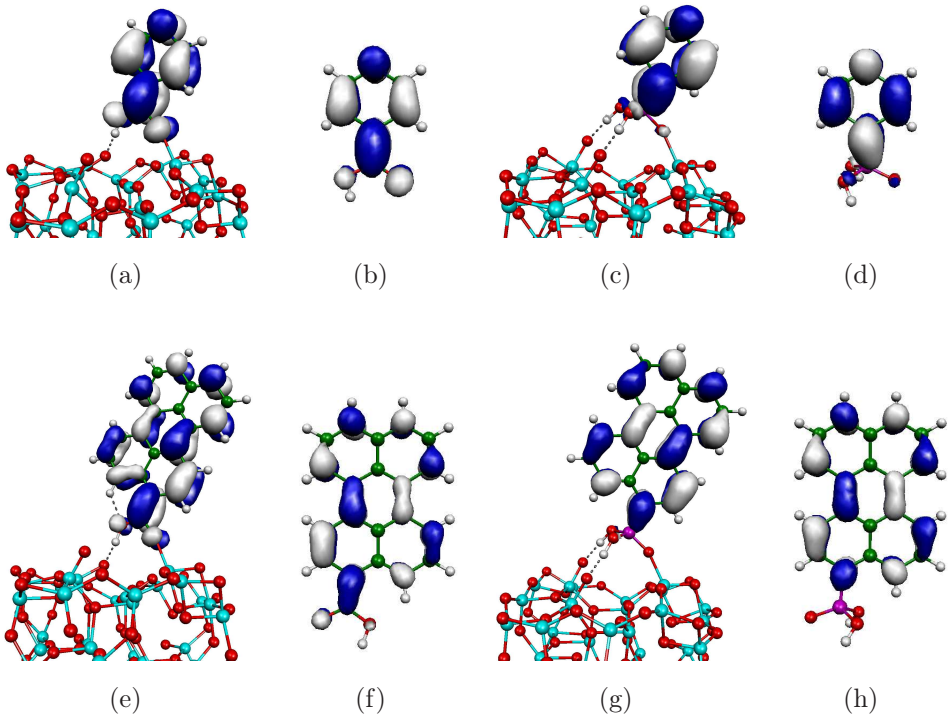

Figure 4.8: Selected localized adsorbate orbitals of the investigated systems (a) PyC-$(TiO_2)_{46}$, (c) PyP-$(TiO_2)_{46}$, (e) PeC-$(TiO_2)_{46}$ and (g) PeP-$(TiO_2)_{46}$ that are associated with the LUMO of corresponding isolated dye molecules (b) PyC, (d) PyP, (f) PeC and (h) PeP.

HOMO of the corresponding isolated dye molecule and also to the HOMO of the complex (data not shown), thus demonstrating that this orbital has negligible interaction with the TiO_2 substrate. On the other hand, the localized orbital associated with the LUMO of the isolated dye molecule, which constitutes the donor state of the ET reaction in each system, show noticeable contribution at the anchor bridge. This contribution is particularly pronounced for the systems containing the carboxylic-acid anchor group. It is also noted that all projected acceptor orbitals are localized in the TiO_2 substrate (data not shown).

Another key factor for the ET dynamics is the strength and the distribution of the donor-acceptor coupling. Figs. 4.9 and 4.10 show the modulus of the donor-acceptor coupling matrix elements V_j^{da} for the four systems (with the scale of the V_j^{da}-axis different in each subfigure). It is seen that the first-principles based models result in a distribution of donor-acceptor coupling matrix elements V_j^{da} that exhibits a rather complicated structure. This is in contrast to the semiempirical Newns model, where the donor-acceptor coupling is often represented by a Lorentzian or semielliptical function. The overall strength of the donor-acceptor coupling varies for the four systems. Thereby, the major effect is caused by the anchor group. Systems which bind via the carboxylic-acid anchor group show a significantly stronger donor-acceptor

coupling. This is in accordance with the character of the donor state orbital as discussed above. Considering systems with the same anchor group, the pyridine-based systems have a somewhat stronger donor-acceptor coupling due to the smaller spatial extension of the chromophore.

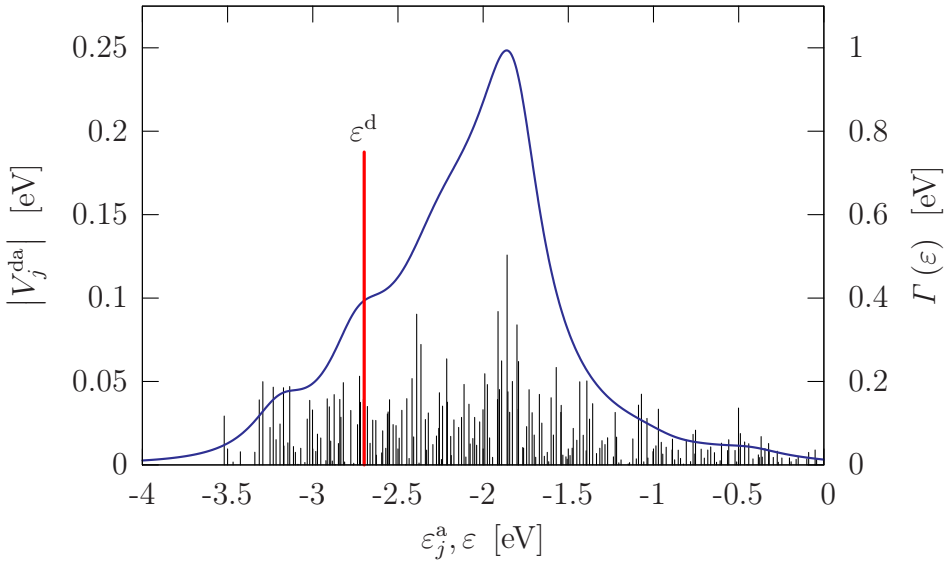

(a)

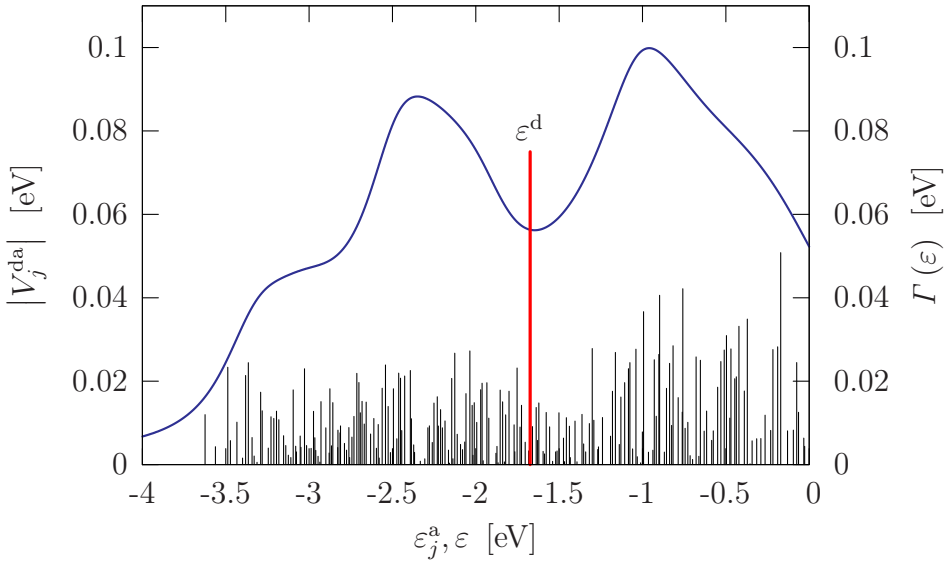

(b)

Figure 4.9: Modulus of donor-acceptor electronic coupling matrix elements V_j^{da} (discrete lines) and the decay-width function $\Gamma(\varepsilon)$ (continuous line) of (a) PyC-$(TiO_2)_{46}$ and (b) PyP-$(TiO_2)_{46}$. For each system, the red vertical line indicates the energy of the donor state ε^{d}.

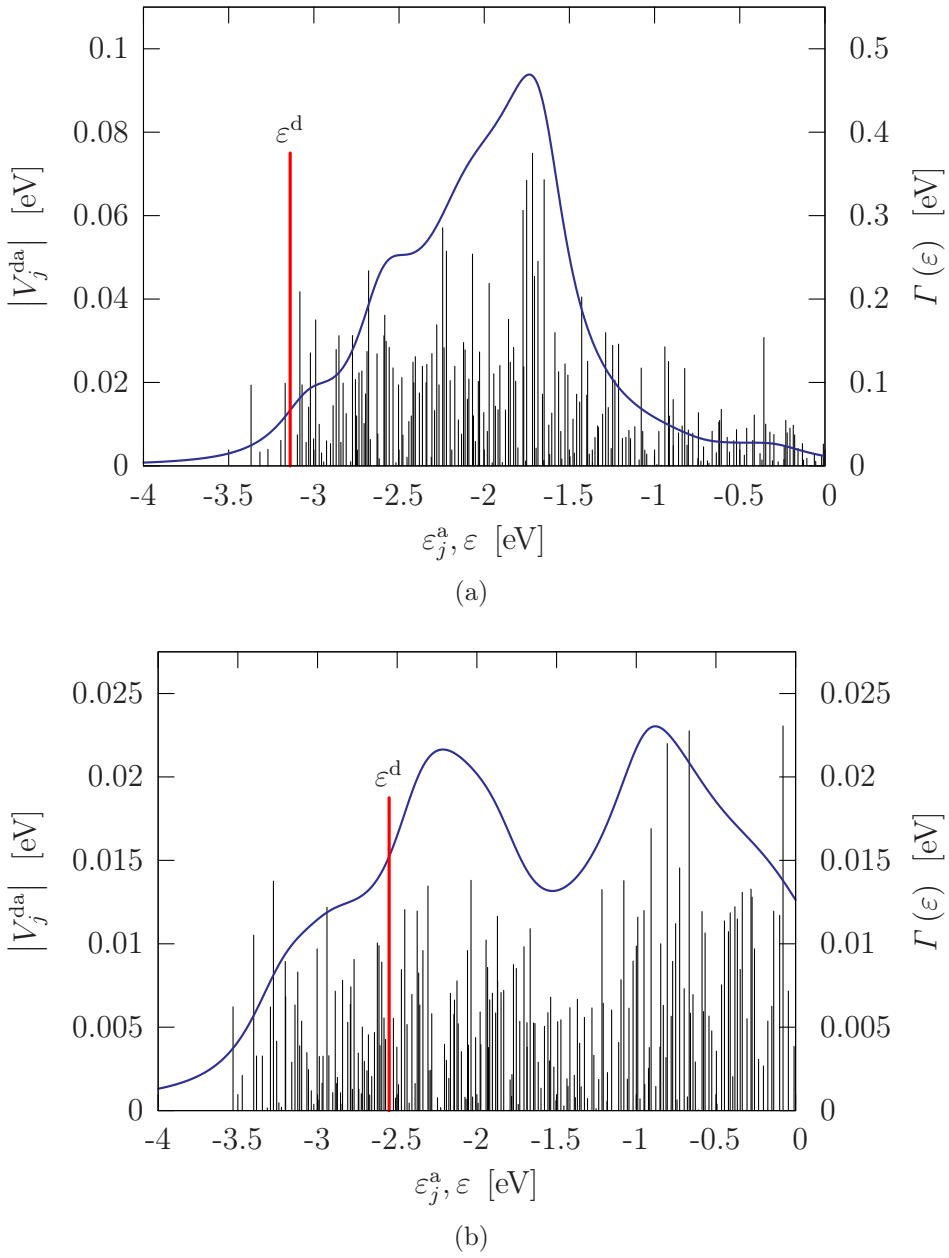

Figure 4.10: Modulus of donor-acceptor electronic coupling matrix elements V_j^{da} (discrete lines) and the decay-width function $\Gamma(\varepsilon)$ (continuous line) of (a) PeC-$(TiO_2)_{46}$ and (b) PeP-$(TiO_2)_{46}$. For each system, the red vertical line indicates the energy of the donor state ε^{d}.

For an extended substrate, the donor-acceptor coupling is characterized by the decay-width function $\Gamma(\varepsilon)$ given by Eq. (2.13). This function is depicted by the continuous lines in Figs. 4.9 and 4.10. In contrast to the functional forms used for $\Gamma(\varepsilon)$ in the Newns-type models [49, 77, 105], the results from the first-principles calculations exhibit pronounced structures and show significant differences for the four systems. In particular, in the complexes containing the carboxylic-acid anchor group, $\Gamma(\varepsilon)$ shows one single maximum, while it has a double-peak structure for the

systems containing the phosphonic-acid anchor group.

4.2.3 Electron injection dynamics

The ET dynamics in the four systems investigated is simulated based on the first-principles model outlined in Chapter 2. All localized acceptor states associated with unoccupied orbitals of the isolated semiconductor cluster are included in the simulation. Figs. 4.11 and 4.12 show the population of the donor state. For each system, the decay of the population of the donor state reflects the electron injection into the (quasi-)continuum of acceptor states in the TiO_2 substrate.

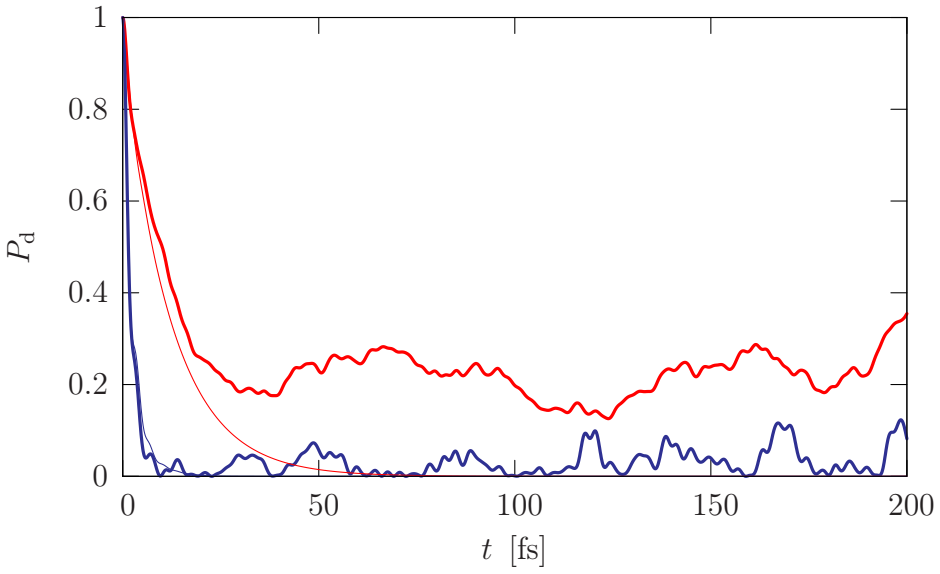

Figure 4.11: Population dynamics of the donor state after photoexcitation in the PyC-TiO_2 (blue lines) and PyP-TiO_2 (red lines) systems. Shown are results obtained for the finite $(TiO_2)_{46}$ cluster (thick lines) and for the model of an infinite TiO_2 surface (thin lines).

All systems show an ultrafast initial decay of the population of the donor state. The timescale of this initial injection as well as the character of the long-time dynamics depend on the specific system. In PyC-TiO_2, the population of the donor state decays within a few femtoseconds almost completely into the acceptor states. In the other three systems, the injection process is somewhat slower and incomplete, *i.e.*, there is a finite probability to find the electron for longer times at the adsorbates. The initial injection process is significantly faster in the systems containing the carboxylic-acid anchor group. By consideration of complexes with the same anchor group, the injection is faster in the pyridine-based systems. Furthermore, the results show oscillatory structures which indicate electronic coherence. This effect is particularly pronounced in the PeP-TiO_2 system.

These findings can be rationalized by the energy-level structure and the donor-acceptor coupling strength discussed in Section 4.2.2. The timescale of the initial injection follows mainly the overall strength of the donor-acceptor coupling. PyC-TiO_2, the system with the largest donor-acceptor coupling, exhibits the fastest injection. On the other hand, PeP-TiO_2, the system with the smallest donor-acceptor coupling, shows the slowest injection. The donor-acceptor coupling in PyP-TiO_2 is overall slightly weaker than that in PeC-TiO_2, while the energy of the donor state of PyP-TiO_2 is located significantly higher relative to the conduction-band minimum than that of PeC-TiO_2. These two features result in a somewhat faster initial injection in PeC-TiO_2 as compared to PyP-TiO_2.

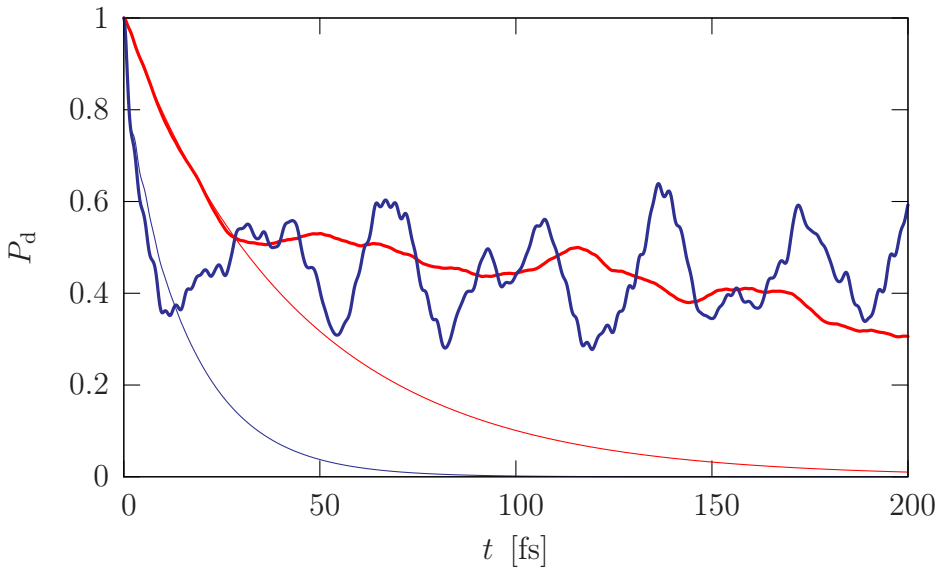

Figure 4.12: Population dynamics of the donor state after photoexcitation in the PeC-TiO_2 (blue lines) and PeP-TiO_2 (red lines) systems. Shown are results obtained for the finite $(TiO_2)_{46}$ cluster (thick lines) and for the model of an infinite TiO_2 surface (thin lines).

As already noted above, the injection process is incomplete for all systems except PyC-TiO_2 which shows an almost complete injection. Model studies [105] indicate that there are two possible reasons for an incomplete injection process: (i) the finiteness of the $(TiO_2)_{46}$ cluster, which results in recurrences of the wave function that would be quenched when an infinite semiconductor surface is mimicked; and (ii) true bound (*e.g.*, surface) states in the band gap with a finite overlap with the donor state, which may result in an incomplete injection even when mimicking an infinite substrate. In order to study the first effect, we have mimicked electron injection at an infinite TiO_2 surface using absorbing boundary conditions by including an imaginary part in the orbital energies at the boundary of the substrate (*cf.* Section 2.3.1 and Appendix B). Corresponding results are depicted in Figs. 4.11 and 4.12 by the thin lines. It is seen that all systems exhibit a complete injection process. This

demonstrates that the incomplete decay of the population of the donor state in all four systems is mainly caused by the finiteness of the $(TiO_2)_{46}$ cluster used in the simulation and can thus be understood as a finite-size effect.

Table 4.1: Characteristic times (in femtoseconds) of the electron injection process in the four investigated systems.

adsorbate	PyC	PyP	PeC	PeP
finite $(TiO_2)_{46}$ cluster				
$\tau_{e^{-1}}$	2.0	13.8	9.0	42.8
extended TiO_2 surface				
$\tau_{e^{-1}}$	1.9	11.3	16.2	41.7
k^{-1}	3.8	12.0	16.1	43.7
$\left(\Gamma\left(\varepsilon^{d}\right)\right)^{-1}$	1.7	11.7	9.9	43.2
Previous studies				
finite TiO_2 cluster [75]				
$\tilde{\gamma}^{-1}$	5	20		
extended TiO_2 surface [67]				
$\tilde{\gamma}^{-1}$	17	35		
experiments [33]			13	24

Table 4.1 lists reaction rate constants of ET processes in all four systems obtained from different rate-theory approaches[1]. It is important to note that, for the complexes with a finite TiO_2 substrate, the time-dependent population dynamics shows that the electron injection is not an exponential process and can thus not be fully characterized by a single rate constant. In particular, the decay is incomplete and shows significant coherence effects for longer times. To characterize the average timescale of the initial injection process, we have fit the initial decay dynamics of the population of the donor state to an exponential function in order to extract the corresponding e^{-1}-time.

The results obtained for the extended substrate show complete injection. Nevertheless, the time-dependent population dynamics is not a purely exponential decay. In the ET rates, this becomes apparent in the difference of the e^{-1}-time and the long-time injection time k^{-1} defined in Eq. (2.91). This deviation is particularly pronounced for PyC-TiO_2, since electronic coherence effects prevail even an extended surface is mimicked for this system. Thus, also in the case of an "infinite" substrate, the electron injection rate has to be considered as an approximate concept and can only give an overall timescale.

[1]Specifically, $\tau_{e^{-1}}$ is defined via Eq. (2.89), k is defined in Eq. (2.91), $\Gamma\left(\varepsilon^{d}\right)$ is defined in Eq. (2.13), and $\tilde{\gamma}$ is defined in, *e.g.*, Ref. [72].

The results in Table 4.1 show ultrafast character of the injection process for all systems. The timescales range from a few femtoseconds for the most strongly coupled system PyC-TiO_2 to a few tens of femtoseconds for PeP-TiO_2. The overall trend for the electron-injection timescale τ for the four systems

$$\tau\,(\text{PeP-TiO}_2) > \tau\,(\text{PyP-TiO}_2) > \tau\,(\text{PeC-TiO}_2) > \tau\,(\text{PyC-TiO}_2)$$

is reproduced by all rate concepts.

For the perylene-based systems, experimental results obtained from transient absorption spectroscopy in ultrahigh vacuum [33] predict an electron-injection time of 13 fs for PeC-TiO_2 and 24 fs for PeP-TiO_2. For PeC-TiO_2, the experimental result is in good agreement with the calculated injection times, while for PeP-TiO_2 the experimental result is about a factor of 2 faster.

Based on the comparison of the results of the different rate concepts, it is seen that the Golden-Rule rate constants agree well with other rate constants for the systems containing the phosphonic-acid anchor group (which create a weaker donor-acceptor coupling in the dye-semiconductor systems) but significantly deviates for PeC-TiO_2. This is to be expected due to the perturbative character of the Golden-Rule rate. For the PyC-TiO_2 system, the good agreement between the Golden-Rule rate and other rate constants is presumably fortuitous, since the applicability of rate theory is questionable in this system.

In previous work [57, 65, 72, 75], the electron injection rates for the pyridine-based systems were characterized based on the lifetime broadening of the donor state. Table 4.1 shows reasonable agreement between the thus obtained results and the results obtained from dynamical calculations. The deviations are presumably due to the fact that the distribution of the donor-acceptor coupling matrix elements significantly deviates from a Lorentzian distribution (*cf.* Figs. 4.9 and 4.10).

4.3 Influence of the spacer group on the electron transfer dynamics

4.3.1 Characterization of the systems

To study the influence of the spacer group on the ET dynamics, we have considered the quantum dynamics of electron injection in dye-semiconductor systems with three different dye molecules. In each system, a bulky $(TiO_2)_{60}$ cluster is used to model the semiconductor substrate. All dye molecules investigated contain a

perylene chromophore group which is directly or indirectly bound to the titanium dioxide substrate via a carboxylic-acid anchor group. Two different spacer groups, -CH=CH- and -CH_2-CH_2-, are selected to insert between the perylene chromophore and the carboxylic-acid group, thus resulting in an acrylic-acid and a propionic-acid anchor group. The thus obtained three different dyes are denoted by PeCOOH, PeCH=CHCOOH and PeCH_2CH_2COOH in the following. In all three cases, we have used a bridge binding mode between the adsorbate and the substrate (different to the monodentate mode used in Section 4.2). The proton detached from the carboxylic-acid group is attached to a surface oxygen atom. Fig. 4.13 shows the chemical structures of the two dyes except PeCOOH which is identical to the PeC shown in Fig. 4.3 (c). The three dye-semiconductor systems are depicted in Fig. 4.14.

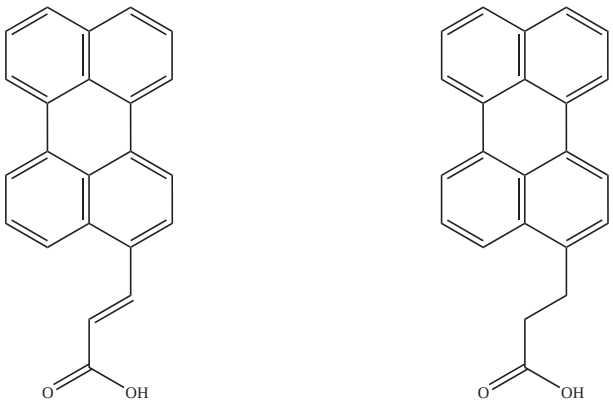

(a) (b)

Figure 4.13: Chemical structure of two dye molecules considered in the study: (a) perylene - acrylic acid (PeCH=CHCOOH) and (b) perylene - propionic acid (PeCH_2CH_2COOH).

The procedure to obtain the structures of the three investigated dye-semiconductor systems and the details of electronic structure calculations were described in Ref. [72]. All calculations were carried out using the GAUSSIAN 03 package [114].

4.3.2 Energy-level scheme, donor-acceptor separation and coupling matrix elements

To discuss the donor-acceptor partitioning, we first consider the energy-level scheme. Fig. 4.15 shows energies of the MO of the overall dye-TiO_2 complexes as well as those of the donor and acceptor orbitals obtained from the partitioning procedure for the three systems investigated. For each system, the MO-energies (shown in the middle panel of the corresponding subfigure) exhibit a dense level structure with a valence and a conduction band separated by a band gap. In addition, for each system there is

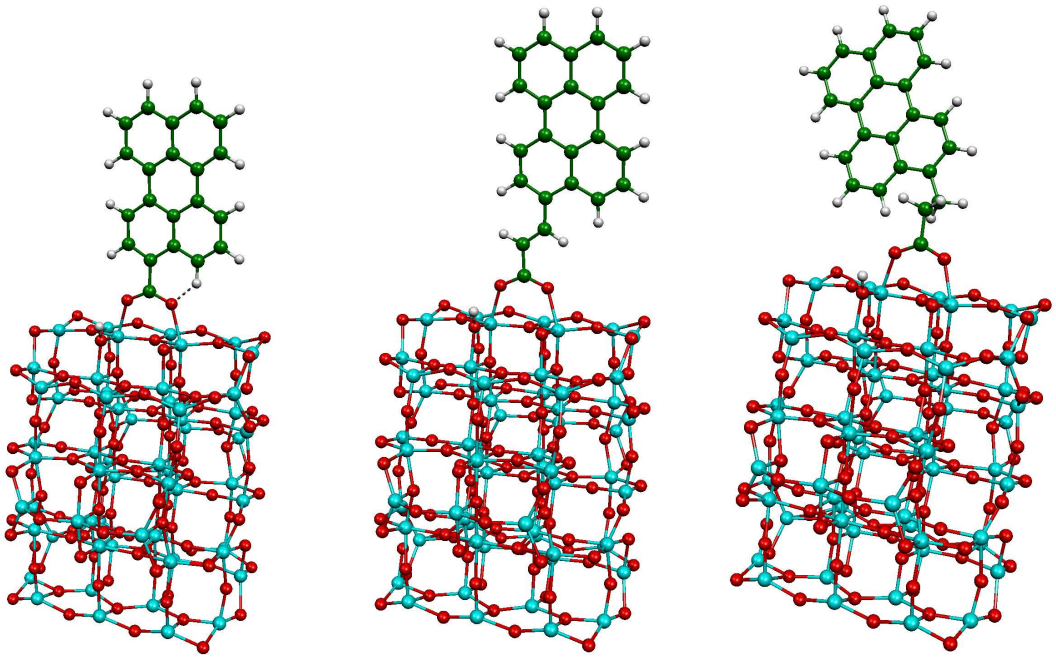

(a) (b) (c)

Figure 4.14: The three complexes considered in the study: (a) PeCOOH-$(TiO_2)_{60}$, (b) PeCH=CHCOOH-$(TiO_2)_{60}$ and (c) $PeCH_2CH_2COOH$-$(TiO_2)_{60}$.

one isolated level (the HOMO of the overall complex) in the band gap. The calculated value for the band gap is 3.1 eV, which is somewhat smaller than experimental value (3.4 eV [116]) for anatase TiO_2 nanoparticles. This finding also differs from the result obtained for the $(TiO_2)_{46}$ cluster as shown in Section 4.2. This is a result of the higher coordination of the titanium atoms in the $(TiO_2)_{60}$ cluster considered [75].

The partitioning procedure results in donor and acceptor orbitals that are localized in the adsorbate and the $(TiO_2)_{60}$ substrate, respectively. The energy-level scheme of acceptor orbitals shows a structure very similar to that of the isolated $(TiO_2)_{60}$ cluster [72]. For each system, the energy level in the band gap of the complex is localized in the adsorbate, and, therefore, results within the partitioning procedure in a donor orbital, which is associated with the HOMO of the corresponding isolated dye molecule. The energy of this donor level is very close to the energy of the HOMO in the complex, indicating almost negligible interaction with the substrate. This is corroborated by the fact that the overlap of this donor orbital with the HOMO of the complex is larger than 0.99.

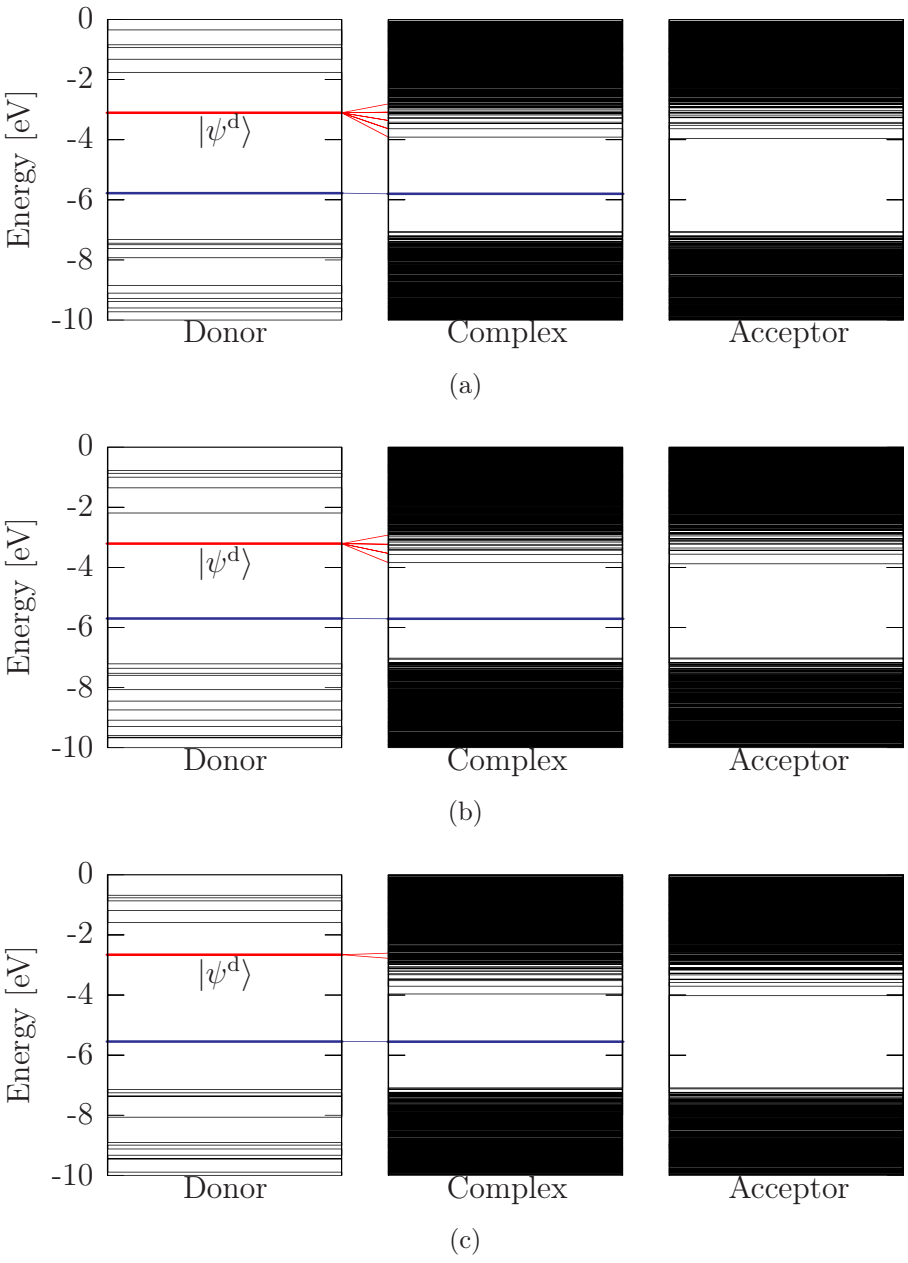

Figure 4.15: Energy-level schemes of the investigated complexes with perylene-based adsorbates: (a) PeCOOH, (b) PeCH=CHCOOH and (c) $PeCH_2CH_2COOH$ adsorbed at the $(TiO_2)_{60}$ substrate. From left to right in each subfigure: energy levels of the donor orbitals (obtained from the partitioning procedure) which are localized in the adsorbate, energy levels of the overall complex, and energy levels of the acceptor orbitals (obtained from the partitioning procedure) which are localized in the semiconductor substrate. The selected donor state $|\psi^{\mathrm{d}}\rangle$ as well as the correlations among some energy levels relevant for the ET reaction are indicated.

For each system, energies of the lowest unoccupied orbitals of the dye, on the other hand, are located in the conduction band of TiO_2. As a consequence, these levels are dissolved in the dense manifold of conduction-band levels of TiO_2. In the dynamical calculations discussed below, we have chosen the lowest donor orbital in the conduction band which corresponds to the LUMO of the isolated dye molecule as the donor state $\left|\psi^{\mathrm{d}}\right\rangle$. TD-DFT calculations for the isolated dye molecules indicate that the first excited state of perylene corresponds almost exclusively to the HOMO-LUMO excitation [72, 131]. Therefore, the use of the LUMO as a model for the excited state is well justified in these systems.

An important parameter for the ET process is the energy of the donor state relative to the conduction-band minimum of the TiO_2. For PeCOOH-TiO_2 and PeCH=CHCOOH-TiO_2, the energy of the donor state is close to the lower edge of the conduction band, while it is well above the conduction-band minimum in $PeCH_2CH_2COOH$-TiO_2. This feature can be rationalized by the coupling strength between the chromophore and the different anchor groups (carboxylic acid, acrylic acid and propionic acid): the coupling to the propionic-acid anchor group is much weaker and tends to a higher donor level as compared to both carboxylic-acid and acrylic-acid bridge.

The local character of the two frontier orbitals for each investigated system and the resemblance between them and the corresponding orbitals (HOMO and LUMO) of isolated dye molecules are illustrated in Figs. 4.16 and 4.17, respectively. For each system, the localized orbital associated with the HOMO is almost identical to the HOMO of the corresponding isolated dye molecule and also to the HOMO of the complex (data not shown), thus demonstrating that this orbital has negligible interaction with the TiO_2 substrate. On the other hand, all projected acceptor orbitals are localized in the TiO_2 substrate (data not shown). For both PeCOOH-$(TiO_2)_{60}$ and PeCH=CHCOOH-$(TiO_2)_{60}$, the localized orbital associated with the LUMO of the isolated dye molecule, which constitutes the donor state of the ET reaction, show noticeable contribution at the anchor bridge. In particular, for PeCH=CHCOOH-$(TiO_2)_{60}$, the localized orbital associated with the LUMO of the isolated dye molecule shows pronounced contribution at the spacer group -CH=CH-. In contrast, for $PeCH_2CH_2COOH$-$(TiO_2)_{60}$, the distribution of the probability density of the localized orbital which is associated with the LUMO of $PeCH_2CH_2COOH$ is almost completely restricted in the perylene chromophore group.

Fig. 4.18, showing the modulus of the donor-acceptor coupling matrix elements V_j^{da} for the three systems (with the scale of the V_j^{da}-axis for $PeCH_2CH_2COOH$-$(TiO_2)_{60}$ different to that for the other two systems), illustrates the strength and the distribution of the donor-acceptor coupling, which is regarded as another key factor

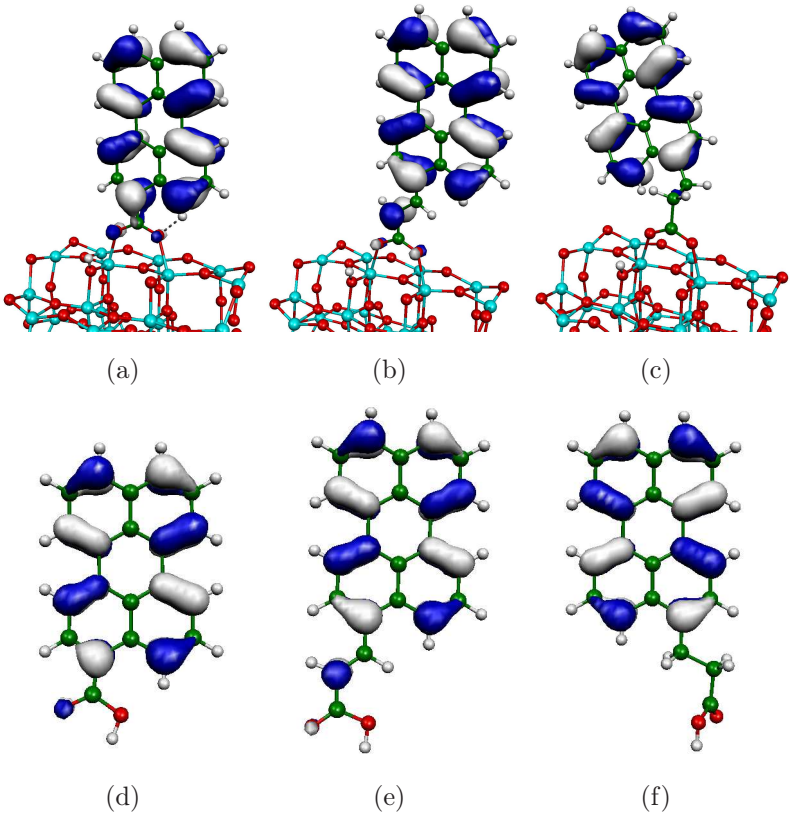

Figure 4.16: Selected localized adsorbate orbitals of the investigated systems (a) PeCOOH-$(TiO_2)_{60}$, (b) PeCH=CHCOOH-$(TiO_2)_{60}$ and (c) $PeCH_2CH_2COOH$-$(TiO_2)_{60}$ that are associated with the HOMO of corresponding isolated dye molecules (d) PeCOOH, (e) PeCH=CHCOOH and (f) $PeCH_2CH_2COOH$.

for the ET dynamics. Similar to Figs. 3.6, 4.9 and 4.10, the first-principles based models result in a distribution of donor-acceptor coupling matrix elements V_j^{da} that exhibits a rather complicated structure. The overall strength of the donor-acceptor coupling varies for the three systems. Thereby, the major effect is caused by the spacer group. The system with a perylene chromophore bound to the substrate directly via the carboxylic-acid anchor group shows the strongest donor-acceptor coupling, while the donor-acceptor coupling for the system containing a -CH=CH- spacer group between the perylene chromophore and the carboxylic-acid anchor group is slightly weaker. The donor-acceptor coupling for the system containing a $-CH_2CH_2-$ spacer group between the perylene chromophore and the carboxylic-acid anchor group is significant weaker than that of the other two systems. This is in accordance with the different character of the donor orbitals in the different systems as discussed above.

For an extended substrate, the donor-acceptor coupling is characterized by the decay-width function $\Gamma(\varepsilon)$ given by Eq. (2.13). This function is depicted by the continuous lines in Fig. 4.18. These results from the first-principles calculations exhibit pronounced structures and show significant differences for the three systems.

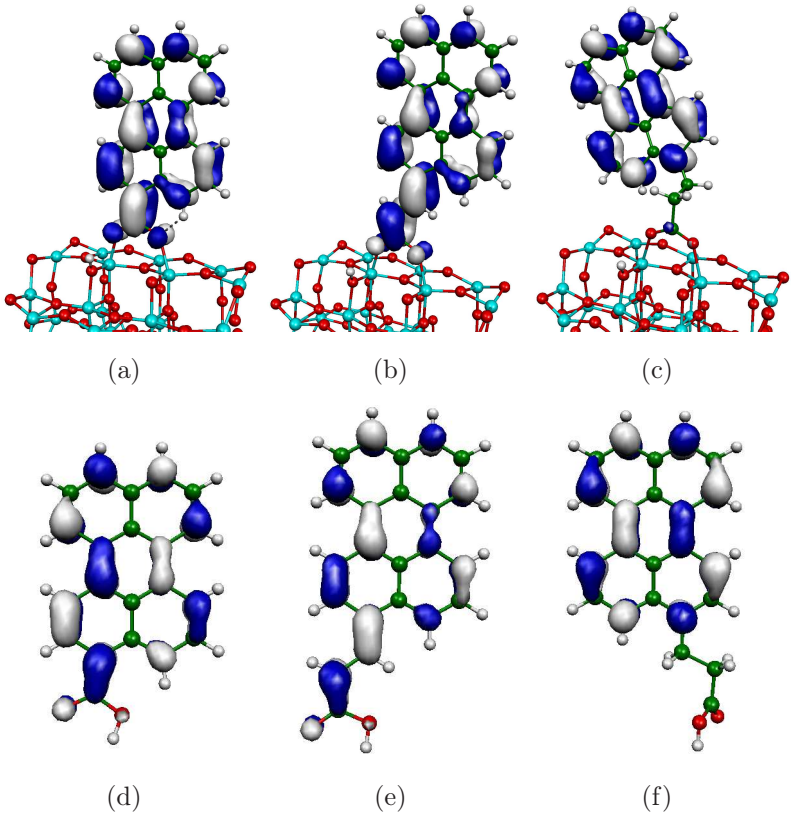

Figure 4.17: Selected localized adsorbate orbitals of the investigated systems (a) PeCOOH-$(TiO_2)_{60}$, (b) PeCH=CHCOOH-$(TiO_2)_{60}$ and (c) $PeCH_2CH_2COOH$-$(TiO_2)_{60}$ that are associated with the LUMO of corresponding isolated dye molecules (d) PeCOOH, (e) PeCH=CHCOOH and (f) $PeCH_2CH_2COOH$.

Different to Figs. 4.9 (a) and 4.10 (a), the carboxylic-acid anchor group in each system investigated here results in a $\Gamma(\varepsilon)$ function containing more than one maxima.

4.3.3 Electron injection dynamics

The ET dynamics in the three systems investigated is simulated based on the first-principles model outlined in Chapter 2. All localized acceptor states associated with unoccupied orbitals of the isolated semiconductor cluster are included in the simulation. Fig. 4.19 shows the population of the donor state for all systems, reflecting the electron injection into the (quasi-)continuum of acceptor states in the TiO_2 substrate.

All systems show an ultrafast initial decay of the population of the donor state. The timescale of this initial injection as well as the character of the long-time dynamics depend on the specific system. In both PeCOOH-TiO_2 and PeCH=CHCOOH-TiO_2, the population of the donor state decays within a few femtoseconds to about 0.1, while the injection process in $PeCH_2CH_2COOH$-TiO_2 is significantly slower. These findings

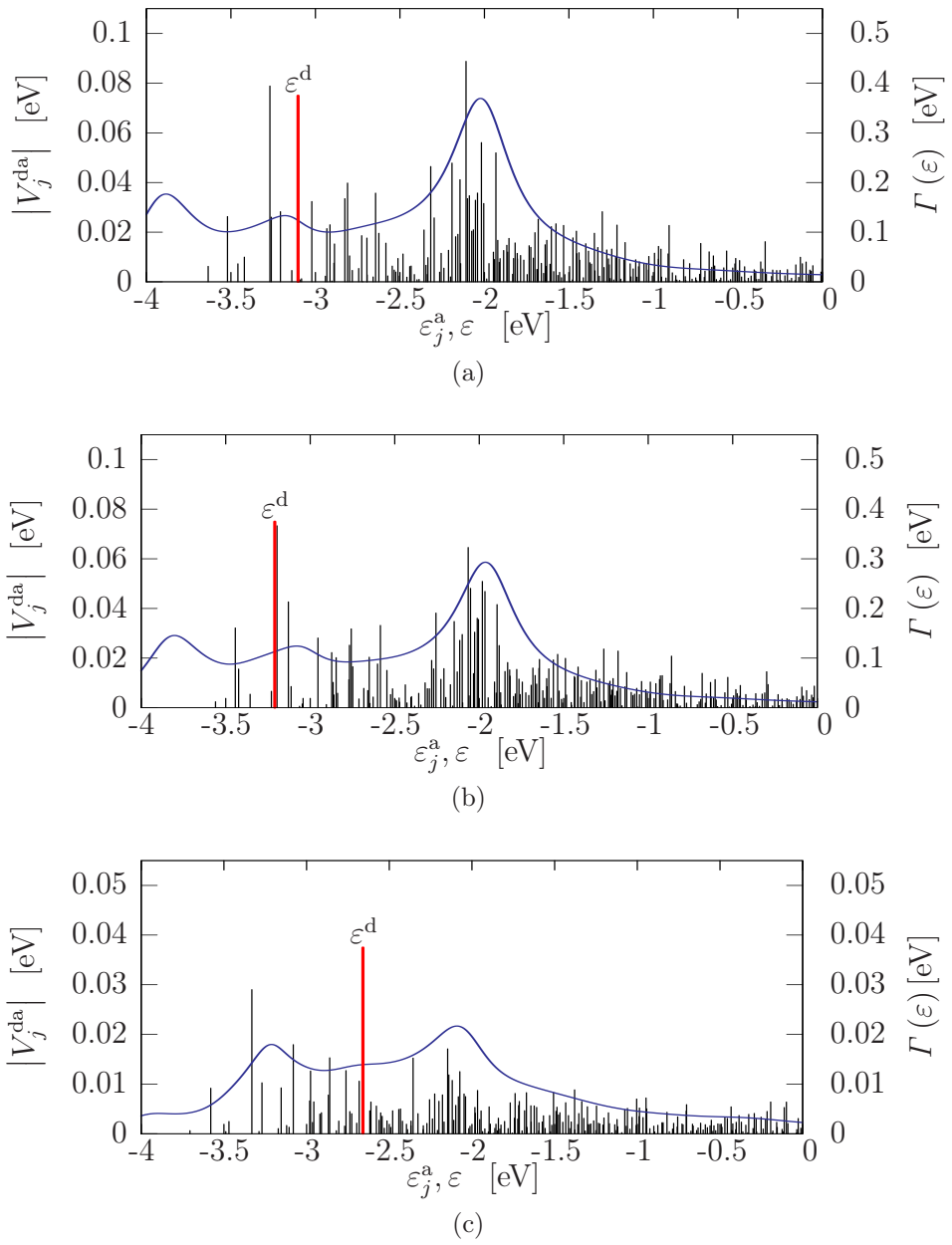

Figure 4.18: Modulus of donor-acceptor electronic coupling matrix elements V_j^{da} (discrete lines) and the decay-width function $\Gamma(\varepsilon)$ (continuous line) of (a) PeCOOH-$(TiO_2)_{60}$, (b) PeCH=CHCOOH-$(TiO_2)_{60}$ and (c) $PeCH_2CH_2COOH$-$(TiO_2)_{60}$. For each system, the red vertical line indicates the energy of the donor state ε^d.

can be rationalized by the energy-level structure and the donor-acceptor coupling strength discussed in Section 4.3.2. As shown in Figs. 4.15 and 4.18, the position of the donor level with respect to the conduction-band minimum and the strength of the donor-acceptor coupling are both very similar in the dye-semiconductor systems PeCOOH-TiO_2 and PeCH=CHCOOH-TiO_2. This results in similar ET dynamics in these two systems, exhibiting a much faster injection than in $PeCH_2CH_2COOH$-TiO_2, where the donor-acceptor coupling is much weaker. Furthermore, the results for both

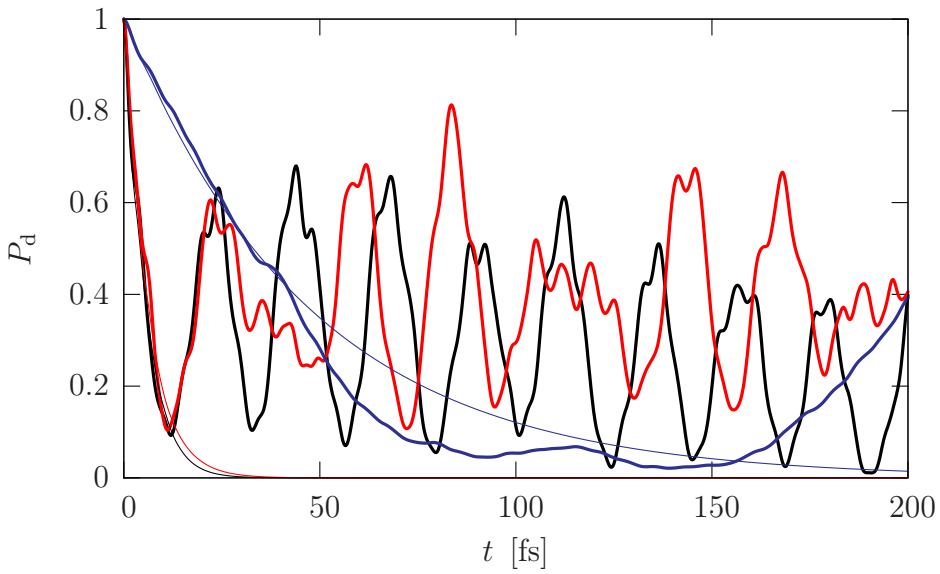

Figure 4.19: Population dynamics of the donor state after photoexcitation in the investigated systems PeCOOH-TiO_2 (black lines), PeCH=CHCOOH-TiO_2 (red lines) and PeCH_2CH_2COOH-TiO_2 (blue lines). Shown are results obtained for the finite $(TiO_2)_{60}$ cluster (thick lines) and for the model of an infinite TiO_2 surface (thin lines).

PeCOOH-TiO_2 and PeCH=CHCOOH-TiO_2 show pronounced oscillatory structures which indicate electronic coherence. The decay in PeCH_2CH_2COOH-TiO_2 is rather smooth with some recurrences of a large period, which can be classified as a finite-size effect as discussed below.

Incomplete electron injection is observed for all three investigated systems even for a long injection time. From Fig. 4.19, we can see that this incompleteness is particularly significant for PeCH=CHCOOH-TiO_2. Similar to the analysis outlined in Sections 3.5 and 4.2.3, we have mimicked electron injection at an extended TiO_2 surface using absorbing boundary conditions by including an imaginary part in the orbital energies at the boundary of the substrate. Corresponding results are depicted in Fig. 4.19 by the thin lines. It is seen that all systems exhibit a complete injection process (for PeCH_2CH_2COOH-TiO_2, the population of the donor state decays to zero after 200 fs). This demonstrates that the incomplete decay of the population of the donor state in all three systems is mainly caused by the finiteness of the $(TiO_2)_{60}$ cluster used in the simulation and can thus be understood as a finite-size effect. This finding is similar to the results for other dye-semiconductor systems discussed previously (*cf.* Sections 3.5 and 4.2.3). Furthermore, Fig. 4.19 also shows that electronic coherence effects are almost completely quenched by mimicking an extended substrate surface for all systems.

Table 4.2 lists reaction rate constants of ET processes in all three systems obtained

Table 4.2: Characteristic times (in femtoseconds) of the electron injection process in the three investigated systems.

adsorbate	PeCOOH	PeCH=CHCOOH	$PeCH_2CH_2COOH$
finite $(TiO_2)_{60}$ cluster			
$\tau_{e^{-1}}$	5.2	6.4	43.2
extended TiO_2 surface			
$\tau_{e^{-1}}$	5.8	6.4	47.4
k^{-1}	5.0	5.9	47.2
$\left(\Gamma\left(\varepsilon^{d}\right)\right)^{-1}$	5.3	5.8	47.3
Previous studies			
finite TiO_2 cluster [72]			
$\tilde{\gamma}^{-1}$	5	6	33
experiments [33, 72]	13	10	57

from different rate-theory approaches[2]. It is important to note that, for the complexes with a finite TiO_2 substrate, the time-dependent population dynamics shows that the electron injection is not an exponential process and can thus not be fully characterized by a single rate constant. In particular, the decay is incomplete and shows significant coherence effects for longer times. To characterize the average timescale of the initial injection process, the initial decay dynamics of the population of the donor state is fit to an exponential function in order to extract the corresponding e^{-1}-time.

The results obtained for the extended substrate show complete injection with oscillatory structures almost completely quenched. The time-dependent population dynamics is similar to an exponential decay especially for $PeCH_2CH_2COOH$-TiO_2, where the e^{-1}-time is very close to the long-time injection time k^{-1} defined in Eq. (2.91).

The results shown in Table 4.2 show the ultrafast character of the injection process for all systems. The timescales range from a few femtoseconds to a few tens of femtoseconds. The overall trend for the electron-injection timescale τ for the three systems

$$\tau\left(PeCH_2CH_2COOH\text{-}TiO_2\right) > \tau\left(PeCOOH\text{-}TiO_2\right) \approx \tau\left(PeCH{=}CHCOOH\text{-}TiO_2\right)$$

is reproduced by all rate concepts.

For each system, the results obtained from the different rate concepts (*i.e.*, the e^{-1}-

[2]Specifically, $\tau_{e^{-1}}$ is defined via Eq. (2.89), k is defined in Eq. (2.91), $\Gamma\left(\varepsilon^{d}\right)$ is defined in Eq. (2.13), and $\tilde{\gamma}$ is defined in, *e.g.*, Ref. [72].

time obtained with both finite cluster and infinite surface, the long-time injection time obtained with an infinite surface, and the Golden-Rule injection time) are very close to each other. This is different to the finding in Section 4.2.3. The injection rates obtained for PeCOOH-$(TiO_2)_{60}$ is about a factor of 2 faster than the results obtained for PeC-$(TiO_2)_{46}$ (*cf.* Table 4.1). On the other hand, the Golden-Rule rate constants agree well with other rate constants for all systems, including PeCOOH-TiO_2, which is very different to the finding obtained for PeC-TiO_2 (*cf.* Table 4.1). This can be rationalized by the different distribution scheme of the donor-acceptor coupling (*cf.* Fig. 4.18 versus Fig. 4.10 (a)), which is presumably a result of the different adsorption motifs and different sizes of the cluster.

In previous work [72], the electron injection rate for the investigated systems was characterized based on the lifetime broadening of the donor state. Table 4.2 shows reasonable agreement between the thus obtained results and the results obtained from dynamical calculations.

We can compare the results obtained from dynamical simulations to the experimental results obtained from transient absorption spectroscopy in ultrahigh vacuum [33, 72]. For all three systems, the injection rates obtained from experimental studies are somewhat slower than the theoretical results.

4.4 Summary

In this chapter, we have studied the quantum dynamics of photoinduced heterogeneous ET processes in dye-semiconductor systems with different chromophore groups, anchor groups and spacer groups. In the investigated systems, pyridine or perylene chromophore is anchored to a titanium oxide nanocluster via carboxylic-acid or phosphonic-acid anchor group. Furthermore, different spacer groups are inserted between the perylene chromophore and the carboxylic-acid anchor group, resulting in dye-semiconductor systems with perylene anchored to the substrate via acrylic-acid or propionic-acid anchor group (thus the spacer-group effects can also be classified as anchor-group effects). The ET dynamics has been described employing a model based on first-principles electronic structure (DFT) calculations.

The results show that the electron injection in all investigated systems occurs on an ultrafast timescale which ranges from a few femtoseconds to a few tens of femtoseconds. Because of the finite size of the nanoclusters used for the systems, the injection process is incomplete and, furthermore, shows significant electronic coherence effects. The results demonstrate that the injection dynamics can be strongly

influenced by the chemical nature of the anchor group. The stronger donor-acceptor coupling created by the carboxylic-acid and acrylic-acid anchor groups, which extend the π-system of the planar chromophore group, results in injection processes which are significantly faster than the ET in the systems with the nonplanar phosphonic-acid and propionic-acid anchor groups.

We have also studied the applicability of rate theories to characterize the electron injection process. Since the long-time dynamics in systems with finite TiO_2 nanoclusters exhibits pronounced electronic coherence effects, only the initial dynamics can be approximately characterized by a single decay constant. For some systems, coherence effects are almost completely quenched when an extended surface of the substrate is mimicked and the rate constants can thus be defined. The real-time dynamics of the electron injection process may not follow an exponential decay characteristics especially if electronic coherence effects are pronounced even when mimicking an extended surface.

In the study presented in this chapter, we have considered the purely electronic dynamics of the ET process and neglected the electronic-vibrational coupling. This is expected to be a good approximation for dye-semiconductor systems with very short injection times. In general, the coupling to the nuclear DoF may have profound effects on the ET dynamics especially for systems with longer injection times (such as the PeP-TiO_2 and $PeCH_2CH_2COOH$-TiO_2 systems) as discussed in Chapter 3 and in previous studies [39, 70].

Chapter 5

Dushinsky Effects: Electron Transfer Processes in the Dye-Semiconductor System Coumarin 343 - Titanium Oxide

5.1 Introduction

In the study of the vibronic ET dynamics in alizarin-TiO_2 presented in Chapter 3 as well as in previous studies [41, 70], the electronic-vibrational coupling was characterized employing the simplest harmonic approximation without including Dushinsky rotation. Thereby, in the donor and acceptor states, the vibrational frequency along each normal mode is approximated by its value in the electronic ground-state, and the coupling among the normal modes is neglected. This approximation has been successfully used to describe Franck-Condon and resonance Raman spectra [92]. It is also used in the linear vibronic coupling model of conical intersections [93] and in the Marcus theory of ET [3].

In this chapter, we will employ a more precise characterization of the electronic-vibrational coupling to simulate the vibronic ET dynamics in the dye-semiconductor system coumarin 343 (C343) - titanium oxide. In the recent years, this system has been studied in detail both experimentally [20, 23, 34, 35, 118, 119, 132–136] and theoretically [41, 70, 74]. Thereby the vibronic ET dynamics was simulated based on the simplest harmonic approximation employing a first-principles model [41].

In the dynamical simulation in this chapter, we employ an extended model, where the PES of the ET-related diabatic states are expanded in local second-order polynomials of normal-mode coordinates thereby including the change of vibrational frequencies and the coupling among the normal modes. This modification is often termed as *Dushinsky rotation*. Some experimental and theoretical studies [137–139] revealed that effects of Dushinsky rotation on the ET dynamics may be pronounced in some

systems.

In Section 5.2 we outline a brief introduction of Dushinsky rotation and its effects on heterogeneous ET reactions. The parameters describing the electronic-vibrational coupling with considering Dushinsky rotation and the thus introduced effects on the ET dynamics are discussed in Section 5.3.

5.2 Dushinsky rotation and Dushinsky effects

In the study of the vibronic ET dynamics in Chapter 3, we employed the simplest harmonic approximation to characterize the electronic-vibrational coupling using Eq. (2.29),

$$V_j^{\alpha\alpha}\left(\{q_l\}\right) = V_j^{\alpha\alpha}\left(\{0\}\right) + \sum_l \kappa_l^\alpha q_l + \sum_l \frac{1}{2}\omega_l^2 q_l^2 \tag{5.1}$$

with $\alpha = \mathrm{d}, \mathrm{a}$. The PES of the donor and the acceptor states are given by Eqs. (2.30) and (2.31), respectively. Therefore the PES of each ET-related state has a shape identical to that of the PES of the electronic ground-state given by Eq. (2.27).

In general, without applying the above mentioned approximation, we can expand the PES of the diabatic donor and acceptor states in second-order polynomials as given by Eq. (2.28)

$$V_j^{\alpha\alpha}\left(\{q_l\}\right) = V_j^{\alpha\alpha}\left(\{0\}\right) + \sum_l \kappa_l^\alpha q_l + \sum_{l,l'} \gamma_{ll'}^\alpha q_l q_{l'}.$$

Alternatively, it can be written as

$$V_j^{\alpha\alpha}\left(\{q_l\}\right) = V_j^{\alpha\alpha}\left(\{0\}\right) + \sum_l \kappa_l^\alpha q_l + \sum_l \frac{1}{2}\left(\omega_l^\alpha\right)^2 q_l^2 + \sum_{l\neq l'} \gamma_{ll'}^\alpha q_l q_{l'}, \tag{5.2}$$

with

$$\omega_l^\alpha = \sqrt{2\gamma_{ll}^\alpha}. \tag{5.3}$$

The last two terms in Eq. (5.2) represent diagonal and offdiagonal elements of the *Hessian matrix*, respectively. More specifically, Eq. (5.2) can be written as two equations

$$V^{\mathrm{dd}}\left(\{q_l\}\right) = V^{\mathrm{dd}}\left(\{0\}\right) + \sum_l \kappa_l^{\mathrm{d}} q_l + \sum_l \frac{1}{2}\left(\omega_l^{\mathrm{d}}\right)^2 q_l^2 + \sum_{l\neq l'} \gamma_{ll'}^{\mathrm{d}} q_l q_{l'}, \tag{5.4}$$

$$V^{\mathrm{aa}}\left(\{q_l\}\right) = V^{\mathrm{aa}}\left(\{0\}\right) + \sum_l \kappa_l^{\mathrm{a}} q_l + \sum_l \frac{1}{2}\left(\omega_l^{\mathrm{a}}\right)^2 q_l^2 + \sum_{l\neq l'} \gamma_{ll'}^{\mathrm{a}} q_l q_{l'}, \tag{5.5}$$

for the donor-state PES and the acceptor-state PES, respectively.

Eq. (5.2) has a form similar to Eq. (5.1) with two main differences: (i) the frequency ω_l^α along the l-th normal mode depends on the electronic state α and may, in general, differ from its value ω_l in the ground state, and (ii) the non-vanishing off-diagonal (mode-mixing) terms $\gamma_{ll'}^\alpha q_l q_{l'}$ in the potential energy matrix which describe the coupling between two different (the l-th and the l'-th with $l' \neq l$) normal modes.

The diagonalization of the Hessian matrix in each electronic state results in

$$V_j^{\alpha\alpha}\left(\{\tilde{q}_l\}\right) = V_j^{\alpha\alpha}\left(\{0\}\right) + \sum_l \tilde{\kappa}_l^\alpha \tilde{q}_l + \sum_l \frac{1}{2}\left(\tilde{\omega}_l^\alpha\right)^2 \tilde{q}_l^2 \tag{5.6}$$

with $\{\tilde{q}_l\}$ denoting the normal modes in the corresponding electronic state, which are, in general, different to $\{q_l\}$. Thus, the inclusion of the change of vibrational frequencies and the non-vanishing mode-mixing terms in Eq. (5.2) (as compared with Eq. (2.29)) results in a *rotation* of normal modes. This transformation of the normal-mode coordinate system is called *Dushinsky rotation*, and the thus introduced effects are classified as *Dushinsky effects*.

In this chapter, we will analyze Dushinsky effects based on two aspects. First, the change of vibrational frequencies introduces a difference of the vibrational zero-point energy (ZPE) between the donor and acceptor states. Furthermore, Dushinsky rotation modifies the PES, which results, *e.g.*, in a change of the reorganization energies.

5.3 Parameters of electronic-vibrational coupling and electron transfer dynamics including Dushinsky rotation

The geometry optimization of the investigated dye-semiconductor system C343-TiO_2 (shown in Fig. 5.1) as well as the electronic structure calculation, the determination of ET Hamiltonian matrix elements and the normal-mode analysis for this system were carried out previously as described in Ref. [41]. In this chapter, we will focus on discussions of the vibrational parameters reflecting Dushinsky rotation and Dushinsky effects on the ET dynamics. To this end, we will compare the vibronic dynamics including Dushinsky rotation to the vibronic dynamics without including Dushinsky rotation as well as to the purely electronic dynamics.

In order to simulate the ET dynamics in C343-TiO_2 with including Dushinsky rotation, the PES of the donor and the acceptor states are described via Eqs. (5.4) and (5.5), respectively. All parameters $\omega_l^{\mathrm{d/a}}$, $\kappa_l^{\mathrm{d/a}}$ and $\gamma_{ll'}^{\mathrm{d/a}}$ are obtained from the vibrational analysis for an isolated C343 molecule and the C343-cation using the TURBOMOLE package [113] with the B3LYP functional and the TZV(P) basis set.

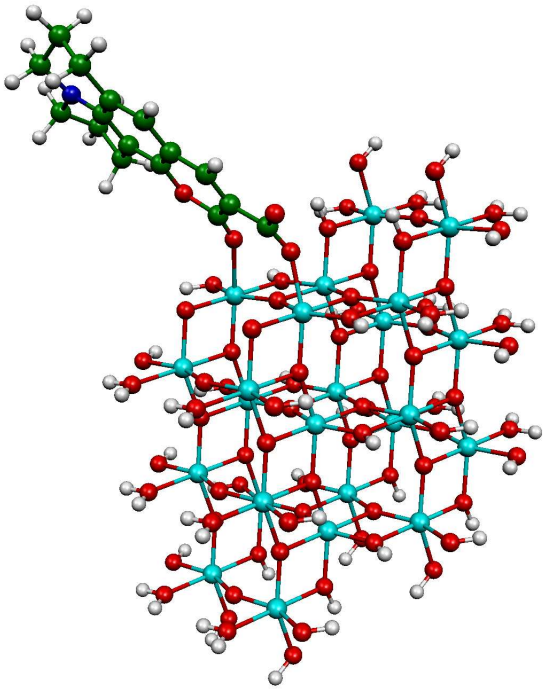

Figure 5.1: Donor-acceptor complex coumarin 343 - $(TiO_2)_{24}(H_2O)_{30}$.

47 of the total 102 vibrational normal modes are selected for the simulation of the vibronic dynamics based on the electronic-vibrational coupling strength (determined in a similar approach as described in Sections 2.3.2 and 3.4). Table 5.1 shows the thus obtained $\omega_l^{\mathrm{d/a}}$ values for the normal modes selected in the dynamical simulation (compared with the corresponding ground-state frequencies ω_l).

When Dushinsky rotation is included in the expansion of the PES of the donor and acceptor states, the reorganization energies for the donor state, the acceptor state and the ET transition change. Furthermore, a difference of the ZPE between the donor state and the acceptor states is introduced. The corresponding data are listed in Table 5.2. The reorganization-energy data in line (a) of Table 5.2 suggest a very weak electronic-vibrational coupling to the electronic excitation but a moderately strong coupling to the ET transition. If Dushinsky rotation is not considered, the selected 47 modes incorporate more than 84% of the total donor-state reorganization energy and more than 90% of the other two total reorganization energies, as indicated by line (b) of Table 5.2. Dushinsky rotation results in an increase of the total donor-state reorganization energy of about 5%, a decrease of the total acceptor-state reorganization energy of more than 20% and a decrease of the total ET reorganization energy of about 10%. It also causes a decrease of the vibrational ZPE in the donor state by 0.057 eV, while the decrease of ZPE in the acceptor states is rather small (0.006 eV).

Table 5.1: Vibrational frequencies of selected normal modes of coumarin 343 included in the dynamical simulation of the ET process. Listed are frequencies in the electronic ground state, the donor state and acceptor states. All data are given in cm^{-1}.

ω	ω^d	ω^a	ω	ω^d	ω^a	ω	ω^d	ω^a
126.6	119.7	130.6	1048.3	1048.3	1053.7	1390.4	1386.0	1403.6
137.7	151.2	190.9	1066.3	1057.3	1061.9	1406.1	1382.1	1408.7
216.7	207.6	230.6	1070.9	1098.5	1087.6	1455.0	1424.2	1450.0
222.3	208.2	237.2	1115.4	1099.3	1110.7	1472.7	1452.3	1457.8
269.6	183.7	268.5	1176.4	1160.4	1169.1	1495.2	1467.8	1471.2
322.7	322.5	370.6	1191.9	1179.3	1202.5	1519.2	1499.6	1502.4
413.9	406.8	408.8	1206.4	1198.7	1205.3	1579.3	1351.5	1499.1
448.9	458.8	453.1	1220.4	1214.9	1225.1	1630.3	1564.8	1565.7
467.1	461.7	468.1	1239.2	1232.6	1250.6	1654.9	1565.6	1606.0
603.1	590.0	603.7	1253.3	1236.2	1245.5	1777.0	1760.0	1758.2
644.7	622.0	632.8	1259.8	1245.9	1259.6	1848.3	1832.3	1814.8
688.4	681.1	691.3	1316.8	1302.5	1313.3	2946.8	2938.9	2970.7
719.3	710.6	688.8	1344.7	1335.2	1342.0	2954.7	2946.7	2978.0
735.4	719.2	724.8	1360.3	1344.4	1357.4	3066.4	3068.1	3084.0
790.8	775.3	786.4	1367.8	1346.9	1369.6	3194.5	3186.3	3201.1
894.7	882.3	899.0	1388.7	1377.4	1415.4			

Table 5.2: Donor-state, acceptor-state and ET reorganization energies as well as the ground-state, the excited-state and the cation-state ZPE of coumarin 343. Shown are (a) reorganization data including all 102 vibrational normal modes without considering Dushinsky rotation, (b) all data for the selected 47 vibrational normal modes without considering Dushinsky rotation and (c) all data for the selected 47 vibrational normal modes with considering Dushinsky rotation. All data are given in eV.

	Λ^d	Λ^a	Λ^{ET}	ZPE^d	ZPE^a
(a)	0.068	0.170	0.263		
(b)	0.057	0.160	0.240	3.516	3.516
(c)	0.060	0.127	0.217	3.459	3.510

Fig. 5.2 shows the modulus of the donor-acceptor coupling matrix elements V_j^{da} obtained from the partitioning procedure which was discussed in Ref. [41].

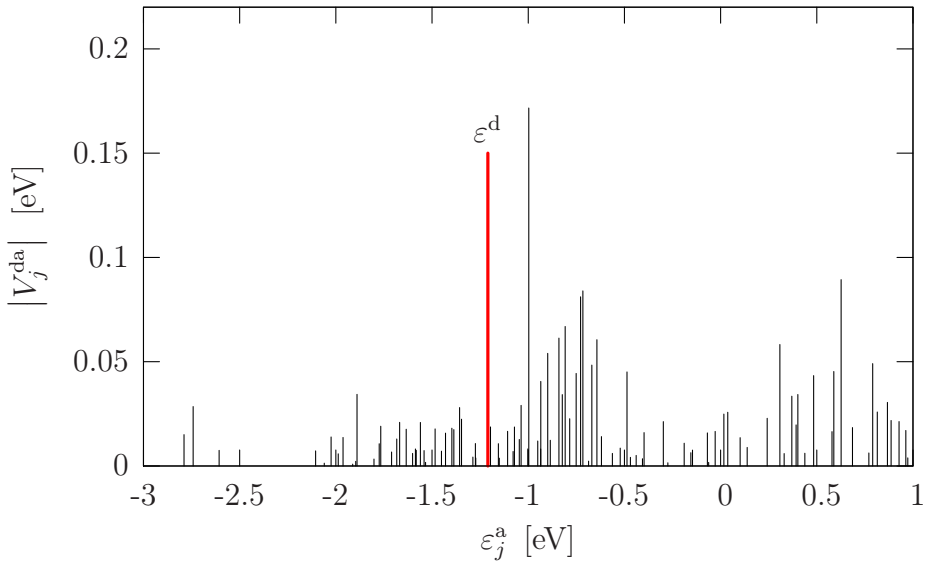

Figure 5.2: Modulus of donor-acceptor electronic coupling matrix elements V_j^{da} (black lines) of C343-TiO_2. The red vertical line indicates the energy of the donor state ε^{d}.

We have simulated the ET dynamics in the C343-TiO_2 system based on the first-principles model. The results are shown in Fig. 5.3. We can observe that there are pronounced oscillatory structures superimposed on the purely electronic dynamics (black line), which indicate electronic coherence. These coherence effects are significantly quenched by the inclusion of the electronic-vibrational coupling in the dynamical simulation (blue line and red line). The incomplete injection shown in Fig. 5.3 can be classified as a finite-size effect of the TiO_2 cluster [41].

Dushinsky effects on the ET dynamics in C343-TiO_2 are reflected by the comparison between the vibronic dynamics including Dushinsky rotation (red line) and that without including Dushinsky rotation (blue line). Fig. 5.3 shows that Dushinsky rotation has a small but noticeable effects on the ET dynamics. In particular, it results in a slower injection at the early stage of the dynamics, while for a long injection time the overall effect is very small. As discussed in Section 5.2, Dushinsky rotation introduces a ZPE-difference between the donor and acceptor states. Based on Table 5.2, this ZPE-difference causes an equivalent shift of the donor level of 0.051 eV towards the conduction-band minimum for C343-TiO_2. Thereby the donor level is shifted away from the region of strongest donor-acceptor coupling based on Fig. 5.2, and thus results in a slower dynamics. Therefore the slower injection dynamics in the first a few femtoseconds can be considered as an effect of the difference of ZPE between the donor and acceptor states, which is caused by Dushinsky rotation.

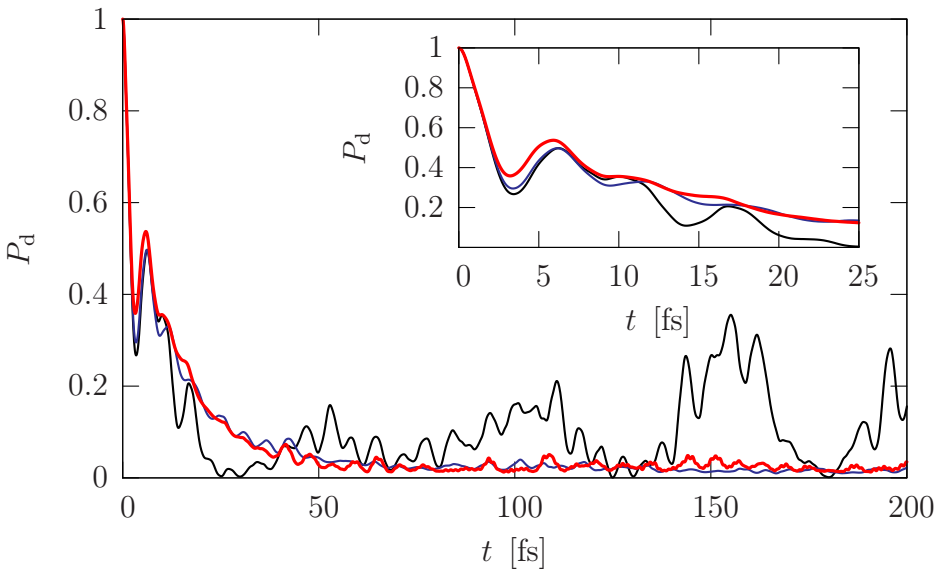

Figure 5.3: Population dynamics of the donor state after photoexcitation in the C343-TiO_2 system. All results are obtained for a finite $(TiO_2)_{24}(H_2O)_{30}$ cluster. Shown are results without vibronic coupling (black line), with vibronic coupling not including Dushinsky rotation (blue line) and including Dushinsky rotation (red line).

This effect of Dushinsky rotation can be tested by a model where the donor level is shifted towards the conduction-band minimum by 0.051 eV in the simulation of purely electronic dynamics (red line in Fig. 5.4). It is seen that, especially in the first a few femtoseconds, this simulation provides a better approximation to the vibronic dynamics including Dushinsky rotation (black line, which is identical to the red line in Fig. 5.3) than the purely electronic dynamics without considering the shift by the ZPE-difference (blue line, which is identical to the black line in Fig. 5.3).

As shown in Table 5.2, Dushinsky rotation also causes a 0.023 eV decrease of the ET reorganization energy for C343-TiO_2 (together with a 0.003 eV increase of the donor-state reorganization energy). According to the reorganization energy values listed in Table 5.2, we can use Fig. 2.4 (c) as a proper model to describe the ET reaction in C343-TiO_2. From Fig. 2.4 (c) we can see that (i) the electronic-vibrational coupling results in a motion of the wavepacket towards the conduction-band minimum due to its vibrational motion along the donor-state PES, and (ii) the modification of reorganization energies results in a slightly faster motion of the wavepacket towards the minimum of the donor-state PES but a slower motion towards the conduction-band minimum. Based on Fig. 5.2, the first feature corresponds to the motion of the wavepacket away from the region of strongest donor-acceptor coupling thus resulting a slower injection dynamics, as indicated by the blue line in Fig. 5.3 when compared with the black line. Also based on Fig. 5.2, the modification of reorganization energies corresponds to that the motion of the wavepacket away from the region of strongest

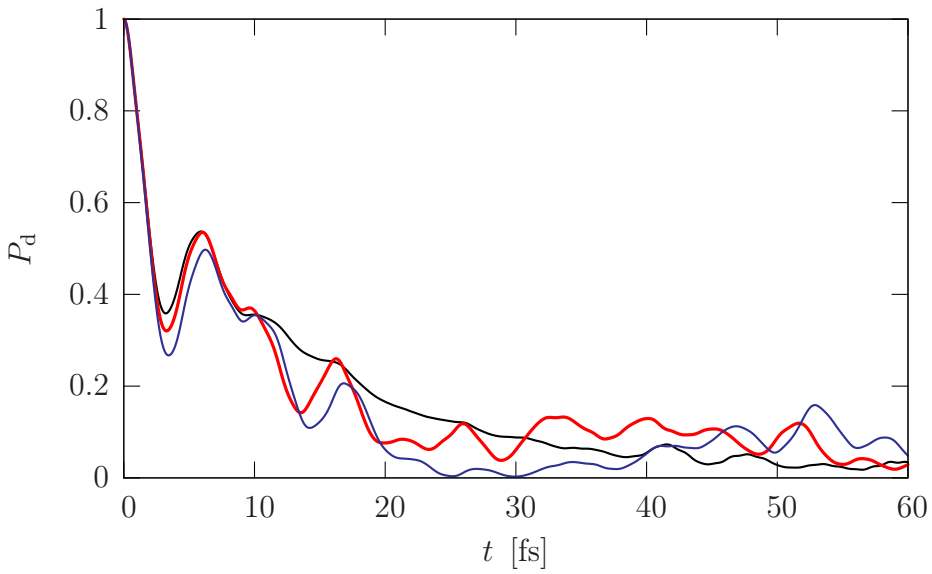

Figure 5.4: Population dynamics of the donor state after photoexcitation in the C343-TiO_2 system. All results are obtained for a finite $(TiO_2)_{24}(H_2O)_{30}$ cluster. Shown are the results with vibronic coupling including Dushinsky rotation (black line), without vibronic coupling (blue line) and without vibronic coupling but with the energy of the donor-state shifted by the ZPE-difference (red line).

donor-acceptor coupling becomes slower. As a result, the injection dynamics with the modification of reorganization energies should be faster. This modification of reorganization energy shows negligible influence on the early dynamics. For long injection times, on the other hand, it is opposite to the effect caused by the ZPE-difference as discussed above. As a result, the total effect on the long-time dynamics is very small.

In order to study this effect of Dushinsky rotation, we have applied a model with enlarging the mode-mode coupling in Eqs. (5.4) and (5.5). The red line in Fig. 5.5 shows results obtained by increasing all $\gamma^{\alpha}_{ll'}$ values in Eq. (5.2) by a factor of 10. With these new mode-mode coupling parameters, the total donor-state, acceptor-state and ET reorganization energies become 0.201 eV, 0.108 eV and 4.929 eV, respectively. Compared with the data shown in line (b) in Table 5.2, we observe that Dushinsky rotation results in a much larger ET reorganization energy for this model system. Based on the physical model given by Fig. 2.4 (c) which corresponds to the reorganization-energy data, Dushinsky rotation is expected to result in a significantly slower dynamics, since the wavepacket will quickly move away from the region of strongest donor-acceptor coupling. This prediction is demonstrated by the results shown in Fig. 5.5, where the vibronic dynamics including Dushinsky rotation of the model system (red line) is significantly slower than the purely electronic dynamics without considering the ZPE-difference (blue line).

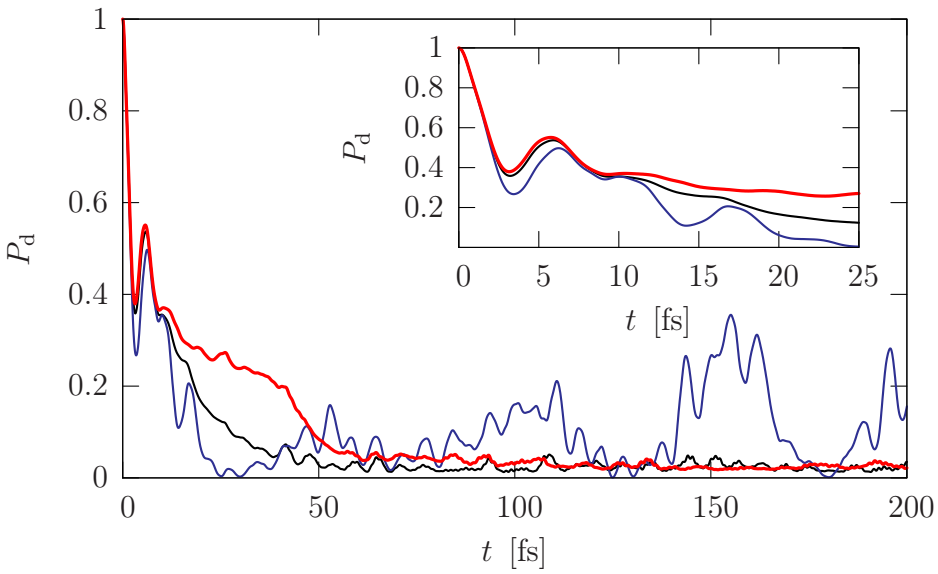

Figure 5.5: Population dynamics of the donor state after photoexcitation in the C343-TiO_2 system. All results are obtained for the finite $(TiO_2)_{24}(H_2O)_{30}$ cluster. Shown are the results without vibronic coupling (blue line), including Dushinsky rotation as obtained from the vibrational analysis (black line) and including Dushinsky rotation with the enlarged mode-mode coupling (red line).

5.4 Summary

In this chapter, we have studied the quantum dynamics of photoinduced heterogeneous ET processes in the dye-semiconductor system C343-TiO_2. The simulation of ET dynamics is based on a first-principles description of the system including the electronic-vibrational coupling with Dushinsky rotation. Within this model, the quantum dynamics of the ET processes has been simulated using the ML-MCTDH method.

The results of the simulations reveal that the inclusion of Dushinsky rotation results in a slightly slower dynamics of the ET process especially in the first a few femtoseconds. This can be understood as a combination of the two effects of Dushinsky rotation: the difference of the vibrational ZPE between the donor state and the acceptor states, and the change of the reorganization energies. For the present system, the former effect causes a slower dynamics while the latter causes a faster dynamics. Since both effects are small and opposite to each other, the total effect introduced by Dushinsky rotation is not pronounced in this system.

Chapter 6

Conclusions and Perspectives

In this thesis, we have studied the quantum dynamics of photoinduced ultrafast electron transfer processes in several dye-semiconductor systems. The study was based on a method which uses first-principles electronic structure calculations to characterize the system and to parametrize a model Hamiltonian including electronic-vibrational coupling. Within this model, ET dynamics was simulated at a fully quantum mechanical level employing different wavepacket-propagation methods. In particular, we used the multilayer multiconfigurational time-dependent Hartree method to simulate the electronic-vibrational dynamics in systems containing many degrees of freedom. Based on the recursive and layered expansion of the wave function, the ML-MCTDH approach provides more flexibility in the variational functional and thus significantly advances the capabilities of performing numerically exact wavepacket propagation for complex systems.

This first-principles based methodology was applied to study a variety of dye-semiconductor systems, including alizarin, coumarin 343 and different pyridine- and perylene-based dye molecules adsorbed at titanium oxide nanoparticles. For all systems, results of dynamical simulations reveal that electron injection processes take place on ultrafast timescales ranging from a few to a few tens of femtoseconds. In most systems, ET timescales obtained from the simulations are in good agreement with experimental results. In particular, we have obtained an electron-injection timescale of about $5 \sim 10$ fs for alizarin-TiO_2, which agrees well with experimental results [29].

In the studies in this thesis, we have employed cluster models to describe the semiconductor substrates in ET reactions. Furthermore, we have mimicked the electron injection to an infinite surface of semiconductor substrate using absorbing boundary condition techniques. For most systems, the decay of the population of the donor state exhibits significant recurrences and electronic coherence effects in the simulations of ET using cluster models. The results of simulations for extended surfaces, on the other hand, agree well with the results obtained with the corresponding cluster mo-

dels for short times and show an almost complete electron injection for longer times. This indicates that the incomplete ET is a finite-size effect of cluster models. For all system investigated, the combination of cluster models and absorbing boundary condition techniques provides an appropriate model to describe the semiconductor substrates.

Pronounced electronic coherence effects were obtained in the ET dynamics for the systems with strong donor-acceptor coupling. This can be rationalized by the complex donor-acceptor coupling scheme of the first-principles model. As a result, for most systems with finite TiO_2 substrate, only the initial dynamics can be approximately characterized by a single decay constant. We have studied electronic coherence effects in detail in the dye-semiconductor system alizarin-TiO_2. The result suggests that the ET process in alizarin-TiO_2 can be described by a two-step mechanism, which involves an intermediate state localized in the dye-semiconductor interface. The coherent electronic motion is a result of the strong coupling between the donor and the intermediate state.

The influence of electronic-vibrational coupling on the ET dynamics in systems of alizarin and coumarin 343 adsorbed at TiO_2 nanoparticles was studied. The results show that the coupling to the nuclear DoF causes a quenching of electronic coherence effects in C343-TiO_2, while the decoherence effect of the electronic-vibrational coupling is not significant in alizarin-TiO_2. Furthermore, effects of vibrational motion on the ET timescale is noticeable but not pronounced in both systems. We have also studied the effects of Dushinsky rotation on the ET dynamics in C343-TiO_2. The analysis shows that two aspects of Dushinsky rotation have to be considered: the change of vibrational zero-point-energy as well as the modification of potential energy surfaces.

The results of our studies demonstrate that the electron injection dynamics can be strongly influenced by the chemical nature of the dye-semiconductor system. Several ways to modify the chemical structure of dye-semiconductor systems have been considered in this thesis, such as using different anchor groups to bind the dye adsorbate to the substrate, inserting different spacer groups between the chromophore and the anchor group, extending the distance between the dye and the semiconductor, and employing different adsorption motifs. These modifications have a noticeable influence on the energy of the donor state and show significant effects on the strength and the distribution of donor-acceptor coupling. Thus, by applying these modifications, we can modulate several aspects of the ET dynamics, including the characteristic timescale and the strength of electronic coherence effects.

We finally mention several perspectives of the work presented in this thesis. In

the present applications, we have assumed that the photoexcitation by an ultrashort laser pulse can be approximated by an instantaneous transition from the electronic ground state to the donor state. The dynamical methodology also allows an inclusion of the laser pulse explicitly in the simulation of the ET process [100]. A particular interesting aspect would be the influence of the laser pulse on the ET reaction.

Another aspect concerns the model employed. In this thesis, we have studied ET reactions in dye-semiconductor systems employing a mean-field single-electron picture and using atomic orbitals to introduce the partitioning. Furthermore, we have characterized the electronic-vibrational coupling based on electronic structure calculations for isolated dye molecules, thereby neglecting the coupling to the semiconductor substrate and to the phonons of the semiconductor. Therefore, further developments of this methodology including a treatment within correlated many-electron states as well as a higher-level characterization of the electronic-vibrational coupling would be of interest.

The first-principles based model used in this thesis is not limited to the study of quantum dynamics of ET reactions in dye-semiconductor systems. It can, in principle, also be employed to describe other types of heterogeneous (interfacial) processes, such as photoinduced electron transport at dye-metal interfaces, surface photoelectrolysis and surface photocatalysis. The first-principles exploration of quantum chemistry and quantum dynamics in the corresponding heterogeneous systems would be of great interest to obtain a comprehensive understanding of the underlying photophysical and photochemical mechanisms, which is a prerequisite for the development of molecular optoelectronic devices.

Acknowledgements

It is a great pleasure to thank the people who made this thesis possible.

My gratitude to Prof. Dr. Michael Thoss, my Ph. D. supervisor, is difficult to present in simple words. During our cooperation, it is not only that I have improved my knowledge of mathematics and physics, not only that I have benefited so much from our discussions from time to time — the more important is that I have learnt so much from his inspiration, his enthusiasm and his attitude as being a scientist.

I appreciate Prof. Dr. Haobin Wang's help very much. As a long-time cooperator of Prof. Dr. Thoss, I have earned many discussions with him and learnt a lot, especially on the field of quantum dynamics and programming. Especially, Prof. Dr. Wang is the author of the codes for the dynamical simulation which I have used throughout this thesis.

Many thanks to Dr. Ivan Kondov, who has introduced me the kernel of the methodology, and provided me many useful programmes and tools together with his experience of previous studies. His logic and patience during our numerous discussions have left me unforgettable impression.

I am also grateful to Dr. Òscar Rubio Pons and Dipl.-Phys. Univ. Rainer Härtle for the helpful discussions.

I wish to thank Dr. Mattias Nilsing, Prof. Dr. Petter Persson as well. As my cooperators in some topics, they have offered me many valuable discussions and have provided many results of fundamental calculations, which is the basis of our research. Also, I have benifited very much from the suggestions by Prof. Dr. Sten Lunell, Prof. Dr. Frank Willig and Dr. Ralph Ernstorfer.

It is hard to express my thankfulness to Prof. Dr. Wolfgang Domcke and all his group members at the Technical University of Munich as they have provided me such an opportunity of working in the group. The atmosphere in this Lehrstuhl is amazing. I am very grateful to Dr. Maxim Gelin, Dr. Zhenggang Lan, Dr.

Venkatesan Thimmakondu, Dr. Sai Ramesh, Dr. Raffaele Borrelli, Dr. Kiran Sankar Maiti, *etc.*, for the uncountable academic discussions. Especially, I wish to thank Mrs. Ruth Mösch for her kind, careful and effective helps on the administrative "paper works". I also thank Mrs. Ulrike Graubner from Friedrich-Alexander-University of Erlangen-Nuremberg for her great efforts of administrative works.

Lastly, I wish to thank my parents and my wife, who support me and love me as always. To them I dedicate this thesis.

The generous allocation of computing time by the Leibniz Rechenzentrum (LRZ) Munich and the financial support by the Deutsche Forschungsgemeinschaft (DFG) are gratefully acknowledged.

Bibliography

[1] V. May and O. Kühn, Charge and Energy Transfer Dynamics in Molecular Systems, 2nd ed., Wiley-VCH, Weinheim, 2003.

[2] A. M. Kuznetsov, Charge Transfer in Physics, Chemistry and Biology, 1st ed., Gordon & Breach, Amsterdam, 1995.

[3] R. A. Marcus and, N. Sutin, *Biochim. Biophys. Acta*, **811**, 265 (1985).

[4] M. Haissinsky, *J. Chim. Phys.*. **47**, 957 (1950).

[5] B. J. Zwolinski, R. J. Marcus and H. Eyring, *Chem. Rev.*, **55**, 157 (1955).

[6] H. Taube, *Chem. Rev.*, **50**, 69 (1952); Electron Transfer Reactions of Complex Ions in Solution, 1st ed., Academic, New York, 1970; *Science*, **226**, 1028 (1984).

[7] J. W. Verhoeven, I. P. Dirkx and Th. J. de Boer, *Tetrahedron*, **25**, 4037 (1969).

[8] M. J. Potasek and J. J. Hopfield, *Proc. Natl. Acad. Sci.*, **74**, 3817 (1977).

[9] J. Deisenhofer, O. Epp, K. Miki, R. Huber and H. Michel, *J. Mol. Biol.*, **180**, 385 (1984).

[10] B. P. Crider, S. W. Carper and J. R. Lancaster, *Proc. Natl. Acad. Sci.*, **82**, 6793 (1985).

[11] M. A. Reed, C. Zhou, C. J. Muller, T. P. Burgin and J. M. Tour, *Science*, **278**, 252 (1997).

[12] R. J. Dwayne Miller, G. L. McLendon, A. J. Nozik, W. Schmickler and F. Willig, Surface Electron Transfer Processes, Wiley-VCH, Weinheim, 1995.

[13] B. O'Regan and M. Grätzel, *Nature*, **353**, 737 (1991).

[14] M. Grätzel and P. Liska, Patent: Photoelectrochemical cells and process for making same (1992);

[15] A. Hagfeldt and M. Grätzel, *Chem. Rev.*, **95**, 49 (1995).

[16] A. Hagfeldt and M. Grätzel, *Acc. Chem. Res.*, **33**, 269 (2000).

[17] J. Asbury, E. Hao, Y. Wang, H. N. Ghosh and T. Lian, *J. Phys. Chem. B*, **105**, 4545 (2001).

[18] M. Grätzel, *Nature*, **414**, 338 (2001).

[19] M. Grätzel, *J. Photochem. Photobiol. C*, **4**, 145 (2003).

[20] J.-E. Moser and M. Grätzel, *Chem. Phys.*, **176**, 493 (1993).

[21] I. B. Martini, J. Hodak, G. V. Hartland and P. V. Kamat, *J. Chem. Phys.*, **107**, 8064 (1997).

[22] H. N. Ghosh, J. B. Asbury, Y. Weng and T. Lian, *J. Phys. Chem. B*, **102**, 10208 (1998).

[23] J. Wachtveitl, R. Huber, S. Spörlein, J.-E. Moser and M. Grätzel, *Int. J. Photoenergy*, **1**, 153 (1999).

[24] R. Huber, S. Spörlein, J.-E. Moser, M. Grätzel and J. Wachtveitl, *J. Phys. Chem. B*, **104**, 8995 (2000).

[25] F. Willig, C. Zimmermann, S. Ramakrishna and W. Storck, *Electrochim. Acta*, **45**, 4565 (2000).

[26] C. Zimmermann, F. Willig, S. Ramakrishna, B. Burfeindt, B. Pettinger, R. Eichberger and W. Storck, *J. Phys. Chem. B*, **105**, 9245 (2001).

[27] N. A. Anderson, E. Hao, X. Ai, G. Hastings and T. Lian, *Chem. Phys. Lett.*, **347**, 304 (2001).

[28] G. Ramakrishna, H. N. Ghosh, A. K. Singh, D. K. Palit and J. P. Mittal, *J. Phys. Chem. B*, **105**, 12786 (2001).

[29] R. Huber, J.-E. Moser, M. Grätzel and J. Wachtveitl, *J. Phys. Chem. B*, **106**, 6494 (2002).

[30] J. Schnadt, P. A. Brühwiler, L. Patthey, J. N. O'Shea, S. Södergren, M. Odelius, R. Ahuja, O. Karis, M. Bässler, P. Persson, H. Siegbahn, S. Lunell and N. Mårtensson, *Nature*, **418**, 620 (2002).

[31] N. A. Anderson and T. Lian, *Annu. Rev. Phys. Chem.*, **56**, 491 (2005).

[32] V. V. Matylitsky, M. O. Lenz and J. Wachtveitl, *J. Phys. Chem. B*, **110**, 8372 (2006).

[33] R. Ernstorfer, L. Gundlach, S. Felber, W. Storck, R. Eichberger and F. Willig, *J. Phys. Chem. B*, **110**, 25383 (2006).

[34] J. M. Rehm, G. L. McLendon, Y. Nagasawa, K. Yoshihara, J.-E. Moser and M. Grätzel, *J. Phys. Chem.*, **100**, 9577 (1996).

[35] R. Huber, J.-E. Moser, M. Grätzel and J. Wachtveitl, *Chem. Phys.*, **285**, 39 (2002).

[36] S. Ramakrishna and F. Willig, *J. Phys. Chem. B*, **104**, 68 (2000).

[37] W. M. Stier and O. V. Prezhdo, *J. Phys. Chem. B*, **106**, 8047 (2002).

[38] L. G. C. Rego and V .S. Batista, *J. Am.Chem. Soc.*, **125**, 7989 (2003).

[39] M. Thoss, I. Kondov and H. Wang, *Chem. Phys.*, **304**, 169 (2004).

[40] W. R. Duncan and O. V. Prezhdo, *Annu. Rev. Phys. Chem.*, **58**, 143 (2007).

[41] I. Kondov, M. Čížek, C. Benesch, H. Wang and M. Thoss, *J. Phys. Chem. C*, **111**, 11970 (2007).

[42] H. Wang and M. Thoss, *J. Chem. Phys.*, **119**, 1289 (2003).

[43] R. A. Marcus, *J. Chem. Phys.*, **24**, 966 (1956); **26**, 867 (1957); **26**, 872 (1957); *J. Phys. Chem.*, **67**, 853 (1963); *J. Chem. Phys.*, **43**, 679 (1965); *J. Electroanal. Chem.*, **483**, 2 (2000).

[44] N. Sutin, *Ann. Rev. Nucl. Sci.*, **12**, 285 (1962).

[45] J. Jortner and K. F. Freed, *J. Chem. Phys.*, **52**, 6272 (1970); N. R. Kestner, J. Logan and J. Jortner, *J. Phys. Chem.*, **78**, 2148 (1974); J. Ulstrup and J. Jortner, *J. Chem. Phys.*, **63**, 4358 (1975); J. Jortner, *ibid.*, **64**, 4860 (1976).

[46] C. Cohen-Tannoudji, B. Diu and F. Lalo"e, Quantum Mechanics, **1st ed.**, John Wiley & Sons, Paris, 1977.

[47] J. J. Sakurai, Modern Quantum Mechanics, **2nd ed., rev.**, Addison-Wiley, USA, 1994.

[48] Y. Q. Gao, Y. Georgievskii and R. A. Marcus, *J. Chem. Phys.*, **112**, 3358 (2000); Y. Q. Gao and R. A. Marcus, *ibid.*, **113**, 6351 (2000).

[49] Å. Petersson, M. A. Ratner and H. O. Karlsson, *J. Phys. Chem. B*, **104**, 8498 (2000).

[50] P. Persson, R. Bergström and S. Lunell, *J. Phys. Chem. B*, **104**, 10348 (2000).

[51] S. Ramakrishna, F. Willig and V. May, *Phys. Rev. B*, **62**, 16330 (2000).

[52] S. Ramakrishna, F. Willig and V. May, *J. Chem. Phys.*, **115**, 2743 (2001).

[53] M. Schreiber, I. Kondov and U. Kleinekathöfer, *J. Lumin.*, **94-95**, 471 (2001).

[54] S. Ramakrishna, F. Willig and V. May, *Chem. Phys. Lett.*, **351**, 242 (2002).

[55] P. Persson, S. Lunell and L. Ojamäe, *Chem. Phys. Lett.*, **364**, 469 (2002).

[56] W. M. Stier and O. V. Prezhdo, *Israel J. Chem.*, **42**, 213 (2002).

[57] P. Persson, R. Bergström, L. Ojamäe and S. Lunell, *Adv. Quant. Chem.*, **41**, 203 (2002).

[58] S. Ramakrishna, F. Willig, V. May and A. Knorr, *J. Phys. Chem. B*, **107**, 607 (2003).

[59] W. M. Stier, W. R. Duncan and O. V. Prezhdo, *Adv. Mater.*, **16**, 240 (2004).

[60] L. Wang and V. May, *J. Chem. Phys.*, **121**, 8039 (2004).

[61] W. R. Duncan and O. V. Prezhdo, *J. Phys. Chem. B*, **109**, 365 (2005).

[62] L. G. C. Rego, S. G. Abuabara and V .S. Batista, *J. Chem. Phys.*, **122**, 154709 (2005).

[63] L. Wang, R. Ernstorfer, F. Willig and V. May, *J. Phys. Chem. B*, **109**, 9589 (2005).

[64] W. R. Duncan, W. M. Stier and O. V. Prezhdo, *J. Am. Chem. Soc.*, **127**, 7941 (2005).

[65] P. Persson and M. J. Lundqvist, *J. Phys. Chem. B*, **109**, 11918 (2005).

[66] W. R. Duncan and O. V. Prezhdo, *J. Phys. Chem. B*, **109**, 17998 (2005).

[67] M. Nilsing, P. Persson and L. Ojamäe, *Chem. Phys. Lett.*, **415**, 375 (2005).

[68] S. G. Abuabara, L. G. C. Rego and V .S. Batista, *J. Am. Chem. Soc.*, **127**, 18234 (2005).

[69] L. Wang, F. Willig and V. May, *J. Chem. Phys.*, **124**, 014712 (2006).

[70] I. Kondov, M. Thoss and H. Wang, *J. Phys. Chem. A*, **110**, 1364 (2006).

[71] K. L. Sebastian and M. Tachiya, *J. Chem. Phys.*, **124**, 064713 (2006).

[72] P. Persson, M. J. Lundqvist, R. Ernstorfer, W. A. Goddard III and F. Willig, *J. Chem. Theor. Comput.*, **2**, 441 (2006).

[73] K. K. Liang, C.-K. Lin, H.-C. Chang, M. Hayashi and S. H. Lin, *J. Chem. Phys.*, **125**, 154706 (2006).

[74] I. Kondov, H. Wang and M. Thoss, *Int. J. Quant. Chem.*, **106**, 1291 (2006).

[75] M. J. Lundqvist, M. Nilsing, P. Persson and S. Lunell, *Int. J. Quant. Chem.*, **106**, 3214 (2006).

[76] P. W. Anderson, *Phys. Rev.*, **124**, 41 (1961).

[77] D. M. Newns, *Phys. Rev.*, **178**, 1123 (1969).

[78] H. Wang, M. Thoss and W. H. Miller, *J. Chem. Phys.*, **115**, 2979 (2001).

[79] M. Thoss, H. Wang and W. H. Miller, *J. Chem. Phys.*, **115**, 2991 (2001).

[80] J. Li, M. Nilsing, I. Kondov, H. Wang, P. Persson, S. Lunell and M. Thoss, *J. Phys. Chem. C*, **112**, 12326 (2008).

[81] J. Li, I. Kondov, H. Wang and M. Thoss, *J. Phys. Chem. C*, **114**, 18481 (2010).

[82] H. Feshbach, *Ann. Phys.*, **19**, 287 (1962).

[83] W. Domcke, *Phys. Rep.*, **208**, 97 (1991).

[84] T. O'Malley, *Phys. Rev.*, **162**, 98 (1967).

[85] W. Domcke, *Phys. Rev. A*, **28**, 2777 (1983).

[86] I. V. Kurnikov and D. N. Beratan, *J. Chem. Phys.*, **105**, 9561 (1996).

[87] M. Galperin, S. Toledo and A. Nitzan, *J. Chem. Phys.*, **117**, 10817 (2002).

[88] P.-O. Löwdin, *J. Chem. Phys.*, **18**, 365 (1950).

[89] I. Mayer, *Int. J. Quant. Chem.*, **90**, 63 (2002).

[90] Y. Xue and M. A. Ratner, *Phys. Rev. B*, **68**, 115406 (2003).

[91] F. Dushinsky, *Acta Physicochim. URSS*, **7**, 551 (1937).

[92] A. B. Myers, *Chem. Rev.*, **96**, 911 (1996).

[93] W. Domcke, D. R. Yarkony and, H. Köppel, Eds., Conical Intersections: Electronic Structure, Dynamics and Spectroscopy, World Scientific, Singapore, 2004.

[94] D. J. Tannor, Introduction to Quantum Mechanics: A Time Dependent Perspective, University Science Press, Sausalito, 2007.

[95] H.-D. Meyer, U. Manthe and L. S. Cederbaum, *Chem. Phys. Lett.*, **165**, 73 (1990).

[96] U. Manthe, H.-D. Meyer and L. S. Cederbaum, *J. Chem. Phys.*, **97**, 3199 (1992).

[97] M. H. Beck, A. Jäckle, G. A. Worth and H.-D. Meyer, *Phys. Rep.*, **324**, 1 (2000).

[98] H.-D. Meyer and G. A. Worth, *Theor. Chem. Acc.*, **109**, 251 (2003).

[99] H.-D. Meyer, F. Gatti and, G. A. Worth, Eds., Multidimensional Quantum Dynamics: MCTDH Theory and Applications, Wiley-VCH, Weinheim, 2009.

[100] H. Wang and M. Thoss, *J. Chem. Phys.*, **124**, 034114 (2006).

[101] P. A. M. Dirac, *Proc. Cambridge. Philos. Soc.*, **26**, 376 (1930).

[102] J. Frenkel, Wave Mechanics, Clarendon, Singapore 1934.

[103] H. Wang, *J. Chem. Phys.*, **113**, 9948 (2000).

[104] H. Wang and M. Thoss, *J. Phys. Chem. A*, **107**, 2126 (2003).

[105] M. Thoss, W. Domcke and H. Wang, *Chem. Phys.*, **296**, 217 (2004).

[106] H. Wang and M. Thoss, *Chem. Phys. Lett.*, **389**, 43 (2004).

[107] M. Thoss and H. Wang, *Chem. Phys.*, **322**, 210 (2006).

[108] L. C. T. Shoute and G. R. Loppnow, *J. Chem. Phys.*, **117**, 842 (2002).

[109] L. Dworak, V. V. Matylitsky and J. Wachtveitl, *ChemPhysChem*, **10**, 384 (2009).

[110] J. K. Burdett, T. Hughbanks, G. J. Miller, J. W. Richardson, Jr. and J. V. Smith, *J. Am. Chem. Soc.*, **109**, 3639 (1987).

[111] T. Bredow and K. Jug, *J. Phys. Chem.*, **99**, 285 (1995).

[112] P. C. Redfern, P. Zapol, L. A. Curtiss, T. Rajh and M. C. Thurnauer, *J. Phys. Chem. B*, **107**, 11419 (2003).

[113] R. Ahlrichs, M. Bär, M. Häser, H. Horn and C. Kölmel, *Chem. Phys. Lett.*, **162**, 165 (1989).

[114] M. J. Frisch, G. W. Trucks, H. B. Schlegel, G. E. Scuseria, M. A. Robb, J. R. Cheeseman, J. A. Montgomery, Jr., T. Vreven, K. N. Kudin, J. C. Burant, J. M. Millam, S. S. Iyengar, J. Tomasi, V. Barone, B. Mennucci, M. Cossi, G. Scalmani, N. Rega, G. A. Petersson, H. Nakatsuji, M. Hada, M. Ehara,

K. Toyota, R. Fukuda, J. Hasegawa, M. Ishida, T. Nakajima, Y. Honda, O. Kitao, H. Nakai, M. Klene, X. Li, J. E. Knox, H. P. Hratchian, J. B. Cross, V. Bakken, C. Adamo, J. Jaramillo, R. Gomperts, R. E. Stratmann, O. Yazyev, A. J. Austin, R. Cammi, C. Pomelli, J. W. Ochterski, P. Y. Ayala, K. Morokuma, G. A. Voth, P. Salvador, J. J. Dannenberg, V. G. Zakrzewski, S. Dapprich, A. D. Daniels, M. C. Strain, O. Farkas, D. K. Malick, A. D. Rabuck, K. Raghavachari, J. B. Poresman, J. V. Ortiz, Q. Cui, A. G. Baboul, S. Clifford, J. Cioslowski, B. B. Stefanov, G. Liu, A. Liashenko, P. Piskorz, I. Komaromi, R. L. Martin, D. J. Fox, T. Keith, M. A. Al-Laham, C. Y. Peng, A. Nanayakkara, M. Challacombe, P. M. W. Gill, B. Johnson, W. Chen, M. W. Wong, C. Gonzalez and J. A. Pople, *Gaussian 03, Revision E.01*, (Gaussian, Inc., Wallingford, CT, 2004).

[115] M. Nilsing, S. Lunell, P. Persson and L. Ojamäe, *Surf. Sci.*, **582**, 49 (2005).

[116] C. Kormann, D. W. Bahnemann and M. R. Hoffmann, *J. Phys. Chem.*, **92**, 5196 (1988).

[117] A. Furube, R. Katoh, K. Hara, S. Murata, H. Arakawa and M. Tachiya, *J. Phys. Chem. B*, **107**, 4162 (2005).

[118] A. Furube, R. Katoh, T. Yoshihara, K. Hara, S. Murata, H. Arakawa and M. Tachiya, *J. Phys. Chem. B*, **108**, 12583 (2004).

[119] D. Stockwell, Y. Yang, J. Huang, C. Anfuso, Z. Huang and T. Lian, *J. Phys. Chem. C*, **114**, 6560 (2010).

[120] H. Němec, J. Rochford, O. Taratula, E. Galoppini, P. Kužel, T. Polívka, A. P. Yartsev and V. Sundström, *Phys. Rev. Lett.*, **104**, 197401 (2010).

[121] J. Asbury, E. Hao, Y. Wang and T. Lian, *J. Phys. Chem. B*, **104**, 11957 (2000).

[122] P. Piotrowiak, E. Galoppini, Q. Wei, G. J. Meyer and P. Wiewiór, *J. Am. Chem. Soc.*, **125**, 5278 (2003).

[123] G. Liu, A. Klein, A. Thissen and W. Jaegermann, *Surf. Sci.*, **539**, 37 (2003).

[124] N. A. Anderson, X. Ai, D. Chen, D. L. Mohler and T. Lian, *J. Phys. Chem. B*, **107**, 14231 (2003).

[125] N. A. Anderson, X. Ai and T. Lian, *J. Phys. Chem. B*, **107**, 14414 (2003).

[126] N. A. Anderson and T. Lian, *Coord. Chem. Rev.*, **248**, 1231 (2004).

[127] B. Burfeindt, T. Hannappel, W. Storck and F. Willig, *J. Phys. Chem.*, **100**, 16463 (1996).

[128] L. Gundlach, R. Ernstorfer and F. Willig, *Appl. Phys. A*, **88**, 481 (2007).

[129] P. Durand and J.-C. Barthelat, *Theor. Chim. Acta*, **38**, 283 (1975).

[130] Y. Bouteiller, C. Mijoule, M. Nizam, J.-C. Barthelat, J. P. Daudey, M. Pélissier, and B. Silvi, *Mol. Phys.*, **65**, 295 (1988).

[131] T. M. Halasinski, J. L. Weisman, R. Ruiterkamp, T. J. Lee, F. Salama, and M. Head-Gordon, *J. Phys. Chem. A*, **107**, 3660 (2003).

[132] H. N. Ghosh, J. B. Asbury and T. Lian, *J. Phys. Chem. B*, **102**, 6482 (1998).

[133] G. Ramakrishna and H. N. Ghosh, *J. Phys. Chem. A*, **106**, 2545 (2002).

[134] K. A. Walters, D. A. Gaal and J. T. Hupp, *J. Phys. Chem. B*, **106**, 5139 (2002).

[135] E. Hao, N. A. Anderson, J. Asbury and T. Lian, *J. Phys. Chem. B*, **106**, 10191 (2002).

[136] V. Biju, M. Micic, D. Hu and H. P. Lu, *J. Am. Chem. Soc.*, **126**, 9374 (2004).

[137] S. Nakashima, Y. Nagasawa, K. Seike, T. Okada, M. Sato and T. Kohzuma, *Chem. Phys. Lett.*, **331**, 396 (2000).

[138] G. M. Sando, K. G. Spears, J. T. Hupp and P. T. Ruhoff, *J. Phys. Chem. A*, **105**, 5317 (2001); G. M. Sando and K. G. Spears, *ibid.* **105**, 5326 (2001).

[139] T. Cimei, A. R. Bizzarri, G. Cerullo, S. de Silvestri and S. Cannistraro, *Biophys. Chem.*, **106**, 221 (2003).

Chapter A

Decay from a discrete state to a continuous set of states: Fermi's Golden Rule

We have studied heterogeneous ET reactions in several dye-semiconductor systems in this thesis. Such an ET process can be described by a model of transition from a discrete initial state to a set of final states. In this appendix, we will discuss this model, in particular, we will derive the general formula of the transition rate employing time-dependent perturbation theory.

The transition from an initially prepared discrete state $|0\rangle$ to a set of final states $\{|j\rangle\}$ which form a (quasi-)continuum provides a proper physical model for many applications. If all involved states are orthogonal to each other and form a complete set, the system Hamiltonian can be expanded in the basis $\{|0\rangle, \{|j\rangle\}\}$ as

$$\hat{H} = |0\rangle \varepsilon_0 \langle 0| + \sum_{j>0} |j\rangle \varepsilon_j \langle j| + \sum_{j>0} (|0\rangle V_{0j} \langle j| + |j\rangle V_{j0} \langle 0|) \tag{A.1}$$

with ε_j ($j \geq 0$) denoting the energy of state $|j\rangle$ and V_{0j} ($j > 0$) denoting the electronic coupling between $|0\rangle$ and $|j\rangle$ (for a Hermitian Hamiltonian we have $V_{0j} = V_{j0}^*$). Here $j > 0$ denotes the quantum number of the j-th final state. $|0\rangle$ and $|j\rangle$ are eigenstate of the Hamiltonian in Eq. (A.1) only when all $V_{0j} = 0$.

At $t = 0$, the system is prepared at the initial state, *i.e.* $|\Psi(0)\rangle = \sum_{j\geq 0} c_j(0) |j\rangle = |0\rangle$. The wave function at $t > 0$ can be written as

$$|\Psi(t)\rangle = \sum_{j\geq 0} c_j(t) \, \mathrm{e}^{-\mathrm{i}\varepsilon_j t} |j\rangle . \tag{A.2}$$

If the final states form a true continuum, the summation over the final states should be replaced by the integration with respect to the quantum number, thus,

$$\hat{H} = |0\rangle \varepsilon_0 \langle 0| + \int \mathrm{d}j \, |j\rangle \varepsilon_j \langle j| + \int \mathrm{d}j \, (|0\rangle V_{0j} \langle j| + |j\rangle V_{j0} \langle 0|) \tag{A.3}$$

with the orthonormality condition among the final states given by

$$\langle j \,|j'\rangle = \delta\left(j - j'\right) \tag{A.4}$$

and the completeness condition of the basis set given by

$$|0\rangle \langle 0| + \int \mathrm{d}j \,|j\rangle \langle j| = 1. \tag{A.5}$$

The physical model of such a transition is given by Fig. 2.2 (with replacing $\left|\psi^{\mathrm{d}}\right\rangle$ by $|0\rangle$ and $\left|\psi_j^{\mathrm{a}}\right\rangle$ by $|j\rangle$).

The Hamiltonian given by Eq. (A.1) can be divided into two parts

$$\hat{H} = \hat{H}_0 + \hat{V}\left(t\right) \tag{A.6}$$

with

$$\hat{H}_0 = |0\rangle \,\varepsilon_0 \langle 0| + \sum_{j>0} |j\rangle \,\varepsilon_j \langle j| \tag{A.7}$$

denoting the *unperturbed* Hamiltonian. The *time-dependent perturbation* operator $\hat{V}\left(t\right)$ is given by

$$\hat{V}\left(t\right) = \begin{cases} 0, & t < 0 \\ \hat{V}_0 \mathrm{e}^{\eta t}, & t \geq 0 \end{cases} \tag{A.8}$$

with taking the limit $\eta \to 0^+$. Here

$$\hat{V}_0 = \sum_{j>0} \left(|0\rangle \, V_{0j} \langle j| + |j\rangle \, V_{j0} \langle 0|\right). \tag{A.9}$$

The wave function in the *interaction picture* (*Dirac picture*), $|\Psi\left(t\right)\rangle^{\mathrm{I}}$, can be related to the wave function in the *Schrödinger picture*, $|\Psi\left(t\right)\rangle$, via

$$|\Psi\left(t\right)\rangle^{\mathrm{I}} = \mathrm{e}^{\mathrm{i}\hat{H}_0 t} \,|\Psi\left(t\right)\rangle \tag{A.10}$$

and accordingly

$$|\Psi\left(t\right)\rangle^{\mathrm{I}} = \sum_j c_j\left(t\right) |j\rangle \,. \tag{A.11}$$

The perturbation operator in the interaction picture is defined as

$$\hat{V}^{\mathrm{I}}\left(t\right) = \mathrm{e}^{\mathrm{i}\hat{H}_0 t} \hat{V}\left(t\right) \mathrm{e}^{-\mathrm{i}\hat{H}_0 t}, \tag{A.12}$$

and the Schrödinger equation in the interaction picture is given by

$$\mathrm{i}\frac{\partial}{\partial t} |\Psi\left(t\right)\rangle^{\mathrm{I}} = \hat{V}^{\mathrm{I}}\left(t\right) |\Psi\left(t\right)\rangle^{\mathrm{I}} \,. \tag{A.13}$$

The zeroth-order solution for the expansion coefficients $c_j\left(t\right)$ is given by $c_j^{(0)}\left(t\right) = 0$ for all $j > 0$. The first-order correction (and thus the first-order solution) is given by

$$c_j^{(1)}\left(t\right) = -\mathrm{i} \langle j| \lim_{t_0 \to -\infty} \int_{t_0}^{t} \mathrm{d}t_1 \hat{V}^{\mathrm{I}}\left(t_1\right) |0\rangle \,, \tag{A.14}$$

i.e.,

$$c_j^{(1)}(t) = -\mathrm{i}V_{j0}\frac{\mathrm{e}^{\eta+\mathrm{i}(\varepsilon_0-\varepsilon_j)}}{\eta+\mathrm{i}(\varepsilon_0-\varepsilon_j)}. \tag{A.15}$$

The population of the j-th state ($j>0$) and its time-derivative are thus given by

$$P_j(t) = \left|c_j^{(1)}(t)\right|^2 = |V_{j0}|^2\frac{\mathrm{e}^{2\eta t}}{\eta^2+(\varepsilon_0-\varepsilon_j)^2} \tag{A.16}$$

and

$$\dot{P}_j(t) = 2|V_{j0}|^2\frac{\eta\mathrm{e}^{2\eta t}}{\eta^2+(\varepsilon_0-\varepsilon_j)^2}, \tag{A.17}$$

respectively. For short times, *i.e.*, $P_0(t)\approx 1$, the rate constant of the transition from $|0\rangle$ to $\{|j\rangle\}$ can be calculated as

$$k = -\frac{\dot{P}_0(t)}{P_0(t)} \approx \sum_{j>0}\lim_{\eta\to 0^+}\dot{P}_j(t) = 2\pi\sum_{j>0}|V_{j0}|^2\delta(\varepsilon_0-\varepsilon_j). \tag{A.18}$$

This equation is the Golden-Rule formula of transition rate. Thereby the relationship

$$\lim_{\alpha\to 0^+}\frac{1}{\pi}\frac{\alpha}{\alpha^2+x^2} = \delta(x)$$

is used.

Usually, we relate the transition rate with the *self-energy* in the donor state $\Sigma(\varepsilon_0)$ via

$$k = \Gamma(\varepsilon_0) = -2\Im\Sigma(\varepsilon_0). \tag{A.19}$$

The influence of the continuous set of final states as well as the coupling between the initial state and the acceptor states enters only through the self-energy

$$\Sigma(\varepsilon_0) = \sum_{j>0}\lim_{\eta\to 0^+}\frac{|V_{j0}|^2}{\varepsilon_0-\varepsilon_j+\mathrm{i}\eta}. \tag{A.20}$$

This effect can be understood as a shift of the energy of $|0\rangle$ from ε_0 to $[\varepsilon_0+\Sigma(\varepsilon_0)]$. The imaginary part of the self-energy

$$\Gamma(\varepsilon_0) = -2\Im\Sigma(\varepsilon_0) = 2\pi\sum_{j>0}|V_{j0}|^2\delta(\varepsilon_0-\varepsilon_j) \tag{A.21}$$

represents the *decay width* of the initial state.

Chapter B

Description of electron transfer from an adsorbate to an extended surface

In this appendix, we will outline an approximate approach towards the description of electron transfer from an adsorbate to an extended surface. This can be carried out employing the slab model and electronic calculations with periodic boundary conditions [67]. In this thesis, we describe the effect of an infinite semiconductor substrate using an approximate variant [41] of surface Green's function techniques [90].

In the dynamical study, if the system is initially prepared in the donor state, the equation of motion for the electronic projection of the time-dependent vibronic wave function on the donor state, $\left\langle \psi^{\mathrm{d}} \right| \left. \Psi\left(t\right) \right\rangle$, can be obtained using projection-operator techniques [83] as

$$\begin{aligned} &\frac{\partial}{\partial t} \left\langle \psi^{\mathrm{d}} \left| \Psi\left(t\right) \right\rangle \right. \\ &= -\mathrm{i}\hat{H}^{\mathrm{d}}_{\mathrm{nucl}} \left\langle \psi^{\mathrm{d}} \right| \left. \Psi\left(t\right) \right\rangle - \int_0^t \mathrm{d}\tau \Gamma\left(\tau\right) \exp\left(-\mathrm{i}\hat{H}^{\mathrm{a}}_{\mathrm{nucl}} t\right) \left\langle \psi^{\mathrm{d}} \right| \left. \Psi\left(t-\tau\right) \right\rangle, \end{aligned} \tag{B.1}$$

where

$$\hat{H}^{\mathrm{d}}_{\mathrm{nucl}} = \varepsilon^{\mathrm{d}} + \sum_l \left(\frac{1}{2}\hat{p}_l^2 + \frac{1}{2}\omega_l^2 q_l^2 + \kappa_l^{\mathrm{d}} q_l \right) \tag{B.2}$$

denotes the nuclear Hamiltonian in the donor state, and

$$\hat{H}^{\mathrm{a}}_{\mathrm{nucl}} = \varepsilon^{\mathrm{a}} + \sum_l \left(\frac{1}{2}\hat{p}_l^2 + \frac{1}{2}\omega_l^2 q_l^2 + \kappa_l^{\mathrm{a}} q_l \right) \tag{B.3}$$

denotes the nuclear Hamiltonian in the acceptor state. Thus, when only observables that are localized at the donor part (*i.e.*, the dye adsorbate) are of interest, the influence of the semiconductor substrate and of the donor-acceptor coupling on the dynamics is fully characterized by the function

$$\Gamma\left(t\right) = \sum_j \left|V_j^{\mathrm{da}}\right|^2 \exp\left(-\mathrm{i}\varepsilon_j^{\mathrm{a}} t\right) \tag{B.4}$$

or, equivalently, its Fourier transform $\Gamma(\varepsilon)$.

As already mentioned in Appendix A, the $\Gamma(\varepsilon)$ function is the imaginary part of the self-energy in the initial (donor) state and usually written as

$$\Gamma(\varepsilon) = -2\Im\Sigma(\varepsilon) \tag{B.5}$$

with

$$\Sigma(\varepsilon) = \left\langle \psi^{\mathrm{d}} \right| \hat{V}\hat{G}^{\mathrm{surf}}\hat{V} \left| \psi^{\mathrm{d}} \right\rangle \tag{B.6}$$

with $\hat{V}$ representing the donor-acceptor coupling. The electronic *Green's function* of the semiconductor surface is given by

$$\hat{G}^{\mathrm{surf}} = \left(\varepsilon + \mathrm{i}\eta - \hat{H}^{\mathrm{surf}}\right)^{-1}. \tag{B.7}$$

Here $\hat{H}^{\mathrm{surf}}$ denotes the electronic Hamiltonian of the semiconductor surface and η is the usual positive infinitesima.

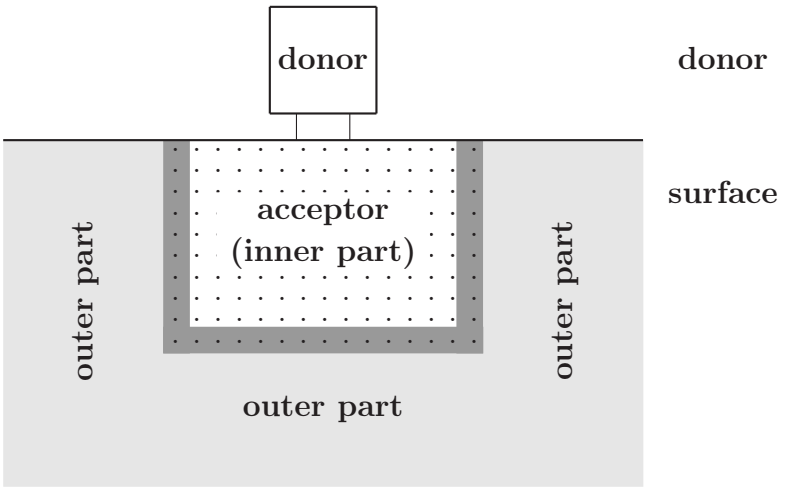

Figure B.1: Partitioning scheme of a dye-semiconductor system containing a dye molecule (labeled as "donor") adsorbed to an infinite surface (labeled as "surface") of the semiconductor. In our approach, the extended surface of semiconductor is partitioned into two parts: the inner part (labeled as "acceptor" and marked by dots) which directly interacts with the donor under our approximation, and the outer part (in light gray, labeled as "outer") which only interacts with the inner part of semiconductor substrate. The influence of the infinite outer part enters the dynamics via a self-energy operator which, under our approximation, acts on all AO centered at the boundary part of the acceptor (in dark gray).

In order to study the effect of the infinite substrate to the ET reaction, we can partition the overall system containing a dye adsorbate and an infinite substrate

into three parts: the donor part that contains the dye adsorbate (labeled by the superscript $^{\mathrm{d}}$), the inner part of the substrate acceptor (labeled by the superscript $^{\mathrm{a}}$) and the outer part of the substrate (labeled by the superscript $^{\mathrm{o}}$). Furthermore, we assume that the infinite outer part of the substrate only interacts with the inner part of the substrate but not with the donor. In the orthogonal basis, the Fock (or Kohn-Sham) matrix of the overall system can be accordingly rearranged as

$$\tilde{\boldsymbol{F}} = \begin{pmatrix} \tilde{\boldsymbol{F}}^{\mathrm{dd}} & \tilde{\boldsymbol{F}}^{\mathrm{da}} & \boldsymbol{0} \\ \tilde{\boldsymbol{F}}^{\mathrm{ad}} & \tilde{\boldsymbol{F}}^{\mathrm{aa}} & \tilde{\boldsymbol{F}}^{\mathrm{ao}} \\ 0 & \tilde{\boldsymbol{F}}^{\mathrm{oa}} & \tilde{\boldsymbol{F}}^{\mathrm{oo}} \end{pmatrix}. \tag{B.8}$$

Here the subblock

$$\begin{pmatrix} \tilde{\boldsymbol{F}}^{\mathrm{dd}} & \tilde{\boldsymbol{F}}^{\mathrm{da}} \\ \tilde{\boldsymbol{F}}^{\mathrm{ad}} & \tilde{\boldsymbol{F}}^{\mathrm{aa}} \end{pmatrix}$$

that describes a finite donor-acceptor system will be treated explicitly employing the methods outlined in Chapter 2.

The effect of the infinite outer part of the substrate enters via a self-energy operator[1] that only acts on the inner part of the substrate, since we have assumed that the outer part of the substrate does not interact with the donor. This self-energy operator is given by

$$\begin{aligned} &\hat{\Xi}\left(\varepsilon'\right) \\ &= \hat{\mathcal{P}}\hat{H}^{\mathrm{surf}}\left(1-\hat{\mathcal{P}}\right)\left[\varepsilon'+\mathrm{i}\eta'-\left(1-\hat{\mathcal{P}}\right)\hat{H}^{\mathrm{surf}}\left(1-\hat{\mathcal{P}}\right)\right]^{-1}\left(1-\hat{\mathcal{P}}\right)\hat{H}^{\mathrm{surf}}\hat{\mathcal{P}}, \end{aligned} \tag{B.9}$$

with the *surface Hamiltonian* given by

$$\hat{H}^{\mathrm{surf}} = \begin{pmatrix} 0 & \boldsymbol{0} & \boldsymbol{0} \\ \boldsymbol{0} & \boldsymbol{F}^{\mathrm{aa}} & \boldsymbol{F}^{\mathrm{ao}} \\ \boldsymbol{0} & \boldsymbol{F}^{\mathrm{oa}} & \boldsymbol{F}^{\mathrm{oo}} \end{pmatrix}. \tag{B.10}$$

The projection operator

$$\hat{\mathcal{P}} = \sum_k \left|\tilde{\phi}_k^{\mathrm{a}}\right\rangle \left\langle\tilde{\phi}_k^{\mathrm{a}}\right| \tag{B.11}$$

projects onto the subspace of the acceptor part of the substrate that is explicitly treated. Here $\left\{\left|\tilde{\phi}_k^{\mathrm{a}}\right\rangle\right\}$ are the orthogonalized orbitals that are localized at the acceptor part.

Based on the analysis above, the self-energy in the donor state in Eq. (B.6) can be calculated via

$$\Sigma\left(\varepsilon\right) = \left\langle\psi^{\mathrm{d}}\right| \hat{V}\hat{\mathcal{P}}\hat{G}^{\mathrm{surf}}\hat{\mathcal{P}}\hat{V}\left|\psi^{\mathrm{d}}\right\rangle \tag{B.12}$$

[1]This must be distinguished to the self-energy to the discrete initial state which presents the effects from an infinite surface, as defined in Eq. (B.6).

with the projected surface Green's function given by

$$\hat{\mathcal{P}}\hat{G}^{\mathrm{surf}}\hat{\mathcal{P}} = \left[\varepsilon + \mathrm{i}\eta - \hat{\mathcal{P}}\hat{H}^{\mathrm{surf}}\hat{\mathcal{P}} - \hat{\Xi}\left(\varepsilon'\right)\right]^{-1}. \tag{B.13}$$

Here $\left[\hat{\mathcal{P}}\hat{H}^{\mathrm{surf}}\hat{\mathcal{P}} + \hat{\Xi}\left(\varepsilon'\right)\right]$ can be understood as the Hamiltonian describing the acceptor part with considering the self-energy effect from the infinite part.

In principle, the energy-dependent self-energy matrix $\boldsymbol{\Xi}\left(\varepsilon'\right)$ can be calculated using surface Green's function techniques. In the application considered in this thesis, we have used a variant of this method, which approximates the self-energy by a constant imaginary part added to all AO energies centered at the boundary atoms of the explicitly treated acceptor part of the substrate. Thus, we have replaced the energy-dependent self-energy matrix $\boldsymbol{\Xi}\left(\varepsilon'\right)$ by a diagonal matrix $\boldsymbol{\Xi}$ with $\Xi_{kk} = -\mathrm{i}\delta/2$ if k belongs to an AO of the boundary atoms, otherwise $\Xi_{kk'} = 0$. Based on test calculations, $\delta = 1$ eV is used in this thesis.

As a result, the Fock matrix is no longer real symmetric but complex symmetric. We can calculate the right eigenvectors of

$$\begin{pmatrix} \tilde{\boldsymbol{F}}^{\mathrm{dd}} & \tilde{\boldsymbol{F}}^{\mathrm{da}} \\ \tilde{\boldsymbol{F}}^{\mathrm{ad}} & \tilde{\boldsymbol{F}}^{\mathrm{aa}} + \boldsymbol{\Xi} \end{pmatrix}.$$

Denoting the matrix of right eigenvectors by $\boldsymbol{U}$, the eigenvalue matrix by $\boldsymbol{\varepsilon}^{\mathrm{a}}$ and the overlap matrix of the eigenvectors by $\boldsymbol{S} = \boldsymbol{U}^{\mathrm{T}}\boldsymbol{U}$, we obtain the energy-dependent decay-width function

$$\Gamma\left(\varepsilon\right) = -2\Im\Sigma\left(\varepsilon\right) = -2\Im\left[\bar{\boldsymbol{F}}^{\mathrm{da}}\boldsymbol{U}\frac{1}{\boldsymbol{S}\left(\varepsilon - \boldsymbol{\varepsilon}^{\mathrm{a}}\right)}\boldsymbol{U}^{\mathrm{T}}\bar{\boldsymbol{F}}^{\mathrm{ad}}\right]. \tag{B.14}$$

Here $\bar{\boldsymbol{F}}^{\mathrm{da}}$ is obtained from the prediagonalization of $\tilde{\boldsymbol{F}}$.

In the dynamical simulations, the continuum of electronic acceptor states, which is implicitly contained in the continuous decay-width function $\Gamma\left(\varepsilon\right)$, is discretized and represented by a finite number (determined by test calculations) of acceptor states employing Eq. (2.13) as described in Ref. [39].

Chapter C

Derivation of equations of motion of the ML-MCTDH method

In this appendix, we provide a detailed derivation of equations of motion in the ML-MCTDH theory. As an example, we will concentrate on the two-layer framework. The extension to a more-layer MCTDH is straightforward.

In the ML-MCTDH theory, the wave function is expanded in a recursive and layered manner given by Eqs. (2.47), (2.77), (2.78), *etc.*:

$$\begin{aligned}
|\Psi(t)\rangle &= \sum_{\boldsymbol{J}} A_{\boldsymbol{J}}(t)\,|\Phi_{\boldsymbol{J}}(t)\rangle \\
&= \sum_{j_1=1}^{J_1}\cdots\sum_{j_M=1}^{J_M} A_{j_1\cdots j_M}(t)\prod_{m=1}^{M}\left|\varphi_{j_m}^{(m)}(t)\right\rangle, \\
\left|\varphi_{j_m}^{(m)}(t)\right\rangle &= \sum_{\boldsymbol{I}} B_{\boldsymbol{I}}^{(m\sim j_m)}(t)\left|U_{\boldsymbol{I}}^{(m)}(t)\right\rangle \\
&= \sum_{i_1=1}^{I_1}\cdots\sum_{i_{F(m)}}^{I_{F(m)}} B_{i_1\cdots i_{F(m)}}^{(m\sim j_m)}(t)\prod_{f=1}^{F(m)}\left|u_{i_f}^{(m,f)}(t)\right\rangle, \\
\left|u_{i_f}^{(m,f)}(t)\right\rangle &= \sum_{\boldsymbol{L}} C_{\boldsymbol{L}}^{\left(m,f\sim i_f\right)}(t)\left|\Xi_{\boldsymbol{L}}^{(m,i_f)}(t)\right\rangle \\
&= \sum_{l_1=1}^{L_1}\cdots\sum_{l_K(m,f)}^{L_K(m,f)} C_{l_1\cdots l_K(m,f)}^{\left(m,f\sim i_f\right)}(t)\prod_{k=1}^{K(m,f)}\left|\xi_{l_k}^{(m,f,k)}(t)\right\rangle, \\
&\cdots
\end{aligned}$$

In the two-layer MCTDH framework, an L2-SP function is expanded in an FCI-manner as

$$\begin{aligned}
\left|u_{i_f}^{(m,f)}(t)\right\rangle &= \sum_{\boldsymbol{L}} C_{\boldsymbol{L}}^{\left(m,f\sim i_f\right)}(t)\left|X_{\boldsymbol{L}}^{\left(m,i_f\right)}\right\rangle \\
&= \sum_{l_1=1}^{L_1}\cdots\sum_{l_K(m,f)}^{L_K(m,f)} C_{l_1\cdots l_K(m,f)}^{\left(m,f\sim i_f\right)}(t)\prod_{k=1}^{K(m,f)}\left|\chi_{l_k}^{(m,f,k)}\right\rangle. \qquad \text{(C.1)}
\end{aligned}$$

Here $K(m,f)$ is the total number of Cartesian (physical) DoF within the f-th L2-SP group which belongs to the m-th L1-SP group, $\left|\chi_{l_k}^{(m,f,k)}\right\rangle$ denotes the corresponding *time-independent* primitive (orthonormal) basis functions for the k-th DoF in the f-th L2-SP group of the m-th L1-SP group. Thus, the functional form for the application of the Dirac-Frenkel variational principle is given by Eqs. (2.47), (2.77) and (C.1).

In order to obtain the equations of motion for all expansion coefficients in different levels, $A_{\boldsymbol{J}}(t)$, $B_{\boldsymbol{I}}^{(m\sim j_m)}(t)$ and $C_{\boldsymbol{L}}^{\left(m,f\sim i_f\right)}(t)$, the Dirac-Frenkel variational principle [101, 102]

$$\langle \delta\Psi(t)|\,\hat{H}-\mathrm{i}\frac{\partial}{\partial t}\,|\Psi(t)\rangle=0$$

is applied. The variation of the wave function reads

$$\delta\,|\Psi(t)\rangle=\sum_{\boldsymbol{J}}\left(\delta A_{\boldsymbol{J}}(t)\,|\Phi_{\boldsymbol{J}}(t)\rangle+A_{\boldsymbol{J}}(t)\,\delta\,|\Phi_{\boldsymbol{J}}(t)\rangle\right). \tag{C.2}$$

The variation of the L1-configuration $\delta\,|\Phi_{\boldsymbol{J}}(t)\rangle$ in the second term can be calculated as

$$\begin{aligned}\sum_{\boldsymbol{J}}A_{\boldsymbol{J}}(t)\,\delta\,|\Phi_{\boldsymbol{J}}(t)\rangle&=\sum_{\boldsymbol{I}}A_{j_1\cdots j_M}(t)\,\delta\left(\prod_{m=1}^{M}\left|\varphi_{j_m}^{(m)}(t)\right\rangle\right)\\&=\sum_{m=1}^{M}\sum_{j_m=1}^{J_m}\left|G_{\mathrm{L1},j_m}^{(m)}(t)\right\rangle\delta\left|\varphi_{j_m}^{(m)}(t)\right\rangle\end{aligned}$$

thus reaching the variation of the L1-SP function $\delta\left|\varphi_{j_m}^{(m)}(t)\right\rangle$. Recursively, this variation can be calculated in a way similar to $\delta\,|\Psi(t)\rangle$ as

$$\delta\left|\varphi_{j_m}^{(m)}(t)\right\rangle=\sum_{\boldsymbol{I}}\left(\delta B_{\boldsymbol{I}}^{(m\sim j_m)}(t)\left|U_{\boldsymbol{I}}^{(m)}(t)\right\rangle+B_{\boldsymbol{I}}^{(m\sim j_m)}(t)\,\delta\left|U_{\boldsymbol{I}}^{(m)}(t)\right\rangle\right). \tag{C.3}$$

The variation of the L2-configuration $\delta\left|U_{\boldsymbol{I}}^{(m)}(t)\right\rangle$ in the second term is calculated as

$$\begin{aligned}\sum_{\boldsymbol{I}}B_{\boldsymbol{I}}^{(m\sim j_m)}(t)\,\delta\left|U_{\boldsymbol{I}}^{(m)}(t)\right\rangle&=\sum_{\boldsymbol{I}}B_{i_1\cdots i_{F(m)}}^{(m\sim j_m)}(t)\,\delta\left(\prod_{f=1}^{F(m)}\left|u_{i_f}^{(m,f)}(t)\right\rangle\right)\\&=\sum_{f=1}^{F(m)}\sum_{i_f=1}^{I_f}\left|G_{\mathrm{L2},i_f}^{(m\sim j_m,f)}(t)\right\rangle\delta\left|u_{i_f}^{(m,f)}(t)\right\rangle\end{aligned}$$

thus turning to the variation of the L2-SP function $\delta\left|u_{i_f}^{(m,f)}(t)\right\rangle$. Based on Eq. (C.1), it can be explicitly written as

$$\delta\left|u_{i_f}^{(m,f)}(t)\right\rangle=\sum_{\boldsymbol{L}}\delta C_{\boldsymbol{L}}^{\left(m,f\sim i_f\right)}(t)\left|X_{\boldsymbol{L}}^{\left(m,i_f\right)}\right\rangle. \tag{C.4}$$

Combining Eqs. (C.2), (C.3) and (C.4), the variation of the wave function in the two-layer MCTDH framework can be explicitly written as the variation with respect to all expansion coefficients in different levels

$$\begin{aligned}\delta\left|\Psi\left(t\right)\right\rangle = & \sum_{\boldsymbol{J}}\delta A_{\boldsymbol{J}}\left(t\right)\left|\Phi_{\boldsymbol{J}}\left(t\right)\right\rangle \\ & +\sum_{m=1}^{M}\sum_{j_m=1}^{J_m}\left|G^{(m)}_{\mathrm{L1},j_m}\left(t\right)\right\rangle\sum_{\boldsymbol{I}}\delta B^{(m\sim j_m)}_{\boldsymbol{I}}\left(t\right)\left|U^{(m)}_{\boldsymbol{I}}\left(t\right)\right\rangle \\ & +\sum_{m=1}^{M}\sum_{j_m=1}^{J_m}\left|G^{(m)}_{\mathrm{L1},j_m}\left(t\right)\right\rangle\sum_{f=1}^{F(m)}\sum_{i_f=1}^{I_f}\left|G^{(m\sim j_m,f)}_{\mathrm{L2},i_f}\left(t\right)\right\rangle \\ & \times\sum_{\boldsymbol{L}}\delta C^{\left(m,f\sim i_f\right)}_{\boldsymbol{L}}\left(t\right)\left|X^{\left(m,i_f\right)}_{\boldsymbol{L}}\right\rangle. \end{aligned} \tag{C.5}$$

Similarly, the time-derivative of the wave function is given by

$$\begin{aligned}\left|\dot{\Psi}\left(t\right)\right\rangle = & \sum_{\boldsymbol{J}}\dot{A}_{\boldsymbol{J}}\left(t\right)\left|\Phi_{\boldsymbol{J}}\left(t\right)\right\rangle \\ & +\sum_{m=1}^{M}\sum_{j_m=1}^{J_m}\left|G^{(m)}_{\mathrm{L1},j_m}\left(t\right)\right\rangle\sum_{\boldsymbol{I}}\dot{B}^{(m\sim j_m)}_{\boldsymbol{I}}\left(t\right)\left|U^{(m)}_{\boldsymbol{I}}\left(t\right)\right\rangle \\ & +\sum_{m=1}^{M}\sum_{j_m=1}^{J_m}\left|G^{(m)}_{\mathrm{L1},j_m}\left(t\right)\right\rangle\sum_{f=1}^{F(m)}\sum_{i_f=1}^{I_f}\left|G^{(m\sim j_m,f)}_{\mathrm{L2},i_f}\left(t\right)\right\rangle\sum_{\boldsymbol{L}}\dot{C}^{\left(m,f\sim i_f\right)}_{\boldsymbol{L}}\left(t\right)\left|X^{\left(m,i_f\right)}_{\boldsymbol{L}}\right\rangle. \end{aligned} \tag{C.6}$$

Recalling the constraints given by Eqs. (2.53) and (2.56) and extending these constraints to the L2-SP functions as

$$\left\langle u^{(m,f)}_{i_f}\left(0\right)\middle|u^{(m,f)}_{i'_f}\left(0\right)\right\rangle = \delta_{i_f i'_f} \tag{C.7}$$

and

$$\left\langle u^{(m,f)}_{i_f}\left(t\right)\middle|\dot{u}^{(m,f)}_{i'_f}\left(t\right)\right\rangle = 0, \tag{C.8}$$

the equations of motion for the expansion coefficients are obtained as follows:

$$\mathrm{i}\dot{A}_{\boldsymbol{J}}\left(t\right) = \left\langle\Phi_{\boldsymbol{J}}\left(t\right)\right|\hat{H}\left(t\right)\left|\Psi\left(t\right)\right\rangle, \tag{C.9}$$

$$\begin{aligned}\mathrm{i}\sum_{j'_m=1}^{J_m}\rho^{(m)}_{\mathrm{L1},j_m j'_m}\left(t\right)\dot{B}^{(m\sim j'_m)}_{\boldsymbol{I}}\left(t\right) = & \left\langle U^{(m)}_{\boldsymbol{I}}\left(t\right)\right|\left[1-\hat{P}^{(m)}_{\mathrm{L1}}\left(t\right)\right] \\ & \times\sum_{j'_m=1}^{J_m}\left\langle\hat{H}\right\rangle^{(m)}_{\mathrm{L1},j_m j'_m}\left(t\right)\left|\varphi^{(m)}_{j'_m}\left(t\right)\right\rangle, \end{aligned} \tag{C.10}$$

$$\mathrm{i}\sum_{i'_f=1}^{I_f}\rho^{(m,f)}_{\mathrm{L2},i_f i'_f}\left(t\right)\dot{C}^{\left(m,f\sim i'_f\right)}_{\boldsymbol{L}}\left(t\right) = \left\langle X^{(m,f)}_{\boldsymbol{L}}\right|\left[1-\hat{P}^{(m,f)}_{\mathrm{L2}}\left(t\right)\right]\sum_{i'_f=1}^{I_f}\left\langle\hat{H}\right\rangle^{(m,f)}_{\mathrm{L2},i_f i'_f}\left(t\right)\left|\chi^{(m,f)}_{i'_f}\right\rangle. \tag{C.11}$$

The above three equations are equivalent to Eqs. (2.79), (2.80) and (2.81).

The L1 single-hold function, L1 mean-field operator, L1 reduce density matrix and L1 projection operator are defined in Eqs. (2.59), (2.65), (2.66) and (2.68), respectively. The corresponding L2 notations are defined as follows: the L2 *single-hole* function

$$G^{(m\sim j_m,f)}_{\mathrm{L2},i'_f}(t)=\sum_{i_1=1}^{I_1}\cdots\sum_{i_{f-1}=1}^{I_{f-1}}\sum_{i_{f+1}=1}^{I_{f+1}}\cdots\sum_{i_{F(m)}=1}^{I_{F(m)}}B^{(m\sim j_m)}_{i_1\cdots i_{f-1}i'_f i_{f+1}\cdots i_{F(m)}}(t)\\ \times\left|u^{(m,1)}_{i_1}(t)\right\rangle\cdots\left|u^{(m,f-1)}_{i_{f-1}}(t)\right\rangle\left|u^{(m,f+1)}_{i_{f+1}}(t)\right\rangle\cdots\left|u^{(m,F(m))}_{i_{F(m)}}(t)\right\rangle, \tag{C.12}$$

the L2 *mean-field operator*

$$\left\langle\hat{H}\right\rangle^{(m,f)}_{\mathrm{L2},i_f i'_f}(t)=\sum_{j_m=1}^{J_m}\sum_{j'_m=1}^{J_m}\left\langle G^{(m\sim j_m,f)}_{\mathrm{L2},i_f}(t)\right|\left\langle\hat{H}\right\rangle^{(m)}_{\mathrm{L1},j_m j'_m}(t)\left|G^{(m\sim j'_m,f)}_{\mathrm{L2},i'_f}(t)\right\rangle, \tag{C.13}$$

the L2 reduced density matrix

$$\rho^{(m,f)}_{\mathrm{L2},i_f i'_f}(t)=\sum_{j_m=1}^{J_m}\sum_{j'_m=1}^{J_m}\rho^{(m)}_{\mathrm{L1},j_m j'_m}(t)\left\langle G^{(m\sim j_m,f)}_{\mathrm{L2},i_f}(t)\right|G^{(m\sim j'_m,f)}_{\mathrm{L2},i'_f}(t)\Big\rangle \tag{C.14}$$

and the projection operator onto the f-th L2-SP space in the m-th L1-SP space

$$\hat{P}^{(m,f)}_{\mathrm{L2}}(t)=\sum_{i_f=1}^{I_f}\left|u^{(m,f)}_{i_f}(t)\right\rangle\left\langle u^{(m,f)}_{i_f}(t)\right|. \tag{C.15}$$

Furthermore, the following equalities are used in the derivation above:

$$\sum_{\boldsymbol{J}}\left\langle G^{(m)}_{\mathrm{L1},j_m}(t)\right|\Phi_{\boldsymbol{J}}(t)\Big\rangle\Big\langle\Phi_{\boldsymbol{J}}(t)\Big|=\hat{P}^{(m)}_{\mathrm{L1}}(t)\left\langle G^{(m)}_{\mathrm{L1},j_m}(t)\right|,$$

$$\sum_{\boldsymbol{I}}\left\langle G^{(m\sim j_m,f)}_{\mathrm{L2},i_f}(t)\right|U^{(m)}_{\boldsymbol{I}}(t)\Big\rangle\left\langle U^{(m)}_{\boldsymbol{I}}(t)\right|=\hat{P}^{(m,f)}_{\mathrm{L2}}(t)\left\langle G^{(m\sim j_m,f)}_{\mathrm{L2},i_f}(t)\right|$$

and

$$\left[1-\sum_{\boldsymbol{I}}\left|U^{(m)}_{\boldsymbol{I}}(t)\right\rangle\left\langle U^{(m)}_{\boldsymbol{I}}(t)\right|\right]\hat{P}^{(m)}_{\mathrm{L1}}=0.$$

Chapter D

Results for further alizarin - titanium oxide systems

In this appendix, we will present results for further alizarin-TiO_2 systems which are not shown in Chapter 3.

D.1 Results for alizarin - titanium oxide systems with different sizes of semiconductor clusters

In this section, we will present results for several alizarin-TiO_2 complexes with different sizes of TiO_2 cluster that have not been shown in Chapter 3. These titanium-oxide substrate are $(TiO_2)_{10}(H_2O)_{18}$, $(TiO_2)_{20}(H_2O)_{28}$, $(TiO_2)_{30}(H_2O)_{38}$, $(TiO_2)_{40}(H_2O)_{48}$, $(TiO_2)_{18}(H_2O)_{30}$ and $(TiO_2)_{36}(H_2O)_{44}$. The structures of the corresponding alizarin-TiO_2 complexes are depicted in Fig. D.1 (except alizarin-$(TiO_2)_{10}(H_2O)_{18}$ which was already shown in Fig. 3.1 (a)).

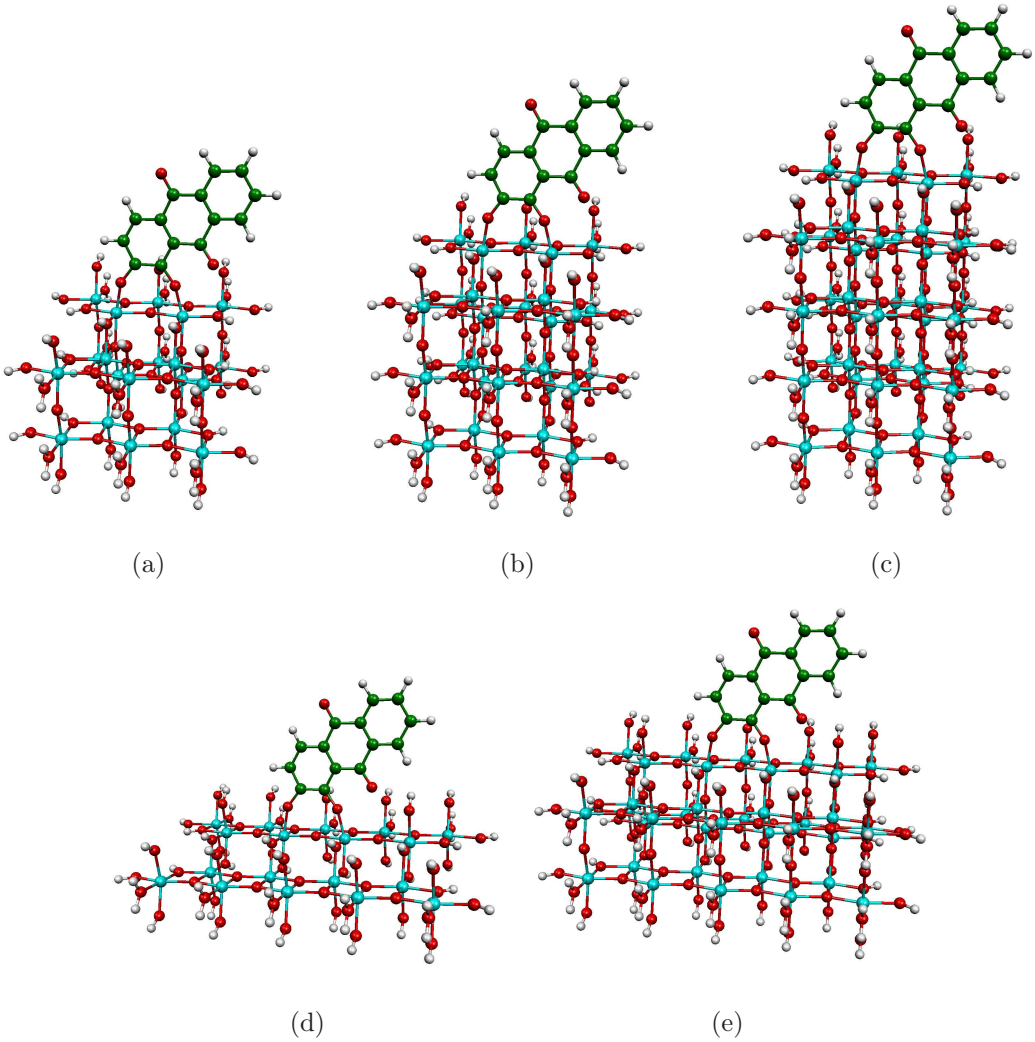

Figure D.1: Complexes of alizarin with titanium oxide clusters of different sizes: (a) $(TiO_2)_{20}(H_2O)_{28}$ (2 layers of 10 TiO_2 units), (b) $(TiO_2)_{30}(H_2O)_{38}$ (3 layers of 10 TiO_2 units), (c) $(TiO_2)_{40}(H_2O)_{48}$ (4 layers of 10 TiO_2 units), (d) $(TiO_2)_{18}(H_2O)_{30}$ (1 layer of 18 TiO_2 units) and (e) $(TiO_2)_{36}(H_2O)_{44}$ (2 layers of 18 TiO_2 units).

Fig. D.2 shows energy-level schemes for all alizarin-TiO_2 systems except alizarin-$(TiO_2)_{54}(H_2O)_{58}$ (which is shown in Fig. 3.2). From these energy-level schemes of the seven investigated alizarin-TiO_2 complexes (Figs. D.2 and 3.2), we can observe some interesting features as follows.

For all systems, the energies of the MO of isolated TiO_2 clusters exhibit a dense level structure with a valence and a conduction band separate by a band gap. The density of state increases with the size of the TiO_2 cluster. The calculated value for the band gap is not clearly affected by the size of the cluster. In all isolated clusters, the lowest unoccupied orbitals have predominant contribution from the oxygen atoms of saturation groups. The value of band gap calculated based on the "true" lower edge of the conduction band (defined by the energy of the lowest unoccupied 3d orbital of the titanium oxides, as defined in Section 3.3) does not clearly depend on the size of the cluster.

One or two energy levels are introduced in the lower part of the band gap through the adsorption of the alizarin molecule. In particular, the HOMO of the overall system can be related to the HOMO of the isolated alizarin molecule. It is located in the band gap during the adsorption and thus retain its discrete structure in the complex. The overlap between the HOMO of the complex and the projected donor orbital that is associated with the HOMO of the alizarin is larger than 0.80 for all systems. On the other hand, the lowest unoccupied levels of alizarin are located energetically in the conduction band of TiO_2. These levels are dissolved in the dense manifold of conduction-band levels in the complex. The correlation scheme between the projected donor orbital that is associated with the LUMO of the alizarin (which is chosen as the donor state of the ET reaction) and the dense manifold of unoccupied orbitals of the complex is similar in all systems investigated.

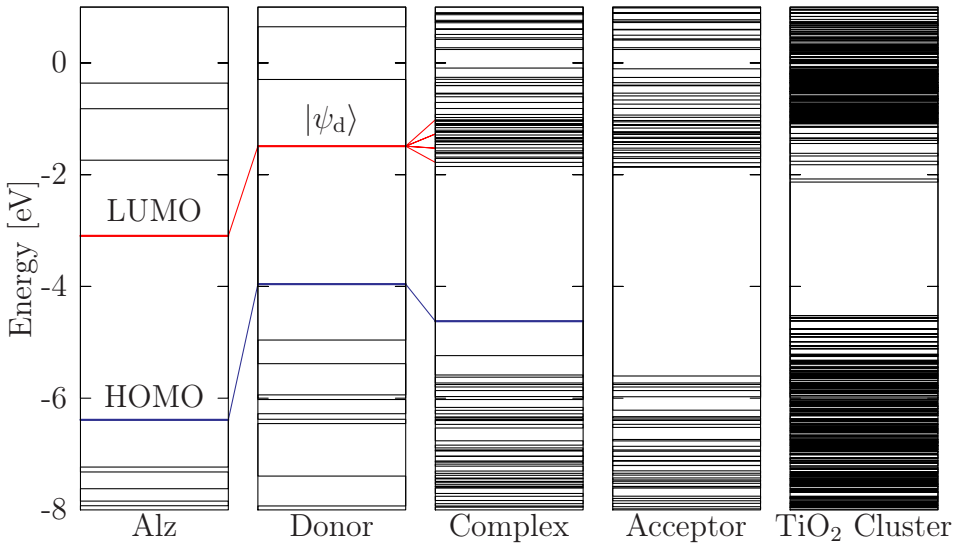
0
-2
-4
-6
-8
Energy [eV]
LUMO
HOMO
$|\psi_d\rangle$
Alz
Donor
Complex
Acceptor
TiO_2 Cluster

(a)

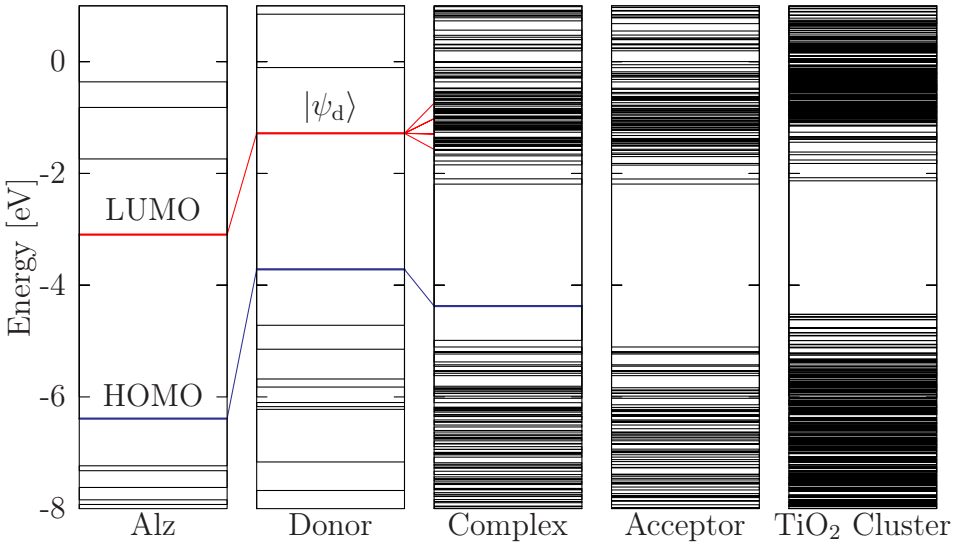
0
-2
-4
-6
-8
Energy [eV]
LUMO
HOMO
$|\psi_d\rangle$
Alz
Donor
Complex
Acceptor
TiO_2 Cluster

(b)

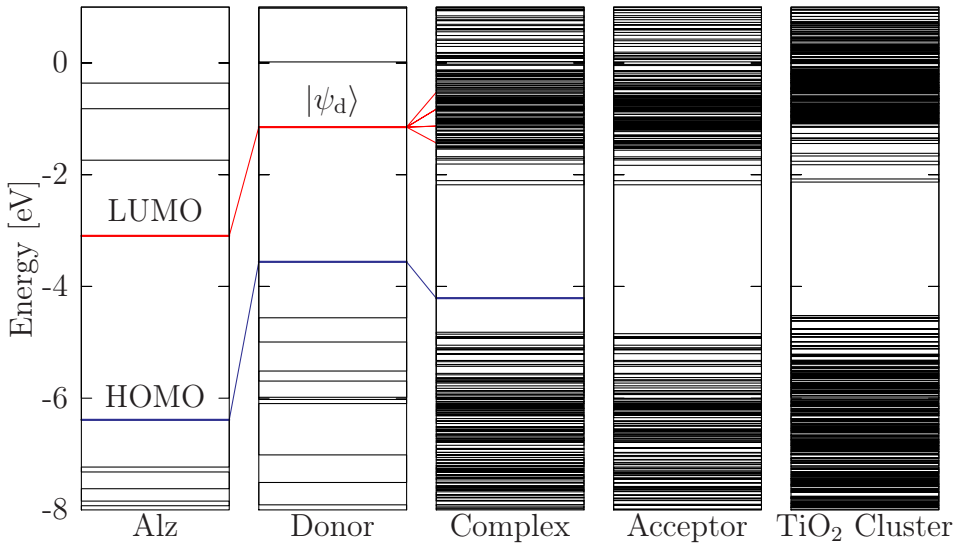
0
-2
-4
-6
-8
Energy [eV]
LUMO
HOMO
$|\psi_d\rangle$
Alz
Donor
Complex
Acceptor
TiO_2 Cluster

(c)

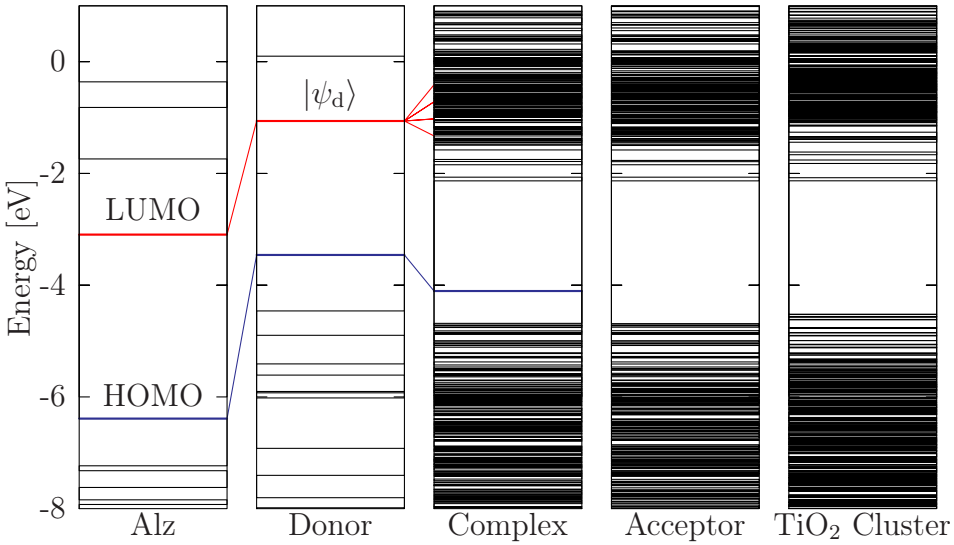
0
-2
-4
-6
-8
Energy [eV]
LUMO
HOMO
$|\psi_d\rangle$
Alz
Donor
Complex
Acceptor
TiO_2 Cluster

(d)

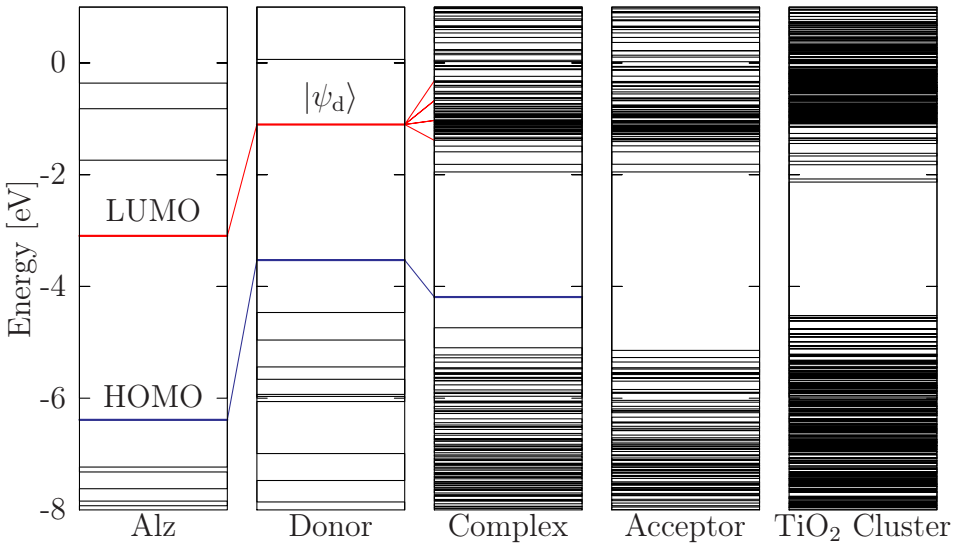

(e)

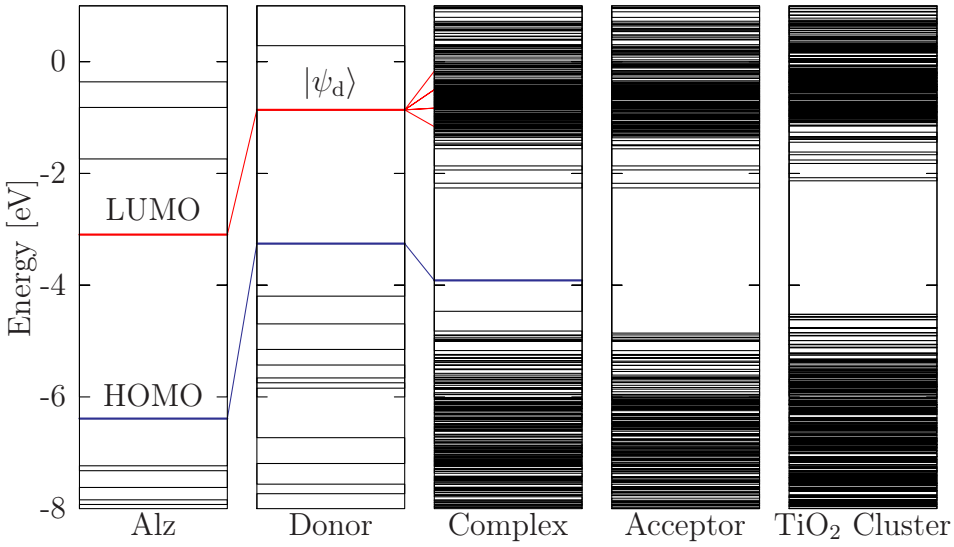

(f)

Figure D.2: Energy-level schemes of the alizarin-TiO_2 complexes studied in this thesis: (a) alizarin-$(TiO_2)_{10}(H_2O)_{18}$, (b) alizarin-$(TiO_2)_{20}(H_2O)_{28}$, (c) alizarin-$(TiO_2)_{30}(H_2O)_{38}$, (d) alizarin-$(TiO_2)_{40}(H_2O)_{48}$, (e) alizarin-$(TiO_2)_{18}(H_2O)_{30}$ and (f) alizarin-$(TiO_2)_{36}(H_2O)_{44}$ (*cf.* Fig. 3.2 for detailed descriptions and legends).

Fig. D.3 shows the modulus of the donor-acceptor coupling matrix elements for all alizarin-TiO_2 systems except alizarin-$(TiO_2)_{54}(H_2O)_{58}$ (which is shown in Fig. 3.6). For each system, the energy-dependent decay-width function is illustrated as well, which can characterize the donor-acceptor coupling for an extended substrate.

The complicated structure exhibited by the distribution of donor-acceptor coupling matrix elements, as a result of the first-principles based model, is similar in all investigated systems. For each system, the position of the peak of the energy-dependent decay-width function is in good agreement with the positions of the acceptor states with largest coupling to the donor state. Fig. D.3 and Fig. 3.6 show that the two important parameters for the electron injection dynamics, *i.e.*, the location of the donor level relative to the conduction-band minimum as well as the strength and the distribution of the donor-acceptor coupling, are similar in all systems.

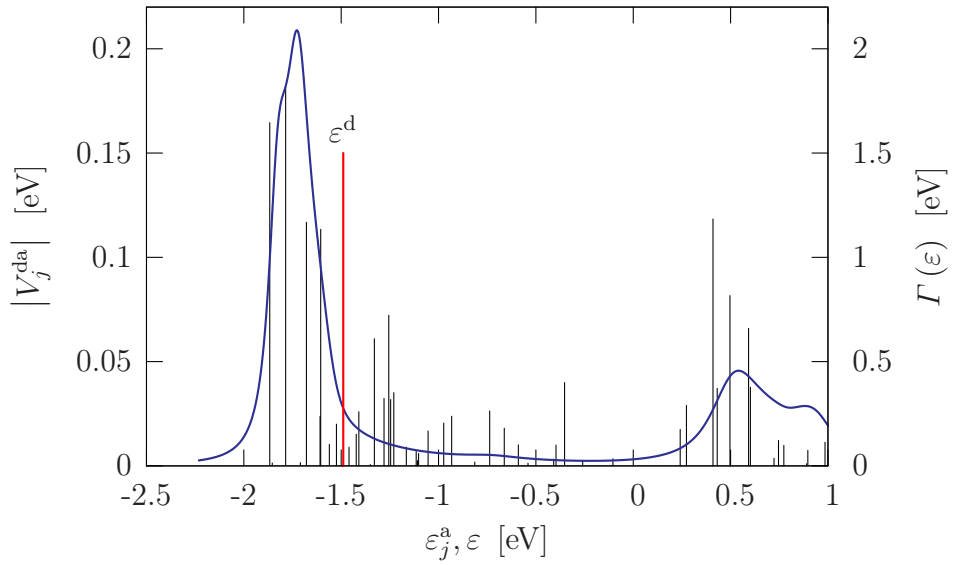
0.2
0.15
0.1
0.05
0
2
1.5
1
0.5
0
-2.5
-2
-1.5
-1
-0.5
0
0.5
1
ε^{d}
$|V_j^{\mathrm{da}}|$ [eV]
$\Gamma(\varepsilon)$ [eV]
$\varepsilon_j^{\mathrm{a}}, \varepsilon$ [eV]

(a)

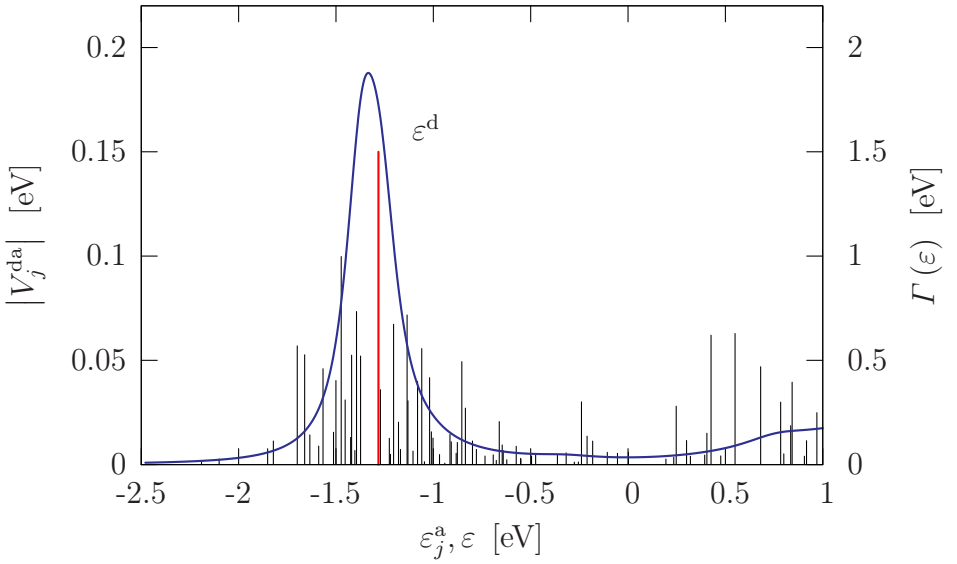
0.2
0.15
0.1
0.05
0
2
1.5
1
0.5
0
-2.5
-2
-1.5
-1
-0.5
0
0.5
1
ε^{d}
$|V_j^{\mathrm{da}}|$ [eV]
$\Gamma(\varepsilon)$ [eV]
$\varepsilon_j^{\mathrm{a}}, \varepsilon$ [eV]

(b)

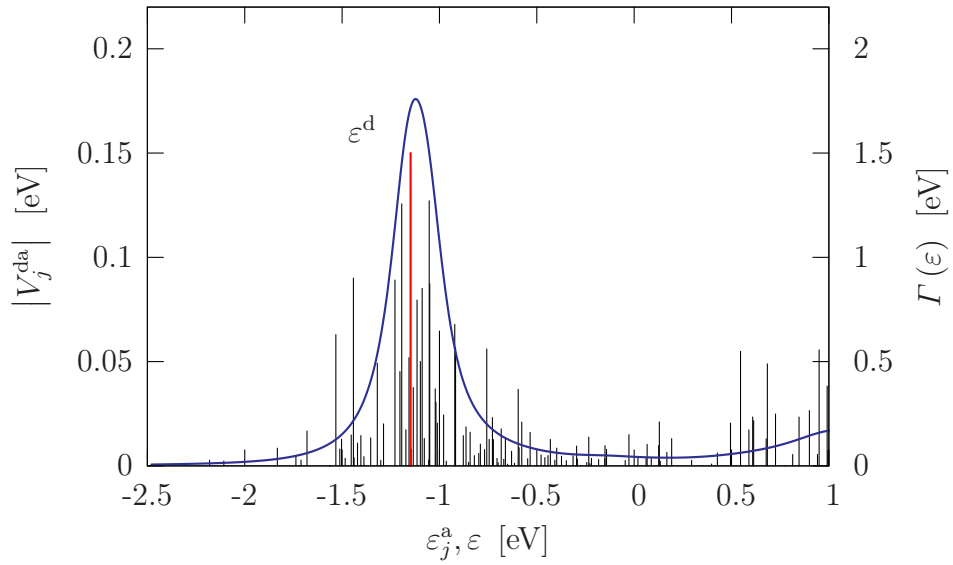
0.2
0.15
0.1
0.05
0
2
1.5
1
0.5
0
-2.5
-2
-1.5
-1
-0.5
0
0.5
1
ε^{d}
$|V_j^{\mathrm{da}}|$ [eV]
$\Gamma(\varepsilon)$ [eV]
$\varepsilon_j^{\mathrm{a}}, \varepsilon$ [eV]

(c)

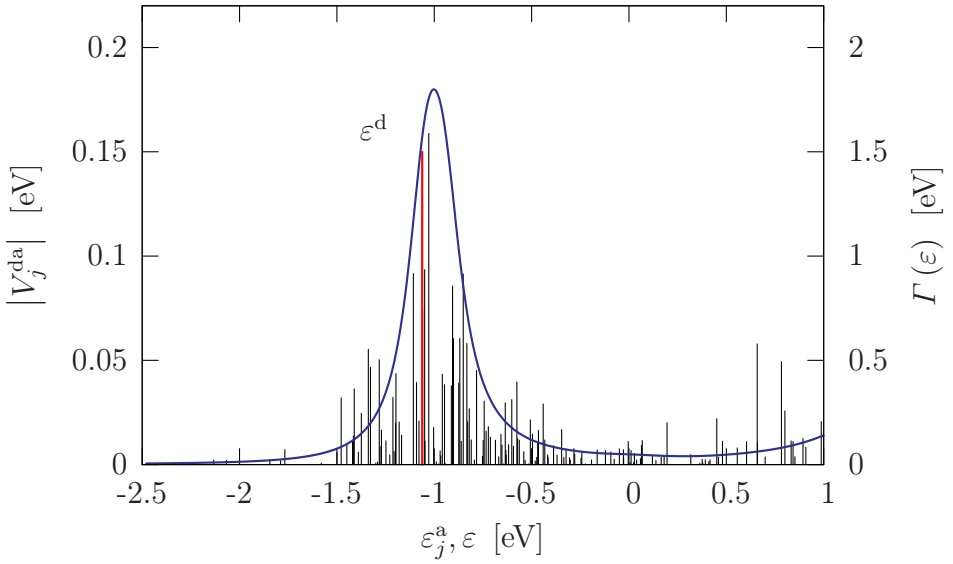
0.2
0.15
0.1
0.05
0
2
1.5
1
0.5
0
-2.5
-2
-1.5
-1
-0.5
0
0.5
1
ε^{d}
$|V_j^{\mathrm{da}}|$ [eV]
$\Gamma(\varepsilon)$ [eV]
$\varepsilon_j^{\mathrm{a}}, \varepsilon$ [eV]

(d)

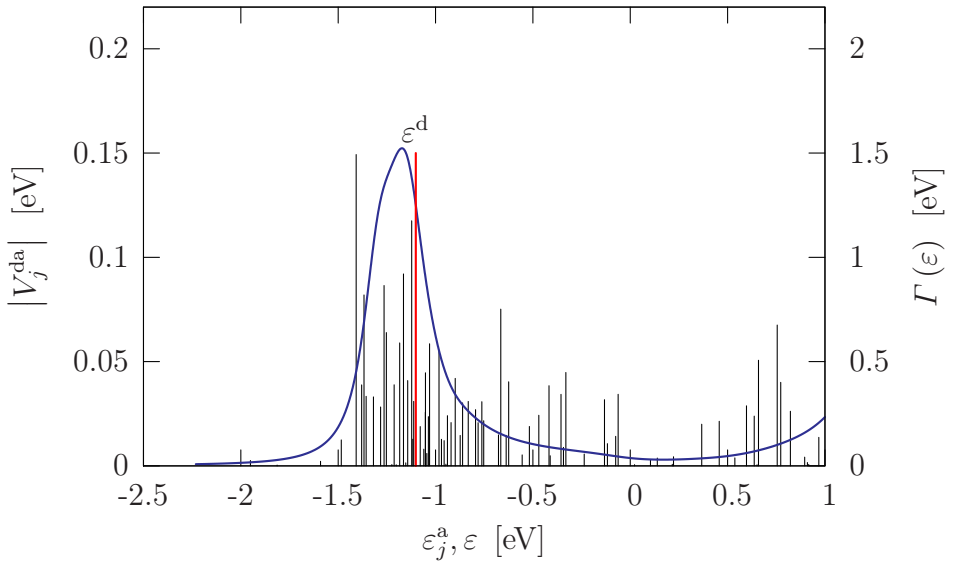

(e)

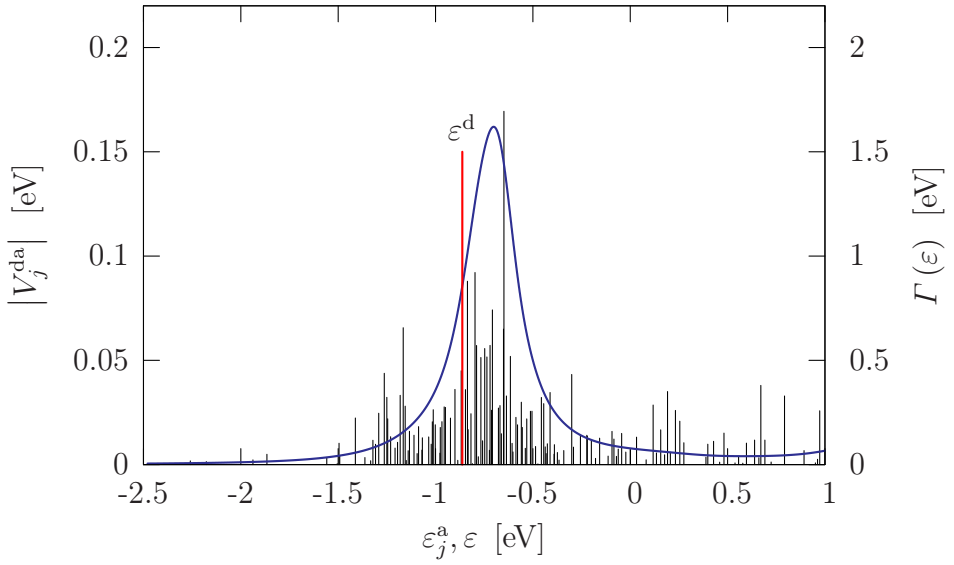

(f)

Figure D.3: Donor-acceptor coupling and the decay-width functions of the alizarin-TiO_2 complexes studed in this thesis: (a) alizarin-$(TiO_2)_{10}(H_2O)_{18}$, (b) alizarin-$(TiO_2)_{20}(H_2O)_{28}$, (c) alizarin-$(TiO_2)_{30}(H_2O)_{38}$, (d) alizarin-$(TiO_2)_{40}(H_2O)_{48}$, (e) alizarin-$(TiO_2)_{18}(H_2O)_{30}$ and (f) alizarin-$(TiO_2)_{36}(H_2O)_{44}$ (*cf.* Fig. 3.6 for detailed descriptions and legends).

Figs. D.4 - D.9 show the results of dynamical simulations for the population of the donor state after photoexcitation for the above mentioned six dye-semiconductor systems.

In all systems, the initial decay of the population of the donor state reveals an ultrafast injection of the electron from the donor state localized in the adsorbate (dye) into the quasi-continuum of acceptor states localized in the TiO_2 substrate on a similar timescale of about $5 \sim 10$ fs femtoseconds, which is similar to the result for alizarin-$(TiO_2)_{54}(H_2O)_{58}$ as shown in Fig. 3.9. There are other findings similar to the results for alizarin-$(TiO_2)_{54}(H_2O)_{58}$: pronounced electronic coherence effects, the overall weak effect of electronic-vibrational coupling on the ET dynamics, and the finite-size effect of the TiO_2 cluster. In particular, all systems exhibit very similar results of ET dynamics with mimicking the electron injection process at an extended TiO_2 substrate.

Figs. D.4 - D.9 and 3.9 show clear dependence of ET dynamics on the size of the semiconductor cluster. As we have discussed in Fig. 3.11, an increase of the number of (101) layers of the TiO_2 substrate does not noticeably affect the intensity of recurrences in the population dynamics but results in an nearly proportional increase of the recurrence period (which can be due to the reflection at the boundaries). On the other hand, an increase of the lateral size of the clusters results in a smaller intensity of the recurrences but has negligible effect on the recurrence period.

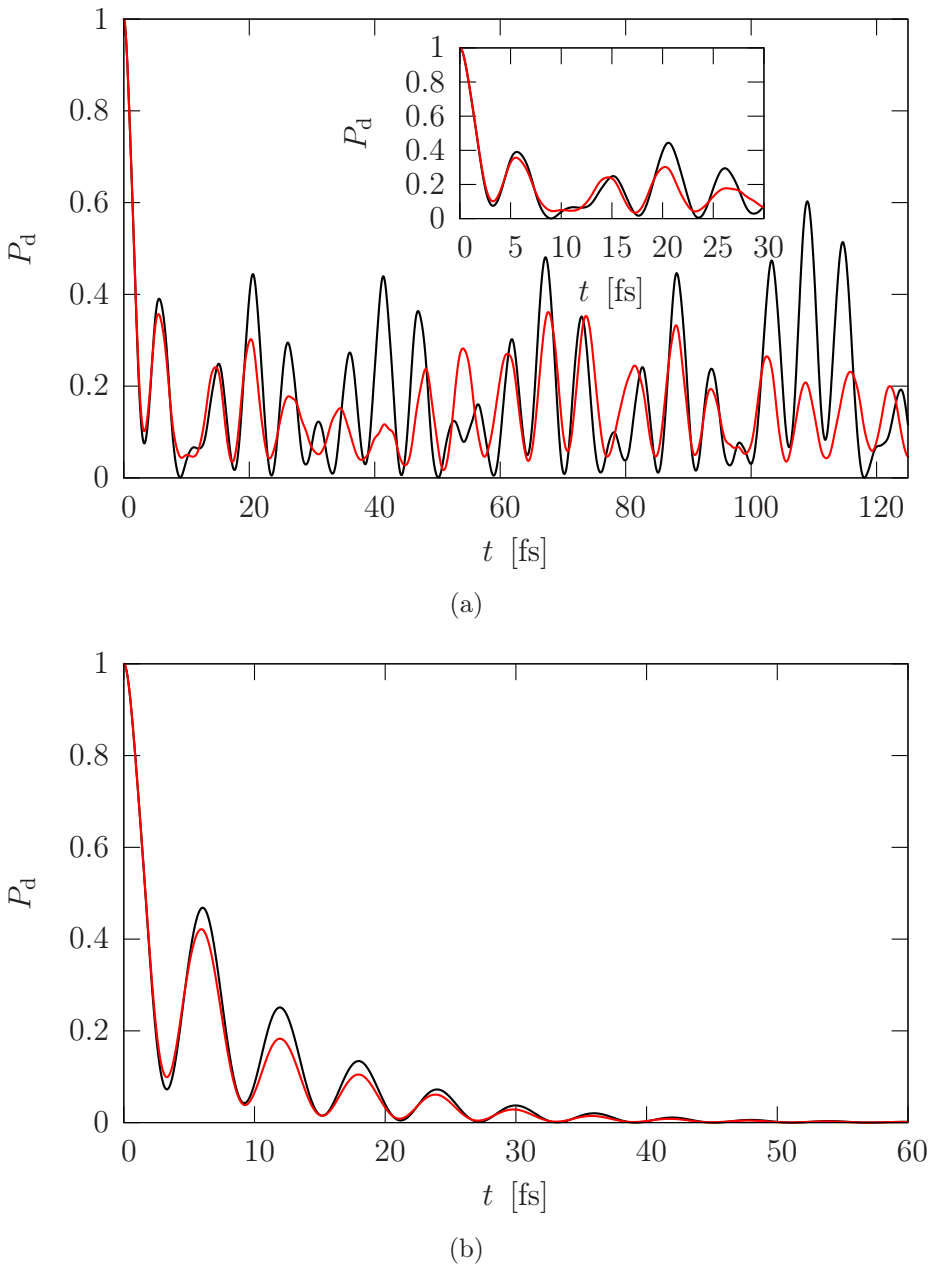

Figure D.4: Population dynamics of the donor state after photoexcitation in the alizarin-TiO_2 system. Shown are results obtained (a) for the finite $(TiO_2)_{10}$ substrate and (b) for the model of an infinite TiO_2 surface. Both results with vibronic coupling (red lines) and without vibronic coupling (black lines) are depicted.

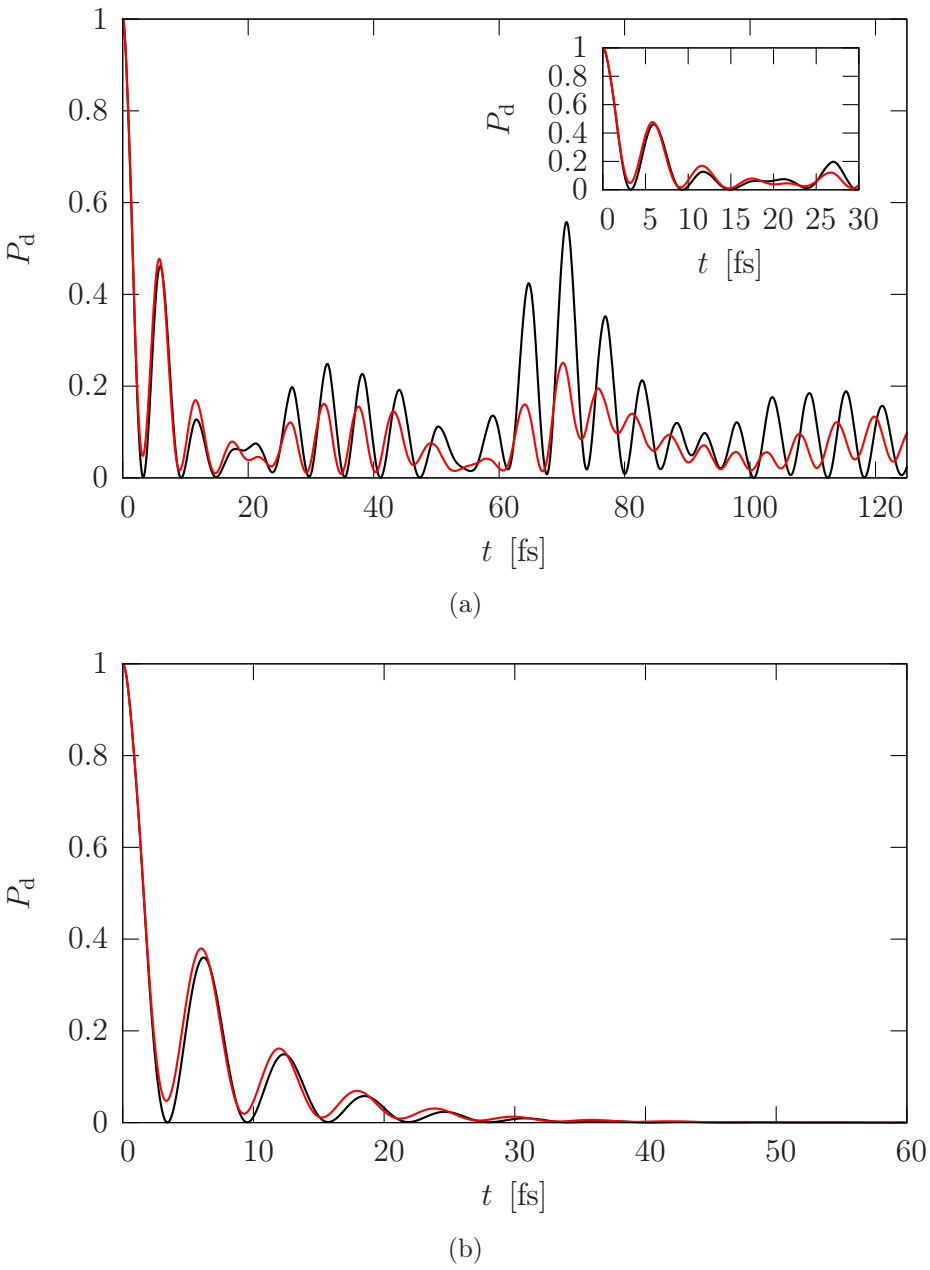

Figure D.5: Population dynamics of the donor state after photoexcitation in the alizarin-TiO_2 system. Shown are results obtained (a) for the finite $(TiO_2)_{20}$ substrate and (b) for the model of an infinite TiO_2 surface. Both results with vibronic coupling (red lines) and without vibronic coupling (black lines) are depicted.

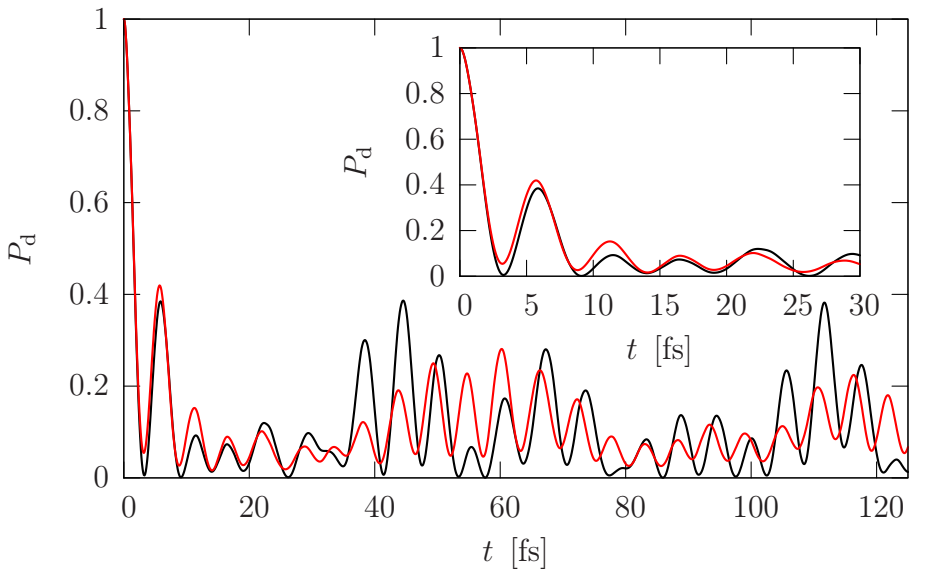

(a)

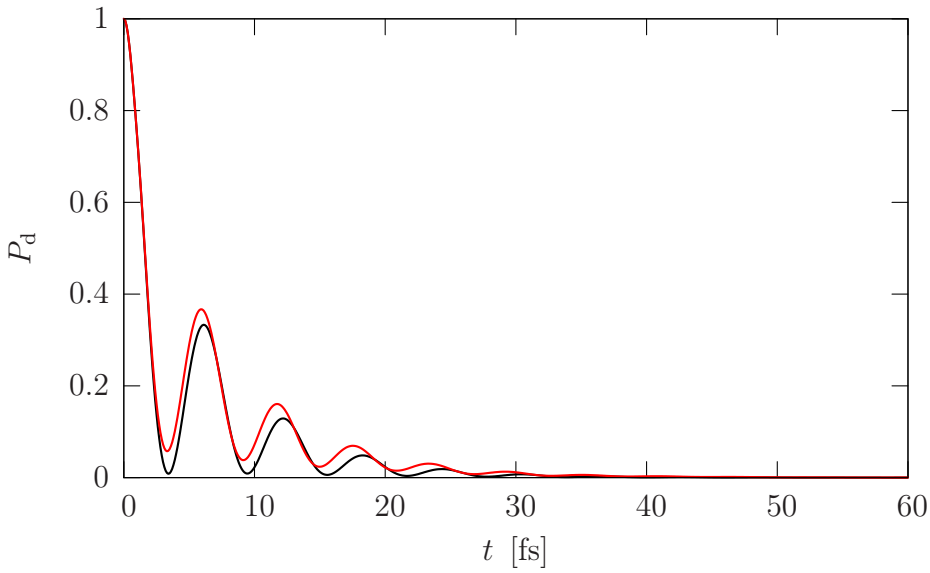

(b)

Figure D.6: Population dynamics of the donor state after photoexcitation in the alizarin-TiO_2 system. Shown are results obtained (a) for the finite $(TiO_2)_{30}$ substrate and (b) for the model of an infinite TiO_2 surface. Both results with vibronic coupling (red lines) and without vibronic coupling (black lines) are depicted.

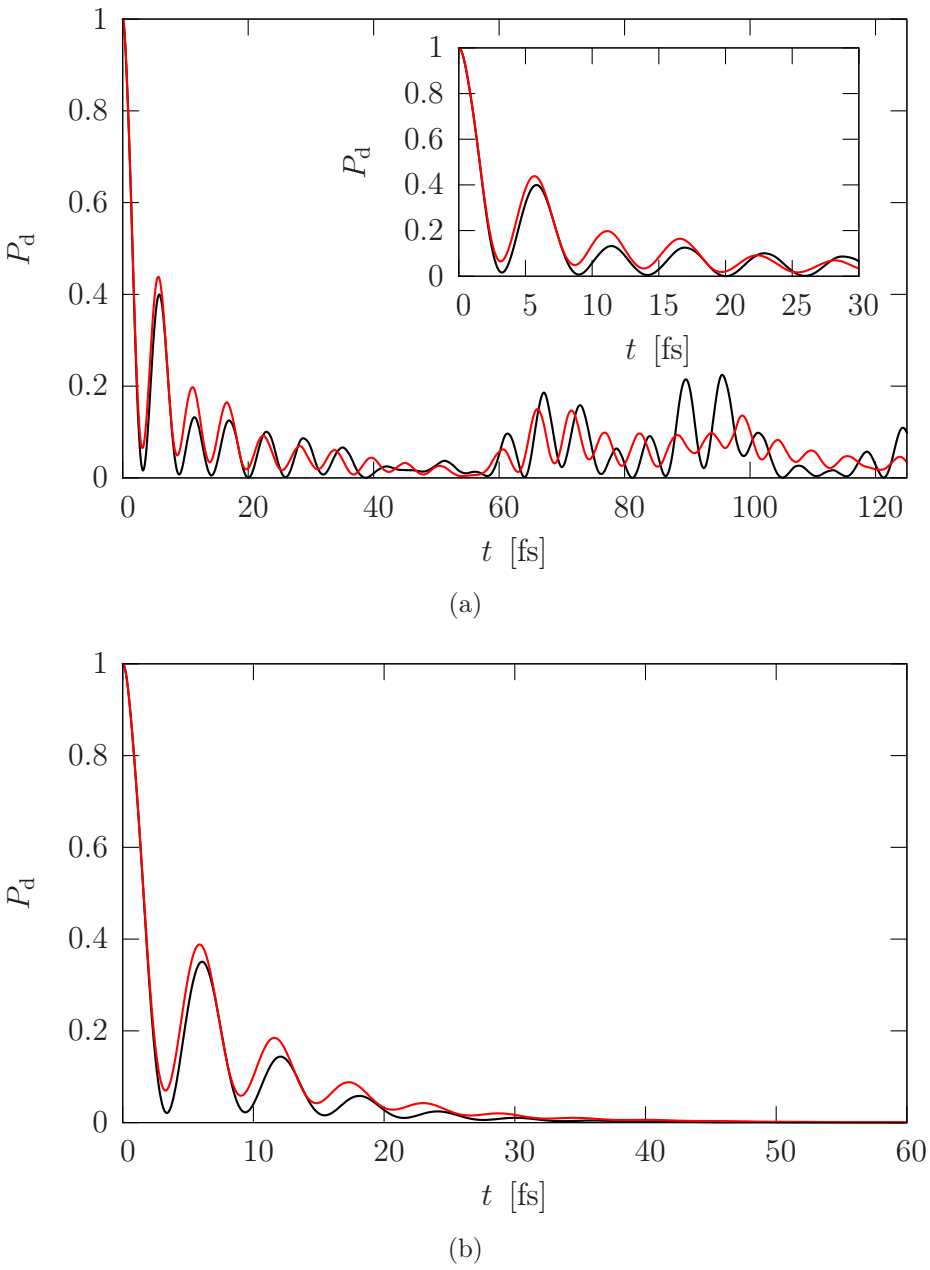

Figure D.7: Population dynamics of the donor state after photoexcitation in the alizarin-TiO_2 system. Shown are results obtained (a) for the finite $(TiO_2)_{40}$ substrate and (b) for the model of an infinite TiO_2 surface. Both results with vibronic coupling (red lines) and without vibronic coupling (black lines) are depicted.

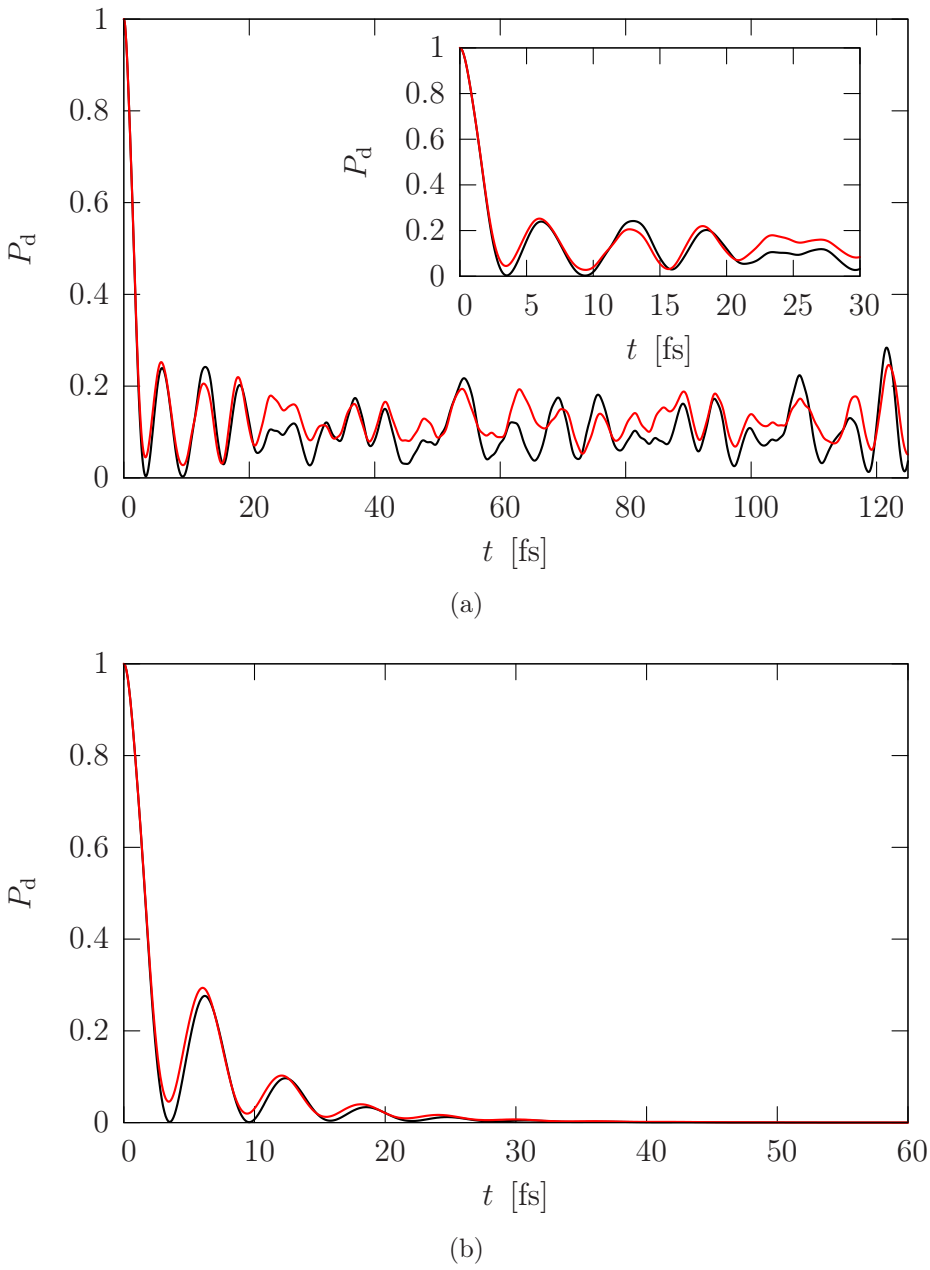

Figure D.8: Population dynamics of the donor state after photoexcitation in the alizarin-TiO_2 system. Shown are results obtained (a) for the finite $(TiO_2)_{18}$ substrate and (b) for the model of an infinite TiO_2 surface. Both results with vibronic coupling (red lines) and without vibronic coupling (black lines) are depicted.

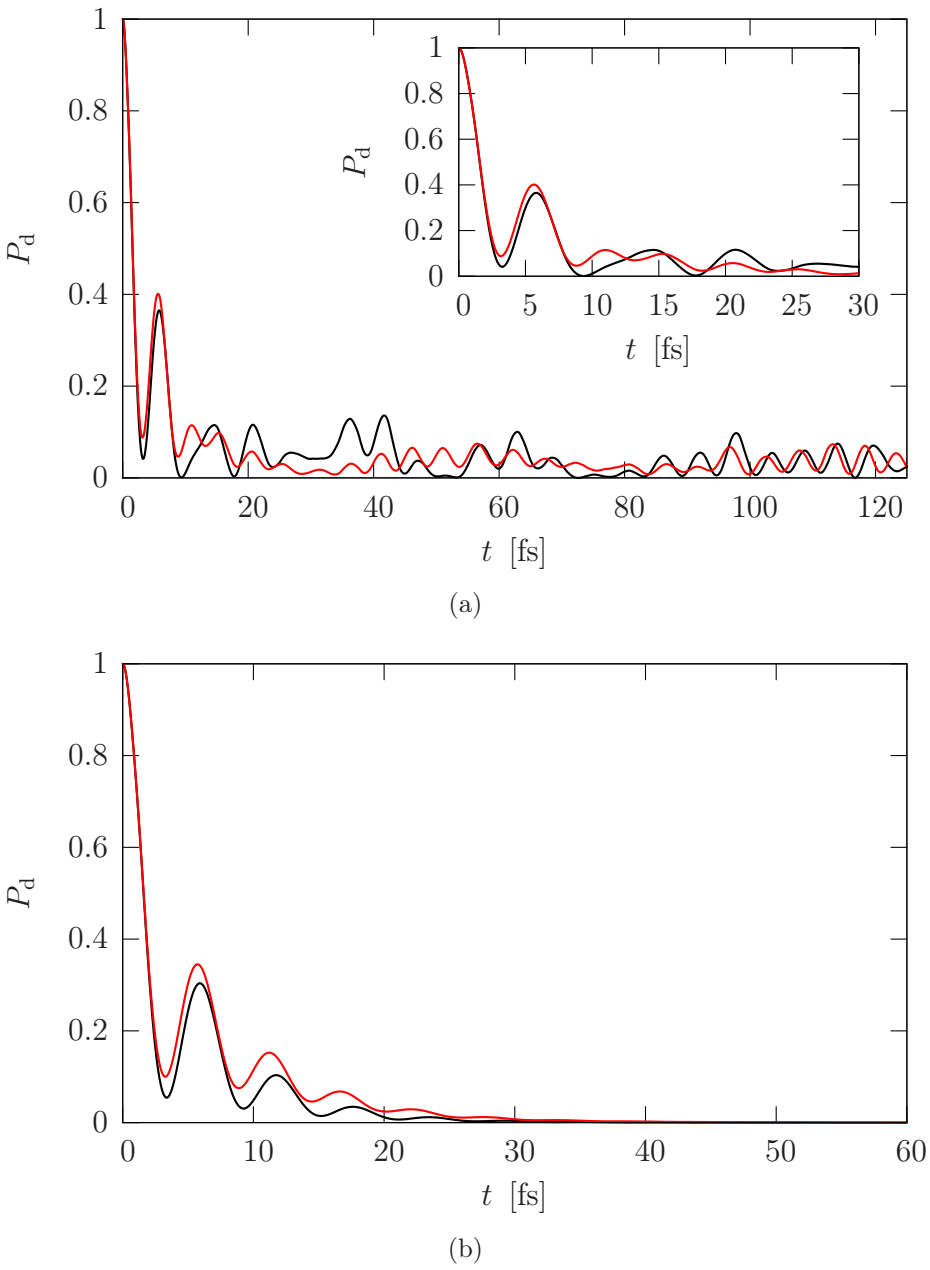

Figure D.9: Population dynamics of the donor state after photoexcitation in the alizarin-TiO_2 system. Shown are results obtained (a) for the finite $(TiO_2)_{36}$ substrate and (b) for the model of an infinite TiO_2 surface. Both results with vibronic coupling (red lines) and without vibronic coupling (black lines) are depicted.

D.2 Results of a model study for alizarin - titanium oxide complexes with larger donor-acceptor distances

In Section 3.7, we have discussed the results of five alizarin-$(TiO_2)_{54}(H_2O)_{58}$ systems with extracting the distance between the alizarin adsorbate and the TiO_2 substrate. Here we show the original energy-level schemes of these five complexes in Fig. D.10 and the donor-acceptor coupling schemes in Fig. D.11. Furthermore, Fig. D.12 shows the population dynamics of the donor state after photoexcitation for systems with the alizarin adsorbate 0.4 Å and 0.5 Å away from its equilibrium position to the TiO_2 substrate along the (100) direction.

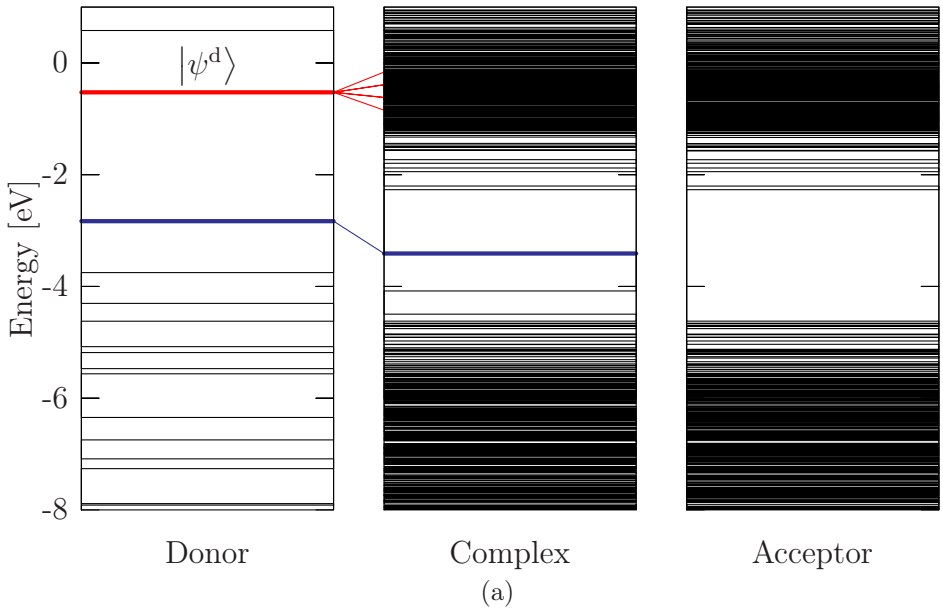
0
-2
-4
-6
-8
Energy [eV]
$|\psi^{\mathrm{d}}\rangle$
Donor
Complex
Acceptor

(a)

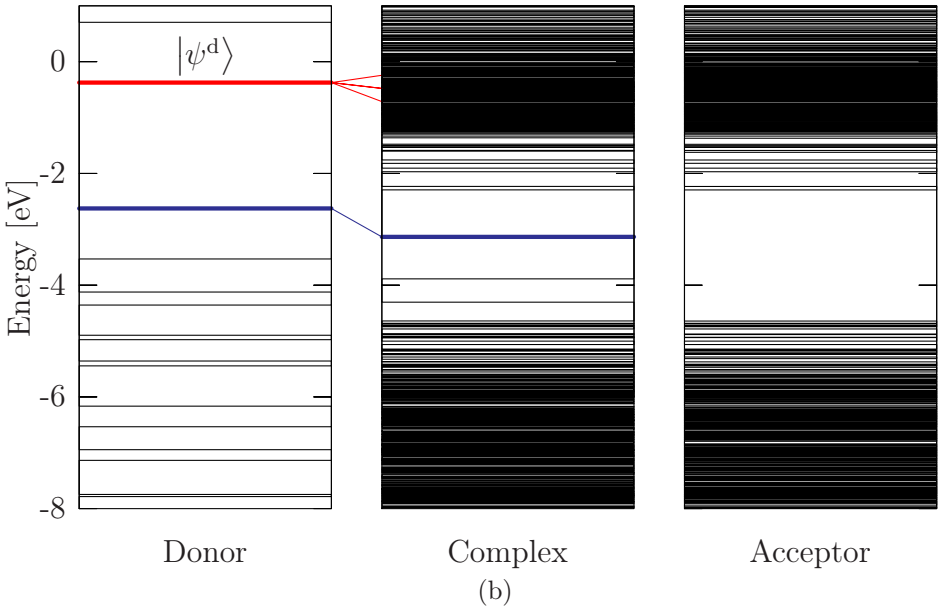
0
-2
-4
-6
-8
Energy [eV]
$|\psi^{\mathrm{d}}\rangle$
Donor
Complex
Acceptor

(b)

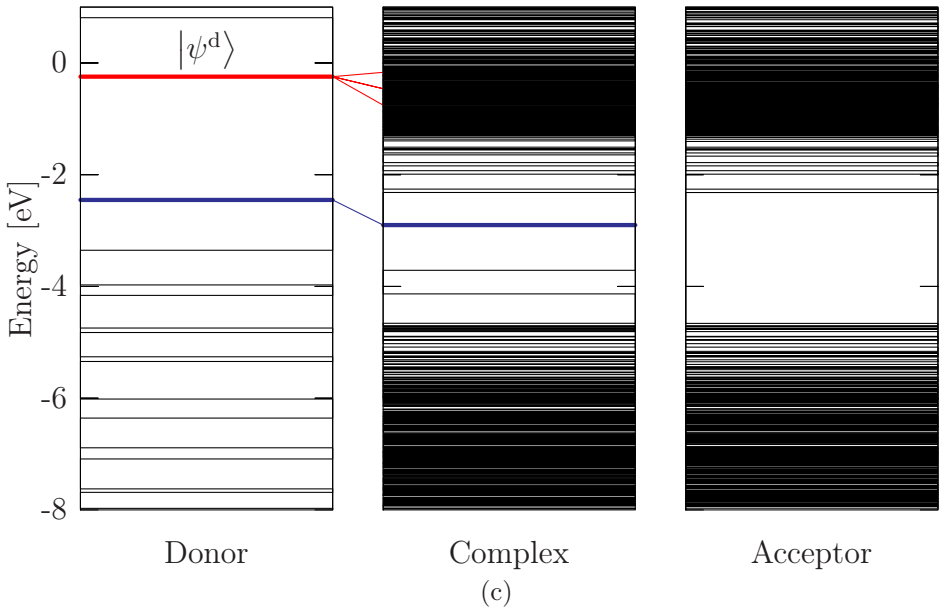
$|\psi^{\mathrm{d}}\rangle$
0
-2
-4
-6
-8
Energy [eV]
Donor
Complex
Acceptor

(c)

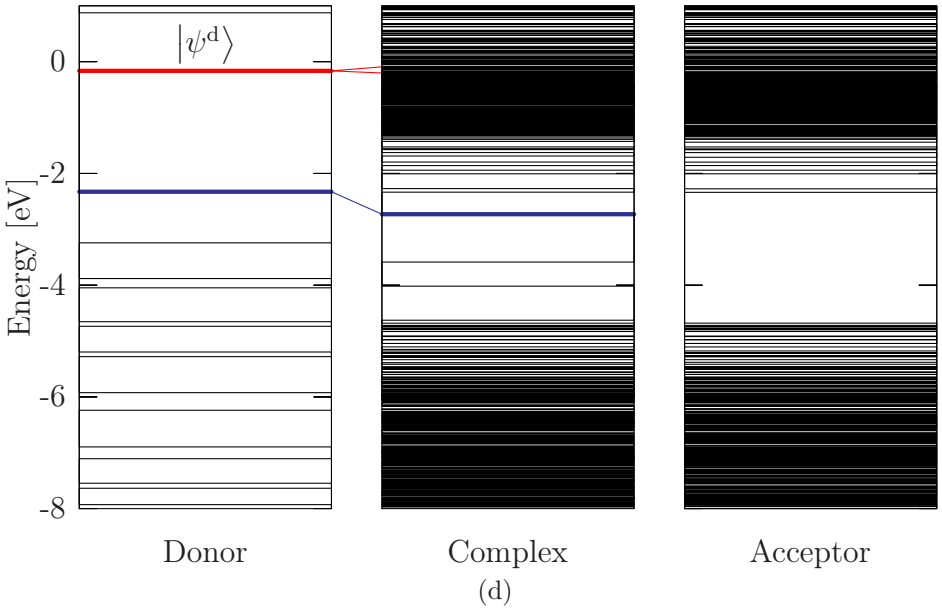
$|\psi^{\mathrm{d}}\rangle$
0
-2
-4
-6
-8
Energy [eV]
Donor
Complex
Acceptor

(d)

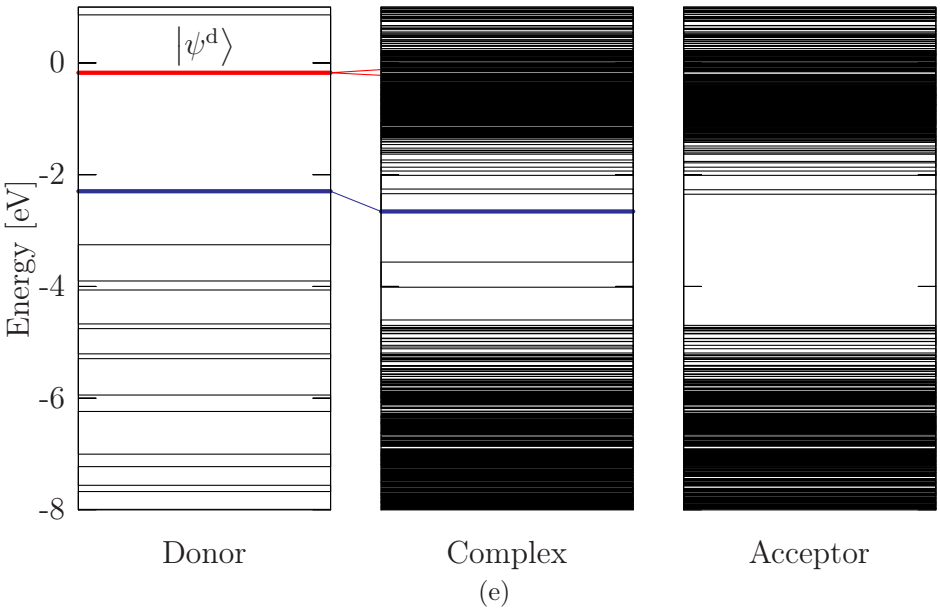

Figure D.10: Energy-level scheme of alizarin-$(TiO_2)_{54}(H_2O)_{58}$ with the alizarin adsorbate (a) 0.1 Å, (b) 0.2 Å, (c) 0.3 Å, (d) 0.4 Å and (e) 0.5 Å away from its equilibrium position to the TiO_2 substrate along the (100) direction. From left to right: energy levels of the donor orbitals (obtained from the partitioning procedure) which are localized in the adsorbate, energy levels of the overall complex and energy levels of the acceptor orbitals (obtained from the partitioning procedure) which are localized in the semiconductor substrate. The selected donor state $|\psi^{d}\rangle$ as well as the correlations among some energy levels relevant for the ET reaction are indicated.

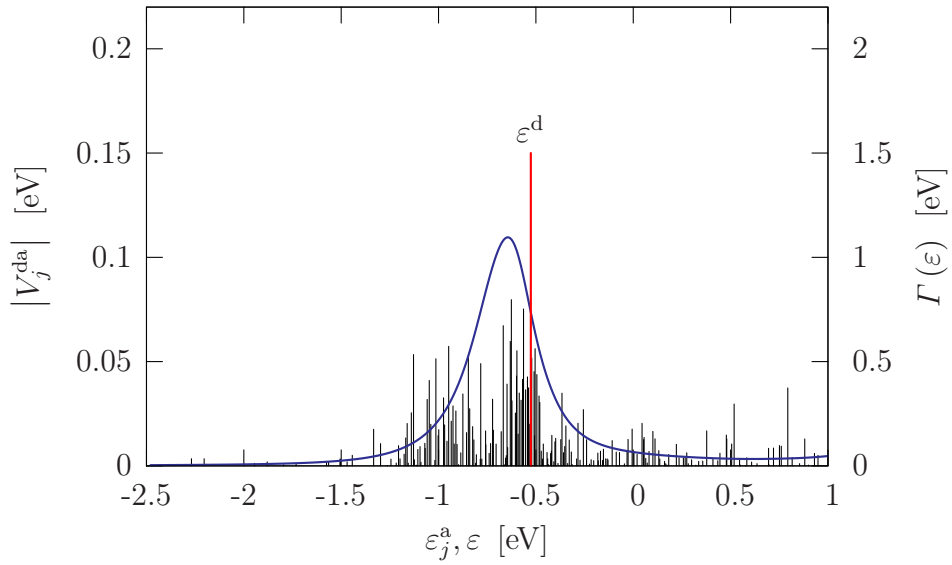
0.2
0.15
0.1
0.05
0
2
1.5
1
0.5
0
-2.5
-2
-1.5
-1
-0.5
0
0.5
1
ε^{d}
$|V_j^{\mathrm{da}}|$ [eV]
$\Gamma(\varepsilon)$ [eV]
$\varepsilon_j^{\mathrm{a}}, \varepsilon$ [eV]

(a)

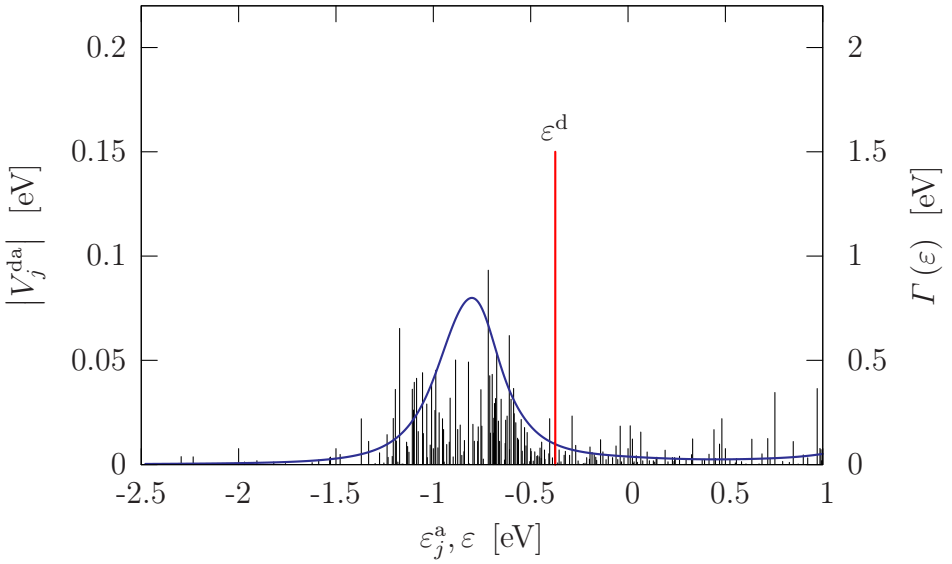
0.2
0.15
0.1
0.05
0
2
1.5
1
0.5
0
-2.5
-2
-1.5
-1
-0.5
0
0.5
1
ε^{d}
$|V_j^{\mathrm{da}}|$ [eV]
$\Gamma(\varepsilon)$ [eV]
$\varepsilon_j^{\mathrm{a}}, \varepsilon$ [eV]

(b)

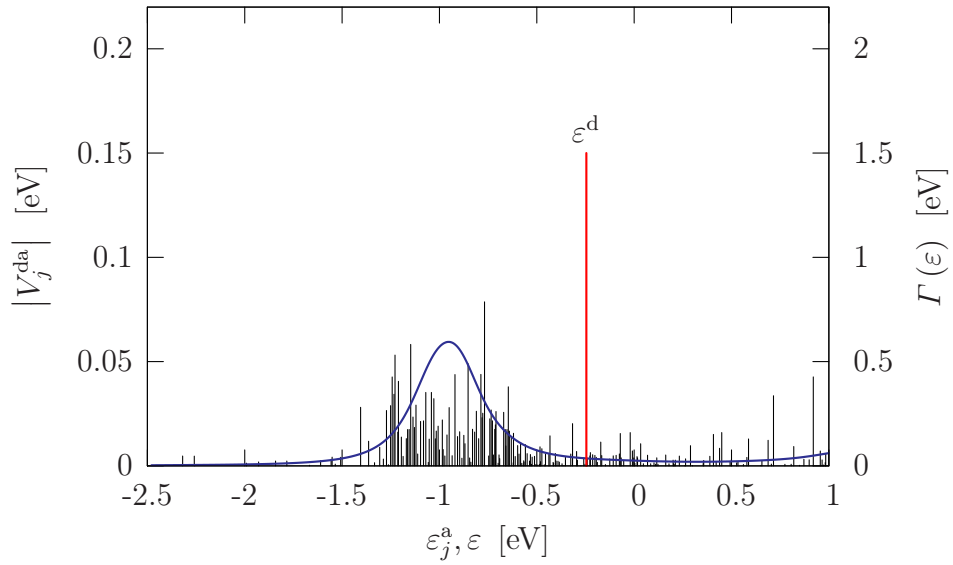
0.2
0.15
0.1
0.05
0
2
1.5
1
0.5
0
-2.5
-2
-1.5
-1
-0.5
0
0.5
1
ε^{d}
$|V_j^{\mathrm{da}}|$ [eV]
$\Gamma(\varepsilon)$ [eV]
$\varepsilon_j^{\mathrm{a}}, \varepsilon$ [eV]

(c)

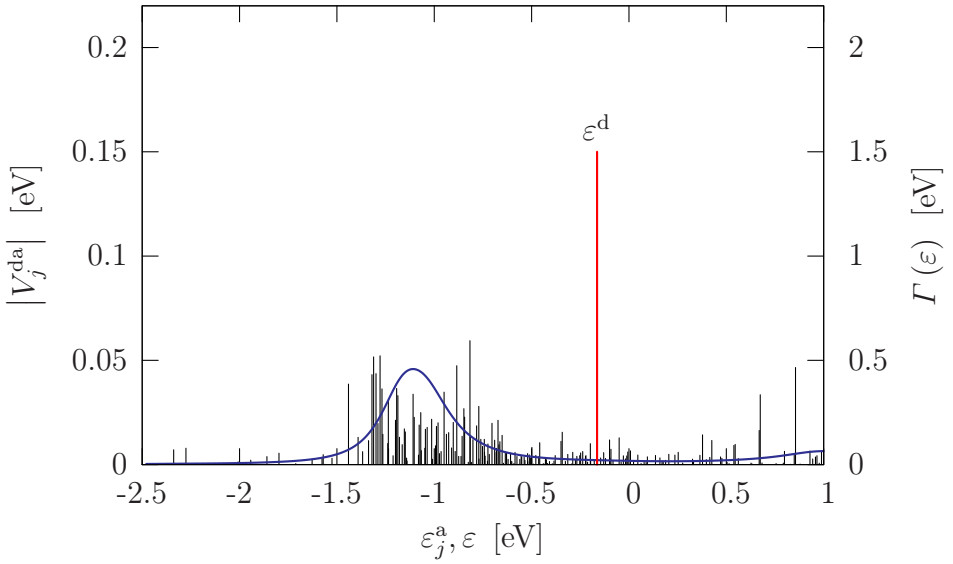
0.2
0.15
0.1
0.05
0
2
1.5
1
0.5
0
-2.5
-2
-1.5
-1
-0.5
0
0.5
1
ε^{d}
$|V_j^{\mathrm{da}}|$ [eV]
$\Gamma(\varepsilon)$ [eV]
$\varepsilon_j^{\mathrm{a}}, \varepsilon$ [eV]

(d)

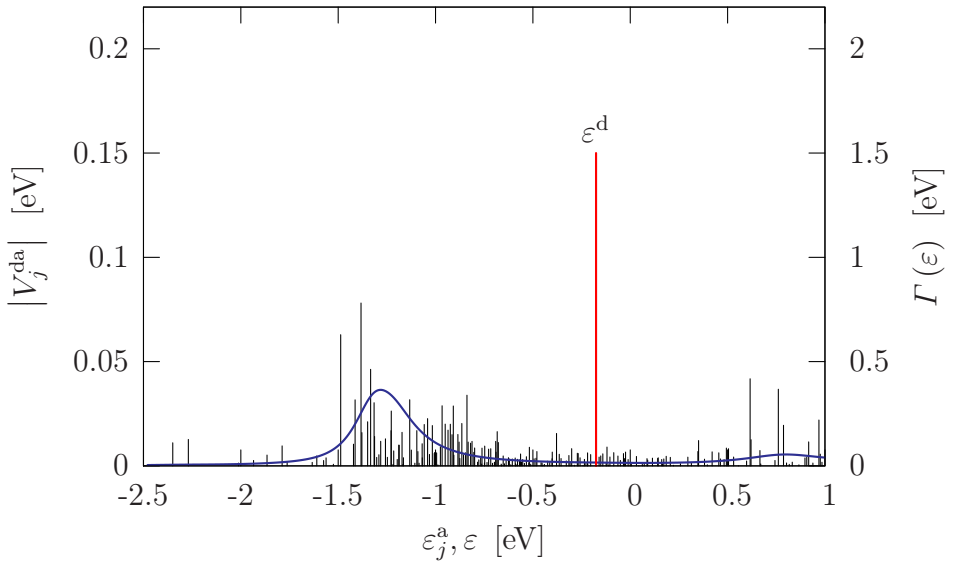

(e)

Figure D.11: Donor-acceptor coupling and the decay-width functions of the investigated complexes alizarin-$(TiO_2)_{54}(H_2O)_{58}$ with the alizarin adsorbate (a) 0.1 Å, (b) 0.2 Å, (c) 0.3 Å, (d) 0.4 Å and (e) 0.5 Å away from its equilibrium position to the TiO_2 substrate along the (100) direction (*cf.* Fig. 3.6 for detailed descriptions and legends).

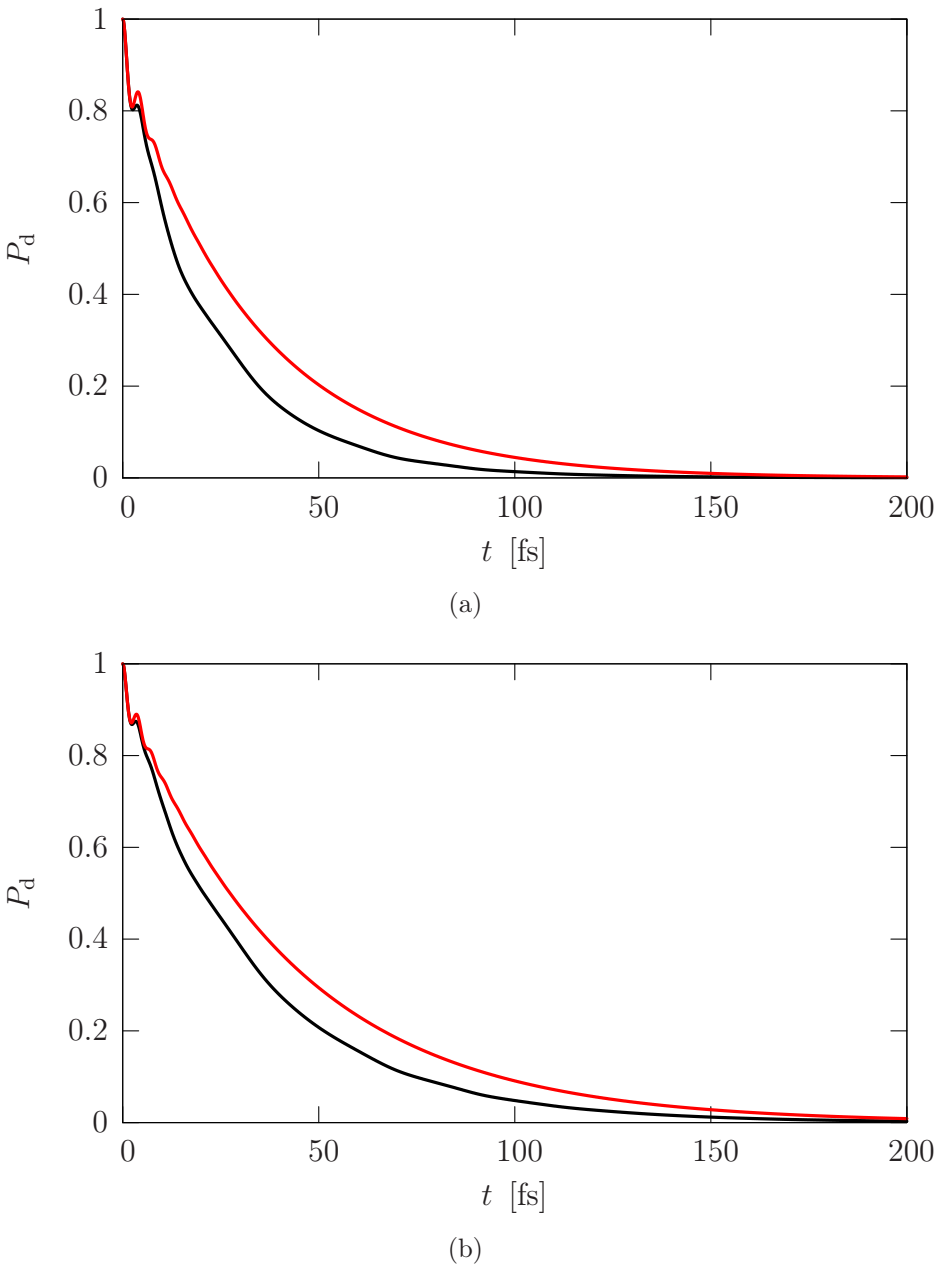

Figure D.12: Population dynamics of the donor state after photoexcitation in the alizarin-TiO_2 systems with the alizarin adsorbate away from its equilibrium position to the TiO_2 substrate along the (100) direction for (a) 0.4 Å and (b) 0.5 Å. Shown are results obtained for the model of an infinite TiO_2 surface. Both results with vibronic coupling (black lines) and without vibronic coupling (red lines) are depicted.

List of abbreviations

C343	coumarin 343
PyC	4-pyridinecarboxylic acid (isonicotinic acid)
PyP	4-pyridinephosphonic acid
PeC	3-perylenecarboxylic acid
PeP	3-perylenephosphonic acid
AO	atomic orbital
DFT	density functional theory
TD-DFT	time-dependent density functional theory
DoF	degree of freedom
DSSC	dye-sensitized semiconductor solar cell
ECP	effective core potential
ET	electron transfer
FC	Franck-Condon
FCI	full configuration interaction
MCTDH	multiconfigurational time-dependent Hartree
ML-MCTDH	multilayer multiconfigurational time-dependent Hartree
L1	level-1
L2	level-2
...	...
MO	molecular orbital
HOMO	highest occupied molecular orbital
LUMO	lowest unoccupied molecular orbital
NAMD	nonadiabatic molecular dynamics
PES	potential energy surface
SCF	self-consistent field
TDSCF	time-dependent self-consistent field
SCH	self-consistent hybrid
SP	single particle
TDH	time-dependent Hartree
TDSE	time-dependent Schrödinger equation
ZPE	zero-point energy